Analysis of P-wave attenuation anisotropy in fractured porous media

Aniekan Martin Ekanem

Thesis submitted in partial fulfilment of

the requirements for the degree of
Doctor of Philosophy

School of GeoSciences

University of Edinburgh

2012

Declaration

I declare that this thesis has been composed solely by me and that it has not been submitted, either in whole or in part, in any previous application for a degree. Except where otherwise acknowledged, the work presented is entirely my own.

Aniekan Martin Ekanem

August, 2012

Abstract

Fractures exert a strong influence on fluid flow in subsurface reservoirs, and hence an adequate understanding of fracture properties could provide useful information on how they may be managed optimally to produce oil and gas or to be used as repositories for carbon dioxide (CO_2) to mitigate climate change. Since fractures are commonly aligned by the stress field, seismic anisotropy is a key tool in investigating their properties. Velocity anisotropy is now a well-established technique for determining properties such as fracture orientation and density, but in recent years, attention has focused on quantifying azimuthal variations in P-wave attenuation to provide additional information, especially on the fracture size. However, the practical application of this attribute in geophysical exploration is still limited due to the uncertainty associated with its measurement and the difficulty in its interpretation in terms of rock properties. There is still a lack of proper understanding of the physical processes involved in the mechanisms of attenuation anisotropy. In this thesis, I use the seismic modelling approach to study the effects of attenuation anisotropy in fractured porous media using P-waves with the main aim of improving the understanding of these effects and exploring the physical basis of using attenuation anisotropy as a potential tool for the characterization of fractured reservoirs.

Fractures with length on the order of the seismic wavelength in reservoir rocks cause scattering of seismic waves which exhibits characteristic azimuthal variations. I study these scattering effects using complementary seismic physical (scale-model laboratory experiments) and numerical (finite difference) modelling approaches. The results of both approaches are consistent in delineating fracture properties from seismic data. The scattered energy is quantified through estimates of the attenuation factor (the inverse of the seismic quality factor Q) and shown to be anisotropic, with elliptical ($\cos 2\theta$) variations with respect to the survey azimuth angle θ. The minor axis of the Q ellipse corresponds to the fracture normal. In this direction, i.e. across the material grain, the attenuation is a maximum. The major axis corresponds to the fracture strike direction (parallel to the material grain) where minimum attenuation occurs.

Empirically, the magnitude of P-wave attenuation anisotropy is greater in fluid-saturated rocks than in dry rocks. I study the influence of fluid saturation on P-wave attenuation through synthetic modelling and compare the attenuation signature to that of dry fractured rocks. The results of the analysis show that the relaxation time strongly controls the frequency range over which attenuation occurs. The magnitude of the induced attenuation increases with polar angle and also away from the fracture strike direction. The attenuation exhibits elliptical variations with azimuth which are also well fitted with a cos2θ function. The magnitude of the attenuation anisotropy is higher in the case of the fluid-saturated rocks. All of these properties of the numerical model are in agreement with the results of empirical experiments in the laboratory.

The same crack density can result from many small cracks, from a few large cracks, or from an equal number of cracks of various sizes with varying thicknesses in the same volume of background material. This makes it difficult to distinguish between the anisotropy caused by micro-cracks and that caused by macro-cracks. I study the effects of fracture thickness or aperture on P-wave scattering attenuation through seismic physical modelling, and find that the induced attenuation has a direct relationship with the fracture thickness or aperture. This result indicates the potential of using P-wave attenuation to get information which might be useful in examining the effects of voids in the rocks, and also provides a basis for further future theoretical development to distinguish the effects caused by thin micro cracks and large open fractures.

Finally, I study the effects of two types of fluid saturation (brine and CO_2 in the supercritical state) on P-wave attenuation through synthetic modelling, with particular attention to varying CO_2 saturation using the CO_2 properties at the Sleipner gas Field in the North Sea. The presence of CO_2 causes more attenuation in the numerical model output than when the rock is saturated with only brine. The induced attenuation increases with decreasing percentage of CO_2 saturation and has a maximum magnitude at 10 % CO_2 saturation. Further work is needed to quantify the additional effect of fractures on these results.

Acknowledgements

Many people have helped me in the actualization of my dream of studying up to the PhD level and I will like to express my sincere gratitude to all of them. First and foremost, I wish to express my profound and sincere gratitude to the Akwa Ibom State University of Science and Technology (AKUTECH) for their sponsorship of my PhD studies at the University of Edinburgh. I am most grateful to my supervisors: Prof Xiang Yang Li, Prof Ian Main and Dr Mark Chapman for their guidance and monitoring of the progress of this thesis throughout the years. In particular, I am very grateful to Prof Xiang Yang Li for his scholarly advice, suggestions, corrections and creating a conducive atmosphere for me during my four years of study in Edinburgh and Prof Ian Main for his patience in answering all my queries and especially for his many academic suggestions. I am also grateful to Dr Mark Chapman from whose wealth of experience and expertise in rock physics I tapped immensely. I am not forgetting all the supports and advice from Dr Dai and Dr David Booth.

I am very grateful to the China National Petroleum Corporation (CNPC) Key Lab at the China University of Petroleum, Beijing - China for providing the physical modelling data used in this thesis. Special thanks to Prof Wei, Prof Wang, Prof Di and Dr Anyong all of the China University of Petroleum - Beijing for being very good host during my visit to the Key Lab.

I am greatly indebted to Dr A. E. Akpan of the University of Calabar, Nigeria for his assistance, co-operation, support, encouragement, and especially for always being there at times of need. I also appreciate all the supports and love from Mr F. S. Akpan of the Obong University - Nigeria and also Mr A. P. Udoh of St Mary’s Science College - Abak, Nigeria and his family for all their help, encouragement and understanding.

I remain ever indebted to my parents and siblings for their supports, patience, love, and encouragements right from my childhood days till now. I am not forgetting all the love, care, encouragement and assistance from my God parents, Archb. and Mrs N. A. Eshiet and his family.

I will not forget in haste all the lovely Lab mates I had while studying in Edinburgh. To Zhongping Q., Adam W., Isabel Varela, Anish V., Heather N, Tieqiang Z., Chuntao Z. Weining Li, Zhiqi, Ben, Yungui Xu etc, I appreciate all your efforts. The nice times we had in Edinburgh will remain ever green in my memory. I am most especially grateful to Yungui

Xu for his helping hands and also making his FD modelling codes available to me for the finite-difference modelling work in this thesis.

I am grateful to the IT support team in the likes of Jane Robertson, Steve Love and Brian Bainbridge for all their help throughout the years. I am not forgetting all the help, love, advice, supports and encouragements from my friends. To Afiya, H., Nwanpka, S., Esuene, S., Usese, A., Ashimolowo, D., Femi O., Imoni, S., Lucky M., Eneanwan, E, Adeoye, O. and Stephen A., I appreciate all your efforts.

Finally, I wish to put on record my special indebtedness to all those (not mention here) who have contributed in one way or the other towards a successful completion of my studies in Edinburgh.

TO GOD BE THE GLORY

In loving memory of my mum

Table of contents

List of Figures

List of Tables

Notations and symbols

Abbreviations

AC	Alternating current
AIC	Akaike’s Information Criterion
AVO	Amplitude Variation with Offset
AVOA	Amplitude Variation with Offset and Azimuth
CDP	Common Depth Point
CMP	Common Mid Point
CNPC	China National Petroleum Corporation
DC	Direct current
FD	Finite Difference
FFID	Field File IDentification number
FFT	Fast Fourier Transform
HTI	Transverse Isotropy with Horizontal axis of symmetry
LPSR	Logarithm of Power Spectral Ratio
NMO	Normal Move Out
P-wave	Compressional wave
QVO	Quality factor Versus Offset
QVOA	Quality factor Variation with Offset and Azimuth
S-wave	Shear wave
SSG	Standard Staggered Grid
TI	Transverse Isotropy
TTI	Transverse Isotropy with Tilted axis of symmetry
VSP	Vertical Seismic Profiling
VTI	Transverse Isotropy with Vertical axis of symmetry

Symbols

a	mean crack radius
A	Element of area
δa	infinitesimal surface area
δF	infinitesimal force
A_0	amplitude at a distance $x = 0$
A(x)	amplitude at a distance x
$C1$	Arbitrary constant
$C2$	magnitude of azimuthal variation in attenuation
c_{ijkl}	elastic or stiffness tensor
D	Number of model parameters
E	net peak strain energy
$-\Delta E$	Energy loss per cycle
f	Frequency
G	Geometrical spreading factor
$\mathbf{G}_{\mathbf{ik}}$	Christoffel’s matrix
I	Intercept
κ	Permeability
K	Bulk modulus
L	Log-likelihood function
m_a	Mass of fluid in element a
N	Number of cracks
$\mathbf{n}$	unit vector
p	Slope
P(f)	Power spectrum
Q	Seismic quality factor
qP	quasi-compressional wave

qS1	fast quasi-shear-wave
qS2	slow quasi-shear-wave
R	Reflectivity factor
S	fracture compliance
S_N	normal fracture compliance
S_T	Tangential fracture compliance
t	Traveltime
T_i	Traction
$\mathbf{U}$	polarization vector
u	displacement
V	Volume
v	Velocity
v_g	Group velocity
v_p	P-wave velocity in an isotropic medium
v_{rms}	Root mean square velocity
v_s	S-wave velocity in an isotropic medium
x	position or distance
$\delta \mathbf{x}$	increment in position
δ_{ij}	Kronecker's delta function
α	Attenuation coefficient
η	Viscosity
θ	survey azimuth direction
θ_o	fracture normal direction
λ	Lame's constant
μ	Shear modulus
π	Pi (constant)
ρ	Density
ρ_f	Fluid density

ω	Angular frequency
ζ	Porosity
ϕ	Grain size
ε_{ij}	Strain tensor
ψ_{ij}	Rotation tensor
χ	Crack density
σ_{ij}	Stress tensor

Chapter 1 Introduction

1.1 Motivation and thesis objectives

Fractures are very common in subsurface reservoirs and exert a tremendous influence on fluid flow. For instance, fractures can control permeability by providing pathways for fluid flow and as such have great impact on the hydrocarbon production (Luo and Evans, 2004). Alternately, in many reservoirs with low permeability, hydraulic fracturing is necessary in order to enhance the natural fracture system sufficiently to increase the rate of production (e.g. Block *et al.*, 1994; House *et al.*, 2004). Consequently, an adequate understanding of fracture properties could provide useful information on how they may be exploited optimally to produce oil and gas to meet the increasing global energy needs or to be used as repositories for carbon dioxide (CO_2) to mitigate climate change.

Among the various geophysical methods, the seismic method provides a rapid and inexpensive means of detecting fracture zones in the subsurface. At depth, fractures tend to be aligned normal to the direction of minimum in-situ stress acting on them (Schoenberg and Sayers, 1995), giving rise to seismic anisotropy. In the past few years, there has been an increasing interest in the use of seismic anisotropy to characterize fractured hydrocarbon reservoirs (e.g. Hall *et al.*, 2000, Gray and Head, 2000; Li *et al.*, 2003, Luo and Evans, 2004). A number of techniques have been developed to derive fracture properties from measurement of seismic anisotropy. These include analysis of shear-wave splitting and azimuthal variations of seismic wave velocity, traveltime, amplitude and amplitude variation with offset (AVO) gradient (Sena, 1991; Sayers and Ebrom, 1997; Li, 1997; Hall *et al.*, 2000; Wang *et al.,* 2007). A shear-wave entering an anisotropic medium is split into two modes; the fast and the slow modes (S1 and S2) respectively. For a near-vertical incidence, the direction of polarization of the fast mode corresponds to the fracture strike while the time delay between the two modes indicates the degree of anisotropy (Yardley and Crampin, 1991 and Liu *et al.*, 2003). Analysis of azimuthal variations of P-wave travel time, velocity, amplitude and AVO gradients have revealed that these seismic attributes exhibit characteristic elliptical ($\cos 2\theta$) variations with respect to the survey azimuth angle θ (Ruger, 1998; Mallick *et al.*, 1998; Grechka and Tsvankin, 1998; Maultzsch *et al.*, 2007). Thus, by using the ellipse-fitting technique, the fracture orientations and density can be inferred from the axes of the ellipse. The wave velocity is fastest in the direction parallel to the fractures and slowest in the direction perpendicular to the fractures. Seismic amplitudes are very sensitive to the presence of aligned fractures (Pyrak-Nolte *et al*., 1990) and the analysis of amplitude variation with offset and azimuth (AVOA) is a common technique of extracting fracture properties from seismic data (e.g. Ruger, 1998; Lynn and Beckham, 1998; Jenner, 2002; Shen *et al*., 2002; Hall and Kendall, 2003; Minsley *et al*., 2004). However, Hall and Kendall (2000 and 2003) observed that there is a possible 90° ambiguity in the fracture orientation obtained from AVOA analysis and thus the need to use other seismic attributes to resolve the ambiguity. Although shear-waves have been shown to be more sensitive to fractures (e.g. Li, 1997), the use of P-waves is still more popular in fracture detection analysis as a result of the problems of requirement of specialized sources and the processing difficulties associated with shear-wave data (e.g. Hall and Kendall, 2000; Luo and Evans, 2004).

The study of P-wave attenuation is also becoming important in seismic exploration as it provides an additional tool for the characterization of fractured hydrocarbon reservoirs. Attenuation has been shown to be very sensitive to fractures (e.g. Walsh

1966; Klimentos and McCann 1990; Rathore *et al.*, 1995; Maultzsch *et al.*, 2007). Adequate knowledge of attenuation could provide useful information on the nature of fluid saturation in the pores of the rocks (e.g. Dvorkin and Mavko, 2006, Odebeatu *et al.*, 2006) and attenuation has been recognized to be more sensitive to variations in fluid saturation than velocity (e.g. Klimentos, 1995; Jones *et al.*, 1997). In partially saturated rocks, for instance the magnitude of attenuation is higher than in fully saturated rocks (Johnson *et al.*, 1979; Winkler and Nur 1982). Furthermore, adequate knowledge of attenuation can lead to a better understanding of AVO and AVOA analysis for fractured reservoir characterization (Dasgupta and Clark, 1998; Dasios *et al.*, 2001). For the propagation of seismic waves in a medium with a set of aligned vertical fractures, equivalent medium theories (e.g. Tod, 2001; Chapman, 2003) predict azimuthal variations in the induced attenuation. Indeed, azimuthal variations in P-wave attenuation have been observed in both laboratory and field data (e.g. Clark *et al.*, 2001; Luo *et al.*, 2006; Chichinina, *et al.*, 2006; Maultzsch *et al.*, 2007; Clark *et al.*, 2009). The task of using P-wave attenuation anisotropy for fracture prediction in the Earth's crust still needs more understanding of the underlying principle which is the major focus of my thesis.

Several mechanisms of attenuation anisotropy have been proposed. Most are based on the observation that rocks contain microscopic cracks and fractures and that the pore space may be saturated with fluids. Frictional dissipation due to relative motions on dry surfaces of thin cracks caused by a passing seismic wave in dry rocks leads to the conversion of the seismic energy into heat, resulting in attenuation (e.g. Walsh, 1966). In fluid saturated rocks, one common cause of attenuation is the 'squirt flow' phenomenon induced by seismic wave propagation (e.g. Mavko and Nur 1979; O'Connell and Budiansky 1977; Chapman, 2003). When a seismic wave passes through the rock, pressure gradients are generated which could be away from the propagation direction of the wave. Fluid then flows along the pressure gradient from the more compliant parts of the pore space into the stiffer parts during compression and back again during dilatation. This phenomenon is known as 'squirt flow'. Chapman (2003) developed a poro-elastic model which predicts that the attenuation suffered by the wave depends both on the source-receiver azimuth and offset or incidence angle. Maultzsch *et al.,* (2007) demonstrated through synthetic modelling studies based on Chapman’s poroelastic model and field data analysis that azimuthal variations in attenuation are measureable from VSP surveys. Chichinina *et al.,* (2006) studied the variation of the seismic quality factor versus offset and azimuth (QVOA) using synthetic PP-reflection data generated for the dissipative HTI model proposed by Hudson *et al.,* (1996) and concluded that seismic wave attenuation is strongest in the direction normal to the fractures and weakest parallel to the fractures. Dasgupta and Clark (1998) introduced a method known as the seismic quality factor (Q) - versus offset (QVO) method to estimate Q from surface seismic reflection data. Clark *et al.,* (2001) utilized the QVO method to estimate azimuthal variations of attenuation from a 3D marine dataset acquired in the offshore of West Africa and found a consistency in their interpreted fracture orientation with the fracture orientation inferred from azimuthally variable AVO. Clark *et al.,* (2009) studied the variation of Q-factor versus offset and azimuth as a means of characterizing fractured reservoir from marine surface-seismic reflection data using the QVO method and found that attenuation is least in the direction closest to the fracture trend and most in the direction normal to the fracture trend. Willis *et al.,* (2006) and Burns *et al.,* (2007) demonstrated through numerical modelling that azimuthal variations in the scattered wavefield caused by aligned fractures and the amount of the scattered energy could both provide useful information on fracture orientations. Seismic physical modelling studies to quantify the amount of the scattering energy caused by fractures through attenuation estimates could help to improve the understanding of these effects and explore the physical basis of using attenuation anisotropy as a potential tool for the characterization of fractured reservoirs. However, these studies are relatively scarce in the literature as most of the physical modelling studies reported are devoted to the effects of aligned fractures on seismic velocity, travel time, AVO gradient and amplitude (e.g. Cheadle *et al.*, 1991; Isaac and Lawton, 1999; Wang *et al.,* 2007; Wei *et al.*, 2007a and 2007b). The same fracture density can result from either a few large cracks or many small ones in the same volume of background material, and an understanding of these effects could be of great importance in fractured hydrocarbon reservoir characterization to differentiate between the effects caused by thin micro-cracks and large open fractures. Wei *et al.,* (2007a and 2007b) used the seismic physical modelling approach to investigate the influence of fracture thickness or aperture on transmitted P-wave data. Their results show significant changes in the P-wave amplitude and waveforms with increasing thicknesses. The P-wave is significantly attenuated as the thickness of the chips increases with more attenuation perpendicular to the fractures. However, their study fails to provide quantitative estimates of the observed attenuation from the waveforms. The presence of CO_2 in the reservoir can result in changes in seismic properties such as travel time, velocity, amplitude and attenuation and such changes can provide useful information for the characterization the reservoir. Time-lapse studies for monitoring CO_2 sequestration have shown that the presence of CO_2 can cause significant changes in both the P- and S- wave velocities (e.g. Arts *et al.*, 2004; Chadwick *et al.*, 2005, Amir and Landro, 2009). There is still a lack of adequate understanding of the effect that CO_2 might have on seismic attenuation especially at varying degrees of saturation. Thus, despite the intensive effort in research and development related to seismic characterization of fractured reservoirs using P-wave attenuation, practical application of this attribute in geophysical exploration is still limited partly because of the uncertainty associated with its measurement and also the difficulty in its interpretation in terms of rock properties (e.g. Jeng *et al*., 1999, MacBeth, 1999; Rongrong *et al.*, 2006). There is still lack of proper understanding of the physical processes involved in the mechanisms of attenuation anisotropy (e.g. Helle *et al.*, 2003; Batzle *et al.*, 2005). An integrated seismic modelling approach comprising the seismic physical and numerical modelling approaches could add more valuable understanding to some of these predictions and observations of attenuation characteristics, and thus provide a physical basis of using attenuation anisotropy for delineation of fracture properties from seismic data. Thus, the main goal of my thesis is to develop a fuller understanding of the attenuation characteristics in aligned fractured and porous media and assess the physical basis of using P-wave attenuation anisotropy to characterize fractured hydrocarbon reservoirs.

Here, I present an integrated seismic modelling study of attenuation anisotropy and its effects in porous fractured media. An integrated seismic modelling study comprising the seismic physical and the numerical modelling approaches will allow for the comparisons of the results to gain a fuller understanding of anisotropic attenuation effects in fractured media. The results provide valuable insight into how fracture characterisation from seismic data may be improved. They also demonstrate how attenuation anisotropy may be used in practice as a potential exploration tool to complement the use of traveltime, velocity, amplitude and AVO gradient attributes.

In specific terms, my research work covers four areas. Firstly, I use complementary seismic physical (scale-model laboratory experiments) and numerical (finite-difference) modelling approaches to study the effects of scattering caused by a set of aligned fractures with scale length on the order of seismic wavelength. Experimental studies with laboratory scale models and numerical simulation studies (e.g. Schultz and Toksöz, 1995; Willis *et al.*, 2004a and 2004b; Willis *et al.*, 2006; Burns *et al.*, 2007) have shown that the scattered energy is more in the direction perpendicular to the fractures than in the parallel direction. Here I quantify the amount of scattering energy through attenuation estimates to get more insight into the current use of the azimuthal variation in the scattered energy for delineating fractures from seismic data.

Secondly, I study the influence of fluid saturation on P-wave attenuation anisotropy through synthetic modelling and compare the attenuation signature to that of dry fractured rocks. P-wave attenuation anisotropy has been observed to have higher magnitude in fluid-saturated fractured rocks (e.g. Maultzsch *et al.*, 2007). Here I study the effects of fluid saturation on P-wave attenuation using the poro-elastic model of Chapman (2003) to gain more understanding of the fluid effects.

Thirdly, I study the effects of fracture thickness or aperture on P-wave scattering attenuation through seismic physical modelling. Hudson's (1980, 1981) equivalent medium theory provides a means of obtaining crack density information from measurement of seismic anisotropy. However, the same crack density can result from many small cracks or from few large cracks or equal number of cracks with the same radius but varying thicknesses (or aperture) in the same volume of background material, thus indicating the inability of the theory to distinguish between the anisotropy caused by micro-cracks and that caused by macro-cracks.

Finally, I study the effects of two types of fluid saturation (brine and CO_2 in the supercritical state) on P-wave attenuation, with particular attention to the effects of CO_2 using the CO_2 properties at the Sleipner gas field in the North Sea. The presence of CO_2 in the reservoir can result in changes in the seismic wave attenuation and these changes can provide useful information for the characterization of the reservoir.

1.2 Thesis layout

This thesis is divided into nine chapters. Following this general introduction (Chapter 1), I give a review of the fundamental theory of seismic anisotropy and seismic wave propagation in fractured media in Chapter 2. Here the equivalent medium theory which provides the basis for using seismic anisotropy to characterize the fractured reservoirs is reviewed. In particular, I give a brief review of Hudson, Schoenberg, Thomsen, and poro-elastic models, and finish the chapter by giving a review of attenuation and its use in fracture characterization from seismic data.

In Chapter 3, I review the methods used in this thesis for the attenuation analysis. I start the chapter by giving a review of the spectral ratio method which is the commonest method of estimating attenuation from seismic data. The seismic quality factor versus offset (QVO) method, which is basically an extension of the spectral ratio method, is also reviewed along with its associated improvements over the years. I finish the chapter by carrying out a synthetic test to assess the performance of the QVO - spectral ratio method on synthetic datasets with known solutions before applying the method to complex scenarios in this thesis.

In Chapter 4, I study the effects of scattering attenuation anisotropy caused by a set of aligned fractures through seismic physical modelling. The construction of the physical models and acquisition of the seismic response from the model all preceded the study. The physical models were built in the China National Petroleum Corporation (CNPC) geophysical key laboratory in China and the seismic reflection response through the model was recorded using the pulse and transmission method. The base model is made up of two horizontal isotropic layers. To simulate a set of aligned fractures, thin penny-shaped chips made from a mixture of epoxy resin and silicon rubber were embedded into the isotropic background material of the second layer and arranged to form two inclined fracture models. The recorded seismograms were provided to me at the start of the project, and the results of the analysis are presented in this chapter.

In Chapter 5, I study the influence of fluid saturation on P-wave attenuation anisotropy through synthetic modelling using Chapman's (2003) model to compare the attenuation signature to that of dry fractured rocks. I consider the case of only one type of fluid saturation in the pores of the rock and start the chapter by giving a review of Chapman's (2003) model. I then examine the influence of fluid mobility on seismic wave attenuation and finally the effects of attenuation anisotropy on the synthetic data.

In Chapter 6, I extend the study of the effects of scattering attenuation done in Chapter 4 to examine the influence of fracture thickness or aperture on the induced attenuation. The physical models used were also built in the CNPC geophysical key laboratory and consists of two horizontal layers. Here thin round chips of the same diameter and varying thicknesses or apertures were made from a mixture of epoxy resin and silicon, embedded into the isotropic background of the second layer, and arranged to form six fracture blocks. The chips in each block have the same density and thickness or aperture, but the thickness varies from block to block. Here I analysed the results in a similar way as in Chapter 4.

In Chapter 7, I carry out a finite-difference modelling study of the effects of scattering attenuation anisotropy to complement the physical modelling study in Chapter 4, and to allow for the comparison of the physical and numerical techniques for modelling layered anisotropic media. The theoretical model was designed to have the same properties as the physical model used in Chapter 4. The chapter concludes with a comparison of the results of the two approaches.

In Chapter 8, I extend the synthetic modelling study of Chapter 5 to examine the effects of two different types of fluid saturation on the induced attenuation with particular focus on CO_2. I start by studying the effects of fluid mobility and then the sensitivity of P-wave attenuation to CO_2 saturation. I finish the chapter by looking at a field data example from the Sleipner gas field in the North Sea to compare the synthetic modelling results. While this is not a study of the effect of fractures per se, it can be used as a benchmark to quantify their effect in later studies, in particular the relative effects of saturation and fracture properties on the seismic wave field.

In Chapter 9, I give a summary of the findings from my thesis and provide some suggestions for future work. The theory of how the anisotropic reflectivity method is implemented in ‘Aniseis’ is given in the appendix followed by a list of the publications from my thesis.

1.3 Datasets and computer resources

1.3.1 Datasets

In this thesis, I make use of a total of six data sets for the attenuation analysis: two physical modelling data sets, three synthetic data sets (one generated using a finite-difference scheme and the other two generated using the ‘Aniseis’ modelling software package) and a field data example from the Sleipner gas field in the North Sea.

Physical modelling data sets

I use the laboratory-scale physical modelling data sets to study the effects of P-wave scattering attenuation anisotropy caused by a set of aligned fractures. The experimental design and all the data produced from the physical models preceded the start of my thesis. The data sets were obtained in the CNPC geophysical laboratory in China where the physical models were built. In both models, fractures are simulated by embedding thin round chips of known radius and thicknesses or apertures into an isotropic background material. The first model has two sets of inclined fractures and I use this model to study the effects of P-wave attenuation anisotropy in Chapter 4. The second model has chips with the same radius but with varying thicknesses or apertures arranged into six blocks. I used this model to study the effect of fracture aperture or thickness on P-wave attenuation in Chapter 6.

Synthetic data sets

I generated three sets of synthetic data to study the effects of P-wave attenuation in fractured rocks. The first synthetic data was generated from a theoretical model that comprise of four horizontal layers. The third layer has a porous fractured fluid-saturated material and I used the model to study the effects of attenuation anisotropy in the presence of a fluid in Chapter 5. The second synthetic data was generated using the finite-difference modelling scheme and I used this data to study the effects of scattering attenuation anisotropy in Chapter 7 to complement the work I did in Chapter 4. The last synthetic data was generated from a theoretical model that has a layer that comprised of a porous cracked material saturated with both brine and CO_2 at different levels of concentration. I used this data to study the effects of CO_2 on P-wave attenuation in Chapter 8.

Field data example from the Sleipner gas field in the North Sea

I use a 3D field data example from the Sleipner gas field in the North Sea to find out if the results of the synthetic study in Chapter 8 can provide practical guidelines for interpreting the field data case. The field is a site for large scale CO_2 injection project specifically designed as a measure to mitigate climate change. The data was acquired after the injection of CO_2 into the reservoir in the field.

1.3.2 Computer resources

I made use of the ‘ProMax’ software for the initial processing of the physical modelling data sets prior to attenuation analysis in Chapters 4 and 6. ‘ProMax’ is a commercial seismic data processing software. I made use of the ‘Aniseis’ software to generate the synthetic data used in Chapters 3, 5 and 8 respectively for attenuation analysis. Aniseis is a commercial software package for seismic modelling in anisotropic media. I made use of the Seismic Unix (SU) for display and analysis of the synthetic seismograms in Chapters 3, 5, 7 and 8. Seismic Unix is an open source seismic utilities package supported by the Centre for Wave Phenomena (CWP) at the Colorado School of Mines (CSM). I made use of the Wave Unix (WU) developed by

Xu *et al.,* (2010) to generate the synthetic data used in Chapter 7 for attenuation analysis. Wave Unix is a finite-difference modelling package for modelling the propagation of seismic wave in 3D anisotropic media, which is free for use by the Edinburgh Anisotropy Project (EAP) students, staff and sponsors. I used ‘Matlab’ to carry out all the computations and generating the plots shown in this thesis. Matlab is a commercial software package used for numerical computation and visualization.

Chapter 2 Review of seismic anisotropy

2.1 Introduction

In this chapter, I give a review of the basic concepts of seismic anisotropy and anisotropic wave propagation in fractured media. I also review the equivalent medium theories for seismic wave propagation in fractured media related to my thesis. In particular, I review the concept of seismic attenuation and its anisotropic behaviour, highlighting possible causal mechanisms, and examine its use as an exploration tool in fractured reservoir characterization since my thesis is primarily focussed on P-wave attenuation anisotropy in fractured porous rocks.

2.2 Basic concepts

2.2.1 Seismic anisotropy, effects and causes

Seismic anisotropy can be defined as the variation of seismic wave properties at a point that depends on orientation. Examples of these properties are seismic wave velocity, travel times, amplitude, AVO gradient, polarization and attenuation

(Crampin 1989, Hall *et al.*, 2002). A material whose physical property is independent of orientation is said to be isotropic. Anisotropy is often confused with in-homogeneity or heterogeneity which is the variation of a physical property depending on the position of measurement, but the property remains the same in all directions. Here anisotropy will be taken only to refer to changes in bulk properties with respect to orientation rather than location. Nevertheless, anisotropy itself results from ordered heterogeneities with scale length smaller than the seismic wavelength (Lynn, 2004). Seismic waves propagate with varying velocities in an elastic anisotropic medium depending on the direction of propagation or wave polarization.

Common causes of seismic anisotropy in the subsurface are the preferential orientation of anisotropic mineral grains or the shapes of isotropic minerals such as clay, thin bedding of isotropic layers on a small scale compared to the seismic wavelength (the layers may be horizontal or tilted) and vertical or dipping fractures or micro cracks (Thomsen, 1986; Sayers and Ebrom, 1997 and Tsvankin, 2001). Anisotropy can also be caused by in-situ stress which modifies pore shapes or pre-existing crack configurations (Winterstein, 1990). Fractures in the crust tend to be aligned normal to the direction of minimum in-situ stress field (Sayers and Ebrom 1997) and thus seismic anisotropy could be used to map the direction of stress fields in the crust through the mapping of the fracture orientations.

2.2.2 Stress, strain and elastic or stiffness tensor

The strain tensor is primarily used to analyze the three-dimensional deformation of a medium subjected to stress. Consider a particle initially at a position *x*. Assuming that the particle is moved to another position $x+\delta x$; its relative displacement can be defined as:

$$\delta u_i = u_i(x+\delta x) - u_i(x), \tag{2.1}$$

where $u_i(x)$ and $u_i(x+\delta x)$ are the particle's displacement at positions x and $x+\delta x$ respectively. As $|\delta x|$ is arbitrarily small, we can expand $u_i(x+\delta x)$ using Taylor series as:

$$u_i(x+\delta x) \approx u_i(x) + \frac{\partial u_i(x)}{\partial x_j} dx_j \ , \tag{2.2}$$

where i and *j* are the free indices respectively which can range over the three coordinates (1, 2, 3) in a three dimensional space. Combining Equations (2.1) and (2.2) above gives:

$$\delta u_i = \frac{\partial u_i(x)}{\partial x_j} dx_j \tag{2.3}$$

Equation (2.3) can be re-written as:

$$\delta u_i = \frac{1}{2}\left(\frac{\partial u_i}{\partial x_j} + \frac{\partial u_j}{\partial x_i}\right) dx_j + \frac{1}{2}\left(\frac{\partial u_i}{\partial x_j} - \frac{\partial u_j}{\partial x_i}\right) dx_j \tag{2.4}$$

Equation (2.4) can further be written in a more compact form as:

$$\delta u_i = (\varepsilon_{ij} + \psi_{ij}) dx_j \, , \tag{2.5}$$

where ε_{ij} is known as the strain tensor and is given by:

$$\varepsilon_{ij} = \frac{1}{2}\left(\frac{\partial u_i}{\partial x_j} + \frac{\partial u_j}{\partial x_i}\right) \tag{2.6}$$

ψ_{ij} is the rotation tensor which describes the rotation of the body and is given by:

$$\psi_{ij} = \frac{1}{2}\left(\frac{\partial u_i}{\partial x_j} - \frac{\partial u_j}{\partial x_i}\right) \tag{2.7}$$

u_i and u_j are the displacement components. It is obvious from Equations (2.6) and (2.7) that the strain tensor and the rotation tensor are symmetric and anti - symmetric respectively.

The concept of traction and stress is used to analyze the internal forces acting mutually between particles within a continuum (Aki and Richards, 2002). To define traction, consider Figure 2.1 in which an infinitesimal force δF acts on an infinitesimal surface area δa of the surface A. '**n**' is a unit vector normal to the surface. The traction, T_i acting in this case is defined as the force per unit area (stress) across the internal surface within the body and has the same direction as the force δF and is dependent on **n**. Mathematically, it can be written as:

$$T_i = \frac{\delta F}{\delta a} \quad \text{limit } \delta a \to 0. \tag{2.8}$$

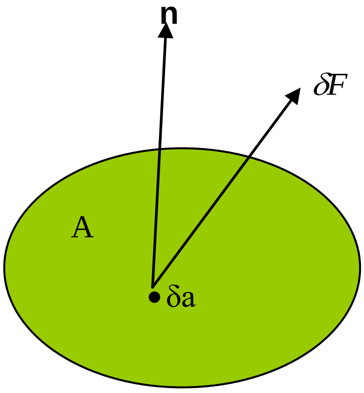

Figure 2. 1: Definition of traction

The surface tractions or stresses acting on a given plane can be broken down into three mutually perpendicular components. These components are the direct stresses (normal to the surface, σ_{ii}) and the shear stresses (in two orthogonal directions tangential to the surface, σ_{ij}, σ_{ik}). In the Cartesian coordinate system for three dimensions, nine components are therefore required to describe the state of stress acting on a particle at a given point. These components can be organized into a matrix form to define the stress tensor as follows:

$$\sigma_{ij} = \begin{pmatrix} \sigma_{11} & \sigma_{12} & \sigma_{13} \\ \sigma_{21} & \sigma_{22} & \sigma_{23} \\ \sigma_{31} & \sigma_{32} & \sigma_{33} \end{pmatrix} \tag{2.9}$$

The diagonal entries of the matrix $(\sigma_{11}, \sigma_{22}, \sigma_{33})$ in Equation (2.9) correspond to the normal stresses while the rest are the shear stresses. The eigenvalues and eigenvectors of this matrix then define the amplitude and direction of the three mutually orthogonal principal components of the stress field. Due to the influence of gravity on geological processes, one of these directions is normally aligned with the vertical in the Earth.

The elastic or stiffness tensor is a 4th order tensor which gives the relationship between the stress tensor and the strain tensor. On the basis of the assumption that the strains associated with seismic wave propagation are usually very small, the strain-stress relationship is expressed by the generalized Hooke's law as:

$$\sigma_{ij} = c_{ijkl}\varepsilon_{kl} \tag{2.10}$$

This relationship is an example of a constitutive relation where c_{ijkl} is the elastic or the stiffness tensor and has 81 components in the general case. Since both the strain tensor and the stress tensor (in the absence of rotational torques) are symmetric, we also have the following relationships:

$$c_{ijkl} = c_{jikl} = c_{ijlk} = c_{klij} \tag{2.11}$$

Thus, the stiffness tensor can be represented more compactly with a change of indices following the 'Voigt' notation (e.g. Thomsen, 1986) as follows:

$$\begin{array}{cccccccc} \text{ij or} & \text{kl} & 11 & 22 & 33 & 32=23 & 31=13 & 12=21 \\ \downarrow & \downarrow & \downarrow & \downarrow & \downarrow & \downarrow & \downarrow & \downarrow \\ \text{m} & \text{n} & 1 & 2 & 3 & 4 & 5 & 6 \end{array} \tag{2.12}$$

c_{ijkl} in Equation (2.11) can be converted into c_{mn} by using Equation (2.12) thus:

$$c_{mn}=\begin{bmatrix} c_{11} & c_{12} & c_{13} & c_{14} & c_{15} & c_{16} \\ c_{21} & c_{22} & c_{23} & c_{24} & c_{25} & c_{26} \\ c_{31} & c_{32} & c_{33} & c_{34} & c_{35} & c_{36} \\ c_{41} & c_{42} & c_{43} & c_{44} & c_{45} & c_{46} \\ c_{51} & c_{52} & c_{53} & c_{54} & c_{55} & c_{56} \\ c_{61} & c_{62} & c_{63} & c_{64} & c_{65} & c_{66} \end{bmatrix} \tag{2.13}$$

Following Equation (2.13), Equation (2.10) can be simplified as:

$$\begin{bmatrix} \sigma_{11} \\ \sigma_{22} \\ \sigma_{33} \\ \sigma_{23} \\ \sigma_{31} \\ \sigma_{12} \end{bmatrix}=\begin{bmatrix} c_{11} & c_{12} & c_{13} & c_{14} & c_{15} & c_{16} \\ c_{21} & c_{22} & c_{23} & c_{24} & c_{25} & c_{26} \\ c_{31} & c_{32} & c_{33} & c_{34} & c_{35} & c_{36} \\ c_{41} & c_{42} & c_{43} & c_{44} & c_{45} & c_{46} \\ c_{51} & c_{52} & c_{53} & c_{54} & c_{55} & c_{56} \\ c_{61} & c_{62} & c_{63} & c_{64} & c_{65} & c_{66} \end{bmatrix}\begin{bmatrix} \varepsilon_{11} \\ \varepsilon_{22} \\ \varepsilon_{33} \\ \varepsilon_{23} \\ \varepsilon_{31} \\ \varepsilon_{12} \end{bmatrix} \tag{2.14}$$

As a consequence of the symmetries implied in Equations (2.11), the number of the independent components in the elastic tensor is reduced to 21 for the general anisotropic case in the absence of rotational tractions and strains. Thus, a maximum of 21 stiffness constants are needed in the most general case to describe an anisotropic medium.

2.2.3 Seismic wave propagation in fractured media

Equation (2.10) gives an expression of Hooke’s law for a linear elastic and anisotropic medium. From the equations of Newton’s second law, the elastodynamic wave equation which relates stiffness to displacement can be written in the form (in the absence of any body forces):

$$\rho\frac{\partial^2 \mathrm{u_i}(\mathrm{x},\mathrm{t})}{\partial \mathrm{t}^2}=\frac{\partial\sigma_{\mathrm{ij}}}{\partial \mathrm{x_j}}, \tag{2.15}$$

where ρ is density. Substituting for stress from Equation (2.10) and re-arranging gives the wave equation as:

$$\rho \frac{\partial^2 u_i(x,t)}{\partial t^2} = \frac{\partial}{\partial x_j}\left[c_{ijkl}(x)\varepsilon_{kl}(x,t)\right], \tag{2.16}$$

where u_i is the ith component of the displacement and t is time. Combining Equation (2.16) with the definition of the strain tensor (Equation 2.6) gives the general wave equation for a 3D inhomogeneous anisotropic media as:

$$\rho \frac{\partial^2 u_i(x,t)}{\partial t^2} = \frac{\partial}{\partial x_j}\left[c_{ijkl}(x,t)\frac{\partial u_{k(x,t)}}{\partial x_l}\right] \tag{2.17}$$

For a homogeneous medium, the elastic constants c_{ijkl} are not dependent on position (x) and thus its derivatives are zero. Equation (2.17) is then simplified as:

$$\rho \frac{\partial^2 u_i(x,t)}{\partial t^2} = c_{ijkl}\frac{\partial^2 u_k(x,t)}{\partial x_j \partial x_l} \tag{2.18}$$

For an isotropic medium, the elastic constants can be expressed in the form (Chapman, 2004; pp. 97):

$$c_{ijkl} = \lambda\delta_{ij}\delta_{kl} + \mu\left(\delta_{ik}\delta_{jl} + \delta_{il}\delta_{jk}\right), \tag{2.19}$$

where λ and μ are the Lame’s parameters and δ_{ij} is the Kronecker delta function defined as:

$$\delta_{ij} = 1, \text{ for i = j and } \delta_{ij} = 0, \text{ for i} \neq \text{j} \tag{2.20}$$

Substituting Equation (2.19) into Equation (2.18) and simplifying further gives the wave equation for the isotropic medium as:

$$\rho \frac{\partial^2 u_i(x,t)}{\partial t^2} = (\lambda+\mu)\frac{\partial}{\partial x_i}\left(\frac{\partial u_k}{\partial x_k}\right) + \mu\frac{\partial^2 u_i}{\partial x_k \partial x_k} \tag{2.21}$$

Assuming a plane wave solution to Equation (2.18) of the form (Tsvankin, 2001, pp. 3):

$$u_k = U_k exp\left[i\omega\left(n_j x_j / v - t\right)\right], \tag{2.22}$$

where U_k are the components of the polarization vector **U**, ***n*** is the unit vector orthogonal to the plane wavefront and ω is the angular frequency. Substituting the assumed plane-wave solution (Equation 2.22) into Equation (2.18) gives the Kelvin-Christoffel's equation for the phase velocity *v* and polarisation vector ***U*** (Tsvankin 2001, pp. 3):

$$\begin{bmatrix} G_{11} - \rho v^2 & G_{12} & G_{13} \\ G_{21} & G_{22} - \rho v^2 & G_{23} \\ G_{31} & G_{32} & G_{33} - \rho v^2 \end{bmatrix} \begin{bmatrix} \mathrm{U}_1 \\ \mathrm{U}_2 \\ \mathrm{U}_3 \end{bmatrix} = 0 \tag{2.23}$$

G_{ik} is the Christoffel's matrix (where *i* and *k* can be 1,2 or 3) and is dependent on both the stiffness of the medium and the direction of wave propagation.

$$G_{ik} = c_{ijkl} n_j n_l \tag{2.24}$$

The Christoffel's matrix is both real and symmetric as a consequence of the symmetry of the stiffness tensor. Equation (2.23) can be written in a more compact form as (Tsvankin 2001, pp. 4):

$$\left(\mathrm{G}_{\mathrm{ik}} - \rho \mathrm{v}^2 \partial_{\mathrm{ik}}\right)\mathrm{U}_{\mathrm{k}} = 0 \tag{2.25}$$

The eigenvalue problem (Equation 2.23) has three real positive roots for ρv^2 with three corresponding orthogonal eigenvectors **U** (Crampin, 1981). The three real roots respectively correspond to the compressional wave (P-wave) and two shear waves (S-waves). Thus, two Shear waves are obtained in an anisotropic medium with varying phase velocities and polarizations. This phenomenon is called 'shear-wave splitting'. The velocities of the two shear-waves may coincide in certain directions, a phenomenon regarded as 'shear-wave singularity' (Crampin, 1981).

The polarization vector for plane-wave propagation in isotropic media is either parallel (for P-wave) or orthogonal (for S-wave) to the slowness vector. For anisotropic media however, the polarization is governed by the vector **n** (a unit vector orthogonal to the plane wavefront) as well as the elastic constants of the medium determined by the form of the Christoffel's matrix (Tsvankin, 2001). Since the Christoffel's matrix is both real and symmetric, the polarization vectors of the three modes are mutually orthogonal. These vectors are not necessarily parallel or perpendicular to the unit vector **n** as in the case of isotropic media. Consequently, there are no pure longitudinal or shear waves in anisotropic media except for specific propagation directions. For this reason, we often talk about the fastest mode as a quasi-P (qP) wave and the two slow modes as quasi-S1 (qS1) and quasi-S2 (qS2) waves respectively (Tsvankin, 2001).

The phase velocity refers to the velocity at which a point of constant wavelet phase travels in a direction perpendicular to the wavefront. The group velocity on the other hand is the velocity at which the wave energy propagates and it determines the direction and speed of energy propagation. This difference is illustrated schematically in Figure 2.2 for the case of an anisotropic medium. In this diagram, the wavefront takes an elliptical shape, so the two velocity vectors are clearly separated. This is ultimately a consequence of velocity dispersion or velocity anisotropy (Tsvankin, 2001). For an isotropic medium the wavefront is a circle and the magnitude and direction of the phase and group velocities would coincide.

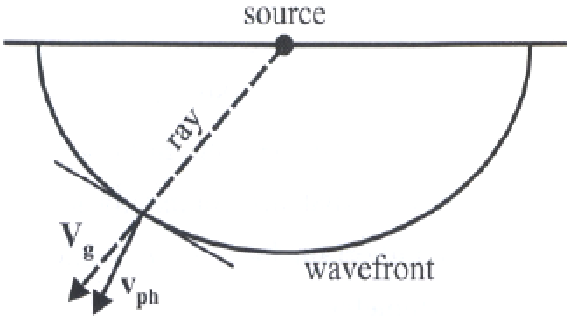

Figure 2. 2: Group and phase velocities in an anisotropic medium (Tsvankin, 2001). Group velocity points into the source direction while phase velocity is normal to the wavefront.

In general, the relationship between the phase and group velocity is of the form given by Berryman (1979) and Thomsen (1986) as:

$$v_g = grad^k(kv) = \frac{\partial(kv)}{\partial k_1} i_1 + \frac{\partial(kv)}{\partial k_2} i_2 + \frac{\partial(kv)}{\partial k_3} i_3, \qquad (2.26)$$

where k is the wave vector parallel to the phase velocity vector and $i_{1,2,3}$ are the unit vectors associated with the co-ordinate system. The phase velocity can also be derived from the projection of the group vector in the phase velocity direction thus (Tsvankin, 2001):

$$v = v_g.\mathrm{n} \qquad (2.27)$$

Equation (2.27) shows that the magnitude of the phase velocity vector usually is either greater or equal to the magnitude of the group velocity vector.

2.2.4 Symmetry systems

The symmetry of a medium is dependent on both the structure of its elastic (stiffness) tensor and its number of independent components. A major distinguishing feature of the symmetry systems encountered in seismology is that each of them has a unique number of elastic or stiffness coefficients that may be less than a maximum of 21. The symmetry class increases with decreasing number of independent elastic coefficients. In general, the higher the number of independent elastic coefficients, the lower the symmetry of the material and vice versa. Isotropy constitutes the highest class of symmetry system with only two independent elastic constants (Lame' parameters, λ and μ respectively) while the lowest symmetry class is the triclinic media which is characterized by 21 independent elastic constants. The number of independent elastic constants for the common classes of symmetry materials is summarized in Table 2.1. The isotropic, hexagonal, orthorhombic, monoclinic and triclinic symmetries constitute the common models identified in the subsurface which are of importance in geophysical studies.

Table 2. 1: Number of independent elastic constants for different symmetry media

Symmetry	Number of elastic constants
Isotropy	2
Cubic	3
Hexagonal	5
Trigonal	6
Tetragonal	6
Orthorhombic	9
Monoclinic	13
Triclinic	21

Isotropic media

The stiffness matrix of an isotropic medium reduces to the form:

$$c_{mn} = \begin{pmatrix} c_{33} & c_{33}-2c_{44} & c_{33}-2c_{44} & 0 & 0 & 0 \\ c_{33}-2c_{44} & c_{33} & c_{33}-2c_{44} & 0 & 0 & 0 \\ c_{33}-2c_{44} & c_{33}-2c_{44} & c_{33} & 0 & 0 & 0 \\ 0 & 0 & 0 & c_{44} & 0 & 0 \\ 0 & 0 & 0 & 0 & c_{44} & 0 \\ 0 & 0 & 0 & 0 & 0 & c_{44} \end{pmatrix} \tag{2.28}$$

where there are 12 non-zero elements, but only two independent stiffnesses c_{33} and c_{44}. The non-zero components shown in the matrix (Equation 2.28) are related to the Lame's parameters λ and μ by:

$$c_{33} = \lambda + 2\mu \tag{2.29}$$

$$c_{44} = \mu \tag{2.30}$$

The stiffness c_{33} corresponds to the axial modulus (pure radial strain), and c_{44} to the shear modulus (pure tangential strain). In practice the bulk modulus K is easier to measure in experimental conditions, so c_{33} is more commonly defined by

$$c_{33} = K + \frac{4}{3}\mu , \tag{2.31}$$

The P-wave velocity and S-wave velocity in this case are respectively given as:

$$v_p = \sqrt{\frac{\lambda + 2\mu}{\rho}} = \sqrt{\frac{c_{33}}{\rho}} \ , \tag{2.32}$$

$$v_s = \sqrt{\frac{\mu}{\rho}} = \sqrt{\frac{c_{44}}{\rho}} , \tag{2.33}$$

Hexagonal or transverse isotropic media

The hexagonal symmetry class, often referred to as transverse isotropy (TI) involves elastic properties that are the same in any direction normal to an axis (axis of symmetry) but are different parallel to this axis (Sheriff and Geldart, 1995). TI media possess five independent stiffness coefficients. The properties of elastic waves propagating in these media are dependent on the angle between the propagation direction and the symmetry axis (Tsvankin, 2001). Two common TI models used in seismic anisotropic studies are the Vertical Transverse Isotropy (VTI) and the Horizontal Transverse Isotropy (HTI) models. The VTI model has a vertical symmetry axis (Figure 2.3) while the HTI model possesses a horizontal symmetry axis (Figure 2.4). Common causes of VTI anisotropy in the subsurface include thin horizontal bedding or the preferential alignment of minerals and grains during deposition while, aligned vertical fractures, cracks or micro-cracks are common causes of the HTI anisotropy. Another TI model also encountered in seismology is the Tilted Transverse Isotropy (TTI) model, where the symmetry axis is tilted with respect to the symmetry plane. Tilted isotropy is typical of a situation of dipping thin layers as a result of tectonic activity or a case of fractures aligned non-vertically. The stiffness matrix of the VTI media has the form:

$$c_{mn} = \begin{pmatrix} c_{11} & c_{11}-6c_{66} & c_{13} & 0 & 0 & 0 \\ c_{11}-6c_{66} & c_{11} & c_{13} & 0 & 0 & 0 \\ c_{13} & c_{13} & c_{33} & 0 & 0 & 0 \\ 0 & 0 & 0 & c_{55} & 0 & 0 \\ 0 & 0 & 0 & 0 & c_{55} & 0 \\ 0 & 0 & 0 & 0 & 0 & c_{66} \end{pmatrix} \qquad (2.34)$$

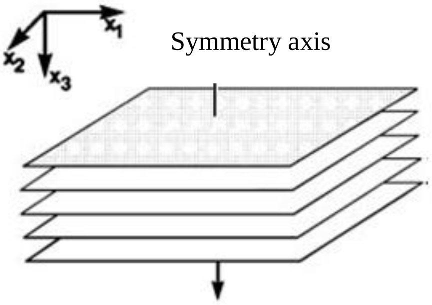

Figure 2. 3: Sketch of the VTI model (Ruger, 1997)

The HTI model has extensively been used in seismological studies of fractured reservoirs (Contreras *et al.*, 1999), with fracture orientation parallel to the maximum principal horizontal stress. This is acknowledged in most cases to be an over-simplification, but can be justified on pragmatic grounds, as discussed under the heading ‘Model selection’ at the end of this section. The stiffness matrix of the HTI model is:

$$c_{mn} = \begin{pmatrix} c_{11} & c_{13} & c_{13} & 0 & 0 & 0 \\ c_{13} & c_{33} & c_{33} - 2c_{44} & 0 & 0 & 0 \\ c_{13} & c_{33} - 2c_{44} & c_{33} & 0 & 0 & 0 \\ 0 & 0 & 0 & c_{44} & 0 & 0 \\ 0 & 0 & 0 & 0 & c_{55} & 0 \\ 0 & 0 & 0 & 0 & 0 & c_{55} \end{pmatrix} \tag{2.35}$$

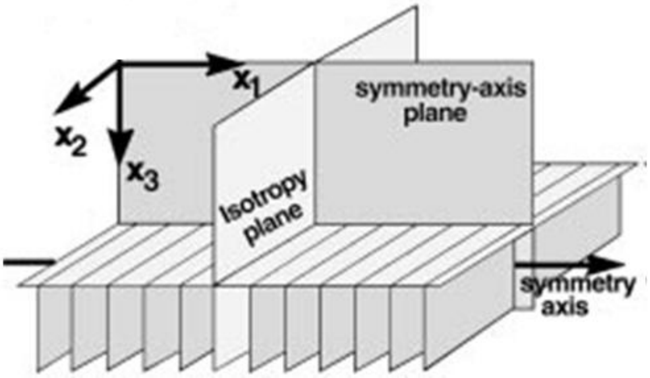

Figure 2. 4: Sketch of the HTI model (Ruger, 1997)

Orthorhombic media

Orthorhombic media have three mutually orthogonal planes of mirror symmetry and are characterized by nine independent elastic or stiffness coefficients. Common causes of orthorhombic anisotropy in sedimentary basins include the combination of parallel vertical fractures with transverse isotropy in the background medium (Bush and Crampin, 1991; Wild and Crampin, 1991), two or three mutually orthogonal fracture systems or two identical systems of fractures making an arbitrary angle with each other (Tsvankin, 2001). The stiffness tensor matrix of the orthorhombic media can be expressed as:

$$c_{mn} = \begin{pmatrix} c_{11} & c_{12} & c_{13} & 0 & 0 & 0 \\ c_{12} & c_{22} & c_{23} & 0 & 0 & 0 \\ c_{13} & c_{23} & c_{33} & 0 & 0 & 0 \\ 0 & 0 & 0 & c_{44} & 0 & 0 \\ 0 & 0 & 0 & 0 & c_{55} & 0 \\ 0 & 0 & 0 & 0 & 0 & c_{66} \end{pmatrix} \tag{2.36}$$

Monoclinic media

Monoclinic media are characterized by 13 independent stiffness or elastic coefficients. A medium containing two different sets of non-orthogonal vertical fracture systems embedded in an isotropic or VTI background is said to be monoclinic with a horizontal symmetry plane (Grechka *et al.*, 2000). If the two vertical fracture sets are orthogonal, the medium becomes orthorhombic. In general, three or more vertical fracture sets are needed to make the resultant medium monoclinic in the long-wavelength limit (Grechka *et al.*, 2000; Tsvankin, 2001). Abundant geological evidence of multiple vertical fracture sets exists which makes the monoclinic model very relevant in reservoir characterization (e.g. Schoenberg and Sayers, 1995). These may arise, for example due to stress-aligned fractures from two different geological epochs. The stiffness tensor matrix of monoclinic media has the form:

$$c_{mn} = \begin{pmatrix} c_{11} & c_{12} & c_{13} & 0 & 0 & c_{16} \\ c_{12} & c_{22} & c_{23} & 0 & 0 & c_{26} \\ c_{13} & c_{23} & c_{33} & 0 & 0 & c_{36} \\ 0 & 0 & 0 & c_{44} & c_{45} & 0 \\ 0 & 0 & 0 & c_{45} & c_{55} & 0 \\ c_{16} & c_{26} & c_{36} & 0 & 0 & c_{66} \end{pmatrix} \tag{2.37}$$

Triclinic media

Triclinic media constitute the most general anisotropic model with 21 independent stiffness or elastic coefficients. The stiffness tensor for triclinic media can be written in the form:

$$c_{mn} = \begin{pmatrix} c_{11} & c_{12} & c_{13} & c_{14} & c_{15} & c_{16} \\ c_{12} & c_{22} & c_{23} & c_{24} & c_{25} & c_{26} \\ c_{13} & c_{23} & c_{33} & c_{34} & c_{35} & c_{36} \\ c_{14} & c_{24} & c_{34} & c_{44} & c_{45} & c_{46} \\ c_{15} & c_{25} & c_{35} & c_{45} & c_{55} & c_{56} \\ c_{16} & c_{26} & c_{36} & c_{46} & c_{56} & c_{66} \end{pmatrix} \tag{2.38}$$

Model selection

Most subsurface geological formations are believed to be triclinic (Tsvankin, 2001). However, the large number of parameters makes the problem of inverting for the parameters of such a general medium inherently intractable, with a high degree of non-uniqueness in the inversion due to parameter tradeoffs (covariance) and marginal gain in residuals compared to the number of additional parameters (formally a loss of 'information' in signal processing terms). In engineering, biometrics and other aspects of geophysics it is common to quantify this trade-off using Akaike's information Criterion $AIC=2L-2D$, where L is the log-likelihood function and D the number of model parameters (e.g. Leonard and Hsu, 1999). This gives a quantifiable, reproducible metric for 'Ockham's razor', i.e. selecting the 'simplest model consistent with the data'. For example preferring a triclinic model (D=21) over a hexagonal one (D=5) would require an increase in the likelihood function of *exp* (21-5=16), completely unrealistic in most if not all practical cases.

In this thesis the model selection is straightforward for the case of the physical models, since they were deliberately constructed with a given symmetry. For the theoretical models, I used appropriately simplified models to correspond to the physical models in order to allow for comparison of the results.

2.2.5 Equivalent medium theories for fractured media

A medium with a set of aligned vertical fractures can be thought of as an equivalent azimuthally anisotropic medium for seismic wave propagation provided the scale length of the fractures is much smaller than the wavelength of the seismic wave. Thus, the equivalent medium theories for materials with aligned fractures can be used to establish a link between seismic anisotropy and fracture properties. A number of equivalent medium models for rocks containing isolated fractures have been developed to simplify the study of fracture-induced seismic anisotropy based on Eshelby's (1957) derivation of the elastic response of an ellipsoidal inclusion embedded in an infinite elastic solid (e.g. O'Connell and Budiansky,1974; Berryman, 1980; Hudson, 1981; Nishizawa, 1982).

Hudson's model

Hudson's model (1980 and 1981) is a commonly-used equivalent medium theory which considers an isotropic background medium containing a set of thin, penny-shaped ellipsoidal cracks or inclusions. The cracks are assumed to have a random distribution in terms of position and either aligned or randomly orientated. The crack density is low (<<1) and the mean crack shape is assumed to be circular with a radius smaller than the wavelength of the associated seismic wave. The cracks are isolated which precludes the possibility of fluid flow into or out of the cracks during seismic wave propagation. However, the cracks may either be empty or filled with solid or fluid material (Hudson, 1981). If the cracks have a preferred orientation, the resulting medium is anisotropic and the effective elastic (stiffness) tensor c is given by:

$$c = c^{(o)} + \chi c^{(1)} + \chi^2 c^{(2)}, \tag{2.39}$$

$c^{(0)}$ is the stiffness tensor of the isotropic background, $c^{(1)}$ are the 1st order corrections due to the presence of the cracks and $c^{(2)}$ accounts for the interactions between the cracks. χ is the crack density defined mathematically as:

$$\chi = Na^3V^{-1}, \tag{2.40}$$

where N is the number of cracks, V is the volume of the base material and a is the mean crack radius. The first order correction depends on the elastic parameters of the un-cracked solid medium and the cracks' response to normal and shear traction which in turn depend on the crack aspect ratio and the elastic moduli of the material filling the cracks.

In seismological applications, Hudson's model is used to derive the crack density from the measured magnitude of the azimuthal anisotropy. However, it can be seen from Equation (2.38) that the same crack density can be obtained from many small cracks as well as from few large cracks within the same volume of material. This indicates the inability of the model to distinguish between the anisotropy caused by micro-cracks and that caused by macro-cracks.

Linear slip model

The linear slip model (Schoenberg, 1980) models fractures as non-welded interfaces between two elastic media. The stress caused by the propagation of seismic wave is continuous across these interfaces while displacement is not, which implies that slip occurs (Coates and Schoenberg, 1995; Schoenberg and Sayers, 1995). Unlike Hudson's (1980, 1981) model, the linear slip assumes nothing about the shape of the fractures. The small displacement Δu and the stress σ are linearly related by the fracture compliance, *S* according to the equation (Coates and Schoenberg, 1995):

$$\Delta \mathrm{u} = \mathrm{S}\sigma.\underline{\mathrm{n}}\,, \tag{2.41}$$

where $\underline{\mathrm{n}}$ is a unit vector normal to the fracture. With the linear slip model, the effective stiffness tensor of the resulting medium can be obtained from the inverse of the effective compliance *S* as follows:

$$S = S_b + S_f \tag{2.42}$$

$$c = S^{-1} \tag{2.43}$$

S_b is the background compliance of the host rock, S_f is the compliance of the fractures and c is the effective stiffness of the resulting medium. The compliance tensor S_f is made up of two independent elements: the normal fracture compliance S_N and the tangential fracture compliance S_T respectively.

The linear slip model is particularly useful in the determination of the elastic constants of media with lower symmetry than the hexagonal, for instance materials with more than one set of aligned fractures (Schoenberg and Douma, 1988; Schoenberg and Sayers, 1995 and Sayers, 2002). Coates and Schoenberg (1995) used the linear slip model to model faults and fractures through finite difference modelling. They computed the effective compliance of each cell in the finite difference grid and the effective stiffness of the resulting medium using Equations 2.42 and 2.43 respectively and then replaced the properties of every cell intersected by the fault or fractures by the effective medium properties of the background rock and the fracture compliance.

Thomsen model

Both the Hudson (1980, 1981) inclusion-based model and the linear slip model of Schoenberg (1980) are frequency-independent equivalent medium theories. In both cases, the fractures or cracks are assumed to be isolated with respect to fluid flow. This is a strong approximation, but these models do describe conditions in the high-frequency limit, where the fluid does not have sufficient time to move due to wave-induced pressure gradients. In addition, only the fracture or crack porosities are considered by the models. However in a real geological setting, the host rock may also be porous and fluid exchange between the pores in the fractures and the pores in the host rock could have tremendous effects on the measured anisotropy of the rock (Mukerji and Mavko, 1994 and Thomsen 1995). On the basis of these ideas, Thomsen (1995) developed a model which takes into account the porosity of the host rock and assumes that the cracks and pores are hydraulically connected. The exchange of fluid between the pores and the cracks allows for the equilibration in the local fluid pressure in both the pores and the cracks. This model can thus be regarded as the low-frequency limit, in the sense that the frequency is sufficiently low to allow adequate time for the fluid pressure to equilibrate locally between the pores and nearby cracks (Thomsen, 1995). The magnitude of the resulting anisotropy is higher because the fluid-filled cracks or fractures are much more compliant than the isolated ones. Thomsen (1995) found that his model matched with the laboratory measurements of Rathore *et al.,* (1995) on samples containing aligned cracks in a porous matrix to a greater extent than the isolated crack model of Hudson (1981).

2.3 Poro-elasticity and squirt flow

Poro-elasticity theory describes the behaviour of a fluid-filled porous medium when subjected to changes in stress, strain, fluid content and pore-pressure. When a fluid-saturated porous rock is compressed, for instance by a passing seismic wave, a change in the pore-pressure occurs which resists the compression and thus stiffens the rock. Gassmann (1951) derived mathematical expressions for the effective bulk and shear moduli K_{sat} and μ_{sat} respectively of an isotropic saturated rock in terms of the bulk modulus of the mineral making up the rock K_m, the fluid bulk modulus K_f, the dry frame bulk modulus K_{dry}, the dry frame shear modulus μ_{dry} and the porosity ϕ as follows:

$$K_{sat} = K_{dry} + \frac{\left(1 - \frac{K_{dry}}{K_m}\right)^2}{\frac{\phi}{K_f} + \frac{1-\phi}{K_m} - \frac{K_{dry}}{K_m^2}} \qquad 2.44$$

$$\mu_{sat} = \mu_{dry} \qquad 2.45$$

The derivation of the Gassmann's equations is based on some assumptions (Wang, 2001). Firstly, it is assumed that the rock (both the matrix and frame) is elastically isotropic. This implies that all the grains have the same bulk modulus and also ensures that the seismic wavelength is much greater than the size of the grains and pores (Wang, 2001). Gassmann's relations have been extended to the case of anisotropic rock by Brown and Korringa (1975). Another assumption is that all the pores in the rock are completely connected. This implies that the fluid has sufficient time to flow to neutralize the pressure gradients generated by a passing seismic wave. Furthermore, the theory assumes that the pores in the rock are saturated with a frictionless liquid (a gas, oil or mixture). This assumption requires the fluid to have zero viscosity to allow for full equilibration of the pore fluid flow (Wang, 2001). Another assumption is that the rock-fluid system is closed such that there is no net flow of fluid into or out of the system. Finally the theory assumes that there is no chemical interaction between the saturating fluid and the rock. For practical applications, Gassmann's relation is commonly used to predict seismic-velocity changes caused by different fluid saturations in the reservoirs (Han and Batzle, 2004). Gassmann's theory is a static theory, meaning that it is only valid at very low frequencies. The low-frequency assumption of the theory is violated at higher frequencies (laboratory frequencies) and Gassmann's predictions in general underestimate the velocities measured in the laboratory (Maultzsch, 2005).

Biot (1956) developed a theory which allows the prediction of the saturated velocities as a function of frequency for a poroelastic material in terms of the dry rock properties. Unlike Gassmann's theory, Biot incorporates fluid viscosity and permeability of the frame into his theory and allows the movement of fluid between the connected pores which generates energy losses due to viscous friction, providing a mechanism for attenuation by internal energy dissipation. In the low-frequency limit, Biot theory reduces to the Gassmann's theory. Biot theory has two main consequences. The first is the existence of two compressional waves - the normal P-wave and a lower-frequency, highly-attenuated diffusion or 'slow' wave. The second is that the wave velocities are frequency-dependent. Biot (1956) showed that the transition from the low frequency to the high frequency limit occurs at a characteristic frequency f_c given as:

$$f_c = \frac{\phi\eta}{2\pi\rho_f\kappa}, \tag{2.46}$$

where η is the fluid viscosity, ρ_f is the fluid density and κ is the permeability of the rock. At lower frequencies, laminar drag against the solid dominates the wave propagation while at higher frequencies the wave flow pattern is controlled by the effects of fluid inertia (Biot, 1956). The velocities and attenuation measured in the laboratory at ultrasonic frequencies have been found to be significantly higher than those predicted by the Biot model (e.g. Winkler, 1985; Mavko and Jizba, 1991). The linear relationship of f_c and η implied in Equation (2.45) results in the prediction that velocity decreases with increasing fluid viscosity. However, this is inconsistent with the experimental results, which show an increase (e.g. Winkler, 1985; Jones, 1986).

Biot's theory does not take into account the concept of squirt flow. As a result of different geometries and orientations of the pores in the rock, a passing seismic wave generates pressure gradients which can be away from the propagation direction of the wave (Maultzsch, 2005). Thus during compression, fluid flows along the pressure gradient from the more compliant parts of the pore space into the stiffer parts and back again during dilatation. This process, known as 'squirt flow' does predict the observed increase of velocity with increasing fluid viscosity (Maultzsch, 2005). Mavko and Jizba (1991) developed a theory that incorporates the squirt-flow mechanism, and maintained that the discrepancies in the measured laboratory velocities and those predicted by Gassmann's or Biot's theory are due to grain-scale flow (squirt-flow mechanism). They explained that at low frequencies, the fluid can move easily between the pores in the rock when it is loaded but at higher frequencies, pressure builds up in the thinner pores due to viscous effects thereby making them to be isolated from the local flow. This theory has been extended by Dvorkin *et al.,* (1995) to calculate velocities and attenuation as a function of frequencies. The results of their calculated velocities are consistent with the predictions of Gassmann at low frequencies. At high frequencies however, their results are not consistent with the predictions of Biot.

O'Connell and Budiansky (1977) developed a squirt flow model for media with randomly oriented cracks. Dispersion will occur only in the shear modulus and not in the bulk modulus since the same pressure would be introduced in each crack when the rock is subjected to stress. However, this will not be the case in a more realistic situation of the rock's pore space where there are equant pores and cracks of varying aspect ratio. Johnson *et al.,* (1979) proposed a model for squirt flow between thin cracks and spherical pores. Unlike the model of O'Connell and Budiansky (1977), their model predicts no dispersion in the absence of pores and thus squirt flow between cracks of varying orientations is not considered.

Chapman (2001) and Chapman *et al.,* (2002) proposed a poro-elastic model which considers the pore space of a rock to consist of spherical pores and ellipsoidal cracks placed on the vertices of a random lattice and allows local fluid flow between nearest neighbors. At zero frequency, this model is consistent with Gassmann's (1951) relations. At non-zero frequencies, the model also predicts the existence of the slow Biot wave. Chapman (2001) observed that the model can explain the experimental data from Sothcott *et al.*, *(*2000), where velocities were measured as a function of frequency, fluid saturation and effective stress. The presence of fractures with scale much greater than the grain scales constitutes additional pore space heterogeneity in the rocks. Based on this idea, Chapman (2003) extended the earlier poro-elastic model to include the effects of aligned fractures on a scale that is greater than the grain scale. The model thus considers fluid flow at two different scales: the grain scale where squirt flow occurs between micro-cracks and equant pores and between differently oriented micro-cracks, as well as a larger scale where squirt flow occurs between fractures and the porosity in the surrounding matrix. In the high frequency limit the model is consistent with the equivalent medium theory of Hudson (1981) for rock containing isolated fractures. The poro-elastic model of Chapman (2003) is extensively discussed in Chapter 5 where it is used to model the effect of attenuation anisotropy in fractured porous rocks.

2.4 Factors affecting seismic wave amplitudes

A seismic pulse propagating in the Earth gradually suffers energy loss as a result of a number of factors. This leads to changes in the pulse amplitude which may be associated with the subsurface geologic changes provided all the other factors that affect seismic wave amplitude have been considered. The major factors that affect the reflected amplitude of seismic waves travelling from the source to the receiver are (Sheriff, 1975):

- Geometrical spreading
- Energy partitioning at interfaces
- Absorption and attenuation
- Topography of the interfaces and curvature and dipping of reflectors
- Source and receiver array response
- Scattering in the near surface
- Interference due to fine layering

Other factors that may affect the recorded amplitude are the strength and type of source, source directivity, source and receiver depths, mode conversion and anisotropy. Energy partitioning at interfaces, attenuation and interference from the top and bottom of a reservoir for instance can provide vital information on the lithology of the sub-surface, fluid saturation, fracturing and orientation of fractures.

Geometrical spreading

Geometrical spreading, also known as spherical divergence causes the intensity and energy of seismic waves to decrease inversely as the square of the distance from the source or the amplitude varies inversely as the distance travelled (Sheriff, 1975).

Energy partitioning at interfaces

As the seismic wave passes from one medium of different impedance to another of different impedance, part of the energy is reflected at the boundary between the two media and part is transmitted, resulting in cumulative transmission losses. The reflected wave amplitude is scaled by the reflection coefficient of the reflecting boundary.

Absorption and attenuation

Attenuation refers to an exponential decay of the seismic wave amplitude with distance of wave propagation. It can be caused by various physical phenomena which can be divided broadly into elastic processes where the total wave energy is conserved and inelastic dissipation or absorption where the wave energy is converted into heat (Muller *et al*., 2010). Attenuation is fully discussed in section 2.4.1.

Topography of the interfaces and curvature and dipping of reflectors

The reflection surface topography can cause focusing and defocusing of the seismic energy depending on whether it is concave or convex upward (Sheriff, 1975). The waveform can be scattered depending on the degree of curvature of the surface. These might affect the amplitude of the wave recorded.

Source and receiver array response and coupling

The positioning of sources and receivers (source and receiver coupling) on the Earth’s surface sometimes may not be uniform due to near-surface conditions such as wind, rain, temperature changes etc resulting in missing ground positions that can have a moderate effect on the recorded amplitude. For land data, the source and receiver coupling might be dependent on the nature of the ground (dry sand, wet soil etc.). The source and receiver arrays can generate amplitude directivity also known as radiation pattern (Landro and Amundsen, 2010). Waves propagating straight down from the source will have different strength from those propagating in other directions.

Scattering in the near surface

Scattering caused by small heterogeneities in the rocks such as grains with different compositions and edges of small minerals and pores results in seismic amplitude decay when the seismic wave encounter these heterogeneities (Liu, 1988). This will result in a decrease in the seismic wave amplitude or energy with distance of propagation.

Interference due to fine layering

Interference due to fine layering can result in amplitude changes. Whenever reflections overlap, the wave amplitude may be increased or decreased by constructive or destructive interference from the reflectors (Hackert and Parra, 2004).

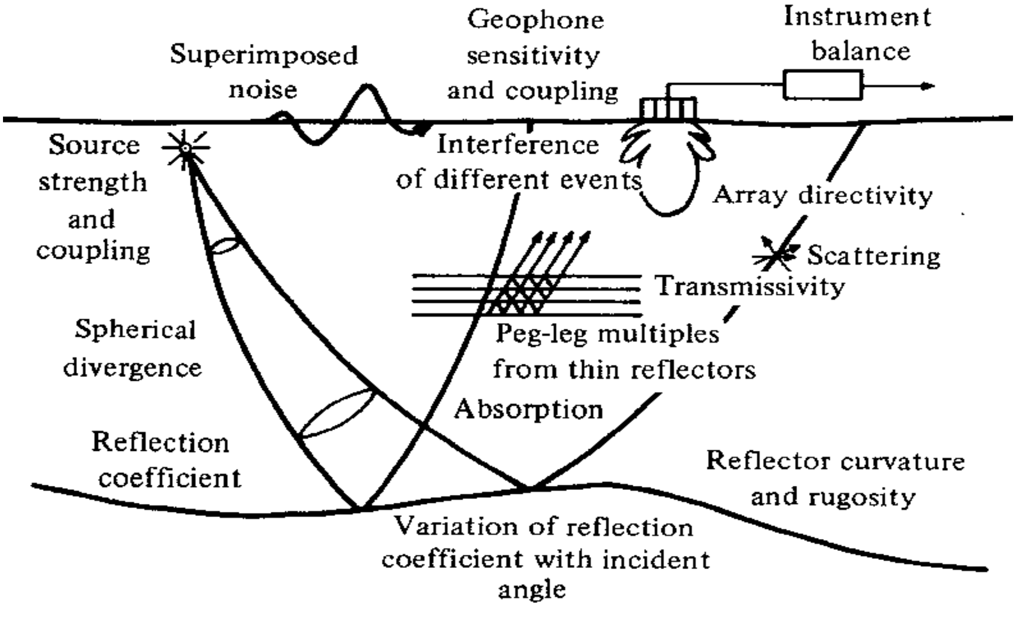

Figure 2.5: Factors affecting seismic amplitude (Sheriff, 1975)

2.4.1 Attenuation

Attenuation is defined as the gradual reduction in amplitude, magnitude or intensity of a seismic wave as it propagates through a given medium (Sheriff, 1975). This loss of energy could be the result of two effects. Firstly, it could result from energy conversion to heat and fluid displacement as the wave passes through the medium; commonly regarded as intrinsic or anelastic attenuation. Secondly, it could be the result of scattering and tuning effects; commonly termed apparent or extrinsic attenuation. The resultant effect of both forms of attenuation is called effective attenuation.

Seismic attenuation is commonly characterized by the seismic quality factor Q which is defined mathematically as (Shearer, 1999):

$$\frac{1}{Q} = -\frac{\Delta E}{2\pi E}, \tag{2.47}$$

where E is the net peak strain energy and $-\Delta E$ is the energy loss per cycle. An inverse relationship exist between Q and the strength of attenuation. High Q implies low attenuation and vice versa. For small $\Delta E/E$, Q >> 1 (Shearer, 1999), Equation (2.47) predicts an exponential decay of seismic wave amplitude in a homogeneous medium of the form:

$$A(x) = A_o \exp(-\alpha x), \tag{2.48}$$

where $A(x)$ is the amplitude at a distance x along the propagation direction, α is the attenuation coefficient and A_o is the initial amplitude at a distance $x = 0$. The seismic quality factor and the attenuation coefficient are both related by the expression (Johnson *et al.*, 1979):

$$Q = \frac{\pi f}{\alpha v}, \tag{2.49}$$

where f is frequency and v is velocity. The relationship between the intrinsic attenuation Q_i^{-1} and apparent attenuation Q_s^{-1} could be written as (Spencer *et al.*, 1982):

$$\frac{1}{Q} = \frac{1}{Q_i} + \frac{1}{Q_s} \tag{2.50}$$

Several mechanisms have been proposed to be responsible for seismic attenuation in crustal rocks. Most of the proposed mechanisms are based on the observation that rocks contain microscopic cracks and the pores space in the rock may be saturated with fluids. Walsh (1966) proposed that attenuation in dry rocks is caused by frictional dissipation due to relative motions on dry surfaces of thin cracks. As described in the previous section, Mavko and Nur (1979) and O'Connell and Budiansky (1977) proposed squirt-flow phenomena to be responsible for attenuation in fluid saturated rocks. The presence of gas bubbles enhances fluid movement within the cracks. Johnson *et al.*, (1979) maintained that friction on thin cracks and grain boundaries is the dominant attenuation mechanism for consolidated rocks in the Earth's upper crust and listed the following factors as the possible causes of seismic attenuation:

- Matrix anelasticity
- Frictional dissipation due to relative motions at grains boundaries and across crack surfaces
- Fluid flow which causes relaxation of shear motions at pore-fluid boundaries
- Relative motion of the matrix frame with respect to the fluid inclusions in the case of fully saturated rocks
- Squirt-flow phenomena
- Gas pocket squeezing with partial saturation
- Scattering
- Tuning
- Stratigraphic attenuation

The last three factors are due to geometrical effects which are not dependent on the intrinsic properties of the rocks and are therefore responsible for extrinsic attenuation. All the other factors depend on the intrinsic properties of the rock and are therefore responsible for intrinsic attenuation. Johnson *et al.*, (1979) argued that increasing pressure tends to close up the cracks; thus decreasing its number which leads to a decrease in attenuation. They further maintained that the introduction of fluid into a dry rock will lubricate the crack surfaces and grain boundaries and facilitate frictional sliding which results in increasing attenuation. In heterogeneous porous media, one major cause of attenuation is wave-induced flow of pore fluid between heterogeneities of various scales (Muller *et al*., 2010). It is believed that for frequencies below 1 kHz, wave-induced flow between mesocopic in-homogeneities which are large compared with individual pore size but small compared to the wavelength constitutes the prominent cause of attenuation (Muller *et al*., 2010). Frequencies used in seismic exploration are generally less than 100 Hz. Thus, frictional dissipation due to relative motion at grain boundaries and across crack or fracture surfaces, fluid saturation, fluid flow mechanisms and scattering can be considered as the important factors that cause seismic attenuation.

2.4.2 Energy partitioning at interfaces

When a seismic wave is incident on the interface between two media, the wave undergoes refraction and reflection in accordance with Snell's law. Provided the interfaces between the media are welded, both displacements and stresses are continuous. These constraints can be used to calculate the reflection and transmission coefficients using the 'Zoeppritz equations (Sheriff and Geldart, 1995). If the two media are isotropic, an incident P-wave (P_i) for instance splits into four directions namely; reflected P-wave (P_r) and transmitted P-wave (P_t) as well as reflected S-wave (S_r) and transmitted S-wave (S_r) as illustrated in Figure 2.6. If however, the two media are anisotropic and the incident plane is not a plane of symmetry, the incident P-wave is split into six directions as illustrated in Figure 2.6. The reflection coefficient will depend on both the incidence angle and the azimuthal angle if the media are HTI for instance in the case of vertically aligned fractures (Hall *et al*., 2002).

Table 2. 2: Average Q values for different rock types (Sheriff and Geldart, 1995)

Rock type	Q
Sedimentary rocks	20-200
Sandstone	70-130
Shale	20-70
Limestone	50-200
Chalk	135
Dolomite	190
Rocks with gas in pore space	1-50
Metamorphic rocks	200-400
Igneous rocks	75-300

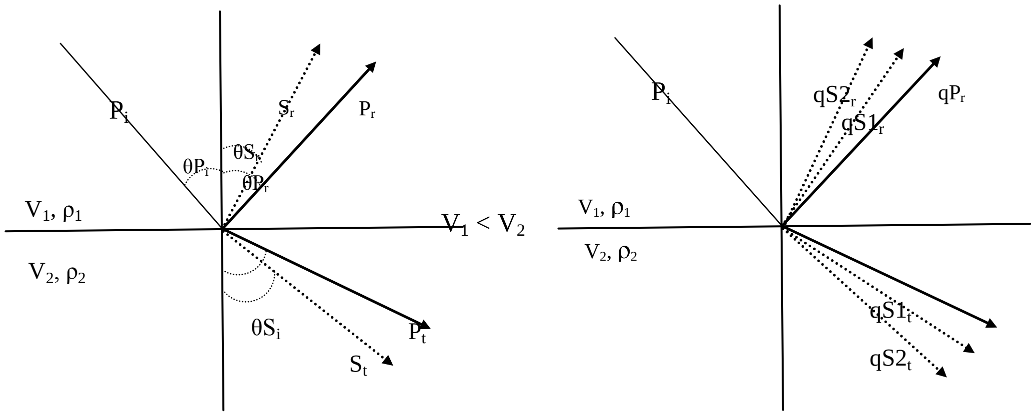

(a) (b)

Figure 2.6: Energy partitioning at interfaces

2.5 QVOA analysis for fracture characterization

Common methods of detecting natural fractures from P-wave data have relied on the analysis of azimuthal variations of travel time, velocity amplitude and AVO gradients. Attenuation has long been shown to be sensitive to fractures and fluid saturations (e.g. Walsh, 1966; Mavko and Nur, 1979; O’Connell and Budiansky, 1977). Klimentos and McCann (1990) demonstrated that the presence of fractures could lead to high magnitude of attenuation, indicating the potential of using attenuation as an indicator of fractures.

In recent times, Geoscientists have taken an increasing interest in the study of azimuthal variations in seismic quality factor Q as a means of characterizing fractures from seismic data. For the propagation of seismic waves in a medium with a set of aligned vertical fractures, equivalent medium theories (e.g. Tod, 2001; Chapman, 2003) predict that the attenuation suffered by the wave depends both on the source-receiver azimuth and offset or incidence angle. The seismic wave is expected to suffer more attenuation in the fracture normal direction than in the fracture strike direction. These predictions have been observed in both laboratory and field data (e.g. Clark *et al.,* 2001; Luo *et al.,* 2006; Chichinina, *et al.,* 2006; Maultzsch *et al.,* 2007; Clark *et al.,* 2009). Chichinina *et al.,* (2006) studied the variation of the seismic quality factor versus offset and azimuth (QVOA) using synthetic PP-reflection data generated for the dissipative HTI model proposed by Hudson *et al*., (1996) and derived an expression similar to Ruger's (1998) approximation for PP-wave reflection coefficients in AVOA analysis for the P-wave attenuation. The HTI model allows for fluid flow between cracks and random pores, resulting in P-wave attenuation (Hudson *et al*., 1996). They generated synthetic data for the model for different crack filling fluids (gas, brine and oil) in different azimuthal directions and computed the relative variations in Q values with azimuth. The main conclusion from their results is that seismic wave attenuation is strongest in the direction normal to the fractures and weakest parallel to the fractures. Maultzsch *et al.,* (2007) demonstrated through synthetic modelling studies based on Chapman's poroelastic model (2003) and field data analysis that azimuthal variations in attenuation can be measured from VSP surveys. They also computed the differences in the attenuation as a function of azimuth and found that the azimuthal variations satisfied the relation:

$$\Delta Q^{-1} = C1 + C2\cos[2(\theta - \theta_o)], \tag{2.51}$$

where *C1* is an arbitrary constant, *C2* is the magnitude of azimuthal variation, θ is the azimuthal angle and θ_o is the fracture normal direction in which attenuation is maximum. Their results show that attenuation increases with polar angle and azimuth away from the fracture strike which is consistent with the predictions of Chapman's model (2003), also indicating the potential of using QVOA analysis to obtain fracture properties from seismic data. Clark *et al.,* (2009) studied the variation of Q-factor versus offset and azimuth as a means of characterizing fractured reservoir from marine surface-seismic reflection data. They observed that attenuation is least in the direction where the stacking velocity is fastest and interpreted this direction to be closest to the fracture trend while attenuation is most in the direction normal to the fracture trend where the stacking velocity is slowest. The azimuthal variations in their computed effective attenuation were also well fitted by a '$\cos 2\theta$' function with θ being the survey azimuth direction. In this thesis, I adopt the seismic modelling approach to study the attenuation effects in porous fractured rocks to gain more understanding into the common practice of using the QVOA analysis method for reservoir characterization from seismic data.

2.6 Summary

In this chapter, I have given a review of the fundamental concept of seismic anisotropy and anisotropic wave propagation in fractured media. The basis of using seismic anisotropy for fracture detection is provided by the equivalent medium theories which have been studied for many years. According to these theories, a medium with a set of aligned fractures can be modelled as an equivalent anisotropic medium provided the scale length of the fractures is much smaller than the seismic wavelength. P-wave attenuation is sensitive to the presence of fractures and fluid saturation and thus constitutes a useful exploration tool for fractured reservoir characterization to complement the use of other seismic attributes (amplitude, velocity travel time and AVO gradients). In fractured media, azimuthal variations in the P-wave attenuation are elliptical and the azimuth corresponding to minimum attenuation is parallel to the fracture strike direction while the azimuth normal to the fracture direction corresponds to the azimuth of maximum attenuation.

Chapter 3 Measurement of attenuation from seismic data

Measurement of attenuation from seismic data is a difficult task mainly because of interference effects on the primary reflection being analysed by noise or other nearby arrivals. The spectral ratio method is the most common method of estimating attenuation (inverse of the seismic quality factor Q) from seismic data perhaps because it is easier to use and more stable. In this chapter, I give a review of the spectral ratio method of measuring attenuation from seismic data. The method makes use of the changes in the signals’ spectral characteristics. I also discuss the Q-versus offset (QVO) method, which is an extension of the spectral ratio method of estimating attenuation from seismic data and is the method adopted in this thesis. I finally test the performance of the QVO method on simple models with known attenuation before applying the method to complex data sets in this thesis.

3.1 Introduction

Accurate measurement of attenuation from seismic data is difficult because of the effects of geometric spreading of the wavefront, reflections, noise, interference due to fine layering and scattering from heterogeneities on the seismic wave amplitudes (e.g. Sheriff, 1975; Johnson *et al*., 1979; Jeng *et al*., 1999). These factors have to be corrected for in order to get an accurate measurement of attenuation which could sometimes be difficult. Other factors which might influence the accuracy of attenuation measurement include the instability of the source pulse, differences in receiver coupling and processing artefacts. If different shots have different characteristics (e.g. shape, energy or strength), this might result in the variation in the recorded seismic response. Thus, when spectral estimates are made, the attenuation estimates may be in error. Consequently, attenuation estimates from seismic data have sometimes been found to be unreliable most especially for data with low signal-to-noise ratio (e.g. Raikes and White, 1984; Sams and Goldberg, 1990). The major difficulty is the interference effects which might cause distortion of the primary seismic reflection of interest (e.g., Spencer *et al*., 1982).

Existing methods of estimating attenuation from seismic data include the spectral ratio method, the amplitude decay method, the rise-time method, the centroid frequency-shift method, the wavelet modelling method, the pulse broadening method and the inversion method (Tonn, 1991). The frequency-shift method measures pulse broadening in the frequency domain while the time-shift method measures pulse broadening in the time domain (Quan and Harris, 1997). Measurement of attenuation in the frequency domain might be more convenient and stable (Tonn, 1991; Quan and Harris, 1997; Matsushima *et al.*, 2008). Quan and Harris (1997) used the frequency shift method in cross-well tomography to estimate attenuation for both synthetic and field data. Dasgupta and Clark (1998) introduced a method known as the Q-versus-offset (QVO) method to estimate attenuation by comparing the amplitude decay rate at two levels in pre-stack CMP gathers. Zhang and Ulrych (2002) utilized the peak frequency variation in the amplitude spectra at two time windows to estimate attenuation from pre-stack CMP gathers. Matsushima *et al.,* (2008) applied both the spectral ratio method and the centroid frequency-shift method to estimate attenuation in the frequency range of 150 - 1000 kHz in partially frozen brines.

In the following sections, I give a review of the spectral ratio method which is the commonest method of estimating attenuation from seismic data and the QVO method which is adopted in this thesis for attenuation analysis.

3.2 Spectral ratio method

This is the most commonly used method of estimating attenuation from seismic data (Hauge 1981; Pujol and Smithson, 1991; Dasgupta and Clark, 1998; Dasios *et al.*, 2001; Shaw *et al.*, 2008) and is commonly used to measure Q as a function of depth in vertical seismic profiles (VSP) (e.g. Hauge, 1981; Raikes and White, 1984; Pujol and Smithson, 1991; Tonn, 1991; Hackert and Parra, 2004). It involves the selection of data at two different receiver depths across a medium in which Q is assumed to be constant and is applied in the frequency domain. Here, the amplitude spectrum of a seismic wave entering a given medium is compared with the amplitude spectrum of the wave leaving the medium according to the formula (Aki and Richards, 2002):

$$\mathrm{A}(f) = \mathrm{A_o}(f)\mathrm{RG}\exp(-\alpha x), \tag{3.1}$$

where $\mathrm{A_o}(f)$ is the initial spectral amplitude at frequency *f*, $\mathrm{A}(f)$ is the spectral amplitude of the wave after travelling through a distance *x*, *α* is the attenuation coefficient, *R* is the reflectivity of any boundaries within *x* and *G* is the geometrical spreading factor. Taking the natural logarithm of both sides of equation (3.1) and re-arranging gives:

$$\ln\left(\frac{A(f)}{A_o(f)}\right) = \ln(RG) - \alpha x \tag{3.2}$$

Noting that;

$$\alpha = \frac{\pi f}{Q v}, \tag{3.3}$$

where *v* is the phase velocity, Equation (3.2) can be written as:

$$\ln\left(\frac{A(f)}{A_o(f)}\right) = \ln(RG) - \frac{\pi f \Delta t}{Q}, \tag{3.4}$$

where Δt is the travel time between the wave entering the medium and leaving the medium. With Q assumed to be frequency-independent within the bandwidth used, Equation (3.4) predicts a linear graph of the logarithm of the amplitude ratio against frequency f with slope, p given by:

$$p = -\frac{\pi \Delta t}{Q} \tag{3.5}$$

Thus, the quality factor Q can be estimated from the slope (Equation 3.5) of the linear regression of the logarithm of the spectral ratios and frequency while the intercept term on the vertical axis corresponds to a measure of the elastic losses, which is a function of the energy partitioning and geometric spreading. The standard errors of the least-squares regression can be used to estimate the errors in the computed Q values. A schematic illustration of the spectral ratio method is shown in Figure 3.1.

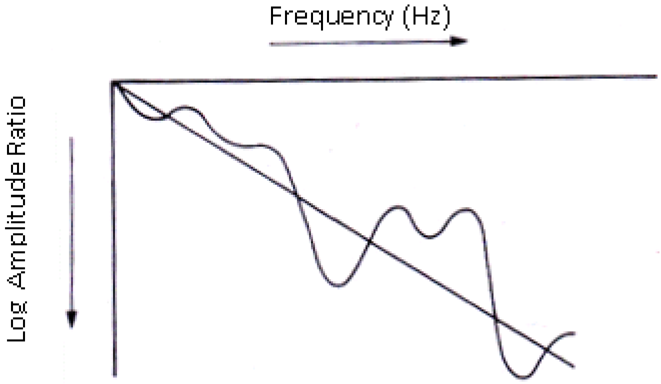

Figure 3.1: A schematic illustration of the spectral ratio method. Logarithm ratio of amplitude spectra at two levels is plotted as a function of frequency and attenuation is derived from the slope of the linear trend. Multiple scattering and other noise interference causes oscillations of the spectral ratios (adapted from Spence *et al*., 1982).

The accuracy of Q estimates from the spectral ratio method is influenced by trace windowing and frequency bandwidth over which regression is carried out (Sams and Goldberg, 1990; Pujol and Smithson, 1991; Matheney and Nowack, 1995; Dasios *et al*., 2001). When large time gates are used to window the traces, there is a tendency to include noise interference in the analysis window which will lead to spectral holes in the Fourier amplitude spectra (Sams and Goldberg, 1990) and consequently results in erroneous measurements when least-squares regression is applied. These interference effects however, may be reduced by the use of a short time window. But this might result in the under-sampling of the data at low frequencies and cause spectral instability (Sams and Goldberg, 1990; Dasios *et al.,* 2001). A trade-off between these two limits is to choose a time window that is long enough to capture only the events of interest and short enough to eliminate possible inclusion of any noise interference.

Multiple scattering combined with other noise interference in the analysis window can also distort the expected linear trend in the logarithm spectral ratio (LSR) - frequency regression (Spencer *et al*., 1982). This will produce strong local variations and notches in the computed spectra and result in oscillation of the spectral ratios (Figure 3.1). Thus, the result of Q computation from the spectral ratio method is also dependent on the frequency bandwidth used for the regression (e.g. Spencer *et al*., 1982; Sams and Goldberg, 1990; Pujol and Smithson, 1991 and Matheney and Nowack, 1995). A wider regression bandwidth can produce more stable results of Q estimates but this, however, might lead to analysis being done outside the signal bandwidth. The choice of the regression bandwidth therefore remains very subjective. Carter (2003) suggested that a logical way is to carry out the linear regression over the smaller of the two signal bandwidths in the windows bounding the interval of interest.

3.3 Q-versus-offset (QVO) method

This method which is basically an extension of the spectral ratio method described in section 3.2 was developed by Dasgupta and Clark (1998) to estimate the quality factor, Q from surface seismic data and is based on the attenuation model of Futterman (1962). The method requires that the effective attenuation is independent of frequency over the measurement bandwidth. I now give a review of the method.

First, the seismic data are pre-processed in a manner to ensure the preservation of all amplitude information and thereafter Normal Moveout (NMO) correction is applied to the data for ease of identification of the reflection events of interest. Next, a reference reflection is selected and its amplitude spectrum computed using the fast Fourier transform (FFT). In each pre-stacked CMP gather, the amplitude spectra of the target reflections of interest are also computed using FFT. The NMO correction applied to the data stretches the reflection pulse especially at longer offsets, causing a change in its amplitude and a shift in the pulse spectrum to lower frequencies (e.g. Dunkin and Levin, 1973; Barnes 1992). To correct for this effect, the trace complex spectrum $A_a\ (f)$ after the application of NMO correction is restored to its pre-NMO state, $A_b\ (f)$, using the formulation of Dunkin and Levin (1973) and Barnes (1992):

$$A_a(f) \approx kA_b(kf), \tag{3.6}$$

where;

$$k = (1 + x^2 / [v_{rms}{}^2(t_o)t_o{}^2])^{1/2} / (1 - [x^2 v_{rms}'(t_o)] / [t_o v_{rms}{}^3(t_o)]), \tag{3.7}$$

x is the source receiver offset, t_o is the zero offset travel time and $v_{rms}(t_o)$, $v_{rms}'(t_o)$ are the root mean square (rms) velocity and its derivative with respect to t_o. Next, the corrected spectra are stacked over an offset- range window of a few traces and rolled across the CMP gather to increase the S/N ratio. The natural logarithm of the amplitude spectral ratios of the target and the reference reflections are then computed and the spectral ratio slope and its uncertainty bound for each offset window is obtained by least-squares regression of the logarithm of the spectral ratios and frequency using the regression method of Williamson (1968) which takes into consideration the error bounds in both the abscissa and the ordinate. The range of the stacked spectral ratios provide uncertainty bounds on the ordinate while the bandwidth of each fast Fourier transform (FFT) harmonic provides uncertainty bound on the abscissa. Since the traveltime is hyperbolic and also based on the assumption of small-spread conditions, the resultant logarithm of the spectral ratio slopes relate linearly with the square of the offsets as a result of path-length (travel time) effects in a 1-D structure where intrinsic Q in each layer is constant and isotropic. Thus, another least-square regression of the spectral ratio slopes and the square of the offset is performed also using the regression method of Williamson (1968) to get the zero-offset spectral ratio slope from where Q, the average source-to reflector quality factor can be computed. The uncertainties in the spectral ratio slopes and the offset range window width are used as inputs in the second regression and the error bounds in the spectra ratio slope intercept is propagated into the computed average source-to reflector Q values to get their error bounds. These procedures are summarized in the flow chart of Figure 3.2.

Dasgupta and Clark (1998) applied the procedures described above to a number of reflectors in surface reflected CMP NMO - corrected gathers and computed the interval Q_i for a given interval between two reflectors at a time t_n and t_{n-1} using the relation:

$$Q_i = \frac{[t_n - t_{n-1}]}{t_n / Q_n - t_{n-1} / Q_{n-1}}, \tag{3.8}$$

where Q_n and Q_{n-1} are the quality factors for the reflectors at two-way travel times of t_n and t_{n-1} respectively. They computed the associated error in the interval Q_i from the respective individual Q errors (Δ) using the relation;

$$\{\Delta Q_i^{-1})\}^2 = (t_{n-1}/T)\{\Delta(Q_{n-1}^{-1})\}^2 + (t_n/T)\{\Delta(Q_n^{-1})\}^2, \tag{3.9}$$

where $T = (t_n - t_{n-1})$. The Q values computed using the QVO method are the effective values which include the effects of apparent attenuation. Dasgupta and Clark (1998) reported three case studies of successful application of their method. First, the Q^{-1}_{eff} estimates obtained from their method were consistent with estimates derived from a VSP from the Southern North Sea. Also, the results from two other case studies using data from the North Sea indicated the success of their method in lithology discrimination in a frontier area and detection of the presence of gas in the reservoir through lateral changes in the interval Q^{-1}_{eff} estimates. They cautioned, however, that their method is a prototype and still subject to improvements.

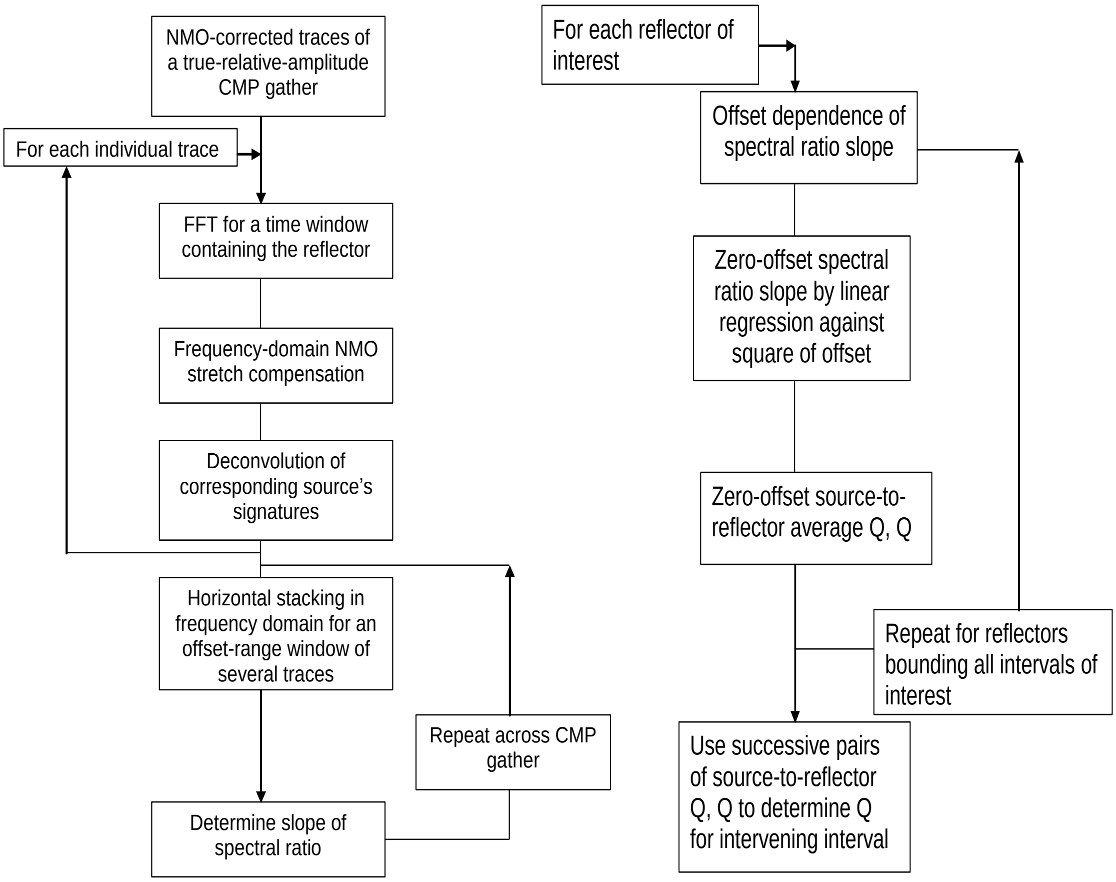

Figure 3.2: Flowchart of the QVO method (Dasgupta and Clark, 1998)

The major assumption of isolating only the primary reflection of interest in the use of the QVO method often breaks down as pointed out by the authors from their experience with the method since this is seldom encountered in field data (e.g. O'Doherty and Anstey 1971). Hustedt and Clark (1999) examined the effects of frequency - dependent source and receiver directivities on the Q values estimated using the QVO method and concluded that these two effects have insignificant influence on the QVO-derived attenuation results except for shallow targets where the two-way travel time (TWT) is either equal to or less than 500 ms. The seismic modelling data used in this thesis in contrast to the field data case have high S/N ratio and as such the primary reflections of interest can easily be isolated. Consequently, the QVO method is suitable for estimating the Q values from the data as the noise and multiple interference effects which might affect the spectral estimates are absent.

Carter (2003), based on his primary concerns about the negative Q values obtained from the QVO method carried out a critical assessment of the method. If the power spectral ratios are used instead of amplitude spectral ratios, then Equation (3.4) can be written as:

$$ln \frac{P(f)}{P_o(f)} = 2ln(RG) - \frac{2\pi \mathrm{f}}{\mathrm{Q}}(\Delta \mathrm{t}) \tag{3.10}$$

where $P_o(f)$ is the initial spectral power at frequency f, and $P(f)$ is the spectral power of the wave after travelling through a distance x. Considering the fact that the travel times are hyperbolic, Carter (2003) showed that the slope, p of the regression from Equation (3.10) in general could be written as:

$$p = \frac{2\pi}{Q}\left(t_{ref} - t_o - \frac{x^2}{2t_o v^2{}_{rms}} \right), \tag{3.11}$$

where t_{ref} is the travel time of the reference event. If the actual travel times, t of the target event are used, Equation (3.11) could be written as:

$$p = \frac{2\pi}{Q}\left(t_{ref} - t\ \right), \tag{3.12}$$

Thus, with the use of the actual travel times, Carter (2003) removes the second regression of the spectral ratio slopes against squared offset and simply finds the average of the $\mathrm{Q}^{-1}{}_{\mathrm{eff}}$ estimates computed from Equation (3.12). This improvement allows far offset traces to be included in Q computation using the QVO method. Carter (2003) pointed out that the removal of the second regression reduces the effect of scatter in the estimated $\mathrm{Q}^{-1}{}_{\mathrm{eff}}$ values.

Carter (2003) also tested the use of the Boxcar, Dasgupta, Hanning and Papoulis tapers in windowing the pulses before the application of FFT and concluded that the original Dasgupta taper used in the QVO method produces huge side lobes and thus, results in the underestimation of the $\mathrm{Q}^{-1}{}_{\mathrm{eff}}$ values. He recommended the use of the

Hanning or Papoulis taper and noted that the Boxcar and Dasgupta tapers limit the usable bandwidth and thus reduced the accuracy of the estimated Q^{-1}_{eff} values. The Hanning or Papoulis tapers are less sensitive to the higher amplitudes at the start of the window which are richer in high frequencies than the lower amplitude tail of the window.

Guerrero Moreno (2006) noted that static problems in the gathers, systematic errors in the NMO velocities and anisotropy in the data can greatly influence the Q estimates derived from the QVO method, since the relative position of the traces and window can vary from one trace to another. To solve this problem, he suggested either following the peak, the zero crossing or the trough of the reflected wavelet from the target reflector along the hyperbolic travel path. This allows a long window to be extracted for Q estimation and has an advantage in that no NMO correction is applied to the data, so the NMO stretch effect does not influence the computation.

The QVO method of estimating attenuation for seismic data involves spectral estimates. Spectral estimates could be made by using the short-time Fourier transform (STFT) (Dasgupta and Clark, 1998), the Gabor transform (Rioul and Vetterli, 1991), the continuous wavelet transform (Chakraborty and Okaya, 1995) and the S-transform (Stockwell *et al.*, 1996). The computed spectrum is greatly influenced by the interference effects caused by noise or short-path multiples which might enter the analysis window. More confident attenuation measurements can be made if spectra that are less affected by these interference effects can be obtained. On this basis, Reine *et al.*, (2009) examined the robustness and accuracy of attenuation measurements when the spectral estimates are made using either the fixed-window or the variable window transforms. For the fixed-window transforms, they used the short-time-Fourier transform (STFT) and the Gabor transform while the S-transform and the continuous wavelet transform were used for the varying window transforms. They carried out two experiments: first, a synthetic transmission experiment to estimate frequency-dependent scattering attenuation and, second, a zero-offset reflection synthetic experiment to estimate frequency-independent attenuation through linear regression of spectral ratios. They concluded from their results that the use of variable window transforms such as the S-transform and the continuous wavelet transform gives more robust and accurate measurement of attenuation with respect to the choice of regression bandwidth, thus allowing more flexibility in the choice of the regression bandwidth. They further confirmed their findings in the analysis of a real field data set where they observed consistency in their results with previous measured values. Reine *et al.*, (2009) maintained that the variable window transforms reduce the fluctuations in the spectra for two reasons. First, the primary arrival is better isolated from the coda by the shorter time windows used to analyze high frequencies. At high frequencies, more energy is scattered to the coda and there is an increase in the degree of nonstationarity in the data (Reine *et al*., 2009). The primary arrival is better isolated from the coda since the variable time windows use shorter time windows to analyse these high frequencies. Second, as a result of the Gabor uncertainty principle (Hall, 2006), the effective frequency window increases as the time becomes shorter. This implies that the shorter windows allow for an increased spectral averaging which smoothes out any fluctuations in the spectrum. Again, the seismic modelling data used in this thesis all have very high S/N ratio and as such the effects of noise or multiple interference are absent or very insignificant. Consequently, this improvement on the QVO method is not applied to the data sets in this thesis.

Clark *et al.*, (2009) used the QVO method to measure the azimuthal variation in apparent attenuation in a marine seismic reflection data and found both qualitative and quantitative consistency between the azimuthal attenuation variation and stacking velocity, and published amplitude variation with offsets results in terms of the inferred fracture direction. Hackert and Parra (2004) incorporated a method of removing the effects of thin bed into the QVO method for measuring attenuation from seismic reflection data. Thin bed reflections may contaminate the spectrum of the target reflection and thus renders the Q estimates unreliable. The spectrum may contain significant component from interfering thin bed reflections (Hackert and Parra, 2004) as a result of the tuning effect (e.g., Sheriff and Geldart, 1995). Whenever reflections overlap, the wave amplitude may be increased or decreased by constructive or destructive interference from the reflectors (Hackert and Parra, 2004).

In addition to these amplitude changes, interference by thin bed reflections can also cause systematic changes in the apparent frequency of the reflected wave (e.g. Robertson and Nogami, 1984). Thus, the presence of a thin bed near the target reflector may cause changes in the reflection spectrum. In this case, the spectrum of the primary reflector is modified by the thin bed effects which may result in Q estimates that are less reliable. To correct the effects of thin bed that may enter into the analysis window, they divided the target reflection spectrum by the local spectrum of a known reflectivity sequence from a nearby well log prior to Q computation and argued that the success of their method is dependent on a good tie from the well log data and the seismic data.

3.4 Synthetic testing of the QVO - methodology

In this section, I carry out a synthetic test to assess the performance of the QVO - spectral ratio method discussed in section 3.3 on synthetic datasets with known solutions using the 'Aniseis' modelling package (Taylor, 2001). The software makes use of the reflectivity method. The goal of the synthetic test is to assess if the analysis method can produce known solutions from simple models before applying it to complex cases in this thesis. First, I give a brief review of how wave propagation is modelled in 'Aniseis' which is a far field approximation. I then computed synthetic data for six different simple models (with and without attenuation) and estimated the seismic quality factor, Q from the models using the QVO-spectral ratio method. I demonstrate that the method is capable of recovering the known solutions in the models at 95 % confidence level.

3.4.1 Reflectivity method in 'Aniseis'

In Chapter 2, I introduced the wave equation which I recall below:

$$\rho \frac{\partial^2 u_i(x,t)}{\partial t^2} = c_{ijkl} \frac{\partial^2 u_k(x,t)}{\partial x_j \partial x_l} \tag{3.13}$$

where u_i is the ith component of the displacement, c_{ijkl} is the elastic or the stiffness tensor, ρ is density and t is time. Equation (3.13) has a plane wave solution of the form (Tsvankin 2001, pp. 3):

$$u_k = U_k exp\lfloor i\omega (n_j x_j / v - t)\rfloor, \tag{3.14}$$

where U_k are the components of the polarization vector **U**, ***n*** is the unit vector orthogonal to the plane wavefront and ω is the angular frequency.

Consider a simple model with two half-space layers separated by a horizontal interface and a plane wave impinges on the interface (Figure 3.3). It is well known that when a wave impinges upon an interface, it reflects and refracts and formulae are available for the reflection and transmission coefficients for both the isotropic case (Aki and Richards, 2002) and anisotropic case (Schoenberg and Protazio, 1992). These formulae are useful for simple two-layered models, but for practical purposes we want to handle the cases of multi-layered models and curved wavefront. The reflectivity method deals with these two problems together (Fuchs and Muller, 1971). The propagation of a single plane wave through a layered model can be handled through the successive application of the reflection and transmission coefficient formulae. The method works by writing the source solution as the sum of plane waves, propagating each plane wave through the model individually and then summing up the responses to get the final solution.

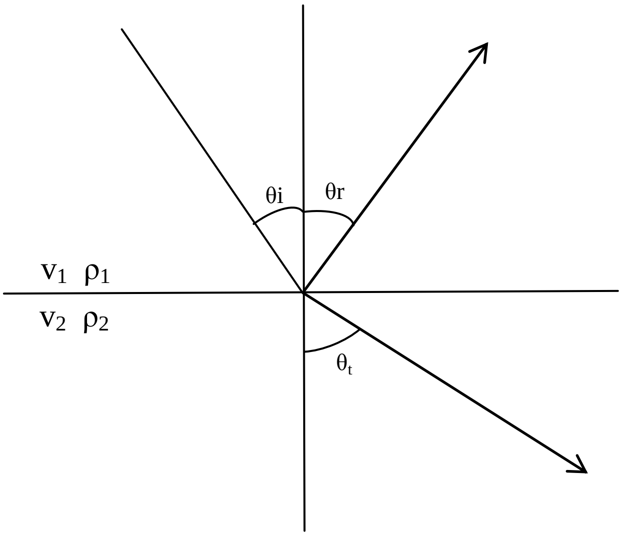

Figure 3.3: Reflection and refraction of a plane wave at a horizontal interface between two media with velocities v_1 and v_2 respectively. θ_i, θ_r and θ_t are the incidence, reflected and refracted angles respectively.

For an explosive source in an infinite isotropic and homogenous medium, a spherical polar symmetry exists around the source and the solution to the wave equation can be written in terms of displacement potential ϕ as (Ziolkowski, 1993):

$$\phi(r,t) = \frac{1}{r} q\left(t - \frac{r}{c}\right), \tag{3.15}$$

where q(t) has the dimension of volume and is referred to as the volume injection function, c is velocity and r is the radial distance from the source. The particle displacement is the spatial derivative of the displacement potential and can be written as (Ziolkowski, 1993):

$$u(r,t) = -\frac{\partial \phi(r,t)}{\partial r} \tag{3.16}$$

From where:

$$u(r,t) = \frac{1}{r^2} q\left(t - \frac{r}{c}\right) + \frac{1}{rc} q'\left(t - \frac{r}{c}\right), \tag{3.17}$$

The prime indicates differentiation with respect to r. The particle velocity is the time derivative of the displacement and could also be written as (Ziolkowski, 1993):

$$v(r,t) = \frac{\partial u}{\partial t} = \frac{1}{r^2} q'\left(t - \frac{r}{c}\right) + \frac{1}{rc} q''\left(t - \frac{r}{c}\right) \tag{3.18}$$

From Equations (3.17) and (3.18), it can be seen that both the particle displacement and velocity have two terms: the near field ($1/r^2$) term and the far field (1/r) term. The Fourier transform of Equation (3.15) can be written in integral form as (Fuchs and Muller, 1971):

$$\phi(r,z,\omega) = F(\omega)\int_0^\infty \frac{k}{iv_1} J_o(kr)\exp(-iv_1 z)dk, \tag{3.19}$$

where F(ω) is the Fourier transform of the volume injection function q(t), $J_o(kr)$ the Bessel function of the first kind and order zero, k the horizontal wave number and z is depth. The integrand of Equation (3.19) consists of a plane wave expressed in cylindrical coordinate system (Aki and Richards, 2002, pp. 193-194). The reflectivity method of Fuchs and Muller (1971) propagates each plane wave through the model individually and sums up the responses to obtain the solution in term of potential functions. The displacements are calculated by spatial derivatives of the potential and therefore both the near and far field terms are accounted for in the analysis. The ‘Aniseis’ package (Taylor, 2001) extends this theory to the anisotropic case. In going to the anisotropic case, there are two problems. First, there is no convenient potential formulation for the anisotropic wave propagation and second, there is a lack of analytical solution for a source in an anisotropic medium (Booth and Crampin, 1983). There are two-fold solutions to these problems. Firstly, ‘Aniseis’ is formulated in terms of displacement and not potential and secondly, it can only handle the case where the source layer is isotropic (Taylor, 2001). Appendix A (written by Mark Chapman) describes in details how anisotropic reflectivity method is implemented in ‘Aniseis’. Note in particular that ‘Aniseis’ is a far field approximation and does not account for the near source term so that solutions within a wavelength from the source are unreliable (Booth, 1982).

The user of ‘Aniseis’ is required to specify an input wavelet which is the volume injection function ($q(t)$ in Equation (3.15)). The default output for the synthetic seismogram is in particle displacement (Taylor, 2001) and in this case, the far field pulse shape is proportional to the time derivative of the volume injection function (as shown in Appendix A). Alternative options are available to output synthetic seismograms in particle velocity, pressure or stress (Taylor, 2001).

3.4.2 Synthetic data

I generated the synthetic data from six simple horizontally layered models. Four of the models have no attenuation while two of them have a known attenuation, $1/Q = 0.04$ (i.e. $Q = 25$). Details of the models are given below.

Model 1

Model 1 is a simple homogeneous isotropic acoustic half-space separated from a second acoustic half-space by a horizontal plane interface (Figure 3.4). In this model there is no attenuation. The parameters of the model are summarized in Table 3.1. A Ricker wavelet with a centre frequency of 25 Hz and a start time of 100 ms (Figure 3.5) was used as the source wavelet (q (t) in Equation (3.15)) and has the dimension of volume. The source is an explosive source and was placed 1 km above the interface. Twenty-one receivers were placed at the same level as the source at a spacing of 100 m with a minimum receiver-offset of 0 m to achieve a maximum receiver-offset of 2000 m in the data. Data were recorded with a sample rate of 1 ms and a total time of 3 s. The synthetic data are displayed in Figure 3.6 for the vertical component of the particle displacement.

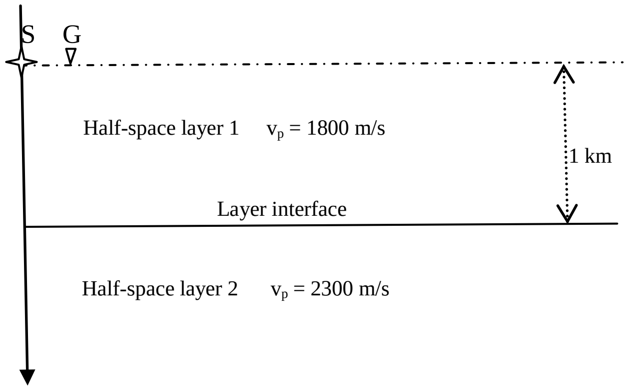

Figure 3.4: Configuration of model 1. The model comprises two horizontal half-space layers separated by a horizontal interface. An explosive source S was placed at 1 km above the interface and twenty-one receivers (G) were placed at the same level with the source at 100 m spacing.

Table 3. 1: Parameters of model 1

Layer	P-wave velocity (m/s)	S-wave velocity (m/s)	Density (kg/m^3)
1	1800	0	900
2	2300	0	1200

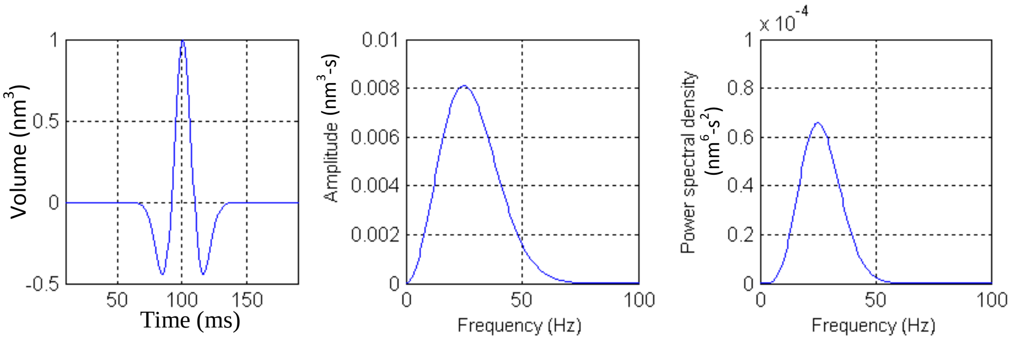

(a). (b). (c).

Figure 3.5: Ricker wavelet used as source wavelet (a) time series (b) amplitude spectrum (c) power spectrum. The centre frequency is 25 Hz. The wavelet has dimension of volume

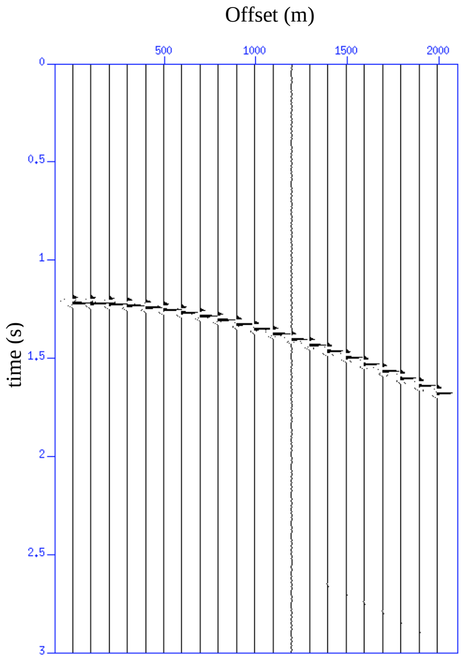

Figure 3.6: Synthetic data for model 1 for the vertical component of the particle displacement.

Figure 3.7 shows a comparison of the time series of the Ricker wavelet and the reflected wavelet at an offset of 1000 m. The far field pulse shape (reflected wavelet) is proportional to the time derivative of the Ricker wavelet (as shown in Appendix A). The corresponding spectra of the source wavelet and the reflected wavelet are shown in Figure 3.8 for comparison. I used a constant time gate of 180 ms to window these events. Compared with the source wavelet spectrum, the peak frequency of the reflected wavelet has been shifted to the right (30.8 Hz). Lange and Almoghrabi (1988) and Chung and Lawton (1995) have derived a mathematical expression to explain the shift in the peak frequency of the derivative of the Ricker wavelet, which I now reproduce.

Consider the time-domain expression of the Ricker wavelet (Ricker, 1940):

$$x(t) = (1 - 2\pi^2 f_o{}^2 t^2) e^{-\pi^2 fo^2 t^2} \tag{3.20}$$

where f_o is the peak frequency and t is time. The amplitude spectrum of the wavelet is given by (Ricker, 1945):

$$F(\omega) = A_R = \left(\frac{f}{f_o}\right)^2 e^{-\left(\frac{f}{f_o}\right)^2} \tag{3.21}$$

where f is frequency. The Fourier spectrum derivative of the wavelet $X_d(f)$ is given by (Lange and Almoghrabi, 1988):

$$X_d(f) = (-f)X(f), \tag{3.22}$$

where X(f) is the Fourier spectrum of the Ricker wavelet defined in Equation (3.20). The amplitude spectrum of the derivative of the Ricker wavelet is given by (Lange and Almoghrabi, 1988):

$$A_d(f) = |X_d(f)| = f|X(f)| = fA_R(f) \tag{3.23}$$

Substituting Equation (3.21) into Equation (3.23) and simplifying gives:

$$A_d(f) = f_o \left(\frac{f}{f_o}\right)^3 e^{-\left(\frac{f}{f_o}\right)^2} \tag{3.24}$$

Differentiating Equation (3.24) with respect to frequency gives:

$$\frac{dA_d(f)}{df} = -2\left(\frac{f}{f_o}\right)^4 e^{-\left(\frac{f}{f_o}\right)^2} + 3\left(\frac{f}{f_o}\right) e^{-\left(\frac{f}{f_o}\right)^2} \tag{3.25}$$

Equating Equation (3.25) to zero and solving for the new peak frequency f_p where the maximum amplitude occurs gives:

$$2\left(\frac{f_p}{f_o}\right)^4 = 3\left(\frac{f_p}{f_o}\right)^2 , \tag{3.26}$$

So that:

$$f_p = f_o\sqrt{\frac{3}{2}} \tag{3.27}$$

Equation (3.27) gives the relationship between the peak frequency of the Ricker wavelet f_o and that of its derivative f_p. Thus, with a Ricker wavelet with a peak frequency of 25 Hz used as the source wavelet, the peak frequency of the derivative of the wavelet from Equation (3.27) should be 30.6 Hz. The peak frequency is observed in the spectra (Figure 3.8) to be 30.8 Hz, which is consistent with the result of Equation (3.27).

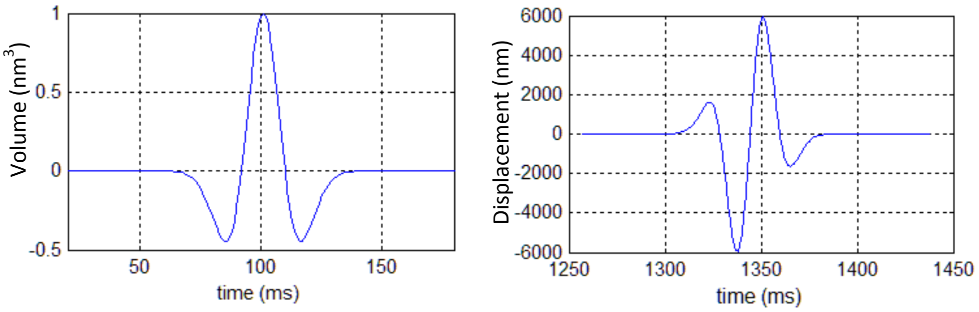

Figure 3.7: Relationship between the Ricker wavelet and the reflected wavelet (a) source wavelet with dimension of volume (b) reflected wavelet at 1000 m offset with dimension of displacement. The reflected wavelet is proportional to the time derivative of the source wavelet.

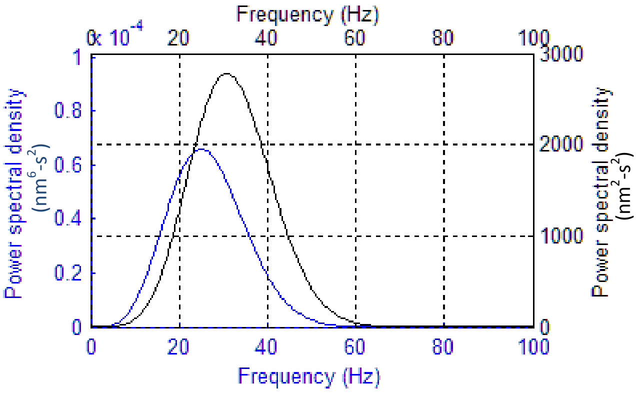

Figure 3.8: Relationship between the frequency spectrum of the Ricker wavelet (blue) and the reflected particle displacement wavelet at an offset of 1000 m (black). The centre frequency of the spectrum of the source wavelet is 25 Hz while that of the reflected wavelet is 30.8 Hz.

Effect of windowing

Carter (2003) performed several tests to assess the influence of window bias (tapers) and window length on Q estimation using the QVO-spectral ratio method. He demonstrated through synthetic modelling that Q estimates improve with increasing window length and regression bandwidth and that the Hanning and Papoulis windows gave the best results as they both allow the use of larger bandwidth for linear regression of the spectral ratios. The Boxcar and Dasgupta windows on the other hand limit the usable bandwidth and thus reduce the accuracy of the Q estimates. Thus, I have not repeated these tests here. I only tested the effects of applying the Hanning taper on the reflected wavelet and the resulting spectra by using a time gate of 180 ms to window the reflection from the interface between the two layers and computing the spectra with and without the taper. Figure 3.9 shows the time series and the corresponding spectral plots at a fixed receiver-offset of 1000 m for the reflected P-wave at the interface. The window causes very minor changes in the wavelet shape and a small reduction in the magnitude of the maximum amplitude in the corresponding spectra. This minor effect of the Hanning window will be common to all the traces analyzed and thus, robust Q estimates could be made. Figure 3.10 shows sample spectral plots at selected offsets with the application of the Hanning Taper using a constant window length of 180 ms. The peak frequency for the offsets shown is constant at 30.8 Hz as expected since there is no attenuation in the model.

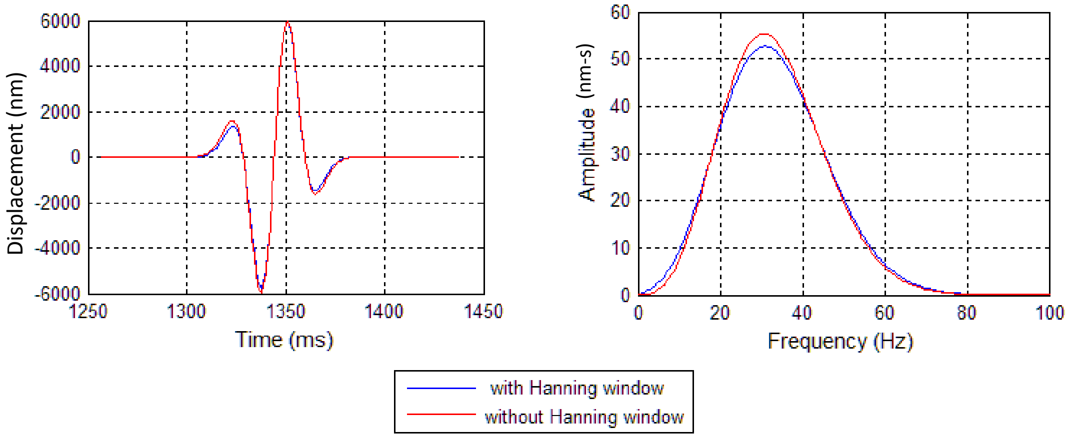

Figure 3.9: Effect of windowing on time series and corresponding spectra for reflected wave at 1000 m offset.

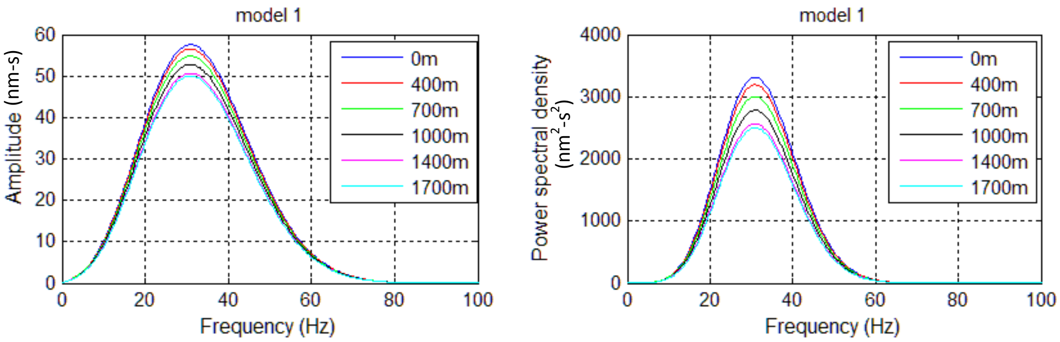

Figure 3. 10: Sample spectra (model 1) with no attenuation. The peak frequency for the offsets shown is constant at 30.8 Hz as expected.

Reference event

The first step in the application of the QVO - spectral ratio method is the selection of a reference event. Here, I used a transmitted wave recorded by a receiver placed at a depth of 100 m below the source. Before arriving at this receiver depth, I considered ten receiver depths of between 10 - 100 m, increasing in steps of 10 m and observed that the LPSR versus frequency plots are sensitive to the receiver locations relative to the distance from the source. With a Ricker wavelet as the source time function with a centre frequency of 25 Hz and a P-wave velocity of 1800 m/s in the source layer, the wavelength of the wave generated is 72 m. The spectral analysis (Figure 3.11) reveals that the ratios are approximately horizontal as expected for reference locations at distances equal to or greater than 80 m from the source (i.e. greater than the wavelength) which is in accordance with the far field approximation of the

‘Aniseis’ modelling package. Thus, I used a reference location at a depth of 100 m below the source (Figure 3.12) for the final analysis. I picked the FFT windows along the reflection hyperbolic travel path as illustrated in Figure 3.13 and computed the Q values from the slopes of the logarithm of the spectral ratio regression using Equation (3.12) on a trace-by-trace basis. A sample LPSR against frequency regression plot is shown in Figure 3.14a for reflection at an offset of 1000 m. The plot is approximately horizontal, indicating no attenuation in the model as expected. The Q profile against offset is shown in Figure 3.14b. The average Q value in the model is 56,000, which shows that there is no measurable attenuation in the model as expected. This result does not depend on the regression bandwidth as the LPSR versus frequency plots are approximately horizontal.

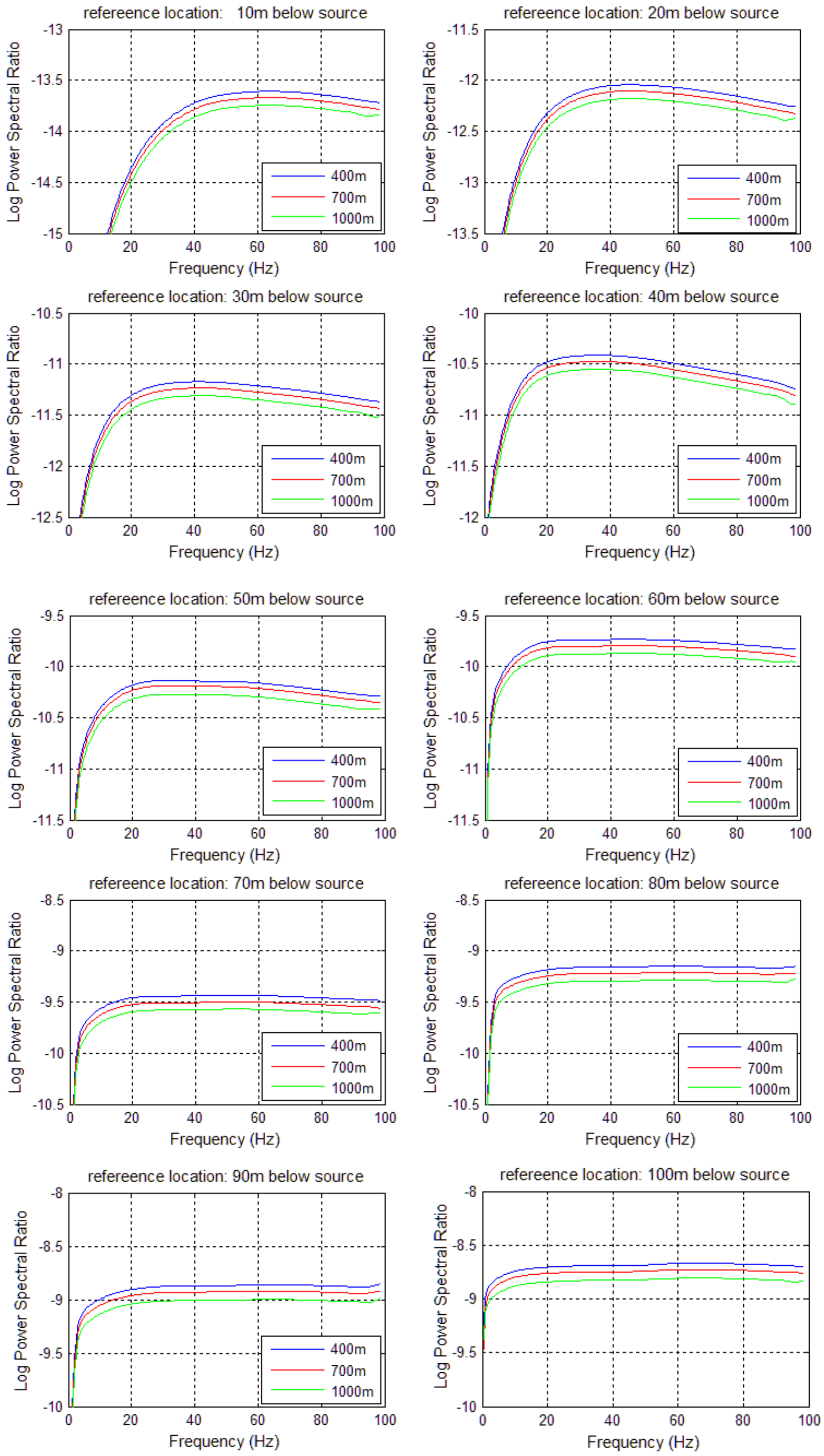

Figure 3.11: Effects of distance of reference location from the source: The Log Spectral ratio plots are approximately horizontal at distances equal to or greater than 80 m from the source. The modelling package is a far field approximation and does not account for the near field effect.

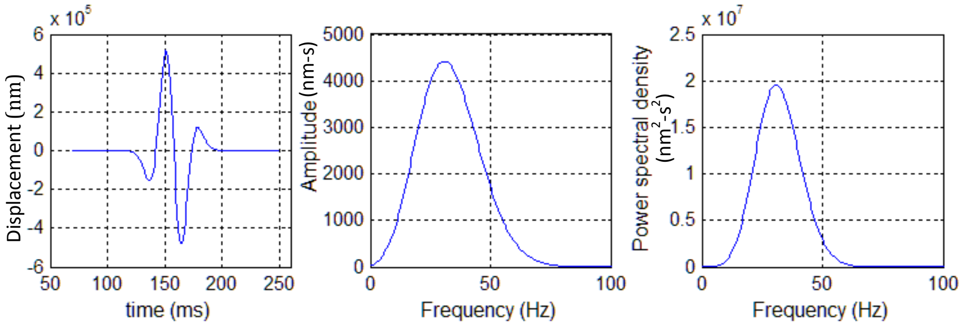

(a) (b) (c)

Figure 3.12: Reference wavelet located 100 m below the source. (a) time series (b) amplitude spectrum (c) power spectrum. The centre frequency is 30.8 Hz.

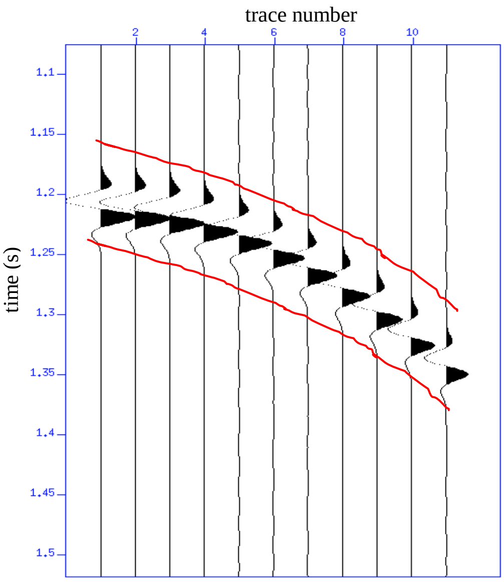

Figure 3.13: Windowing of traces along the reflection hyperbolic travel path. The trace spacing is 100 m.

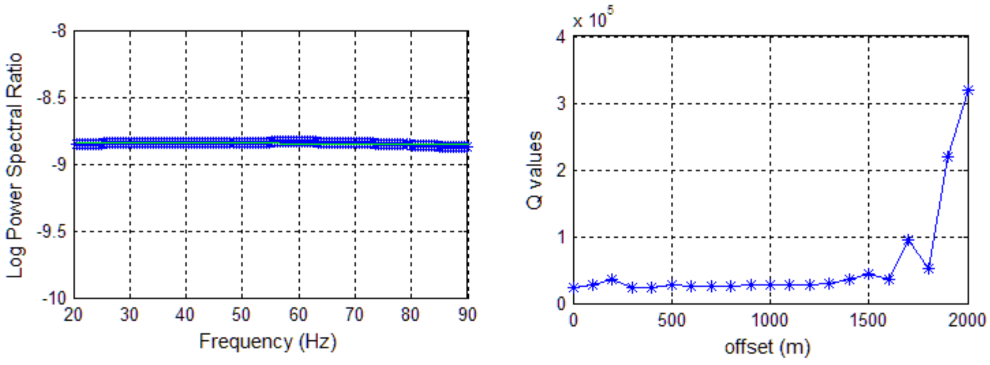

(a) (b)

Figure 3.14: Sample plots (a) sample Log Power Spectral Ratio (LPSR) versus frequency regression plot (1000 m offset). The plot is approximately horizontal, showing that there is no attenuation in the model. (b) Q profile against offset. The average Q value in the model is estimated from the average of the computed Q values for each trace (or offset).

Model 2

Model 2 as in the case of model 1, is also a simple homogeneous isotropic acoustic half-space separated from a second acoustic half-space by a horizontal plane interface (Figure 3.15). In this model there is also no attenuation. Here, the source was placed 2 km above the interface between the two half-space layers. Twenty-one receivers were place at the same level with the source at a spacing of 200 m with a minimum receiver offset of 0 m to achieve a maximum receiver-offset of 4000 m in the data. Data were recorded with a sample rate of 1ms and a total time of 4 s. The synthetic data are displayed in Figure 3.16 for the vertical component of particle displacement.

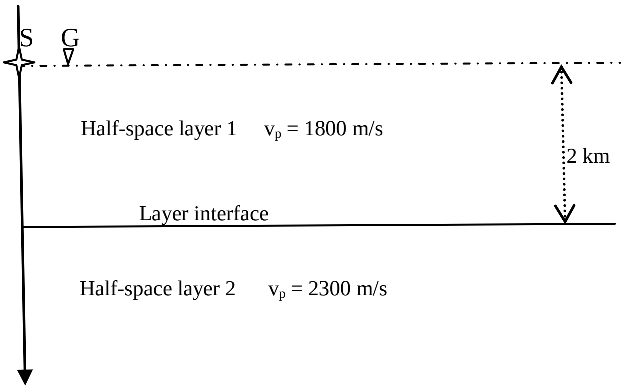

Figure 3.15: Configuration of model 2. The model comprises two horizontal half-space layers separated by a horizontal interface. An explosive source S was placed at 2 km above the interface and twenty-one receivers (G) were placed at the same level with the source at 200 m spacing.

Figure 3.17 shows sample spectral plots at selected offsets. The peak frequency for the offsets shown is constant at 30.8 Hz as expected since there is no attenuation in the model. For the reference wavelet, I also made use of a transmitted wave recorded at a depth of 100 m below the source. A sample LPSR against frequency regression plot is shown in Figure 3.18 while the Q profile against offset is shown in Figure 3.19. The average Q value in the model is 68,000, which shows that there is no measurable attenuation in the model as expected. This result does not also depend on the regression bandwidth as the LPSR versus frequency plots are approximately horizontal.

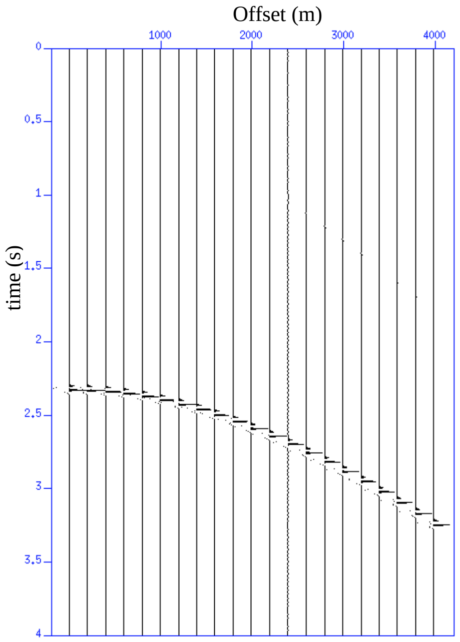

Figure 3.16: Synthetic data for model 2 for the vertical component of the particle displacement.

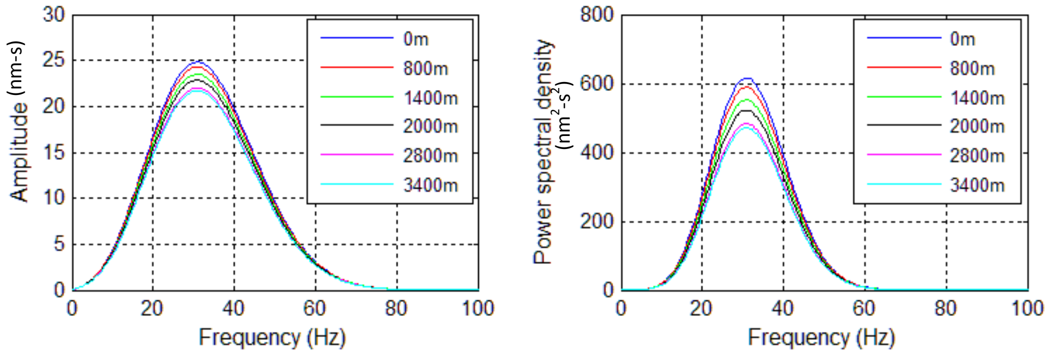

Figure 3. 17: Sample spectra (model 2) with no attenuation. The peak frequency for the offsets shown is constant at 30.8 Hz as expected.

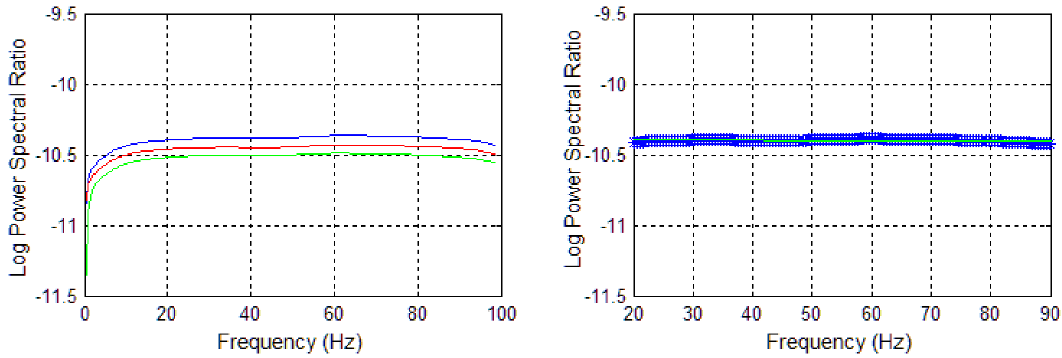

Figure 3.18: Sample Log power spectral ratio versus frequency plots. The plots are approximately horizontal, indicating no attenuation in the model as expected.

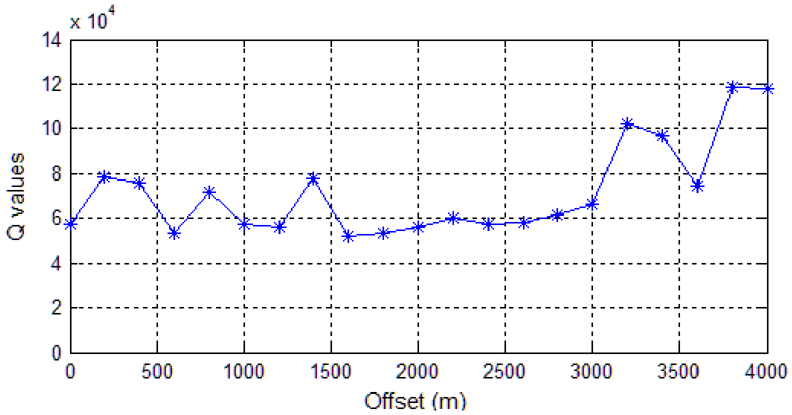

Figure 3.19: Q profile for model 2. High Q values are obtained signifying no measurable attenuation in the model.

Model 3

Model 3 is a simple homogeneous isotropic elastic half-space separated from a second elastic half-space by a horizontal plane interface (Figure 3.20). These will produce S-wave as well as P-wave reflections. In this model there is also no attenuation. The model parameters are summarized in Table 3.2. Here, the source was placed 1 km above the interface between the two half space layers. Twenty-one receivers were place at the same level with the source at a spacing of 100 m with a minimum receiver offset of 0 m to achieve a maximum receiver-offset of 2000 m in the data. Data were recorded with a sample rate of 1 ms and a total time of 3 s and are displayed in Figure 3.21 for the vertical component of particle displacement. The red arrow indicates the reflected P-wave while the blue arrow indicates the converted wave (S-wave).

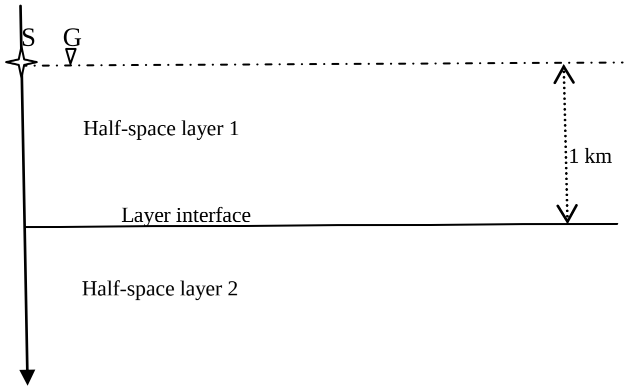

Figure 3.20: Configuration of model 3. The model comprises two horizontal half-space layers separated by a horizontal interface. An explosive source S was placed at 1 km above the interface and twenty-one receivers (G) were placed at the same level with the source at 100 m spacing.

Table 3. 2: Parameters of model 3

Layer	P-wave velocity (m/s)	S-wave velocity (m/s)	Density (kg/m^3)
1	1800	1000	900
2	2300	1300	1200

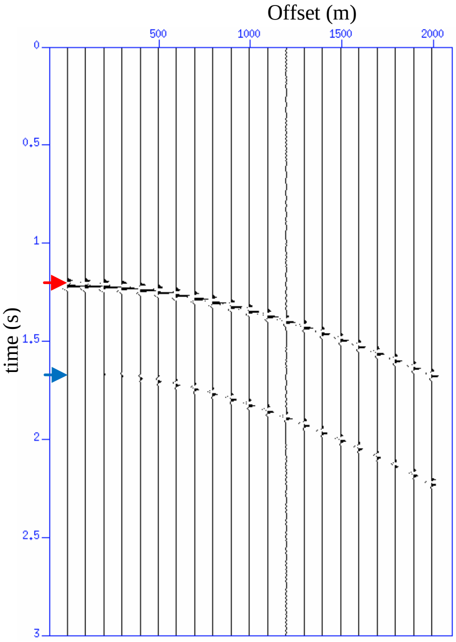

Figure 3.21: Synthetic data for model 3 for the vertical component of particle displacement. The red arrow indicates the reflected P-wave while the blue arrow indicates the converted wave (S-wave).

Figure 3.22 shows sample spectral plots at selected offsets. The peak frequency for the offsets shown is constant at 30.8 Hz as expected since there is no attenuation in the model. I also made use of a transmitted wave recorded at a depth of 100 m below the source as the reference event. Sample LPSR against frequency plots are shown in Figure 3.23 while the Q profile against offset is shown in Figure 3.24. The average Q value in the model is 42,000, which shows that there is no measurable attenuation in the model as expected. This result does not also depend on the regression bandwidth as the LPSR versus frequency plots are approximately horizontal.

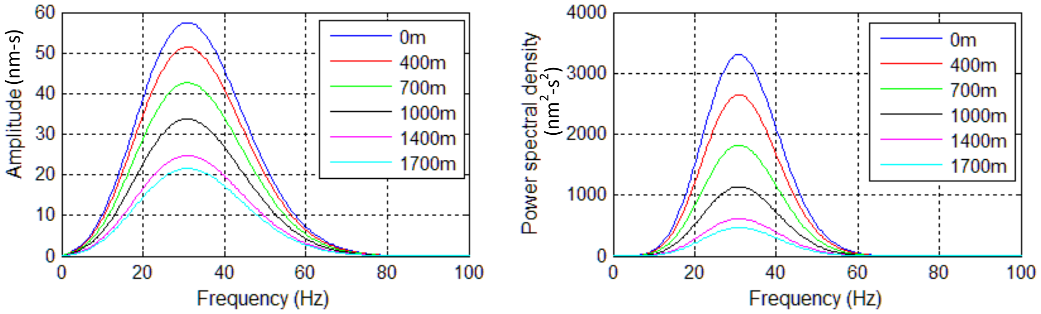

Figure 3.22: Sample spectra model 3. There no attenuation in the model. The peak frequency for the offsets shown is constant at 30.8 Hz as expected.

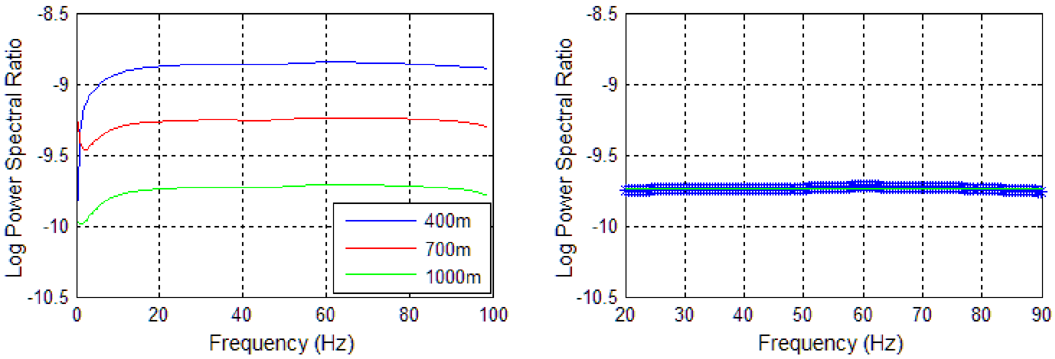

Figure 3.23: Sample Log power spectral ratio versus frequency plots. The plots are approximately horizontal, indicating no attenuation in the model as expected.

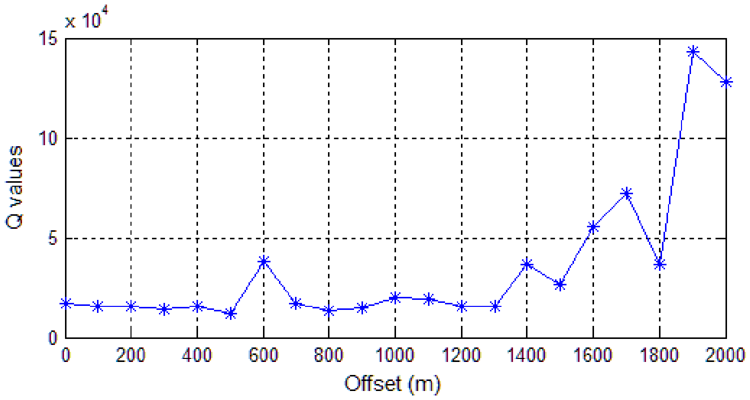

Figure 3.24: Q profile for model 3. High Q values are obtained signifying no measurable attenuation in the model

Model 4

Model 4 is also a simple homogeneous isotropic elastic half-space separated from a second elastic half-space by a horizontal plane interface (Figure 3.25). The upper half-space has an attenuation 1/Q = 0.04 (i.e. Q = 25). As in the case of model 3, an explosive source was placed 1 km above the interface between the two half space layers. Twenty-one receivers were also placed at the same level with the source at a spacing of 100 m with a minimum receiver offset of 0 m to achieve a maximum receiver-offset of 2000 m in the data. Data were recorded with a sample rate of 1ms and a total time of 3 s and are displayed in Figure 3.26 for the vertical component of particle displacement. The red arrow indicates the reflected P-wave while the blue arrow indicates the converted wave (S-wave).

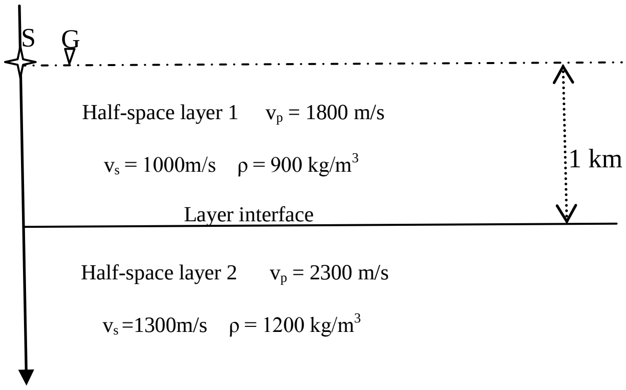

Figure 3.25: Configuration of model 4. The model comprises two horizontal half-space layers separated by a horizontal interface. The upper half-space has an attenuation 1/Q = 0.04. An explosive source S was placed at 1 km above the interface and twenty-one receivers (G) were placed at the same level with the source at 100 m spacing.

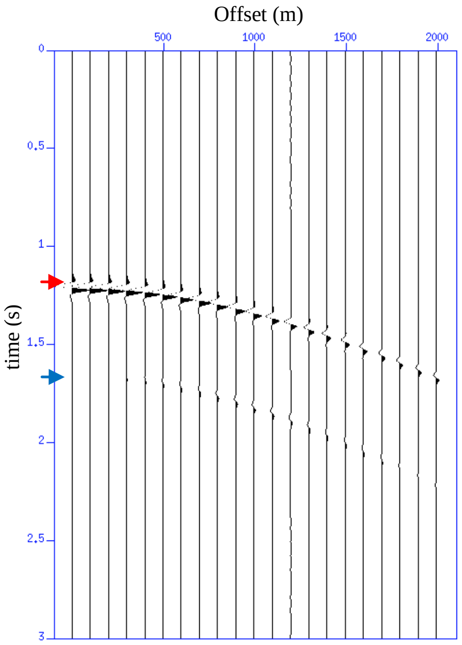

Figure 3.26: Synthetic data for model 4 for the vertical component of particle displacement. The red arrow indicates the reflected P-wave while the blue arrow indicates the converted wave (S-wave).

Figure 3.27 shows sample spectral plots at selected offsets. For the reference trace, I also made use of a transmitted wave recorded at a depth of 100 m below the source in the elastic case where there is no attenuation (model 3). The peak frequencies for the offsets shown are less than that of the reference trace (30.8 Hz) and decrease with increasing offset because of the high attenuation in the upper half-space layer. Sample LPSR against frequency plots are shown in Figure 3.28 while the Q profile against offset is shown in Figure 3.29. The estimated average Q value in the model is

25.6 ± 0.6 which is consistent with the model. The error shown is a standard error and was used to calculate the confidence interval as follows: 95 % confidence interval = 25.6 ± (0.6 x 1.96) = 25.6 ± 1.2. This implies that there is a 95 % confidence that the Q estimate lies between 24.4 and 26.8.

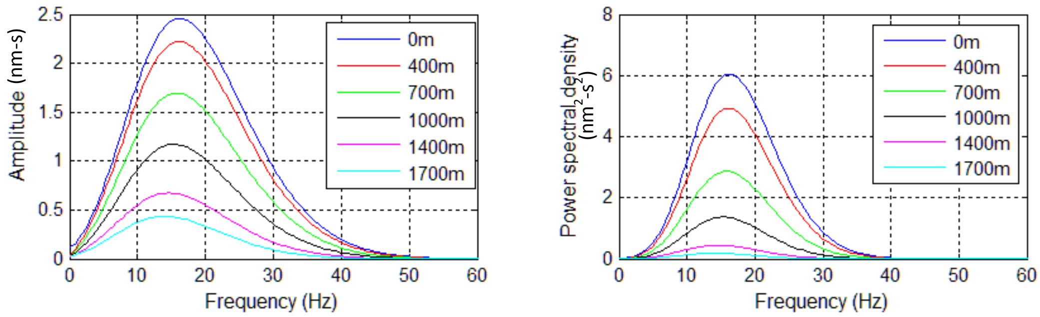

Figure 3.27: Sample spectra (model 4) with Q = 25 at selected offsets. The peak frequencies for the offsets shown are less than that of the reference trace (30.8 Hz) and decrease with increasing offset because of the high attenuation in the upper layer.

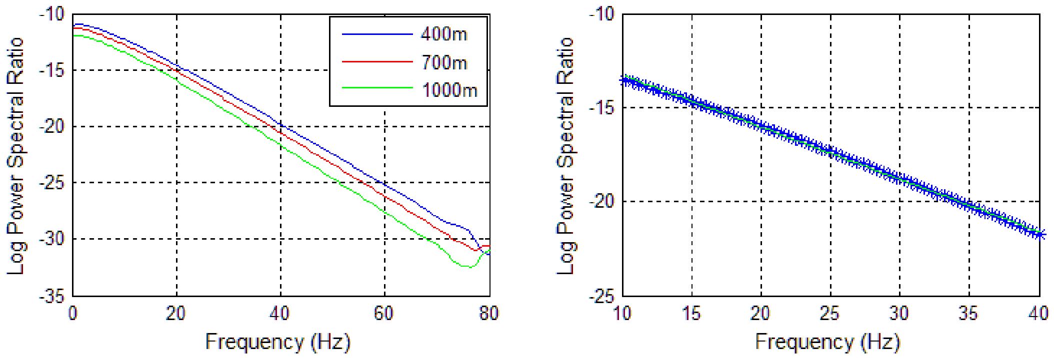

Figure 3.28: Sample Log power spectral ratio versus frequency plot. A frequency bandwidth of 10 – 40 Hz was used for linear regression. This bandwidth lies within the signal bandwidth.

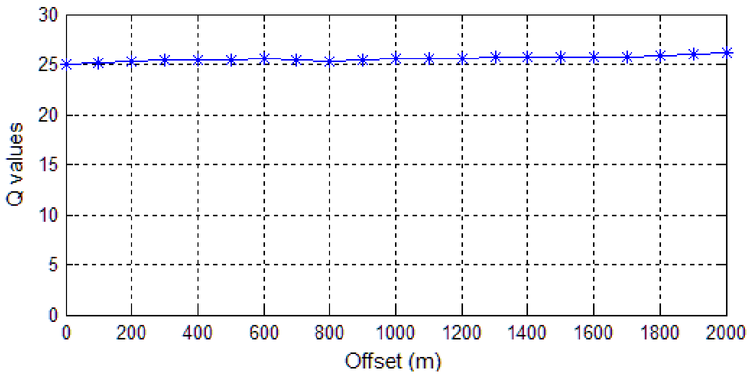

Figure 3.29: Q profile for model 4 with Q = 25. The average Q value estimated in the model is 25.6 ± 0.6.

Model 5

Model 5 consists of two isotropic elastic layers with the second layer as a half-space (Figure 3.30). In this model, there is no attenuation. The thickness of the upper layer is 1 km. The source was located on the surface of the model (free surface) while twenty-one receivers were placed on the same surface at 100 m spacing with a minimum and maximum source-receiver offset of 0 m and 2000 m respectively. This model is similar to model 3 except for the free surface at the level of the source and receivers. The free surface introduces multiple reflections, causing the pressure to be zero, and increasing the amplitude of the vertical component of the particle displacement. Data were recorded with a sample rate of 1 ms and total time of 3 s. The software modifies the explosive source placed on top of the model such that outward waves are suppressed and only contributions from waves directed into the model are generated (Taylor, 2001). The synthetic data produced from the model are displayed in Figure 3.31 for the vertical component of particle displacement. The red arrow indicates the reflected P-wave, the blue arrow indicates the converted wave (S-wave) while the green and purple arrows indicate multiples of the P-and S- waves reflections respectively. The increase in the amplitude caused by the free surface is not noticeable in the synthetic data (Figure 3.31) compared to the synthetic data from model 3 (Figure 3.21) with no free surface. This is due to the auto scaling of the software (Seismic Unix) used to generate the plots. The software scales the amplitude based on the maximum amplitude on the first trace in the gather. To see the effect of the free surface on the synthetic data, I extracted the first trace from the data from model 3 and model 5 both at 0 m offset and plotted the data using Matlab (Figure 3.32). The amplitude of the model 5 data is observed to increase by a factor of 2 as a result of the free surface compared to the data from model 3 where there is no free surface.

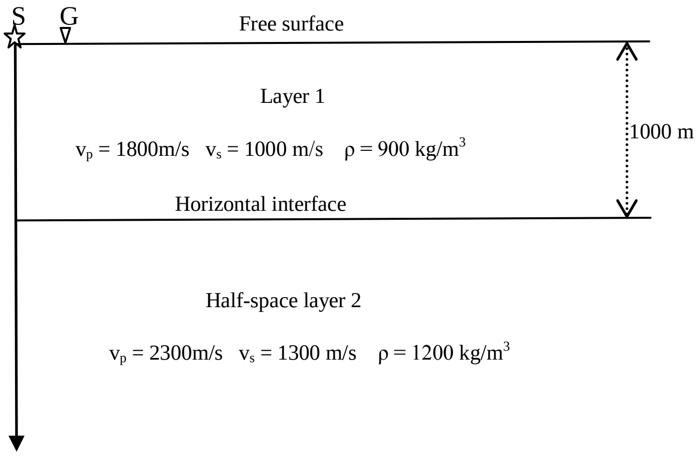

Figure 3.30: Configuration of model 5. The model comprises two horizontal elastic layers separated by a horizontal interface. The thickness of the first layer is 1 km while the second layer is a half-space. There is no attenuation in the model. An explosive source S was placed on the surface of the model while twenty-one receivers (G) were also placed at the surface of the model at 100 m spacing.

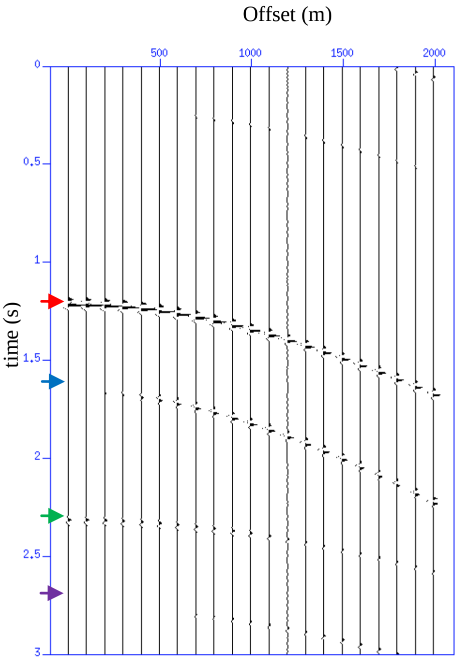

Figure 3.31: Synthetic data for model 5 for the vertical component of particle displacement. The red arrow indicates the reflected P-wave while the blue arrow indicates the converted wave (S-wave). The green and purple arrows indicate multiples of the P-and S- wave reflections.

Figure 3.33 shows sample spectral plots at selected offsets. The peak frequency for the offsets shown is constant at 30.8 Hz as expected since there is no attenuation in the model. I also made use of a transmitted wave recorded at a depth of 100 m below the source as the reference event. Sample LPSR against frequency plots are shown in Figure 3.34 while the Q profile against offset is shown in Figure 3.35. The estimated average Q value in the model is 30,000, which shows that there is no measurable attenuation in the model as expected. This result does not depend on the regression bandwidth as the LPSR versus frequency plots are approximately horizontal.

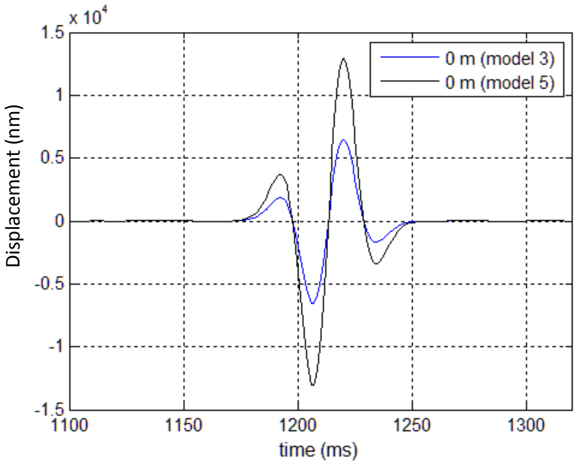

Figure 3.32: Effect of the free surface on the data. There is an increase in the amplitude by a factor of 2 in the model 5 data due to the free surface.

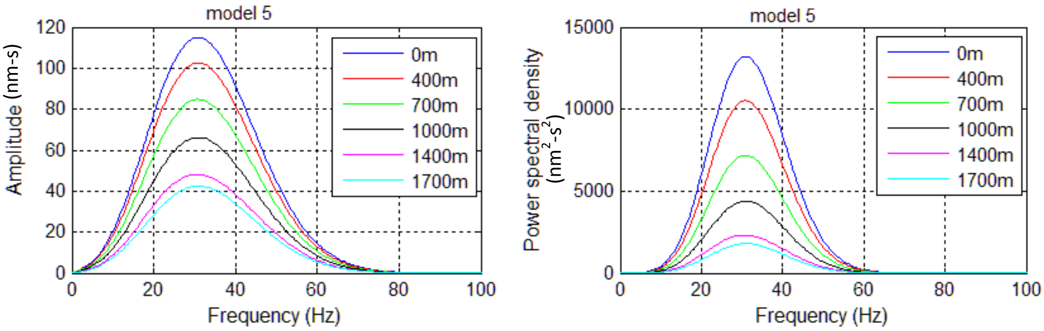

Figure 3.33: Sample spectra of model 5. There is no attenuation in the model. The peak frequency for the offsets shown is constant at 30.8 Hz as expected. Also the amplitude of the reflection is increased as expected due to the effect of the free surface.

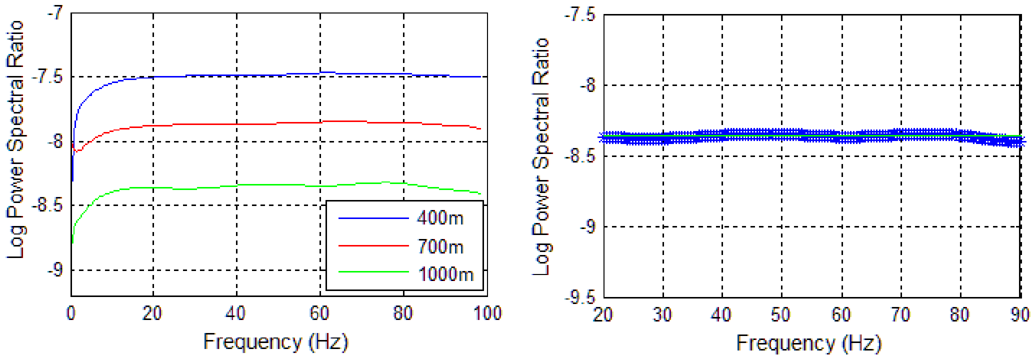

Figure 3.34: Sample Log power spectral ratio versus frequency plots (model 5). The plots are approximately horizontal, indicating no attenuation in the model as expected.

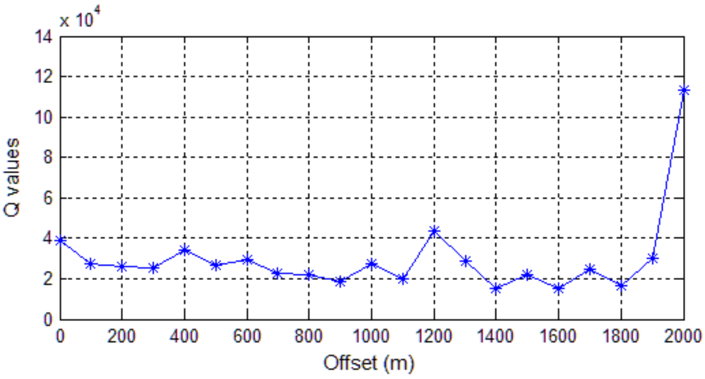

Figure 3.35: Q profile for model 5. High Q values are obtained signifying no measurable attenuation in the model

Model 6

Model 6 also consists of two isotropic elastic layers with the second layer as a half-space (Figure 3.36) as in the case of model 5. The first layer has a thickness of 1 km and an attenuation 1/Q = 0.04 (i.e. Q = 25) as in the case of model 4. The parameters of the model are the same as model 3 (Figure 3.36). The source was located on the surface of the model (free surface) while twenty-one receivers were placed on the same surface at 100 m spacing with a minimum and maximum source-receiver offset of 0 m and 2000 m respectively. The synthetic data are displayed in Figure 3.37 for the vertical component of particle displacement. The red arrow indicates the reflected P-wave while the blue arrow indicates the converted wave (S-wave). The multiples caused by the free surface are not visible in the data as a result of the high attenuation in the upper layer. Again, the increase in amplitude caused by the free surface is not noticeable as a result of the auto scaling of amplitude by the maximum amplitude by the plotting software. However, the effect is noticeable when the first traces at 0 m offset from model 4 and model 6 data are extracted and plotted in ‘Matlab’ for comparison (Figure 3.38). Figure 3.39 shows sample spectral plots at selected offsets. For the reference trace, I also made use of a transmitted wave recorded at a depth of 100 m below the source in the elastic case where there is no attenuation (model 5). The peak frequencies for the offsets shown are less than that of the reference trace (30.8 Hz) and decrease with increasing offset because of the high attenuation in the first layer. Sample LPSR against frequency plots are shown in Figure 3.40 while the Q profile against offset is shown in Figure 3.41. The estimated average Q value in the model is 25.6 ± 0.6 which is consistent with the model. The error shown is a standard error and was used to calculate the confidence interval as follows: 95% confidence interval = 25.6 ± (0.6 x 1.96) = 25.6 ± 1.2. This implies that there is a 95% confidence that the Q estimate lies between 24.4 and 26.8.

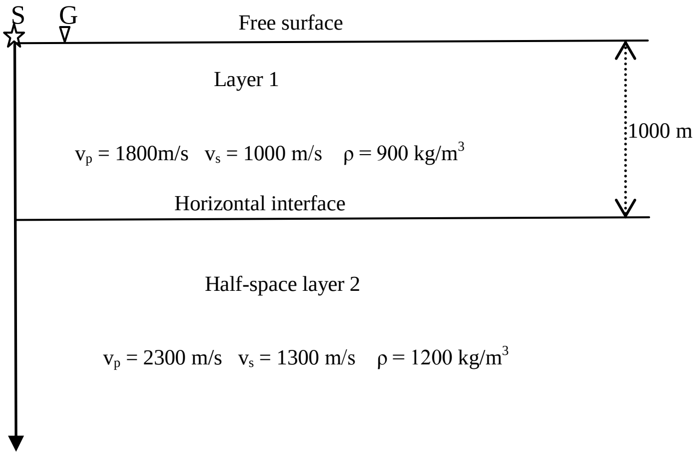

Figure 3.36: Configuration of model 6. The model comprises two horizontal elastic layers separated by a horizontal interface. The thickness of the first layer is 1 km while the second layer is a half-space. There is an attenuation 1/Q = 0.04 (Q = 25) in the model. An explosive source S was placed on the surface of the model (free surface) while twenty-one receivers (G) were also placed at the surface of the model at 100 m spacing.

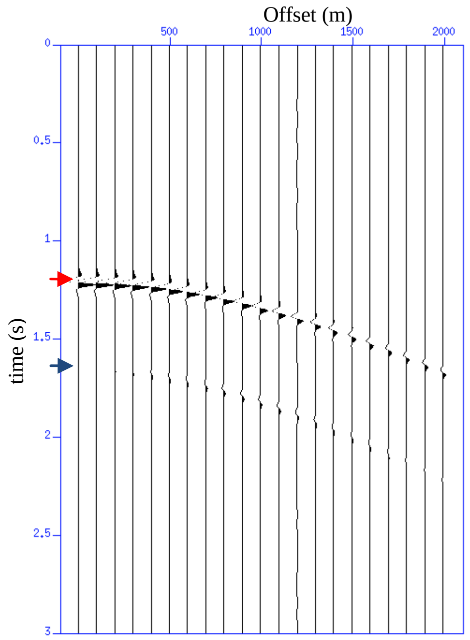

Figure 3.37: Synthetic data for model 6 for the vertical component of particle displacement. The red arrow indicates the reflected P-wave while the blue arrow indicates the converted wave (S-wave). The multiples caused by the free surface are not visible in the data as a result of the high attenuation in the upper layer.

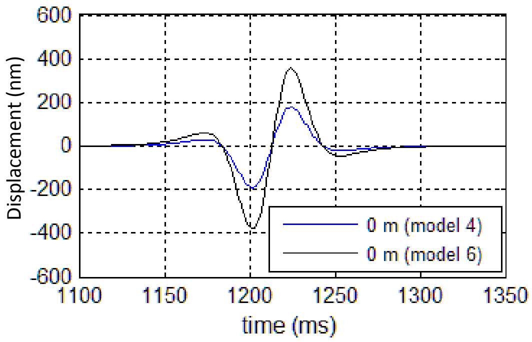

Figure 3.38: Effect of the free surface on the data. There is an increase in the amplitude by a factor of 2 in the model 6 data as a result of the free surface.

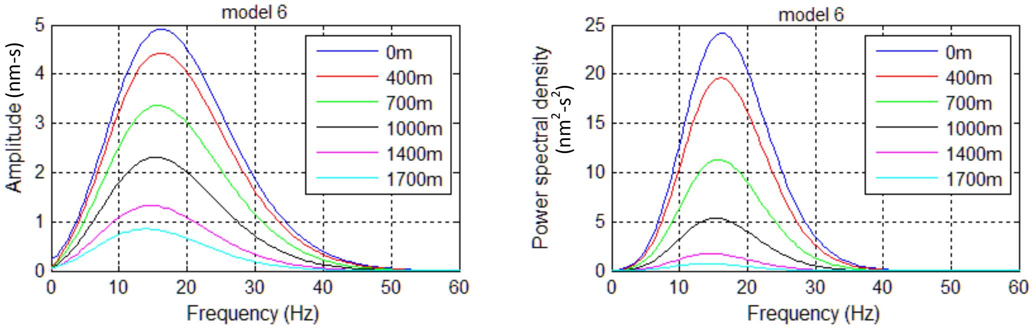

Figure 3.39: Sample spectra (model 6) with Q = 25. The peak frequencies for the offsets shown are less than that of the reference trace (30.8 Hz) and decrease with increasing offset because of the high attenuation in the first layer. Also the amplitude of the reflection is increased by a factor of 2 compared with model 4 data due to the free surface.

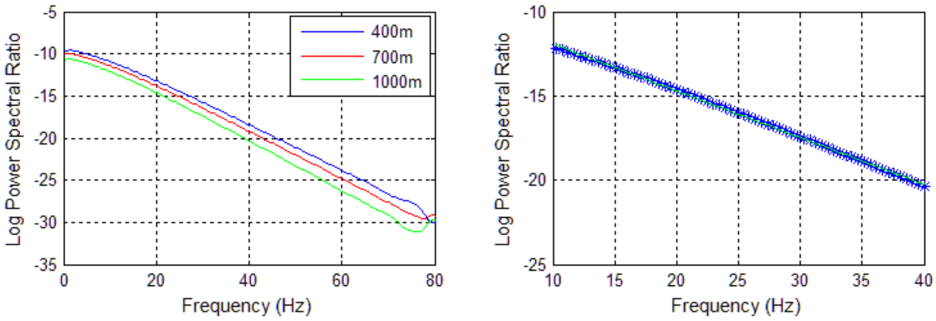

Figure 3.40: Sample Log power spectral ratio versus frequency plot. A frequency bandwidth of 10 - 40 Hz was used for linear regression. This bandwidth lies within the signal bandwidth.

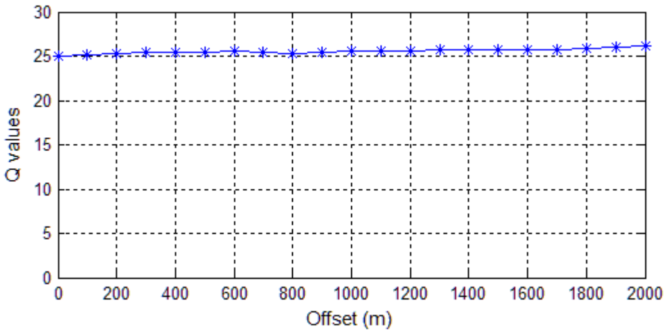

Figure 3.41: Q profile for model 6 with Q = 25. The average Q value estimated is 25.6 ± 0.6

Effect of NMO correction

To examine the effect of NMO correction on the Q estimates, I applied NMO correction to the synthetic data from the two models with Q = 25 (models 4 and 6) to flatten the P-wave reflection event at the interface between the two layers. The NMO-corrected data are shown in Figure 3.42. I then computed the slopes of the windowed event on a trace by trace basis using a constant frequency bandwidth of 10 - 40 Hz. Since the travel times are hyperbolic, I carried out a regression of the LPSR slopes against the square of the offset (Figure 3.43) and computed Q in the model from the intercept of the regression plot and the associated standard error in the estimated Q value from the standard error on the intercept.

For a horizontal layer with a constant velocity v, the NMO correction has a mathematical definition:

$$\Delta t = t(x) - t_o \approx \frac{x^2}{2v^2 t_o} \tag{3.27}$$

This approximation is valid for small offsets (i.e., offset/depth ≤ 1). The amount of NMO correction increases with offset and decreases with depth (z or t_o) and velocity (v).

The application of NMO correction to seismic data causes stretching of the wavelet which results in the distortion of the frequency spectrum. The amplitude of the wavelet is changed and higher frequencies are lost as a result of NMO-stretch effects. These effects are particularly prominent at large offset and shallow depths. Dasgupta and Clark (1998), to compensate for these effects used the formulation of Dunkin and Levin (1973). Carter (2003) maintains that the reversal of the NMO-stretch effects is only an approximation since the high frequencies once lost cannot be recovered as noted by Castoro *et al.*, (2001). The advantage of using NMO-corrected data is that it makes the windowing of the target events more convenient. In the two models, the depth to the reflector is 1000 m and no NMO-stretch compensation was applied. The results of the analysis give a Q value of 25.7 ± 0.2 which is consistent with the known Q value in the models. The standard error on the Q estimate was used to calculate confidence interval thus: 99 % confidence interval = 25.7 ± (0.2 x 2.58) = 25.7 ± 0.5. This implies that there is a 99 % confidence that the Q estimates lies between 25.2 and 26.2.

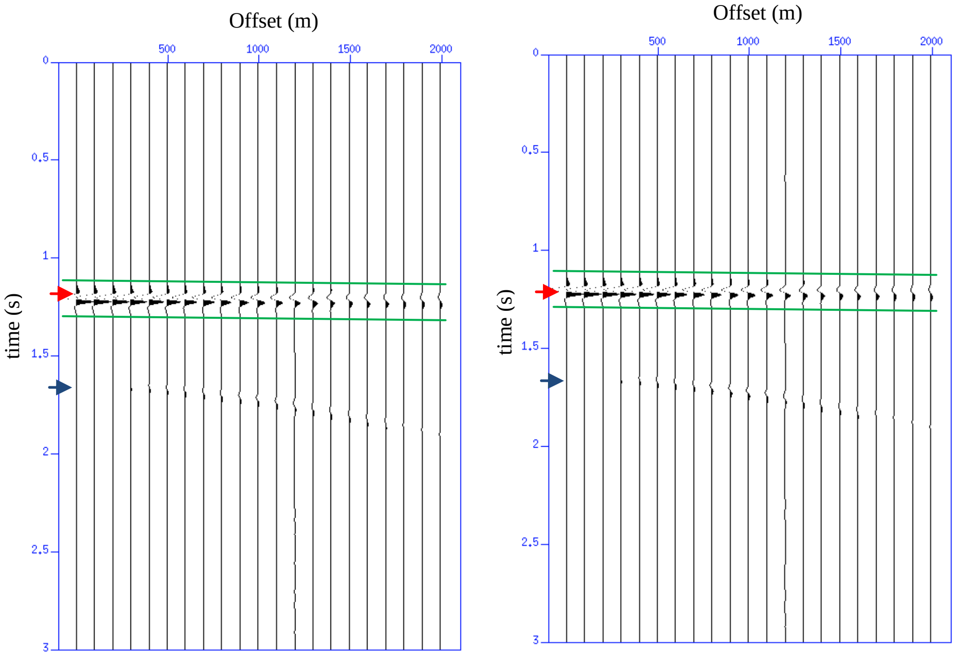

(a) (b)

Figure 3.42: Synthetic data with NMO correction applied to flatten the P-wave reflection event at the interface between the two layers (a) model 4 (b) model 6. The Q value in both models is 25. The red arrow indicates the reflected P-wave while the blue arrow indicates the converted wave (S-wave). The green lines illustrate the windowing of the traces.

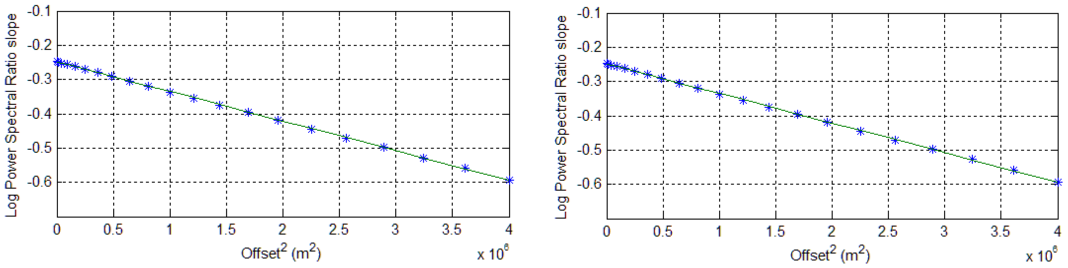

Figure 3.43: Log power spectral ratio slopes versus square offset plots (a) model 4 (b) model 6. The Q value in the model is estimated from the intercepts of the plots.

‘Aniseis’ modelling package provides alternative options to allow the output synthetic data to be specified either as particle displacement, velocity, pressure or stress with particle displacement as the default (Taylor, 2001). In all the model examples above, I have analysed the default particle displacement output synthetic data. For completeness, I consider the output synthetic data as velocity and stress respectively and applied the QVO - spectral ratio method to compute the Q values from the synthetic data. I used model 4 with Q = 25 in the first layer. The synthetic data obtained from the model in the two cases are shown in Figure 3.44.

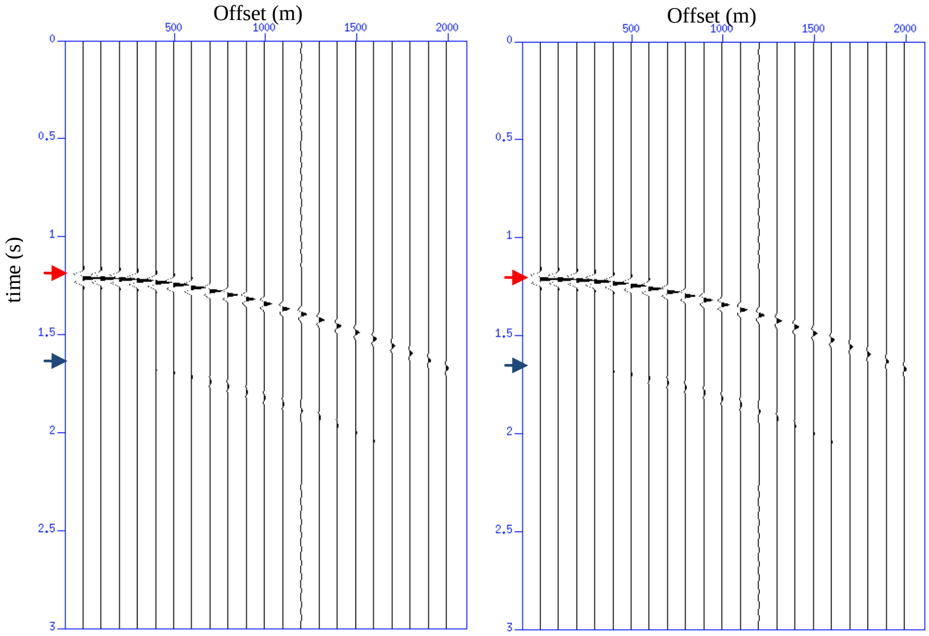

(a) (b)

Figure 3.44: Synthetic data for model 4 (a) vertical component of particle velocity (b) vertical component of stress. The red arrow indicates the reflected P-wave while the blue arrow indicates the converted wave (S-wave).

For the reference trace, I also made use of a transmitted wave recorded at a depth of 100 m below the source in the elastic case where there is no attenuation (Figure 3.45). Particle velocity and stress are the temporal derivatives of displacement in the far field. Hence, the shift in the peak frequency to higher frequency compared with that of the input Ricker wavelet (Figure 3.45). I computed the slopes of the windowed event on a trace by trace basis following the reflection hyperbolic travel path, using a constant window length of 180 ms and frequency bandwidth of 10 - 40 Hz. The Q value for each windowed trace was finally computed from the slope of the logarithm of the spectral ratio regression using Equation 3.12. The Q profiles against offset are shown in Figure 3.48. The estimated average Q values are 26.1 ± 0.6 for the vertical component of particle velocity synthetic data and 25.8 ± 0.6 for the vertical component of stress synthetic data respectively. Noting that the errors quoted are standard errors, there is a 95% confidence that the Q estimates lies between 24.9 and 27.3 for the particle velocity data and 24.6 and 27.0 for the vertical stress component data respectively.

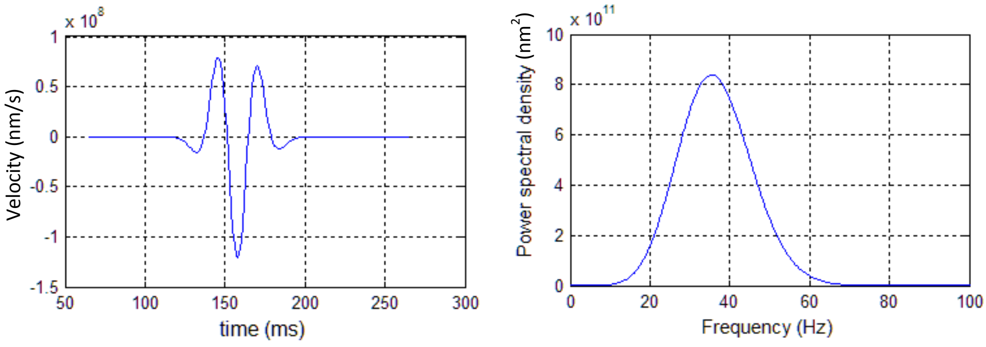

(a) (b)

Figure 3.45: Reference trace - transmitted wave at 100 m below source (vertical component of particle velocity) (a) time series (b) Power spectra.

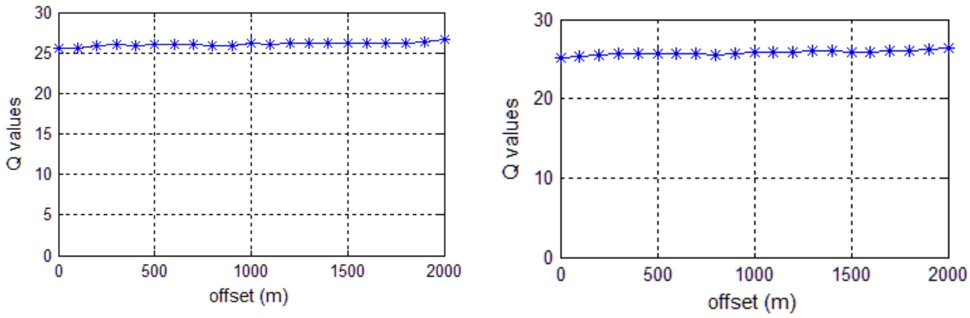

(a) (b)

Figure 3.46: Q profile with offset (a) vertical component of particle velocity. The average Q value estimated is 26.1 ± 0.6 (b) vertical component of stress. The average Q value estimated is 25.8 ± 0.6.

3.5 Summary

Measurement of attenuation from seismic data is difficult because of the influence of the interference between the primary reflection of interest and other arrivals from nearby interfaces, noise and multiples. Among the methods of estimating attenuation from seismic data, the spectral ratio method is very common, easy to use and stable. In this chapter, I have reviewed the spectral ratio method of estimating attenuation from seismic data. The method makes use of the spectral properties of the seismic wave and assumes that Q is frequency independent. It involves the comparison of the spectrum of a target signal with that of a reference pulse and is commonly used to estimate Q from VSP data. I have also reviewed the QVO method introduced by Dasgupta and Clark (1998), which is an extension of the spectral ratio method and have given some successful case studies of the application of the method in Q estimation.

In this thesis, I use the QVO - spectral ratio method introduced by Dasgupta and Clark (1998) for attenuation measurement. Although there are concerns over the use of the QVO method for Q estimation from seismic data mainly as a result of noise interference and problems of isolating only the target event for analysis, the method can still recover effective Q values provided the data have high S/N ratio. Firstly, both the synthetic and physical modelling datasets used in this thesis all have high signal-to-noise ratios, and hence it is possible to only capture the target events for analysis. Thus, interference effects caused by multiples and other noise interference do not bias the Q estimates. Secondly, all the layers in the models are horizontal which meets the requirement of the QVO model of shallow (<5°) dips (Dasgupta and Clark, 1998). I first assessed the performance of the method on models with known solutions using ‘Aniseis’ modelling package before applying it to complex models in this thesis. ‘Aniseis’ is a far field approximation and the default output for the synthetic seismogram is in particle displacement. In this case, the far field pulse shape is proportional to the time derivative of the input wavelet. Alternative options are available to output the synthetic seismograms in particle velocity, pressure or stress. Both particle velocity and stress are the temporal derivatives of particle displacement in the far field. For the models with no attenuation, the results of the synthetic test give very high Q values as expected, which signify that there is no measurable attenuation in the models. For models with known attenuation, the analysis method is able to recover the Q value at 95 % confident level for the non-NMO corrected data and 99 % confident level for the NMO corrected data. This result is not dependent on the whether the output synthetic data are displacement, velocity or stress, indicating the robustness of the QVO-spectral ratio method for Q estimation. Thus, the method is applied in this thesis for Q estimation.

Chapter 4 Seismic physical modelling studies of attenuation anisotropy in fractured media

In this chapter, I study the effects of aligned fractures on P-wave attenuation through seismic physical modelling, by which I mean using laboratory experiments on scale models of heterogeneous and/or anisotropic media. The chapter focuses mainly on attenuation anisotropy with the sole objective of gaining more understanding of scattering attenuation effects caused by a set of aligned fractures and especially the use of attenuation anisotropy as a potential tool for fractured reservoir characterization, after appropriate scale-up.

4.1 Introduction

Aligned fractures are known to cause seismic anisotropy, in which geoscientists have taken an increasing interest over recent years. Azimuthal variations in P-wave amplitude, travel-times, velocity, AVO gradient have all been shown to be diagnostic of the presence of aligned fractures (e.g. Li, 1997; Li, 1999; Hall *et al.*, 2000; Rathore *et al.*, 1995; Wang *et al*., 2007). Azimuthal variations in P-wave attenuation have also been observed in both field and laboratory data (e.g. Clark *et al*., 2001; Luo *et al*., 2006; Chichinina, *et al.*, 2006; Maultzsch *et al*., 2007; Clark *et al.*, 2009) and have been linked to fracture properties. Thus, the use of attenuation anisotropy to delineate fracture properties from seismic data could complement the use of amplitudes, travel time, velocity and AVO gradient attributes. Fractures with lengths on the order of seismic wavelength in reservoir rocks cause scattering of seismic waves which results in seismic coda. Experimental studies with laboratory scale models and numerical simulation studies (e.g. Schultz and Toksöz, 1995; Willis *et al.*, 2004a and 2004b; Willis *et al.*, 2006; Burns *et al.*, 2007) have shown that the scattered energy which exists as coda behind the primary reflection is more in the direction perpendicular to the fractures than in the parallel direction. These azimuthal variations in the scattered wavefield and the amount of the scattered energy could both provide useful information on fracture orientations (Willis *et al.*, 2006 and Burns *et al.*, 2007). The amount of scattered energy could be quantified through attenuation estimates. Seismic physical modelling studies to quantify the amount of the scattering energy through attenuation estimates could provide more understanding into these scattering effects. However, these studies are relatively scarce in the literature as most of the studies reported are devoted to the effects of aligned fractures on seismic velocity, travel time, AVO gradient and amplitude (e.g. Cheadle *et al.*, 1991; Isaac and Lawton, 1999; Wang *et al.*, 2007; Wei *et al.*, 2007a and 2007b). Thus, the main motivation for carrying out a seismic physical modelling study in this chapter is to gain more insight into the scattering effects caused by a suite of aligned fractures and the practice of using azimuthal variations in the scattered energy to characterize fractured reservoirs.

First, the physical modelling study aims to examine the scattering effects of a set of aligned fractures on seismic P-wave attenuation. The modelling involves first building physical scale-models in the laboratory and then using the pulse and transmission method to measure the seismic response in the model. The resulting data, though acquired in the laboratory, have similar features to the data acquired in the field, and hence the results of the attenuation analysis could provide more understanding into the current use of attenuation anisotropy as a tool for fracture characterization from seismic data.

Secondly, the physical modelling study also aims to look at the physical basis of using attenuation anisotropy as a tool to derive fracture properties from seismic data to provide more understanding of the current use of this attribute. Attenuation is expected to be greater in the direction normal to the fracture strike than in the direction parallel to the fracture strike.

The set up of the seismic physical modelling experiment is inspired by Hudson's equivalent medium theory (1980, 1981) which considers dilute inclusions of thin, penny-shaped ellipsoidal cracks in an isotropic background medium. A known number of round thin low-velocity chips are embedded in an isotropic base material to simulate a set of aligned vertical fractures as in Wei, 2004; Wei *et al.*, 2007a and 2007b; Wei *et al.*, 2008 and the fracture density is derived based on Hudson's theory (1980 and 1981).

4.2 The physical model

The experimental design and all the data produced from the physical model preceded the start of this study. The data sets were obtained in the China National Petroleum Corporation (CNPC) Geophysical Laboratory in China, where the physical model was built. The present study was based on these data, but the specific application was not used a priori to condition the experiments. In this section I give a description of the construction of the physical model and data acquisition procedure.

4.2.1 Construction of the physical model

The physical model is constructed from two horizontal layers (Figure 4.1). The first layer is made from epoxy resin and is isotropic with a thickness of 31.6 mm, P-wave velocity of 2314 m/s, S-wave velocity of 1100 m/s and density of 1.15 g/cm^3. The second layer is made from a mixture of epoxy resin and silicon rubber and has a thickness of 59.1 mm, P-wave velocity of 2610 m/s, S-wave velocity of 1183 m/s and density of 1.175 g/cm^3. The P- and S-wave velocities of the materials in the model were measured by using the pulse and transmission method as in Wei *et al.*, (2007a and 2007b) (personal discussion with X. Y. Li and J. Wei, 30/09/2008) and their values were given to me. The measurement errors in these velocities are unavailable. However, typical accuracy of ultrasonic velocity measurement can be ± 1.0 % (King and Marsden, 2002). Thin penny-shaped chips with P-wave velocity of 1300 m/s made from a mixture of epoxy resin and silicon rubbers are introduced into the isotropic background of the second layer to simulate two sets of inclined fracture models **A** and **B** (Figure 4.1). The penny-shaped chips all have the same diameter of 3mm and thickness of 0.128 mm. The two fracture models **A** and **B** are made of 144 and 18 layers of epoxy resin respectively. Once a layer is laid, 120 thin round chips are randomly embedded into the layer and another layer is added on the top. The whole process is repeated until the desired number of layers is achieved. The two fracture models **A** and **B** are then introduced into the isotropic background of the second layer of the physical model in such a way that the simulated fractures in model **A** are aligned vertically while those in model **B** are aligned in a direction making an angle of 29.2° with the vertical. Thus, the angle between the two inclined fracture models is 29.2°. The fracture density of model **A** is 6.4 % while that of fracture model **B** is 5.7 %. Details of the two fracture model parameters are given in Table 4.1. The model is constructed with a scale of 1:10,000 for spatial dimensions and time measurements. It is a simplified analogous representation of a fractured reservoir which has a younger rock overlying a much older rock which has been subjected to two stress regimes in its history, resulting in the two sets of inclined fractures. In a real life situation, the fractured reservoir could of course be much more complex. The layers may not be horizontal flat layers as in the model. There are also possibilities of having structures such as faults, syncline and anticline in the reservoir. Nevertheless, the model contains some complexity to test the performance of the data analysis techniques I will use to a problem with a known answer, to gain more understanding of the real data case.

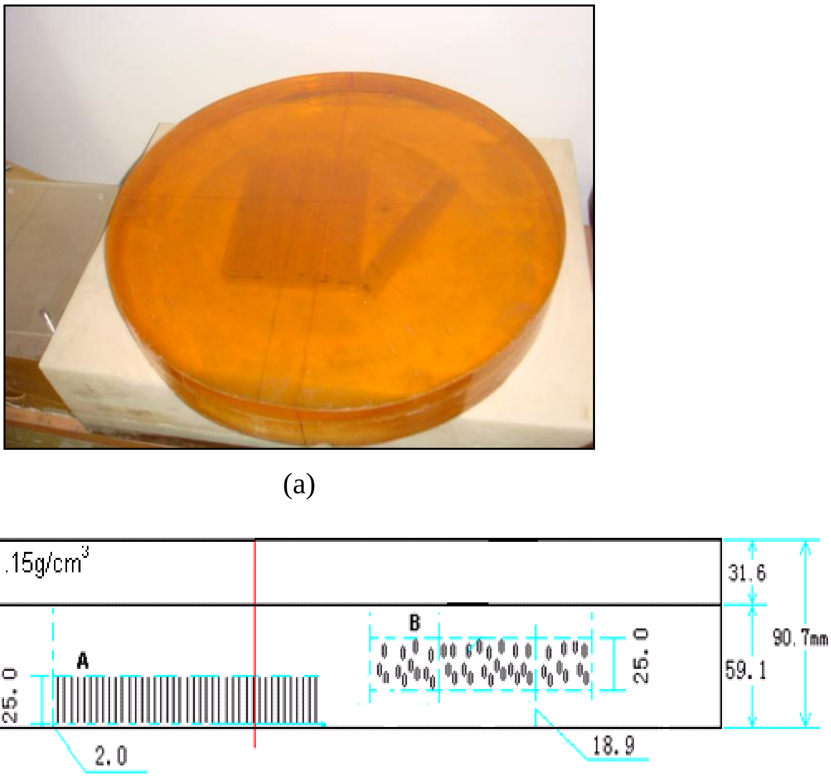

(a)

(b)

Figure 4.1: Physical model comprising two horizontal layers. (a) Base model (b) Sectional view of base model. The first layer is isotropic with a P-wave velocity of 2314 m/s and density of 1.15 g/cm^3 while the second layer has inclusions of two sets of thin penny-shaped mixture of epoxy and silicon rubber chips to simulate two inclined fracture sets - A and B. The isotropic background of this layer has a P-wave velocity of 2610 m/s and a density of 1.175 g/cm^3. The numbers shown specify the model dimensions in millimeters and the model is scaled up by 1:10,000 for spatial dimensions and time measurements**.**

Table 4.1: Parameters of the fracture models. The dimensions are scaled up to 1:10,000. Dimensions shown are not converted to real scaling.

Fracture model	**A**	**B**
No. of layers	144	18
No. of chips per layer	120	120
Total no. of chips in model	17280	2160
Layer thickness (mm)	1.132	1.36
Radius of each chip (mm)	1.5	1.5
Model length (mm)	213.5	214.5
Model breadth (mm)	172.0	24.4
Model height (mm)	25.0	25.0
Model volume (mm^3)	918050.0	130845.0
Fracture density (%)	6.4	5.7

4.2.2 Experimental set-up and data acquisition

The experimental set-up for the data acquisition is illustrated in Figure 4.2(a). The physical model was submerged in a water tank and the water depth to the top of the model is 80 mm. 2-D reflection data were acquired in three principal directions; the South-North (SN) and West-East (WE) and North West-South East (NWSE) directions respectively as indicated by the blue-arrowed lines in Figure 4.2(b). The SN survey line is parallel to the fracture strike (0° azimuth from the North direction), the WE survey line is normal to the fracture strike (90° azimuth from the North direction) and the NWSE survey line is along 135° azimuth from the North direction relative to fracture model **A** whose strike direction is along the 0° azimuth from North direction. The modelling system comprises an ultrasonic pulse source and a receiver system, an analogue/digital converter and a motor driven positioning system with a precision of 0.1 mm (Figure 4.3). The source and receiver were moved along the water surface. A total of 230 shots were made with a spacing of 2 mm and receiver interval of 2 mm at 16 mm minimum offset. The maximum offset-depth ratio to the top of the fractured-layer is 2.3 and 1.5 to the bottom of the fractured-layer. The ultrasonic pulse source has a centre frequency of 230 kHz and a bandwidth of 130 - 330 kHz. The frequency was scaled down by 10,000:1 to fit the scale model dimensions and velocity appropriately. The P-wave generated in the seismic physical modelling experiment has an approximate wavelength of 11.2 mm compared with the fracture diameter of 3 mm. Under the long wavelength approximation of the equivalent medium theory, the condition of equivalence of a fractured medium to an anisotropic medium is as follows (Bakulin *et al*., 2000):

Seismic wavelength >> fracture spacing >> fracture opening

For the physical model used here, 11.3 mm >> 1.132 mm >> 0.158 mm; thus, the model satisfies the long wavelength approximation and may be considered as anisotropic and the simulated fractures are expected to cause scattering of seismic waves which results in seismic coda. Details of the acquisition parameters are summarized in Table 4.2.

4.2.3 Data description

The physical modelling data though acquired in the laboratory have similar features to real field data. The raw data comprise of 230 shot gathers with 120 traces in each gather. On appropriate scaling to effective field dimensions the equivalent trace spacing is 20m, while the minimum and maximum offsets are 160 m and 2540 m respectively. Sample shot gathers for the three survey lines are shown in Figure 4.4 for the purpose of comparisons. The blue numbers corresponds to the reflections from the interfaces highlighted in Figure 4.2(a). The data have high signal to noise ratios, as all the reflection events of interest are quite free from noise contaminations. The target reflections are those from the top of the base model (number 1), the top of the fractured-layer (number 2) and the bottom of the fractured-layer (number 3). The event indicated as a question mark (?) is a multiple of the reflection from top of the base model. The top of the fractured - layer reflection is observed to be continuous up to a scaled offset of 940 m in the three survey lines (Figure 4.4). Beyond these offset range, the event appears to be marred by interference from the top of the base model reflection. A possible reason for this is the insufficient thickness of the second layer for the reflection from the top and bottom of the layer to be separated at higher offsets.

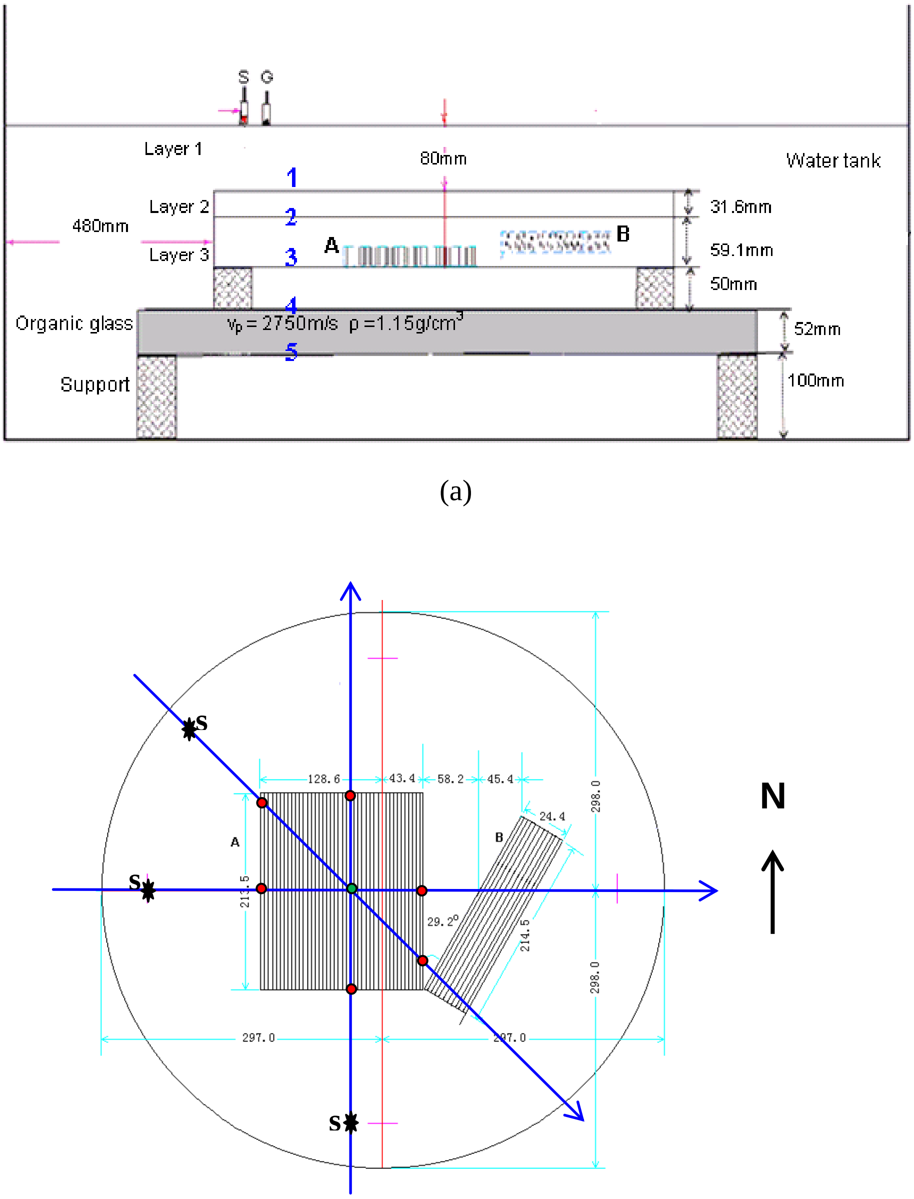

(a)

(b)

Figure 4.2: Experimental set-up. (a) Section view of the base model submerged in water tank where 2-D data were acquired. S is the first shot location and G is the first receiver location on the water surface while the blue numbers indicate the reflection interfaces. (b) Plan view of the fracture models in the second layer of the base model. 2-D data were acquired in the SN, WE and NWSE directions as indicated by the blue-arrowed lines. The numbers indicated specify the model dimensions in millimeters and are scaled up by 1:10000. The red circles indicate various locations on the edges of the fracture block A for the three survey lines while the point of intersection of the three lines (green circle) indicate the centre of the fracture block.

Figure 4.3: The physical modelling system for 2-D data acquisition in the laboratory. The base model is submerged in a water tank.

Table 4.2: Summary of data acquisition geometry - all the acquisition parameters given not converted to actual scales. The model dimensions and acquisition parameters are scaled up by 1:10000 while the frequency is scaled down by 10,000:1.

Water depth to base model (mm)	80
Number of shots	230
Shot interval (mm)	2
Receiver interval (mm)	2
Number of receivers	120
Minimum offset (mm)	16
Maximum offset (mm)	254
Fold of cover	60
Number of samples	3000
Sample rate (µs)	0.1

4.3 Data processing

Prior to attenuation analysis, it is necessary to process the data to highlight the target reflections. Since the data quality is high, the data processing was simple and straightforward with the sole aim of preserving all amplitude information needed for the attenuation analysis. Consequently, I applied the following processing sequence: geometry configuration, common mid-point (CMP) sorting, trace-muting, velocity analysis and NMO correction. The end result of the data processing is a brute stack section for each of the survey lines for ease of identification of the reflection events and picking of the travel-times to the target layers on the corresponding pre-stack NMO corrected CMP gathers for the attenuation analysis.

The raw shot gathers were sorted into 578 CMP gathers with the distance between each CMP as 10m. From the physical model geometry information (Figure 4.2b), the fracture model **A** lies within CMP numbers 145 to 358 for the SN survey line data, 123 to 295 for the WE survey line data and 120 to 344 for the NWSE survey line data respectively. The fracture model B lies within CMP numbers 353 to 399 for the WE survey line data.

Figure 4.5 shows sample CMP gathers for the three survey lines with top mute applied to remove the direct arrival noise. To perform the velocity analysis, super gathers were created from the combination of 5 CMP gathers and the velocity pre-computed using minimum and maximum guide values of 1000 m/s and 4000 m/s respectively prior to the conventional velocity picking. The interactive velocity analysis panels for the three survey lines are shown in Figure 4.6. The final velocity models were used to apply NMO correction to the data. Sample NMO-corrected gathers are shown in Figure 4.7, with no stretch mute applied while brute stacked sections are shown in Figure 4.8 for the three survey lines respectively. Scattering effects caused by the simulated fractures are noticeable on the stacked sections within the time window bounding the top and bottom fractured - layer reflections (numbered 2 and 3 respectively - Figure 4.8). The top model reflection occurs at a two-way zero offset travel time of 1085 ms and is consistent in the three survey lines. The top fractured-layer reflection occurs at a two-way travel time of 1387 ms and is also consistent in the three lines. Table 4.3 shows a comparison of the stacking velocities computed based on the model layer velocities (given to me) and those obtained from interactive velocity analysis picking for CMP 100 in the fractured-layer (layer 3) for the three survey lines where there are no fractures. The percentage difference between the measured stacking velocities and the computed ones ranges from 0.1 - 5 % which is indicative of good quality of data processing. However for the CMP(s) at the centre of fracture model **A**, azimuthal variations are observed in the stacking velocities for the fractured-layer as expected. Physical modelling and numerical modelling studies of seismic wave propagation in fractured media have shown that the variations in the stacking velocities are elliptical (e.g. Hall and Kendall, 2003; Liu, 2003; Wang, *et al.*, 2007). I examined the azimuthal variations in the stacking velocities in the fractured-layer to verify if velocity anisotropy could be observed in the data. Figure 4.9 shows the anisotropic behaviour observed in the stacking velocities in the fractured-layer at the centre of fracture model **A**. The azimuthal variations in stacking velocities observed in the data are approximately elliptical. The P-wave propagates with a faster velocity in the fracture strike direction and a slower velocity in the fracture normal direction, resulting in the observed azimuthal anisotropy.

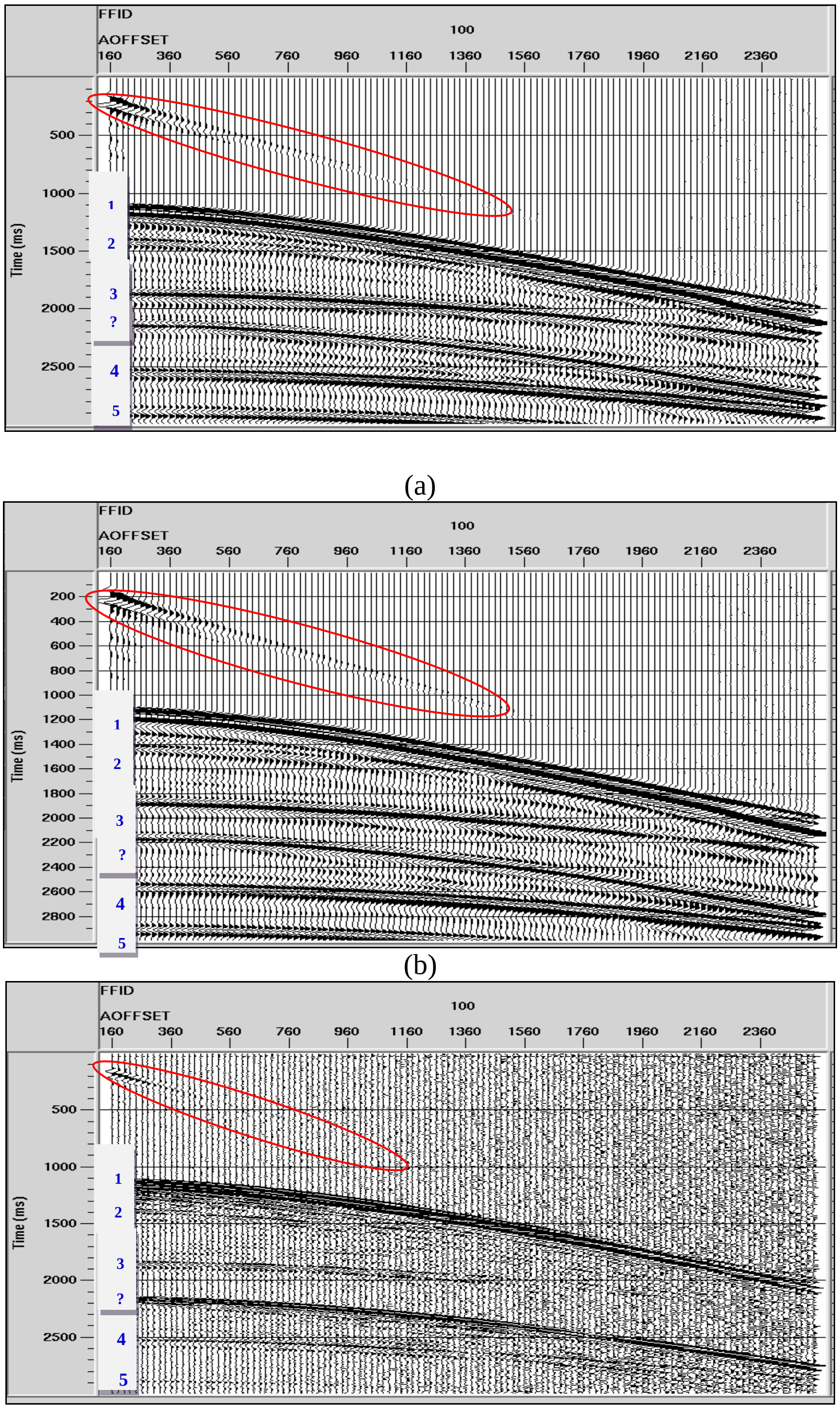

(a)

(b)

(c)

Figure 4.4: Sample shot gathers - field file ID number (FFID) 100 (a) SN survey line (b) WE survey line (c) NWSE survey line. The red ellipse indicates direct arrival noise. The blue numbers indicate reflections from the interfaces shown in Figure 4.2(a) while the question mark highlights multiple of top model reflection.

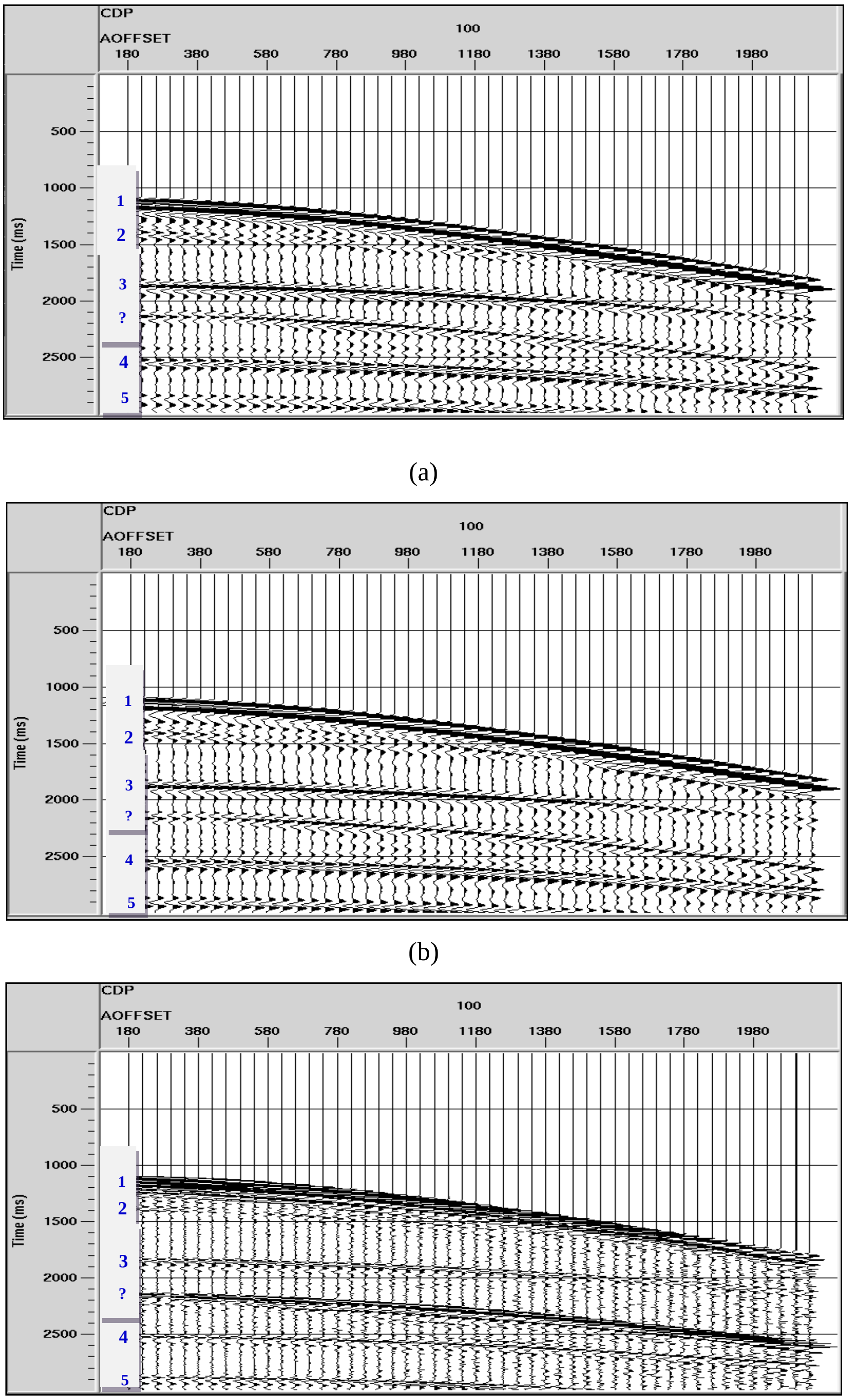

(a)

(b)

(c)

Figure 4.5: Sample CMP gathers (CMP 100) with top mute applied to remove direct arrival noise. (a) SN survey line (b) WE survey line. (c) NWSE survey line. The blue numbers indicate reflections from the interfaces shown in Figure 4.2(a) while the question mark highlights multiple of top model reflection.

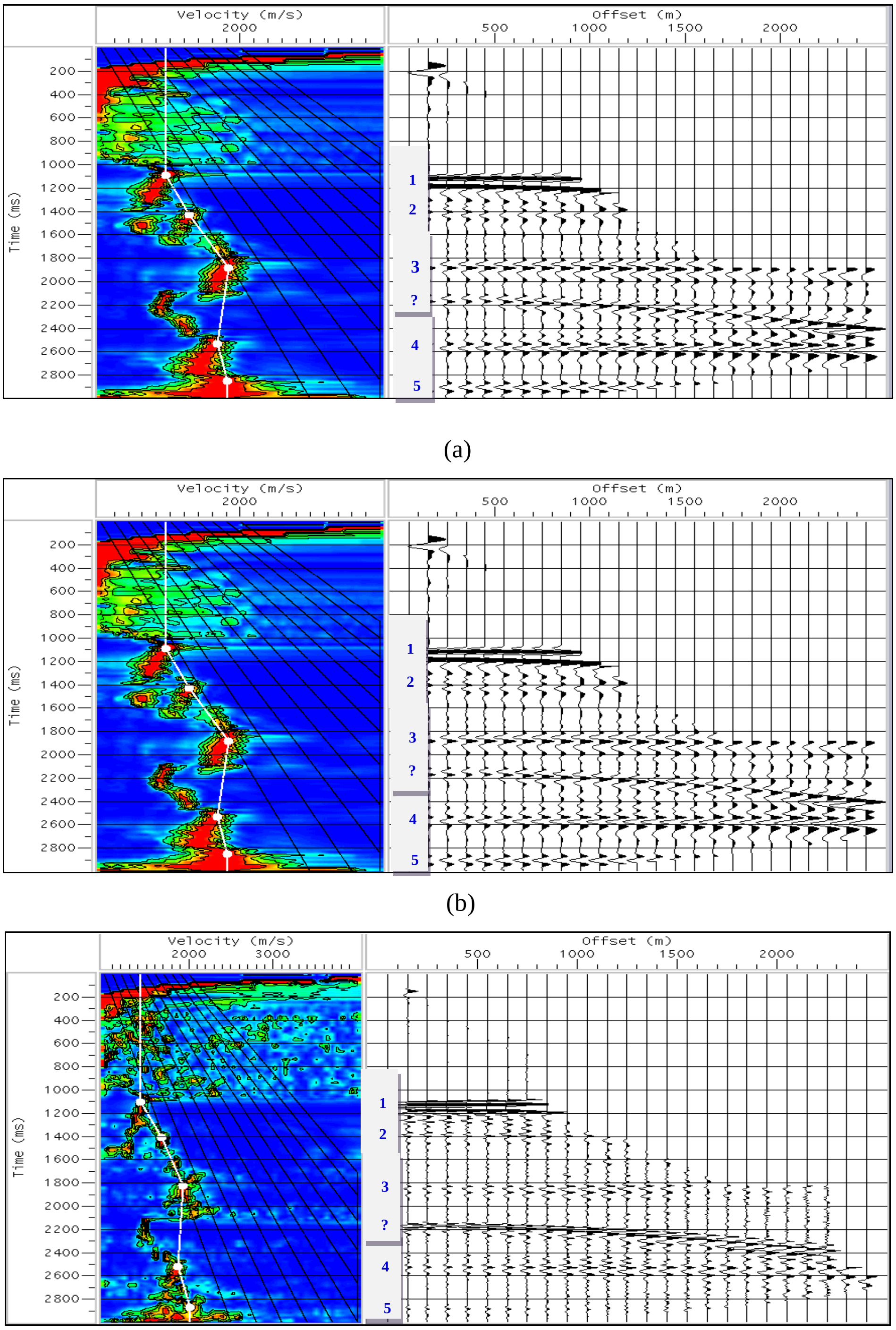

(a)

(b)

(c)

Figure 4.6: Interactive velocity analysis panels at the centre of fracture model **A** (red circle in Figure 4.2b) (a) SN survey line (b) WE survey line (c) NWSE survey line. The white line indicates the velocity picks and NMO correction has been applied to the data with a stretch mute of 30 %. The blue numbers indicate reflections from the interfaces shown in Figure 4.2(a) while the question mark highlights multiple of top model reflection

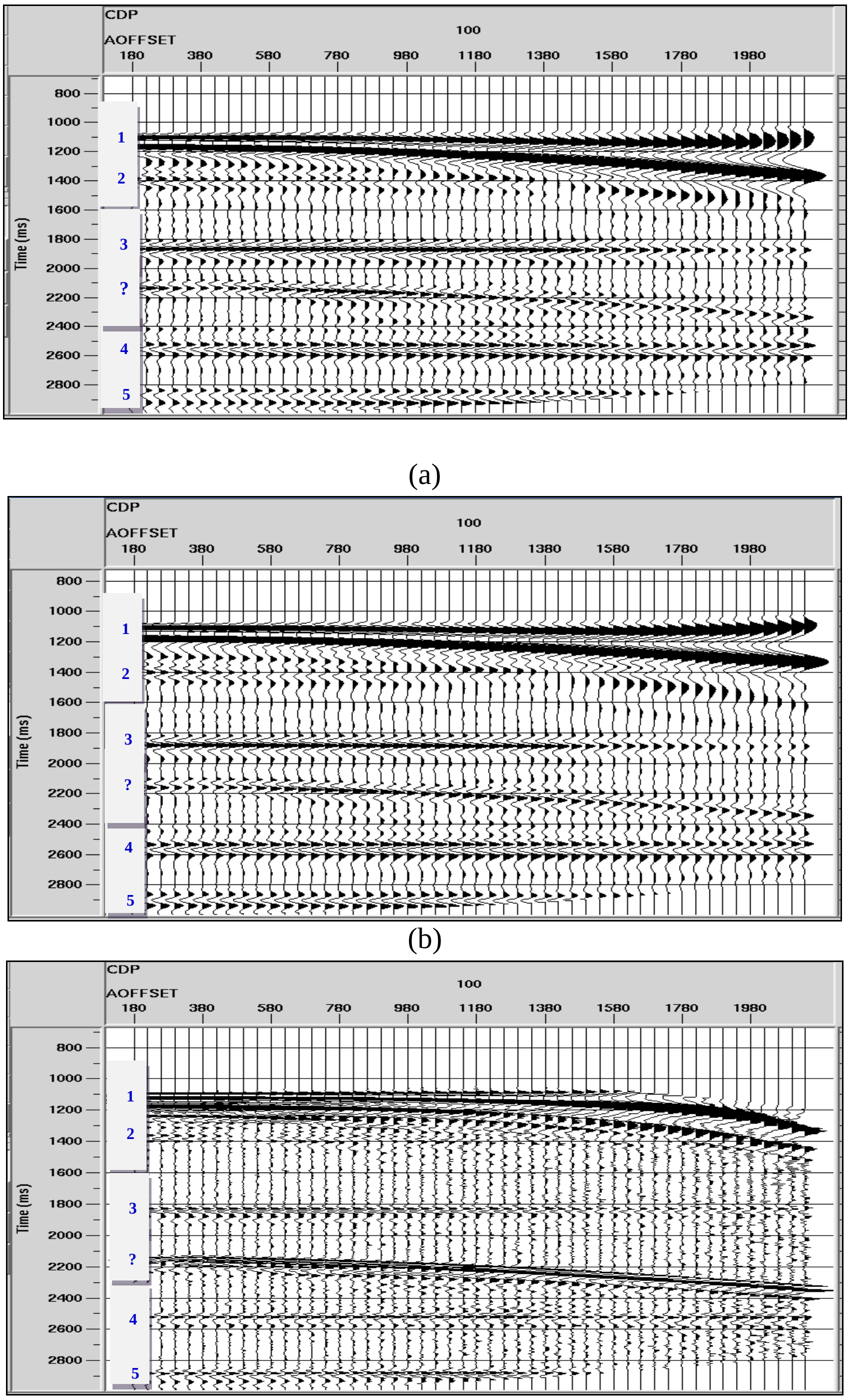

(a)

(b)

(c)

Figure 4.7: Sample NMO-corrected CMP gathers with no NMO stretch mute applied - CMP 100. (a) SN survey line (b) WE survey line. (c) NWSE survey line. The blue numbers indicate reflections from the interfaces shown in Figure 4.2(a) while the question mark highlights multiple of top model reflection. NMO stretch effects are obvious at far offsets especially for the top model reflection. Top fractured-layer reflection is obscured by top model reflection interference at far offsets.

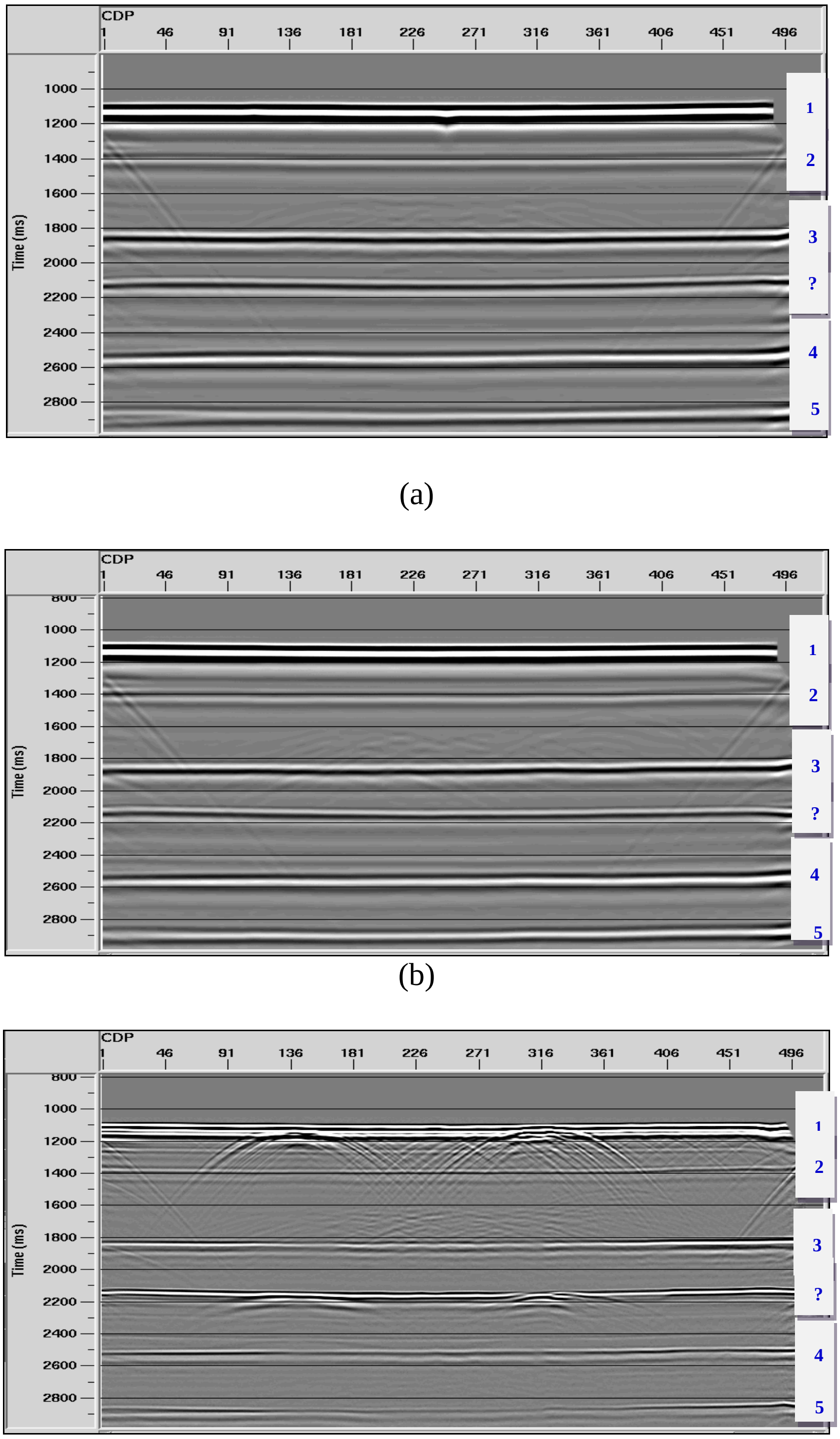

(a)

(b)

(c)

Figure 4.8: Stacked sections (a) SN survey line (b) WE survey line (c) NWSE survey line. The blue numbers indicate reflections from the interfaces shown in Figure 4.2(a) while the question mark highlights multiple of top model reflection.

Table 4.3: Comparison of computed stacking velocities based on actual model velocities (given to me) and the measured velocities obtained from interactive velocity analysis picking (CDP 100). Overall, the percentage difference between the two velocities ranges from 0.1 - 5 %.

		SN survey line		**WE survey line**		**NWSE survey line**	
Layer number	V_{stack} actual m/s	V_{stack} measured m/s	% diff	V_{stack} measured	% diff.	$\mathbf{V_{stack}}$ measured m/s	% diff.
1	1500	1483	1.1	1444	3.7	1479	1.4
2	1690	1630	3.7	1645	3.1	1717	1.2
3	1969	1964	0.3	1936	1.7	1985	0.8
4	1853	1852	0.1	1835	1.0	1865	0.6
5	1996	1919	3.9	1935	3.1	1896	5.0

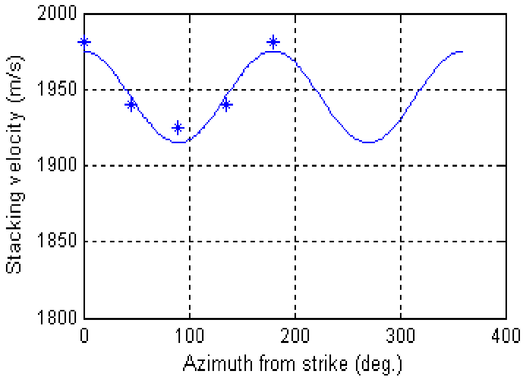

Figure 4.9: Azimuthal anisotropy observed in the stacking velocity at the centre of the fractured-layer (model A). The wave propagates faster in the fracture strike direction and slower in the direction normal to the fractures.

4.4 Q estimation

I used the QVO method described in section 3.2 to estimate the quality factor, Q from the NMO-corrected pre-stack CMP gathers. Since the top fractured-layer reflection is continuous to an offset of 940 m for the SN and WE survey lines, and 1340 m for the NWSE survey lines due to interference effect of the top model reflections, I started the attenuation analysis with these offset ranges for the respective data sets. The minimum offset in the data is 160 m for the three survey lines. In each CMP gather, I used the first trace from the top model reflection at this minimum offset (160 m) as the reference trace for comparison of the spectral ratios. Ideally a source wavelet should be used but in the absence of this, a shallow strong event can be substituted (e.g. Reine *et al.,* 2009). I made use of the power spectra ratios instead of the amplitude ratios as in the original QVO method and this however does not affect the accuracy of the results (Carter, 2003). The power spectra of the windowed reference trace $(P_o(f))$ and the top fractured-layer reflection $(P_1(f))$ were computed respectively on a trace-by-trace basis using the FFT algorithm and a constant time gate of 160ms to window the traces. Samples of the computed spectra are shown in Figures 4.10, 4.11 and 4.12 for the three lines respectively. The apparent shift in the centre frequencies to the lower end of the spectra for the bottom fractured layer for the three survey lines indicates loss of higher frequencies in the fractured-layer due to scattering attenuation effects. Compared with the SN- and WE- lines, the spectra of the NWSE line data are shifted to higher frequencies. A possible reason for this behaviour might be a change in the transducer used in the experiment as data were not acquired at the same time (personal communication with Wei J., 30/9/2008). To reduce the effect of side-lobes observed at both ends of the spectra, I applied the Hanning taper to the FFT window as oppose to the original Dasgupta taper (Carter, 2003). This taper reduces the edges of the signal to zero and positions the events at the centre of the window. Next, the spectral power ratios of the top fractured-layer reflection and the reference event were computed respectively also on a trace-by-trace basis. These spectral power ratios are related by the Equation (White, 1992):

$$\ln\left(\frac{P_1(f)}{P_o(f)}\right) = 2\ln(\mathrm{RG}) - 2\pi f\left(t - t_{ref}\right)/Q, \tag{4.1}$$

where f is frequency, R is the reflectivity term, G is the geometrical spreading term, t is the travel-time of target reflection, t_{ref} is the travel-time of reference event and Q is the quality factor down to the reflector. I then carried out a simple least-square regression of the logarithm of the spectral power ratio (LSPR) against frequency following the procedures in Press *et al.,* (2007, pp. 780) to get the spectral ratio slopes and intercepts and their respective error bounds. I used the variance in the spectral ratios as error on the ordinate and assumed negligible errors in frequencies. No stacking of the spectra was done as in the original QVO method of Dasgupta and Clark (1998). This, according to Carter (2003) should improve the accuracy of Q estimation as the stacking process is mainly to attenuate the impact of incoherent noise in the data. The physical modelling data however have high signal-to-noise ratio and the stacking of the spectra might otherwise reduce the accuracy of the estimated Q values. To ascertain the frequency bandwidth for the regression, I plotted the LSPR against frequencies (Figure 4.13) and carried out a sensitivity analysis to assess the effects of the regression bandwidth on the measured interval Q values in the fractured-layer. The sensitivity of the interval Q values in the fractured layer to the regression bandwidths are shown in Tables 4.4, 4.5 and 4.6 for the three survey lines. The aim is to use a wide bandwidth to get stable Q estimates, but this is limited by the bandwidth present in the data. For the SN- and WE- survey lines, the Q estimates are stable for regression bandwidth of 10 - 30 Hz for both the top and bottom fractured-layer reflections. Thus, I chose this regression bandwidth for the two reflectors as it lies within the signal bandwidth and is also common to all the reflections analyzed. The NWSE line, however, has stable Q estimates for regression bandwidths of 10 - 40 Hz and 10 - 50 Hz for both top and bottom fractured-layer reflections. However, the bandwidth of 10 - 50 Hz is not within the signal bandwidth of the bottom layer reflection and also exceeds the frequency range in which the LPSR versus frequency plot is approximately linear (Figure 4.13). Hence, I chose a regression bandwidth of 10 - 40 Hz for the NWSE line. This bandwidth is common to the three reflections analyzed. The NWSE- line data also appear to have some systematic noise possibly as a result of vibration of the modelling system during data acquisition (personal communictaion with Wei, J., 30/09/2008). These effects are not expected to affect the results of the Q estimates since the analysis was done separately on the respective data sets. Hence, azimuthal variations in attenuation if observed in the data is a useful parameter in extracting fracture property from the seismic data. Figure 4.14 shows samples linear fits of the log of the power spectral ratios against frequency for the three survey lines with their respective R^2 values. The value of R^2 for a perfect fit is 1. Linear regression aims to find the best fitting straight line through the data points such that the sum of the squares of the vertical distances of the points from the line is minimized. The plots all show excellent fits of the spectral ratios within the bandwidths used. The red dashed lines indicate a 95 % confidence interval on the fitted line (green line) and there is a 95 % chance that the interval encloses the best-fitting regression line while the remaining 5 % implies that the line could lie outside the confidence bounds. There are significant systematic deviations from the random fluctuation assumed in the determination of these error bounds which lead to a lower portion in some parts of the curve.

In the absence of a zero-offset reference trace in the data, the slope of the LPSR - frequency regression from Equation (3.10) can be written as:

$$p = \frac{2\pi}{Q}\left(t_{o,ref} - t_{o2} + \frac{x^2}{2}\left\{\frac{1}{t_{o,ref}v^2_{ref,rms}} - \frac{1}{t_{o2}v^2_{2,rms}}\right\}\right), \qquad (4.2)$$

where $t_{o,\, ref}$ is the zero-offset travel-time of reference trace, $t_{o,2}$ is the zero-offset travel-time of target reflection, $V_{ref,\, rms}$ and $V_{2,\, rms}$ are the root mean square velocities of the reference trace and target reflection respectively. Thus, the spectral ratio slope varies linearly with the square of offsets. I then carried out another least-square regression of the ratio slopes against the square of the offsets to get the zero-offset slope (LSPR slope intercept, I) given by:

$$I = 2\pi\left(t_{o,ref} - t_{o,2}\right)/Q, \qquad (4.3)$$

The seismic quality factor, Q down to the top of the fractured-layer was computed from Equation (4.3). The error bounds in the slopes from the first regression were used as input errors in the ordinate while I assumed negligible errors in the offsets for the second regression. The associated error in the computed Q value was obtained from the error bound in the spectral ratio slopes intercept. The entire procedure was repeated for the bottom fractured-layer reflection and all the CMP gathers analyzed. With the pair of Q values computed for the top and bottom of the fractured-layer in each CMP gather, I finally estimated the interval Q_i in the fractured-layer using Equation (3.8). The associated errors in the estimated interval Q_i values were computed from the respective individual errors in the Q values to the top and bottom fractured-layer using Equation (3.9).

Sample plots of the LPSR slopes against squared offsets are shown in Figures 4.15, 4.16 and 4.17 for the three survey lines respectively. For the SN survey line, the plot is linear within an offset range of 160 - 660 m. For the WE survey line however, the plots is linear within an offset range of 160 - 540 m while it is linear within an offset range of 160 - 940 m for the NWSE survey lines. The scatter in the plots beyond these offset ranges is attributed to the interference effects caused by the top model reflection. Consequently, these offset ranges were finally used in the attenuation analysis for the respective survey lines and satisfy the small-spread requirement of the QVO method (Dasgupta and Clark, 1998).

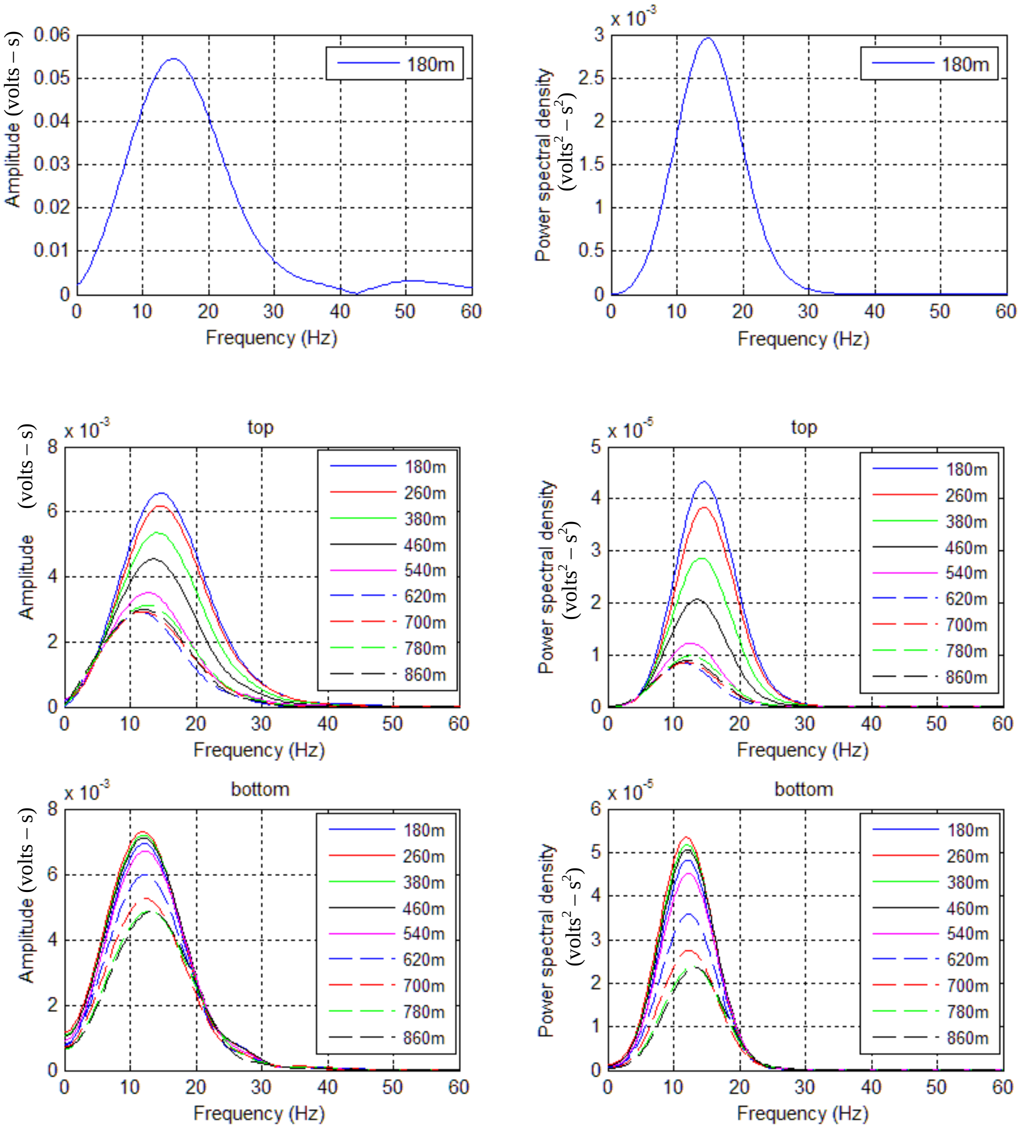

Figure 4.10: Sample spectra of windowed events for fracture model A - SN line (CMP 250). Inserted legend indicates the respective offsets. The observed negative shift in the centre frequencies is indicative of scattering attenuation caused by the fractures.

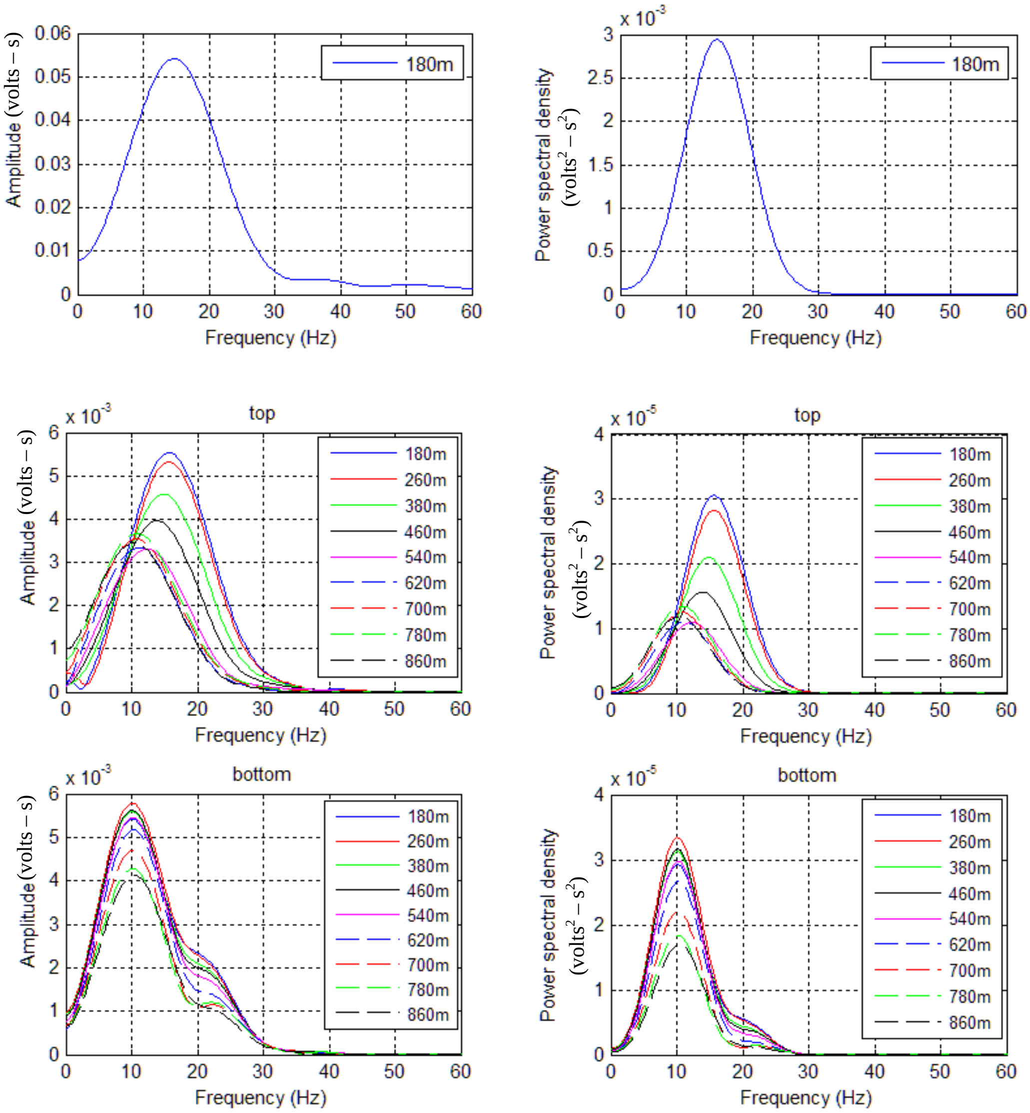

Figure 4.11: Sample spectra of windowed events for fracture model A - WE line (CMP 230). Inserted legend indicates the respective offsets. The observed negative shift in the centre frequencies is indicative of scattering attenuation caused by the fractures.

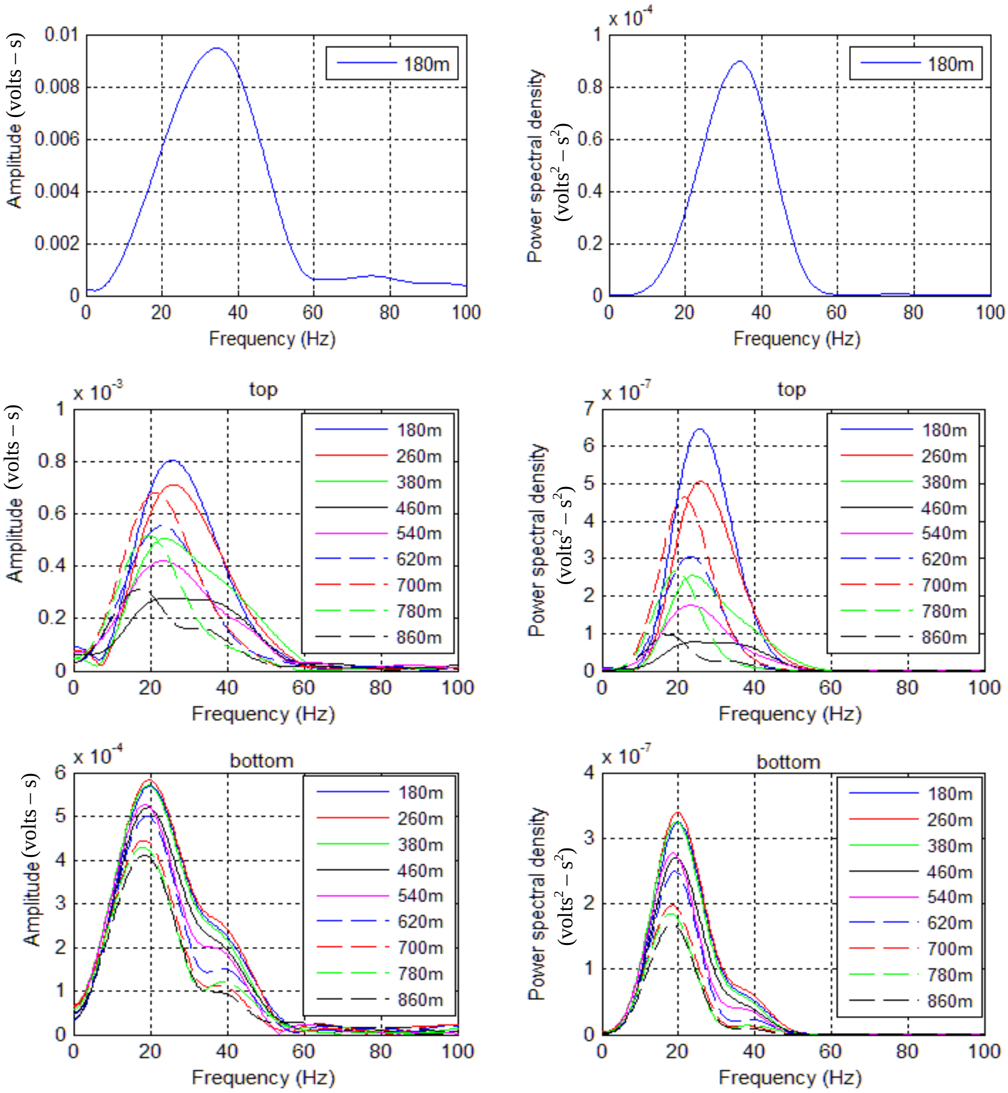

Figure 4.12: Sample spectra of windowed events for fracture model A - NWSE line (CMP 250). Inserted legend indicates the respective offsets. The observed negative shift in the centre frequencies is indicative of scattering attenuation caused by the fractures.

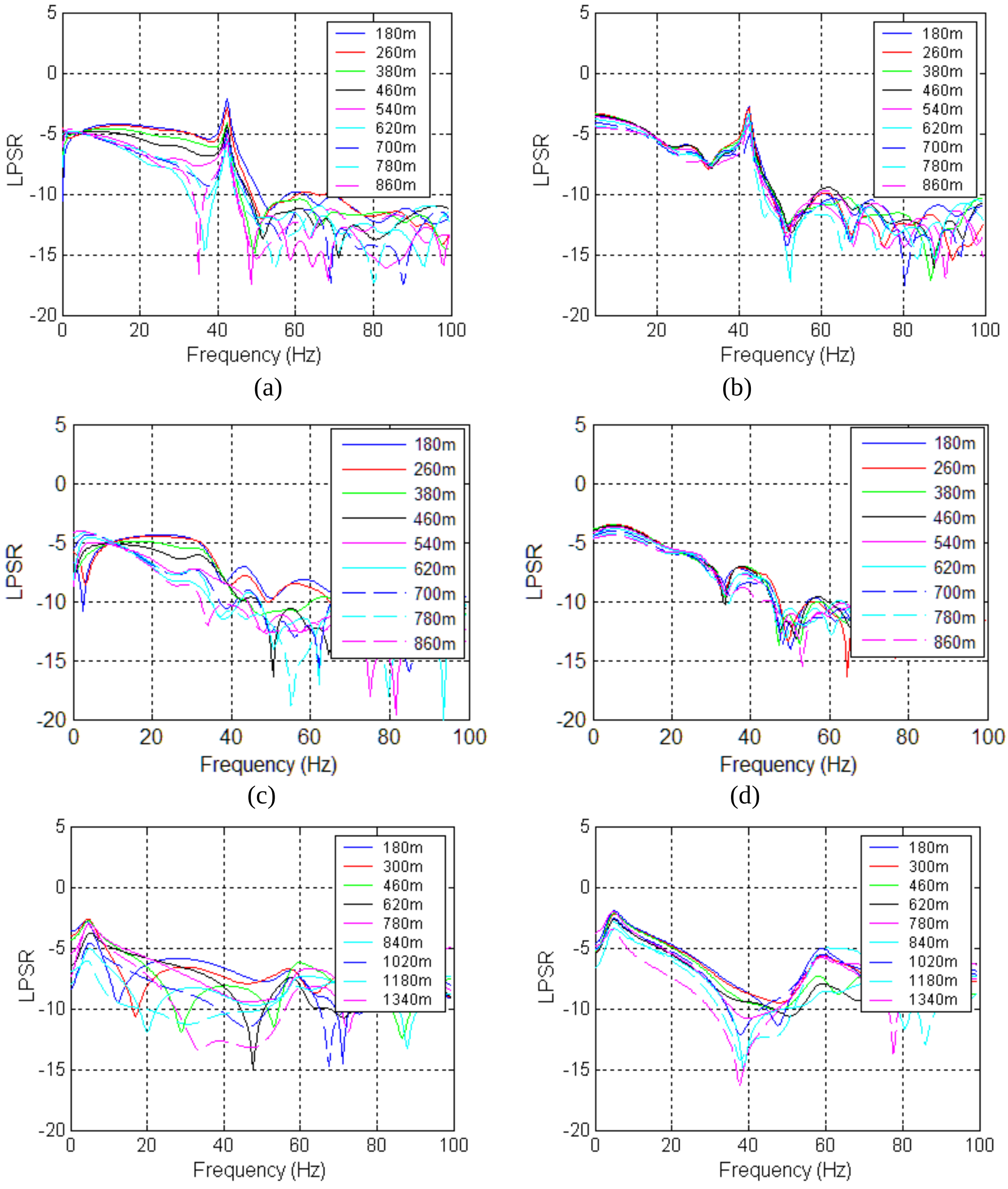

(a) (b) (c) (d) (e) (f)

Figure 4.13: Log Spectral Power Ratio (LSPR) against frequency plot (a) SN survey line - top reflection (CMP 250) (b) survey line - bottom reflection (CMP 250) (c) WE survey line - top reflection (CMP 230) (d) WE survey line - bottom reflection (CMP 230) (e) NWSE survey line - top reflection (CMP 250) (f) NWSE survey line - bottom reflection (CMP 250). The plots are linear for frequency bandwidth of 10 - 30 Hz for both SN and WE lines and 10 - 40 Hz for the NWSE line respectively.

Table 4.4: Sensitivity of the interval Q values in the fractured-layer to the regression bandwidth (SN-survey line)

Frequency bandwidth (Hz)	CMP 120			CMP 260		
	Q1	Q2	Interval Q	Q1	Q2	Interval Q
5-30	-68.5	49.5	9.7	-165.9	37.0	8.4
10-30	192	49.5	16.0	163.7	36.9	11.6
10-20	-50.5	37.4	6.3	-76.2	28.4	5.8
5-20	-26.4	37.4	4.8	-33.7	35.0	5.2
5-25	-35.3	45.5	6.9	-66.6	37.0	6.5
10-25	-240.8	42.5	9.8	4219.2	32.0	8.4

Table 4.5: Sensitivity of the interval Q values in the fractured-layer to the regression bandwidth (WE-survey line)

Frequency bandwidth (Hz)	CMP 80			CMP 100		
	Q1	Q2	Interval Q	Q1	Q2	Interval Q
5-30	-40.5	42.7	6.2	-35.0	47.0	6.1
10-30	135.9	51.0	18.1	182.0	54.1	18.0
10-20	-24.4	23.9	3.6	-23.1	22.5	3.4
5-20	-11.8	27.7	2.6	-10.9	30.5	2.6
5-25	-18.5	35.8	3.8	-17.0	36.0	3.6
10-25	-51.4	40.0	6.6	-48.0	34.8	5.9

Table 4.6: Sensitivity of the interval Q values in the fractured-layer to the regression bandwidth (NWSE-survey line)

Frequency bandwidth (Hz)	CMP 200			CMP 340		
	Q1	Q2	Interval Q	Q1	Q2	Interval Q
5-50	35.0	33.0	28.1	49.8	42.1	27.8
5-40	30.0	29.0	25.3	34.2	35.6	40.9
10-40	81.6	30.4	10.0	83.00	39.7	14.69
10-30	336.0	34.0	8.5	81.2	37.2	13.3
5-30	22.0	30.0	-377.6	22.9	31.6	-125.5
10-50	61.0	36.0	14.8	113.6	47.2	16.2

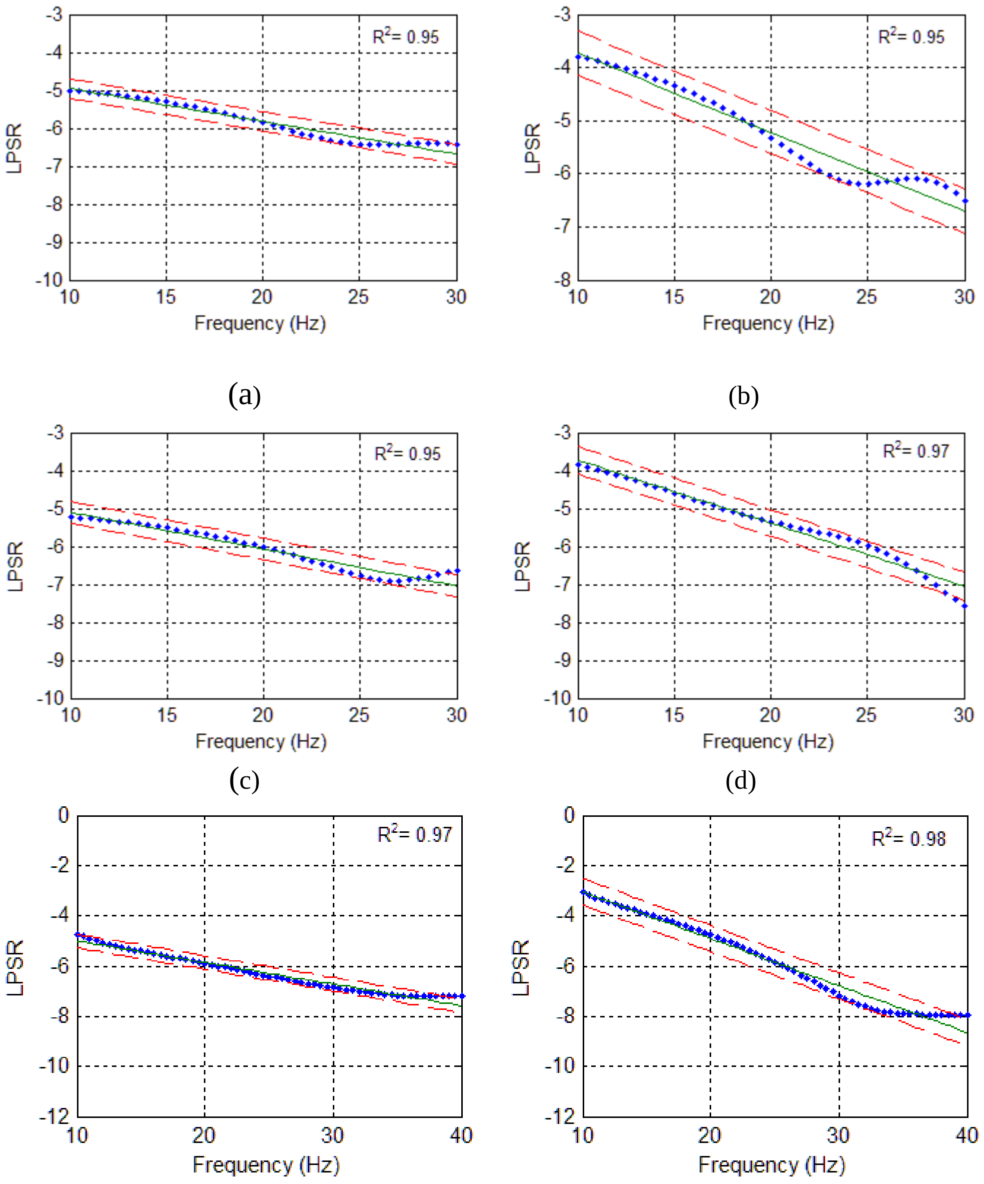

(a) (b)

(c) (d)

(e) (f)

Figure 4.14: Sample LSPR versus frequency plots at 500 m offset at centre of fracture model **A** (a) top reflection - SN survey line (CMP 250) (b) bottom reflection - SN survey line (c) top reflection - WE survey line (CMP 230) (d) bottom reflection - WE survey line (e) top reflection - NWSE survey line (CMP 250) (f) bottom reflection - NWSE survey line. The blue asterisks indicate the data points, the green line indicate the fitted line while the red dashed lines indicate 95 % confidence interval on the fitted line. All the plots show good fits of the LSPR versus frequency within the bandwidths used.

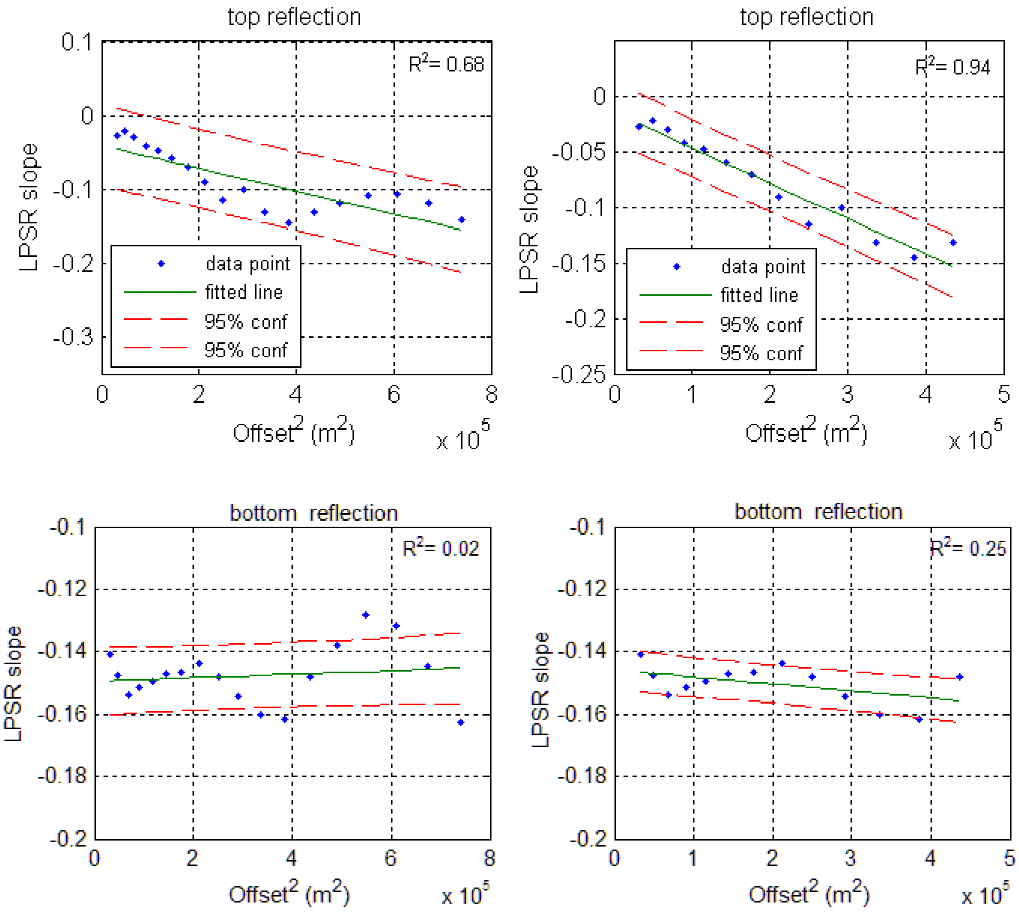

Figure 4.15: Sample LSPR slopes versus offset squared plots for SN survey line (CMP 250). The plot for the top fractured-layer reflection is linear within an offset of 160 - 660 m. Hence an offset range of 160 - 660 m was finally used for attenuation analysis (right plots). The blue asterisks indicate the data points, the green line indicate the fitted line while the red dashed lines indicate 95 % confidence interval on the fitted line.

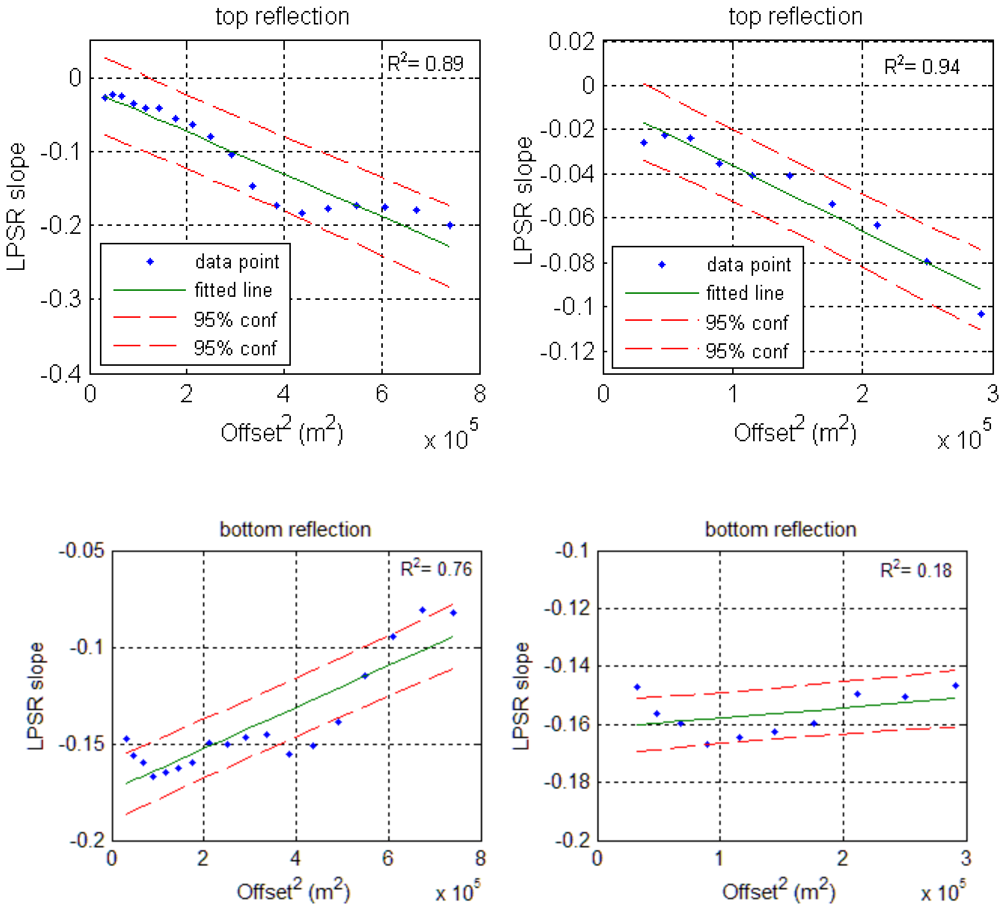

Figure 4.16: Sample LSPR slopes versus offset squared plots for WE survey line - CDP 230**.** The plot for the top fractured-layer reflection is linear within an offset of 160 - 540 m. Hence an offset range of 160 - 540 m was finally used for attenuation analysis (right plots). The blue asterisks indicate the data points, the green line indicate the fitted line while the red dashed lines indicate 95 % confidence interval on the fitted line.

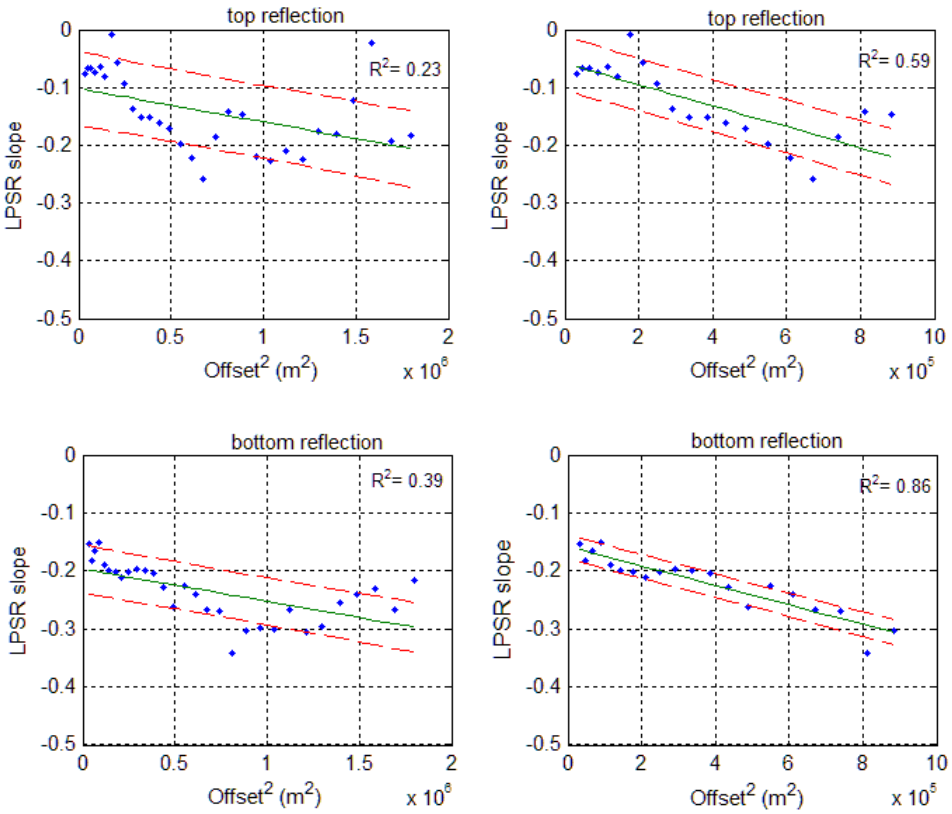

Figure 4.17: Sample LSPR slopes versus offset squared plots for NWSE survey line (CMP 250)**.** An offset range of 160 - 940 m used for attenuation analysis (right plots). The blue asterisks indicate the data points, the green line indicate the fitted line while the red dashed lines indicate 95 % confidence interval on the fitted line.

4.5 Results and analysis

The results of the Q estimation are shown in Figure 4.18. The interval Q values in the fractured-layer decrease systematically to a minimum at the centre of the fracture model **A** for the three azimuthal angles of survey. Interval Q values of 11.0 ± 1.7 (parallel to strike- model **A**, SN survey line), 7.0 ± 1.2 perpendicular to strike - model A, WE survey line), 11.1 ± 2.1 (60.8^{o} to strike - model B, WE survey line) and 8.3 ± 1.1 (135^{o} to strike - model A, NWSE survey) were obtained for the fractured layer.

I also performed a cosine fit according to Equation (2.51) to the interval Q values obtained for fracture model **A** for the three azimuthal angles of survey. Figure 4.19 shows the cosine fit to the Q results for fracture model A at various locations on the model block (indicated in Figure 4.2b) as a function of survey line azimuth. The azimuth of maximum attenuation from the fitting curves is 90° for the various locations considered, which corresponds to the known fracture normal direction from the physical model. The amplitude of the attenuation anisotropy from the cosine curve at the centre of the fracture model (C2) is 2.6 %. This was determined by taking half of the difference between the maximum attenuation in the fracture normal direction and the minimum attenuation in the fracture strike direction. The fit to the data on Fig 4.19 is much better than the error bars would suggest. This may be due to the small number of data points used, or that the error is overestimated by the techniques used here.

A further analysis of the results shows that the azimuthal Q variations in the fractured-layer (fracture model **A)** could approximately be fitted by the ellipse (Figure 4.20). The shape and size of the ellipse is determined by the length of the semi-minor and semi-major axes. For any given azimuth angle θ measured from the North direction (y-axis), the distance from the centre of the ellipse to the surface corresponds to the Q value for that azimuth. The major axis corresponds to the fracture strike (0^o azimuth measured from the North direction) while the minor axis corresponds to the fracture normal (90^o azimuth also measured from the North direction) as indicated in Figure 4.2. Such plots, which are analogous to slowness surfaces, are a convenient graphic representation of attenuation anisotropy.

Attenuation is maximum normal to the fractures and minimum parallel to the fractures. The attenuation anisotropy results correlate with the azimuthal anisotropy results in the stacking velocity observed in the physical modeling data and the fracture orientations inferred are all consistent with the physical model within the measuring errors involved.

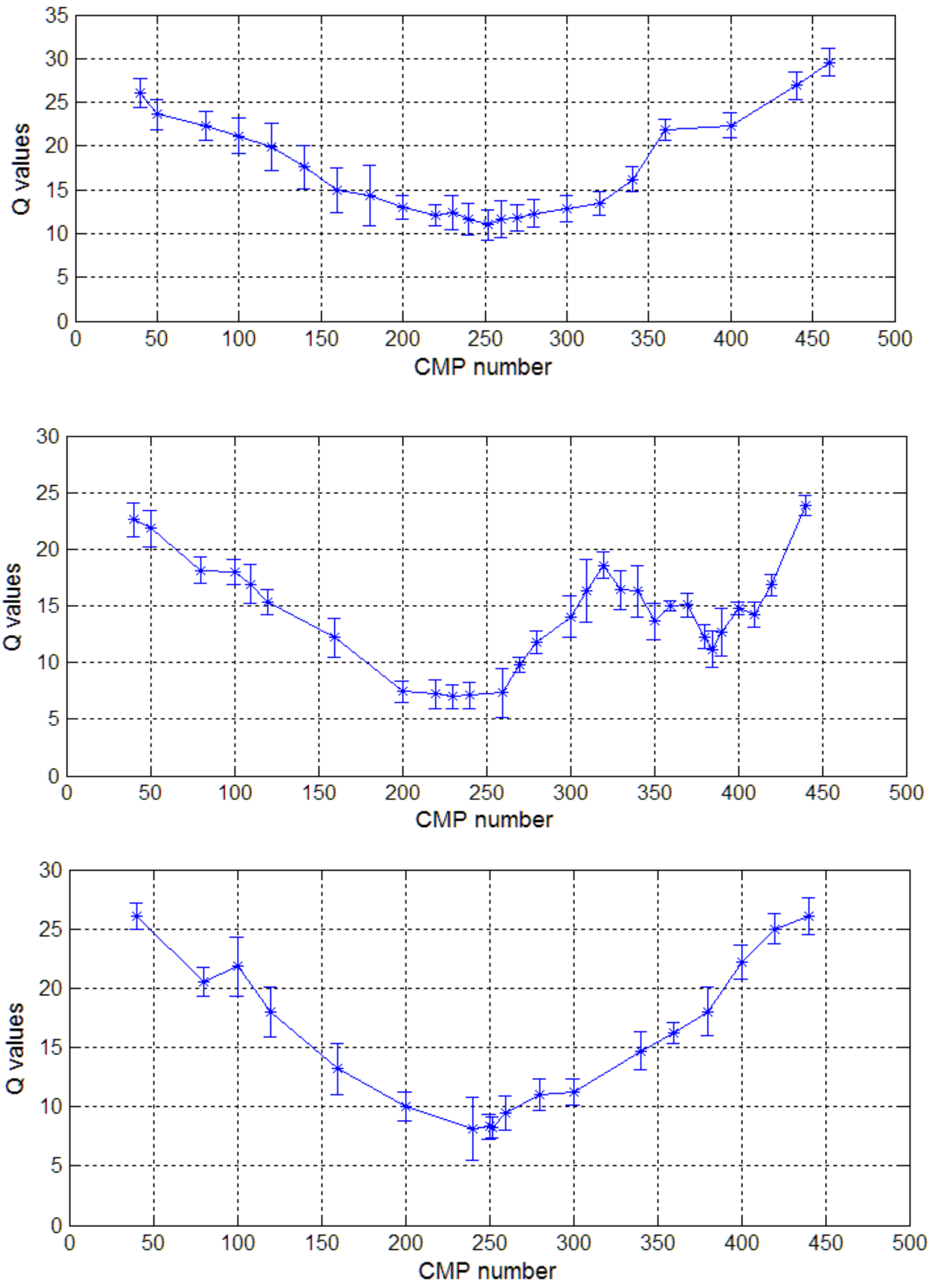

Figure 4.18: Q profile for the fractured layer. (a) SN survey line (b) WE survey line: (c) NWSE survey line. Interval Q values decrease systematically to a minimum at the centre of the fracture model A for the three azimuthal angles of survey.

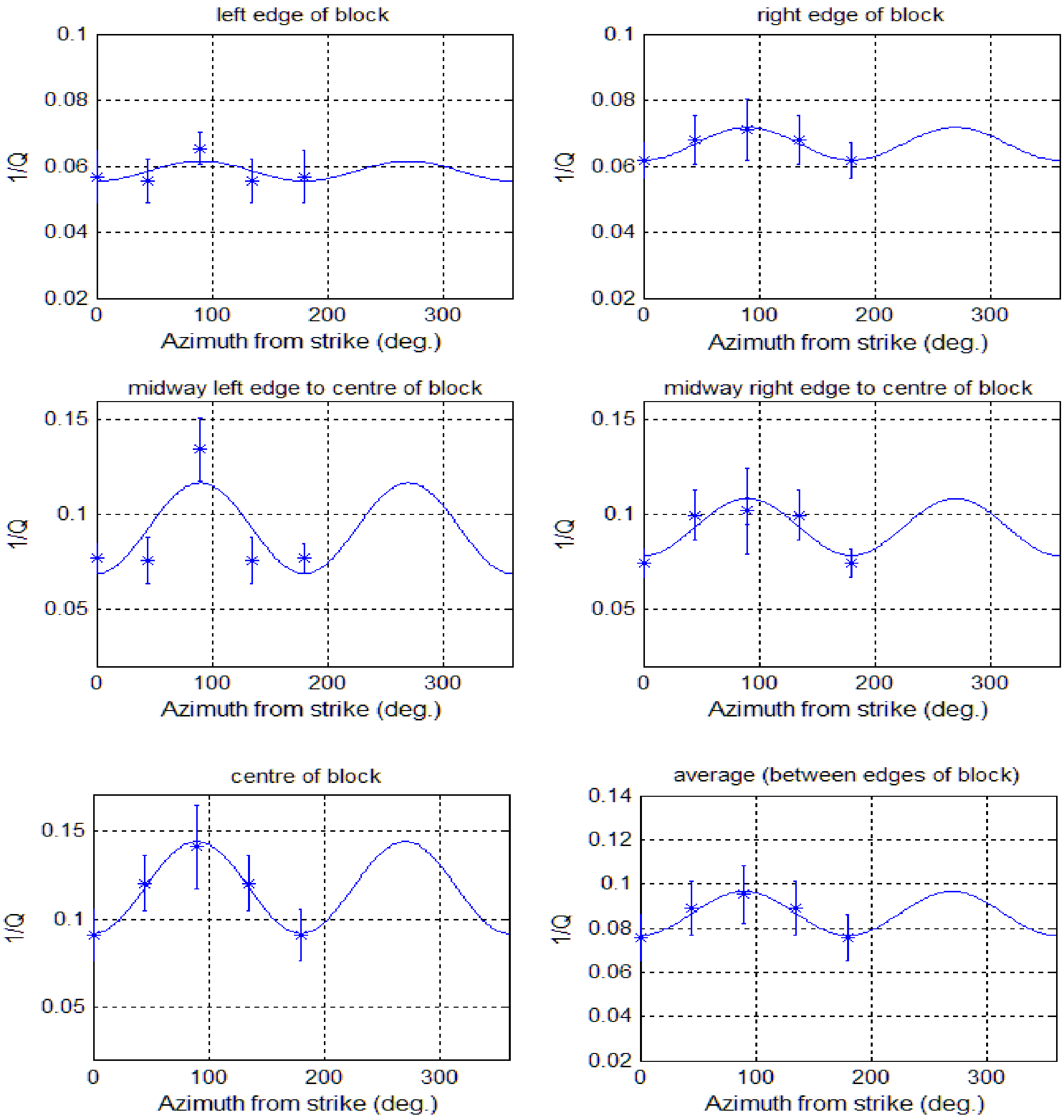

Figure 4.19: Attenuation anisotropy for fracture model '**A** 'fitted with a 'cos2θ' function at various locations on the fracture block shown in Figure 4.2b. The angle of maximum attenuation corresponds to 90° from the fracture strike while the average magnitude of anisotropy is 2.6 % (centre of fracture model).

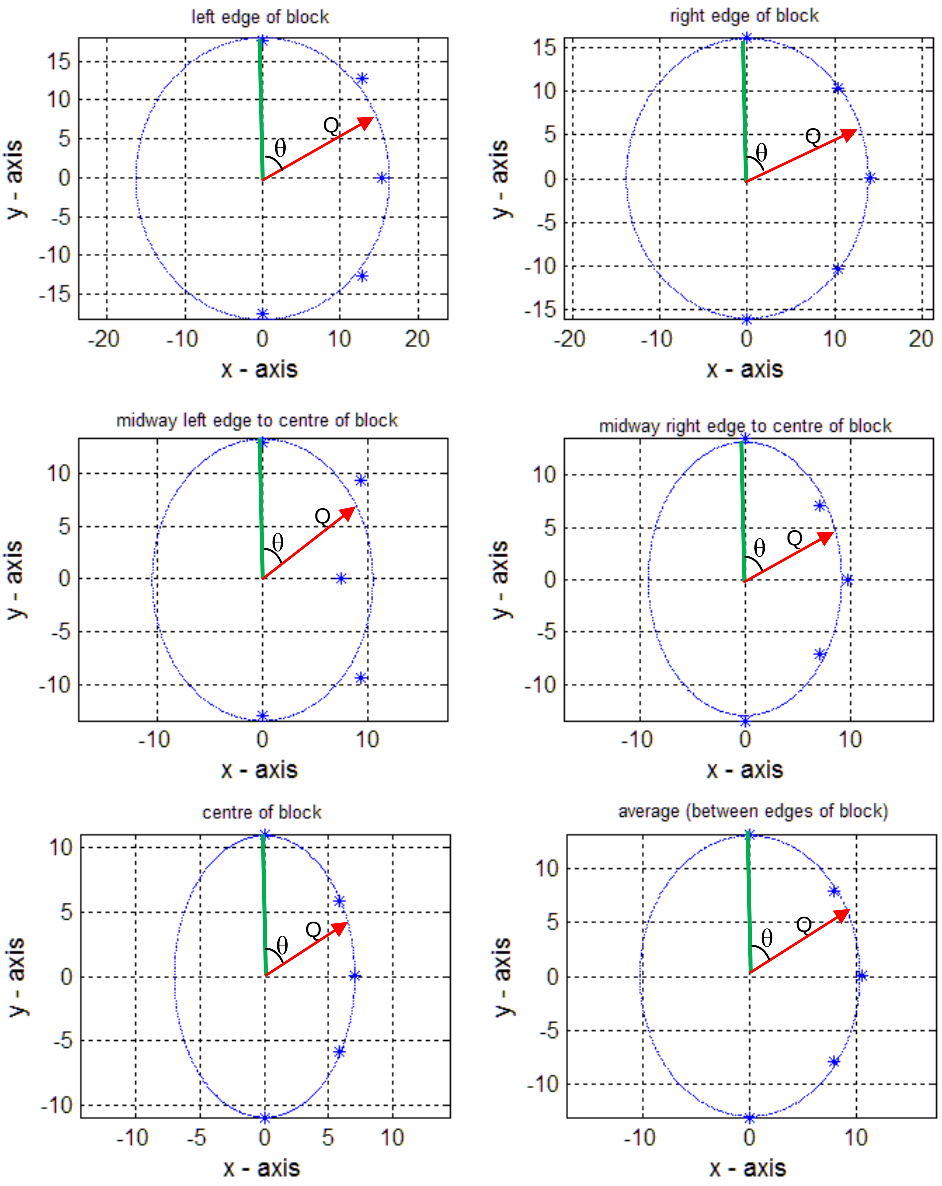

Figure 4.20: Q anisotropy ellipse for fracture model ‘**A**’ at various locations on the fracture block shown in Figure 4.2b. The ellipse has a centre at (0, 0) and the distance from the centre of the ellipse to the surface (red arrow) at any given azimuth angle θ measured from the North direction (y-axis), corresponds to the Q value for that azimuth. The major axis corresponds to fracture strike while minor axis corresponds to fracture normal. The blue asterisks indicate the data points.

Effect of NMO stretching

To investigate the effect caused by NMO-stretching on the Q estimates, I picked the time windows along the hyperbolic travel paths for the target events and computed the Q values on a trace-by-trace basis using the actual travel times according to Equation (3.12). I then computed the average Q value in the fractured-layer from the average of all the Q estimates. This approach has the advantage that no NMO correction is applied to the data and as such there are no effects of NMO stretch. The results of the Q computation are shown in Figure 4.21 for the SN- and WE- lines. The application of NMO correction causes a slight systematic decrease in the Q values. However, as noted by Clark *et al.*, 2001 and 2009, when the QVO - spectral ratio method is used in the azimuthal anisotropy context, any factor that might affect the Q estimates will be common to all the azimuths considered and azimuthal anisotropy in attenuation is robust in extracting fracture properties from the data. In this case, the effect of application of the NMO correction will be common to the three survey line data and hence, azimuthal attenuation anisotropy provides a robust means of extracting fracture properties from the data.

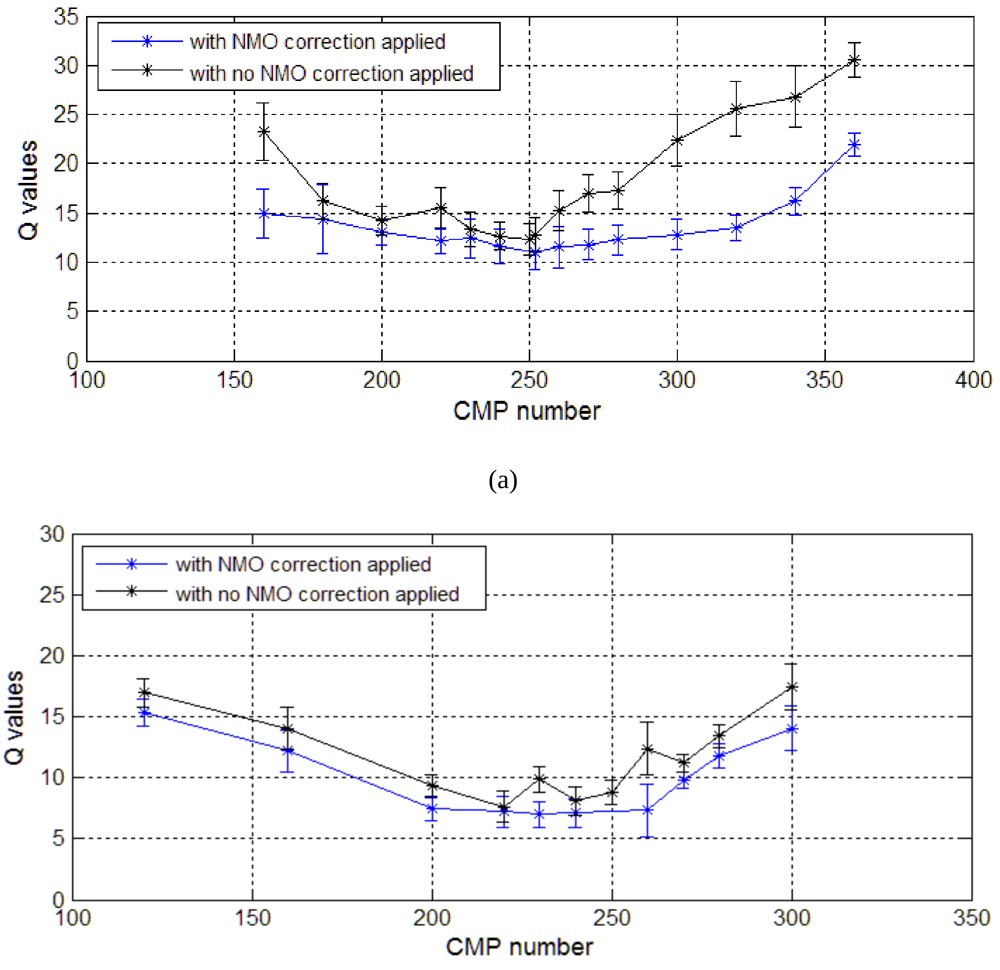

(a)

n

(b)

Figure 4.21: Effect of NMO correction on Q profiles for fracture model **A** (a) SN survey line (b) WE survey line. There is an observable effect of NMO correction on the Q estimates. In both cases however, there is a systematic decrease in the Q values to a minimum at the centre of the fracture model. Thus, the effect is common to the two survey lines and thus Q anisotropy remains a useful parameter for detecting fractures from the data

4.6 Summary and conclusions

I have carried out a detailed analysis of anisotropic P-wave propagation in fractured media in the 2-D physical modelling datasets. The fracture models are simulated by embedding thin penny-shaped chips into an isotropic background medium on the basis of Hudson's theory (1981). A set of aligned fractures gives rise to scattering in the propagating wavefield which is more in the direction normal to the fracture strikes. This azimuthal anisotropy in the scattered energy is useful in the determination of the orientations of the fractures.

I have quantified the scattered energy through attenuation estimates using the QVO-spectral ratio method for the three azimuthal angles of survey relative to the fracture strikes. Attenuation is observed to increase away from the fracture strike towards the fracture normal and is maximum normal to the fractures. The observed azimuthal variations in the P-wave attenuation are elliptical and the fracture orientations are obtained quite accurately from the axes of the ellipse. The major axis of the Q ellipse corresponds to the fracture strike while the minor axis corresponds to the fracture normal. The observed attenuation anisotropy is also well fitted by a ‘cos2θ’ function, giving the angle of maximum attenuation normal to the fracture strikes showing a good agreement with the results of the ellipse fitting. The magnitude of attenuation anisotropy is found to be 2.6 %. The attenuation results show consistency with the azimuthal anisotropy observed in the stacking velocities in the fractured layer and are all consistent with the physical model. The implication of these results therefore is that in the fractured media (HTI media for example) such as encountered in fractured hydrocarbon reservoirs, the azimuth of maximum attenuation is normal to the fractures and the observed attenuation anisotropy is a potential tool for delineation of fractures to complement the use of other seismic attributes.

Chapter 5 Synthetic modelling study of P-wave attenuation anisotropy in fractured porous rocks

Attenuation has been observed to have a higher magnitude in fluid-saturated rocks than in dry rocks (e.g. Gardner *et al*., 1964). In this chapter, I examine the effects of a set of aligned vertical fractures in porous fluid-saturated rocks on P-wave attenuation anisotropy through synthetic modelling, with the sole aim of comparing the results with that of the seismic physical modelling study I did in Chapter 4 for the case of the dry rock. I start by first looking at the effect of fluid mobility on the induced attenuation and then examine the anisotropic behaviour in the induced attenuation.

5.1 Introduction

In Chapter 4, I carried out a seismic physical modelling study to examine the effects of scattering attenuation caused by a set of aligned fractures in dry rocks. The results of the study show that the scattering attenuation caused by the aligned fractures increases away from the fracture strike direction and is maximum normal to the fractures. The anisotropic behaviour in the attenuation observed in the data was elliptical and the fracture orientations were obtained from the axes of the ellipse.

However, attenuation has been observed to have higher magnitudes in fluid-saturated rocks than in dry rocks (e.g. Gardner, *et al*., 1964; Toksöz *et al*., 1979; Johnson and Toksöz, 1980; Johnson, 1981; Winkler 1986). In a porous fluid-saturated fractured-rock, the pressure difference generated when a seismic wave propagates through the rock causes fluid exchange between the fractures and the surrounding pore space, resulting in attenuation and dispersion (Chapman, 2003).

Thus, the aim of this chapter is to examine the influence of fluid saturation on P-wave attenuation and to compare the magnitude of the attenuation anisotropy to that of dry rocks. The theoretical model comprises a fluid-saturated porous layer whose elastic properties are computed using Chapman’s (2003) poro-elastic model and squirt flow is taken into consideration in the model. I first examine the influence of fluid mobility on the induced attenuation and then its anisotropic behavior. Maultzsch *et al.,* (2007) previously used the poro-elastic model to investigate the effects of attenuation anisotropy using a walk away VSP geometry and observed anisotropic attenuation which has an elliptical variation with azimuth. I extend their study in this chapter to the case of surface seismic geometry to gain a fuller understanding of the anisotropic behaviour. Since the poro-elastic model of Chapman (2003) is used in the computation of the elastic properties of the anisotropic layer, I give a detailed review of the model in the subsequent section.

5.2 Chapman’s poro-elastic model

The poro-elastic model of Chapman (2003) considers the pore space of a rock to consist of a lattice configuration of spherical pores, randomly-oriented ellipsoidal micro-cracks and aligned ellipsoidal fractures. The radius of the micro-cracks and spherical pores is identified with the grain size. The fracture size is much larger than the grain size but smaller than the seismic wavelength. Since the fractures have preferential alignment, the resulting medium has hexagonal symmetry (transverse isotropy). Wave-induced pressure gradients cause fluid exchange between adjacent elements of pore space in the rock. The fluid exchange between two adjacent voids ‘a’ and ‘b’ for instance is described by the formula (Chapman, 2003):

$$\partial_t m_a = \frac{\rho_o \kappa \varsigma}{\eta}\left(p_b - p_a\right), \tag{5.1}$$

where ρ_o is the fluid density, κ is the permeability, ς is the grain size, η is the fluid viscosity, p_a is the pressure in element a, m_a is the mass of fluid in element a and p_b is the pressure in element b. Each element of pore space is assumed to be connected to six other elements and the resulting flows can be added linearly. The fractures are connected to a greater number of elements since they are larger than the micro-cracks and the pores. For the purpose of ensuring that there is some spacing between the fractures, the model assumes that each crack or pore is connected to at most one fracture and that the fractures are not connected to each other. These last assumptions require that the number of cracks and pores greatly exceeds the number of fractures.

Chapman (2003) derived expressions for the expected mass flow out of an individual fracture, micro-crack and pore based on Equation (5.1) in terms of the expected pressure gradients. The mass in each element of pore space is expressed as a function of inclusion pressure and applied stress and the derivation ensures mass conservation throughout the pore space. He further solved for the time-dependent response of the pressures in various inclusions to an imposed stress field. He calculated the effective elastic constants using Eshelby's (1957) interaction energy approach for materials with embedded inclusions with the stress and strain inside the inclusions calculated from the established time-dependent pressures. Details of these calculations are given in Chapman (2003). The effective elastic tensor, C given by Chapman (2003) is of the form:

$$C = C^{(0)} - \phi_p C^{(1)} - \varepsilon_c C^{(2)} - \varepsilon_f C^{(3)}, \qquad 5.2$$

where $C^{(0)}$ is the elastic tensor of the isotropic rock matrix with Lame's parameters λ and μ, $C^{(1)}$, $C^{(2)}$ and $C^{(3)}$ are the additional contributions from pores, micro-cracks and fractures, respectively, multiplied by the porosity ϕ_p, the crack density ε_c and the fracture density ε_f. These additional contributions are functions of the Lamé parameters, fluid and fracture properties, frequency and relaxation times associated with squirt flow.

Chapman’s (2003) original model is restricted to very low porosity since the elastic constants are calculated based on Eshelby’s (1957) interaction energy approach which is only valid for dilute concentrations of inclusions (Maultzsch *et al.,* 2003). In cases of high porosities, the calculation of the corrections using the grain moduli λ and μ is expected to result in significant errors and it is not ideal for moduli that cannot be obtained from measured velocities to be specified (Maultzsch, 2005). To address these issues, Chapman *et al.,* (2003) slightly adapted the model to make it more applicable to real data by using Lame’s parameters λ^o and μ^o derived from the density ρ and measured P- wave velocity V_p^o and S-wave velocity V_s^o of the un-fractured rock for the corrections. Also, $C^{(0)}(\Lambda, M)$ has to be defined in such a way that the measured isotropic velocities are obtained by applying the pore and crack corrections at a specific frequency f_o (Chapman *et al.,* 2003 and Maultzsch *et al*., 2003). Thus:

$$\Lambda = \lambda^o + \phi_{c,p}\left(\lambda^o, \mu^o, f_o\right), \quad M = \mu^o + \phi_{c,p}\left(\lambda^o, \mu^o, f_o\right), \tag{5.3}$$

where $\phi_{c,p}$ refers to corrections to the elastic tensor which are proportional to crack density and porosity.

$$\lambda^o = \rho\left(V_p^o\right)^2 - 2\mu^o \; ; \quad \mu^o = \rho\left(V_s^o\right)^2 \tag{5.4}$$

Equation (5.2) can then be re-written as:

$$C = C^{(0)}(\Lambda, M, \omega) - \phi_p C^{(1)}\left(\lambda^o, \mu^o, \omega\right) - \varepsilon_c C^{(2)}\left(\lambda^o, \mu^o, \omega\right) - \varepsilon_f C^{(3)}\left(\lambda^o, \mu^o, \omega\right) \tag{5.5}$$

The form of Equation (5.5) allows the corrections for pores, micro-cracks and fractures which describe the frequency dependence and anisotropy of a material to be obtained from measurements of the velocities (Maultzsch *et al*., 2003). Chapman *et* *al.*, (2003) further simplified the model by setting the crack density to zero in the case of high porosity. The influence of this parameter however is not significant for modelling the effects of fractures provided the spherical porosity is much greater than the crack porosity (Maultzsch *et al.*, 2003).

Fluid flow in Chapman's (2003) model occurs at two scales; the grain scale (associated with the micro-cracks and spherical pores) and the fracture scale. This results in two characteristic frequencies and corresponding relaxation times. The relaxation time, τ_m associated with fluid flow between the micro-cracks and spherical pores is related to the squirt-flow frequency, f_m^c as (Murphy, 1985; Winkler, 1986; Lucet and Zinszner, 1992; Sothcott *et al.*, 2000):

$$f_m^c = \frac{1}{\tau_m} \tag{5.6}$$

$$\tau_m = \frac{c_v \eta (1 + K_c)}{\sigma_c \kappa \varsigma c_1}, \tag{5.7}$$

where c_v is the volume of an individual crack, σ_c is the critical stress and c_1 is the number of connections to other voids. σ_c and K_c are defined by:

$$\sigma_c = \frac{\pi \mu \, r}{2(1 - v)} \tag{5.8}$$

$$K_c = \frac{\sigma_c}{\kappa_f} \tag{5.9}$$

where r is the aspect ratio of the cracks, v is the poison's ratio of the matrix and κ_f is the fluid bulk modulus. Fluid flow in and out of the fractures is associated with a lower characteristic frequency or a higher corresponding relaxation time τ_f which is dependent on the size of the fractures. The relaxation time associated with the grain scale and that associated with the fracture scale are both related by the equation (Chapman, 2003):

$$t_f = \frac{a_f}{\varsigma}\tau_m \tag{5.10}$$

where a_f is the fracture radius. From Equation (5.10), it can be inferred that larger fractures will result in higher relaxation times (or lower characteristic frequencies). These larger relaxation times lead to velocity dispersion and attenuation in the seismic frequency range. Thus, the resulting anisotropy is frequency-dependent.

5.2.1 Parameterization of the model

Chapman’s (2003) model is used to model frequency-dependent anisotropy in porous reservoir rocks. The effective elastic tensor of the model is dependent on the Lame’s parameters λ and μ of the isotropic rock matrix, porosity, crack density, fracture density, aspect ratio of the cracks and fractures, fracture radius, fluid bulk modulus and relaxation time. With the modification of Chapman *et al.*, (2003), the Lame’s parameters can be derived from the density and measured P- and S-velocities of the isotropic rock matrix through Equation (5.4). The crack density can be set to zero (Chapman *et al.*, 2003) to model the effects of aligned fractures, thus reducing the number of variables for practical application of the model.

The aspect ratio of the cracks and fractures also need to be specified in the model. From the combination of Equations (5.8) and (5.9), it can be seen that $K_c << 1$ for small aspect ratios which means that the effective elastic constants will not be sensitive to the exact value of the aspect ratio provided it is very small. The relaxation time τ_m then remains the only parameter that is difficult to ascertain. Maultzsch *et al.*, (2003) made an estimate of this parameter by calibrating the model against the published laboratory data of Rathore *et al.*, (1995) and obtained a value of 0.27 μs. Chapman (2001) earlier estimated the value of the parameter by calibrating the un-fractured poro-elastic model against the resonant bar data from Sothcott *et al.*, (2000) and obtained a value of 20 μs.

5.2.2 Predictions of the model

Chapman (2003) generated some numerical results using some arbitrary set of parameters to demonstrate the predictions of the model. He used reference elastic moduli $\lambda = \mu = 1.75 \times 10^{10}$ Pa, density of 2300 kg/m^3, crack density of 0.1, porosity of 10 % and a relaxation time of 20 μs. In the absence of fractures, the rock is isotopic and the poro-elastic model of Chapman (2003) predicts P-and S-wave velocity dispersion associated with the relaxation time τ_m which represents the traditional squirt flow frequency. However the presence of fractures makes the rock transversely isotropic and the model predicts anisotropic velocity dispersion at a lower frequency associated with the relaxation time τ_f for the fluid flow in and out of the fractures. The dispersion curves are shown in Figure 5.1 and 5.2 for the isotropic and transversely isotropic cases respectively. The fracture density is 0.05 and length is 10 cm. In the anisotropic case, the qP-wave propagating parallel to the fracture strike direction shows no dispersion while strong dispersion occurs for propagation normal to the fracture strike direction. In the same way, the pure-shear wave polarized parallel to the fracture strike direction shows no dispersion while the quasi-shear wave shows velocity dispersion.

The variation of the three body-wave velocities with propagation angle away from the fracture normal is illustrated in Figure 5.3. The qP-velocity exhibits cos4θ variation at a frequency of 1 kHz and cos2θ variation at higher frequency of 40 kHz, where θ is angle measured from fracture normal direction. Figure 5.4 shows the angular variation of attenuation at a frequency of 40 Hz. There is a significant attenuation in the quasi-P and quasi-S wave, whereas there is no attenuation in the pure-shear wave. Both the quasi- P and quasi-S waves cause the compression of the fractures relative to the pore space and thus results in attenuation. In contrast, the pure S-wave does not cause any compression of the fractures or pore space, and thus produces no attenuation. The P-wave attenuation has a maximum magnitude in the direction normal to the fractures and also increases with polar angle (offset). This anisotropic behavior could be exploited as an additional tool for fracture delineation from seismic data.

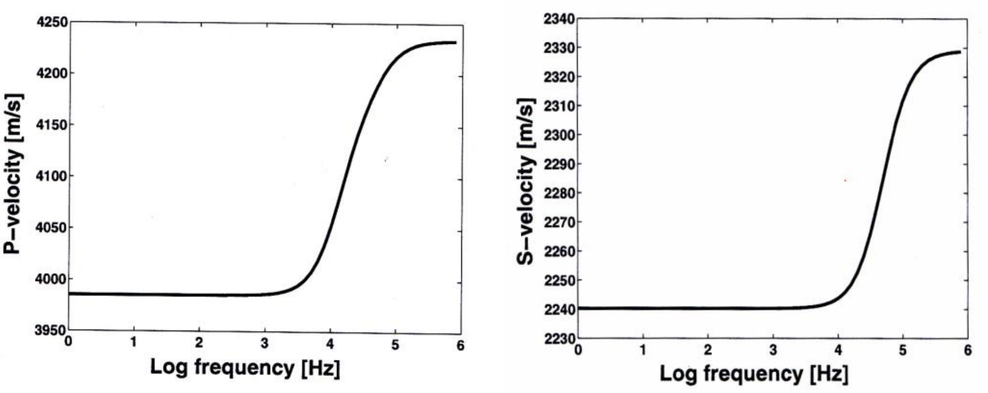

Figure 5.1: Dispersion curves for unfractured layer (a) P-wave (b) S-wave (from Chapman, 2003). Dispersion occurs between a frequency band of around 1 kHz to 100 kHz.

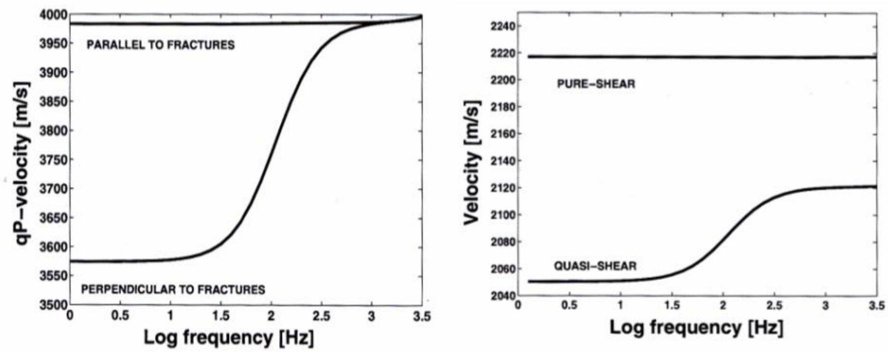

Figure 5.2: Dispersion curves for fractured-layer (a) quasi-P wave (b) quasi- shear and pure-shear modes propagating at 70° to fracture normal (from Chapman, 2003).

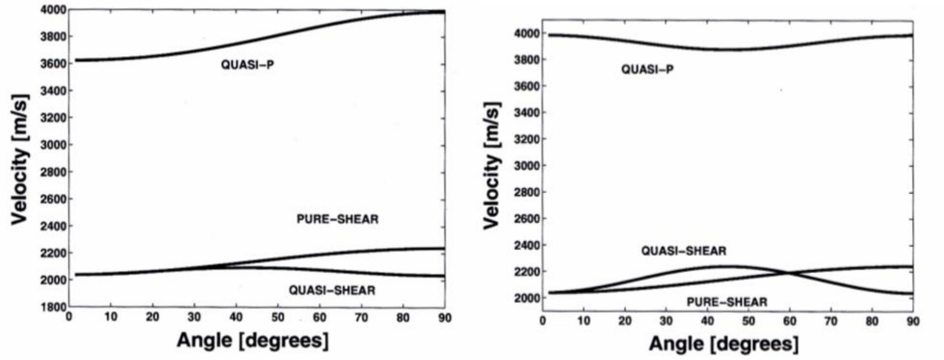

Figure 5.3: Variation of the wave velocity with angle from fracture normal direction for a fracture size of 10 cm (a) at 40 Hz frequency (b) at 1 KHz frequency (from Chapman, 2003).

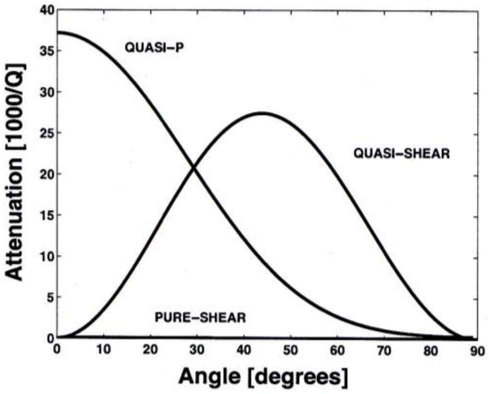

Figure 5.4: Variation of attenuation of quasi-P, quasi-S and pure-S waves with angle from the fracture normal direction at a frequency of 40 Hz and fracture size of 10 cm (from Chapman, 2003). For the quasi-P wave, attenuation increases with polar angle and has a maximum value in the fracture normal direction.

5.3 Effects of fluid mobility

Fluid mobility (m_f) defined as the ratio of permeability to viscosity (Equation (5.11)) is found to greatly influence the propagation of both P- and S-waves, but the effects are generally considered to be more pronounced for P-waves (Batzle *et al.*, 2006).

$$m_f = \frac{k}{\eta} \tag{5.11}$$

The propagation of both P- and S-waves through a given medium causes slight deformation in the medium which generates stress and strains. If the medium is saturated with a fluid and also porous, the stress generated is just sufficient to cause fluid movement (mobility). The time needed to equalize the pressure difference (relaxation time) depends on fluid mobility. High fluid mobility enhances pore-pressure equilibrium, resulting in a low frequency domain where Gassmann’s equations are valid whereas low fluid mobility implies that the pore-pressure remains out of equilibrium, resulting in the high frequency domain (Batzle *et al.*, 2006). Most rocks in the sedimentary basin (e.g. shales, siltstones, tight limestones) have low permeability and mobility and thus are in the high frequency domain even at seismic frequencies (Batzle *et al.*, 2006). In between these two frequency domains is the transition frequency band where seismic anisotropy is frequency-dependent and could be used to deduce fracture and fluid properties (Qian *et al.*, 2007).

There is an inverse relationship between mobility and relaxation time. Higher fluid mobility implies lower relaxation time and vice versa. This relationship is also seen in Equation (5.7) if the other parameters remain constant. Since fluid movement causes attenuation, it follows that changes in the relaxation times could lead to changes in the fluid mobility and hence the induced attenuation. Thus, my aim is this section is to investigate the effects of fluid mobility on the induced P-wave attenuation by considering a range of values of relaxation times using Chapman's (2003) poro-elastic model.

5.3.1 Theoretical model and experimental set up

The theoretical model is made up of one anisotropic and three isotropic horizontal layers. The anisotropic layer consists of a porous fluid-saturated material with aligned vertical fractures, and squirt flow between the pores in the matrix is taken into consideration. The elastic properties of the material are computed using the poroelastic model of Chapman (2003) discussed in section 5.2. The model predicts anisotropic velocity dispersion and attenuation in the seismic frequency range, with attenuation increasing with polar angle and azimuth away from the fracture strike direction. Details of the theoretical model parameters used in this study are given in Table 5.1. The third layer constitutes the anisotropic layer.

Table 5.1: Theoretical model parameters

Layer parameters

Layer	v_p (m/s)	v_s (m/s)	ρ (kg/m^3)	Thickness (m)
1	1500	1000	1000	400
2	2314	1100	1150	600
3	2610	1300	1750	600
4	3100	1800	2200	Half space

Fracture model parameters

Porosity	0.08
Crack density	0
Fracture density	0.1
Fracture radius	10cm
Fluid bulk modulus	2.0Gpa
Frequency	50Hz

5.3.2 Computation of synthetics

Synthetic data were computed from the theoretical model using the ‘Aniseis’ software (Taylor, 2001) which makes use of the reflectivity method. A Ricker wavelet (which has the dimension of volume) with a centre frequency of 25 Hz and a start time of 100 ms (Figure 5.5) was used as the source wavelet. The source is an explosive source and was placed on the surface of the model. The software modifies the explosive source placed on top of the model such that outward waves are suppressed and only contributions from waves directed into the model are generated (Taylor, 2001). Twenty-one receivers were placed on the surface of the model at a regular spacing of 200 m and a source-receiver spacing of 200 m was maintained. The spacing was to ensure that I have more offset data to analyse to investigate the dependence of attenuation anisotropy on offset. This was particularly necessary because Chapman’s model (2003) predicts anisotropy dependence on offset and azimuth. Data were recorded with a sampling rate of 1 ms and a total time of 3 s.

Sample synthetic data are shown in Figure 5.6 for the vertical component of particle displacement. The red and green arrows indicate the top and bottom fractured-layer reflections respectively while the pink ellipse highlights the converted wave. I computed the synthetic data in a direction perpendicular to the fracture strike at relaxation times of 2 x 10^{-8} to 2 x 10^{-2} s. These relaxation times are associated with fluid flow at the grain scale. The average grain size is 200 μm as in Chapman *et al.*, (2002). With fractures radius of 10cm, the relaxation times at the fracture scale can be computed using Equation (5.10). Thus, at the fracture scale, the corresponding relaxation times are 1 x 10^{-5} to 10 s.

5.3.3 Q estimation

The quality factor Q was estimated from the synthetic gathers on a trace by trace basis using the QVO-spectral ratio method discussed in Chapter 3. In each gather, the first trace from the top of the first layer at an offset of 0 m was used as the reference for comparison of the spectral ratios (Figure 5.7). The far field pulse shape (reference trace in this case) is proportional to the time derivative of the input Ricker wavelet (as shown in Appendix A). Thus, the peak frequency of the reference trace is higher than that of the input Ricker wavelet as predicted by Equation (3.27). The power spectra of the events from the top and bottom of the anisotropic layer and their ratios to that of the reference event were computed according to Equation (4.1). A constant time window of 140 ms was used to window these events and the power spectra computed using the FFT algorithm. Figure 5.8 shows sample plots of the power spectra at the various values of relaxation times considered at a fixed offset of 1800 m. I then performed a simple least-square regression of the Logarithm of the Power Spectral Ratios (LPSR) against frequency according to the Equation (4.1). To ascertain the frequency bandwidth for the regression, I plotted the logarithm of the Power ratios against frequencies of up to 200 Hz for all the values of the relaxation times considered (Figure 5.9). The plots are approximately linear between the frequency bandwidth of 20 - 90 Hz. This frequency bandwidth which is approximately within the signal bandwidths were used for the linear regression. Samples linear regression plots of the LPSR against frequency for the chosen bandwidths are shown in Figure 5.10 and 5.11 for the top and bottom fractured-layer reflections respectively with their corresponding R^2 values.

The plots show good fit of the spectral ratios, indicating a linear relationship as predicted by Equation (4.1) even though attenuation is frequency dependent in the model (Equation (5.10)). The Q values down to the target reflector were computed from the slopes, p using Equation (3.12) and the errors in the slopes were used to compute the associated errors in the computed Q values. With the pair of Q values computed for the top and bottom of the fractured-layer, I then used the layer-stripping method of Dasgupta and Clark (1998) to compute the interval Q value in the fractured-layer using Equation (3.8) and the associated errors using Equation (3.9). Figure 5.12 illustrates the variation of the peak frequencies with the relaxation times. There is no variation in the peak frequencies for the reference event and the top fractured-layer reflection (red and blues lines). However for the bottom fractured-layer reflection, slight variations are noticeable in the peak frequencies, indicative of varying degrees of attenuation at these times. There is an obvious variation in the peak frequencies between relaxation time values of 2×10^{-3} s and 2×10^{-6} s (at the grain scale) and no significant variation in the peak frequencies outside this range.

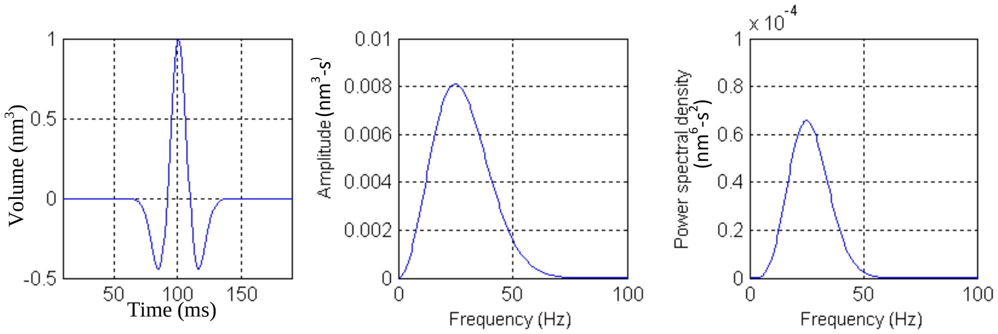

(a). (b). (c).

Figure 5.5: Ricker wavelet used as source wavelet (a) time series (b) amplitude spectrum (c) power spectrum. The centre frequency is 25 Hz. The wavelet has dimension of volume.

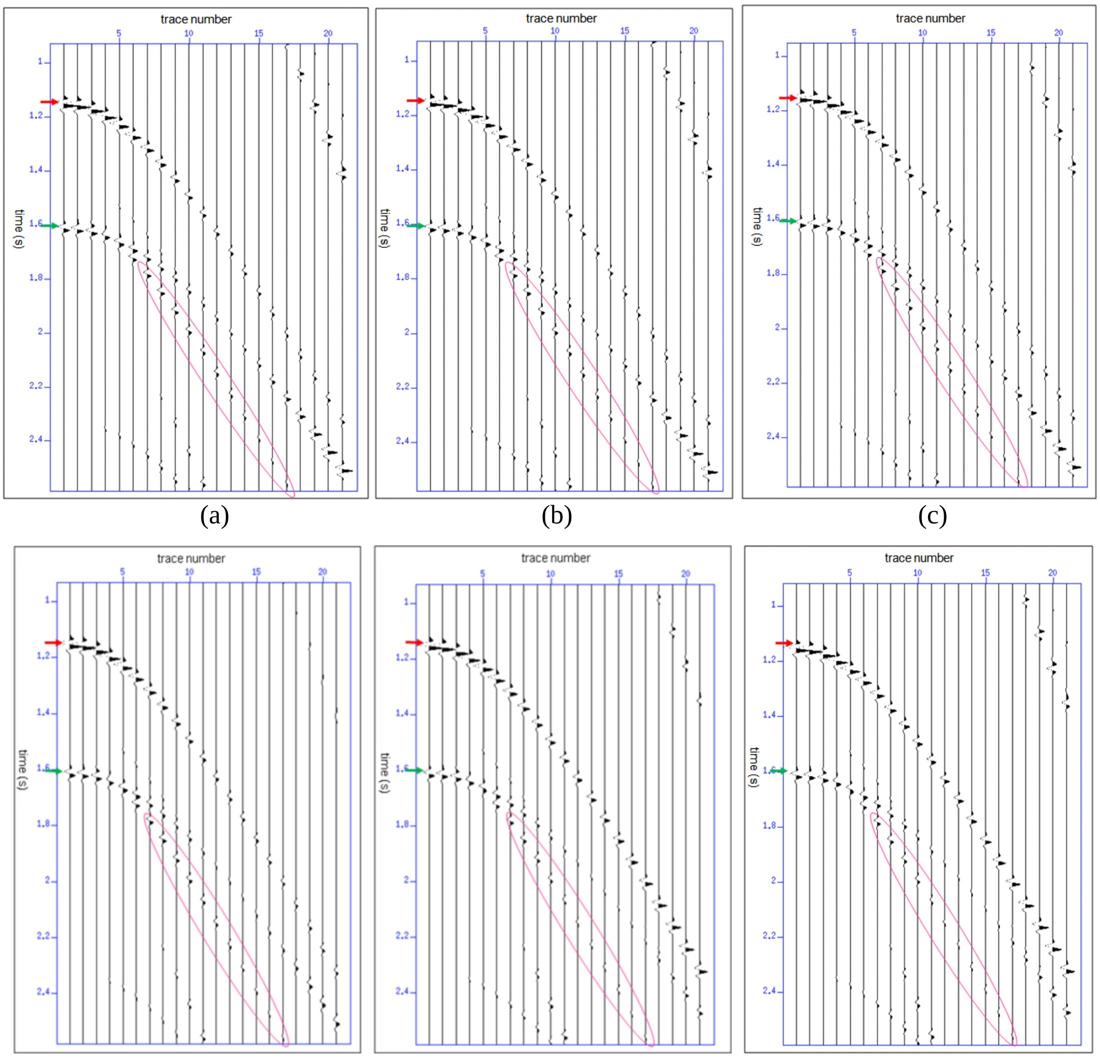

(a) (b) (c)

(d) (e) (f)

Figure 5.6: Sample synthetic gathers for the vertical component of the particle displacement (a) relaxation time = 2 x 10^{-8} s (b) relaxation time = 2 x 10^{-7} s (c) relaxation time = 2 x 10^{-6} s (d) relaxation time = 2 x 10^{-5} s (d) relaxation time = 2 x 10^{-4} s (d) relaxation time = 2 x 10^{-3} s. These relaxation times are associated with fluid flow at the grain scale. The red and green arrows indicate the top and bottom fractured-layer reflections respectively while the pink ellipse highlights the converted wave and the trace spacing is 200 m.

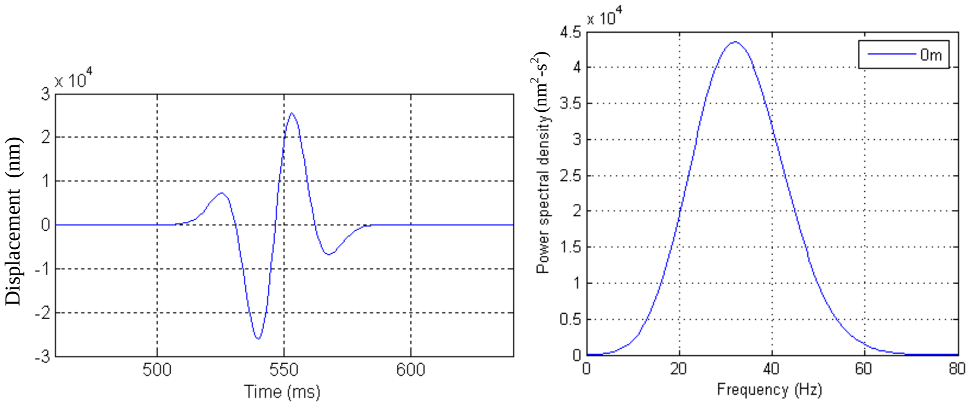

(a) (b)

Figure 5.7: Reference trace - top model reflection at 0m offset. This trace was used as a reference trace for the Q estimation. (a) Time series of reference trace (b) Power spectrum of reference trace. The wavelet is proportional to the time derivative of the source wavelet.

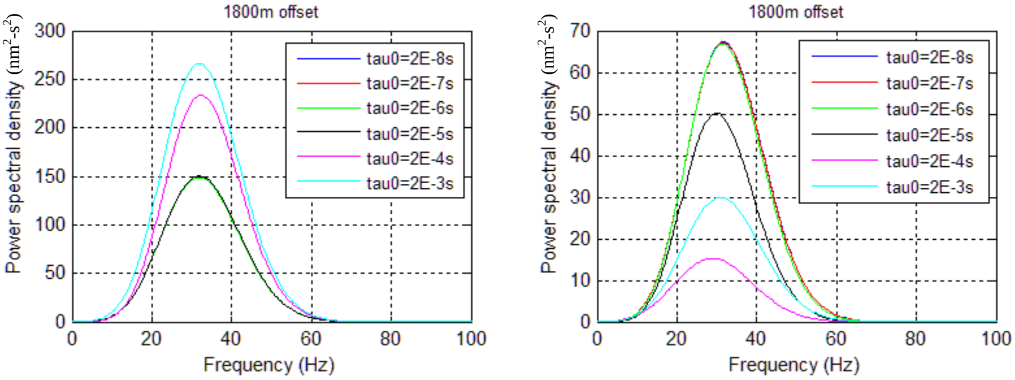

(a) (b)

Figure 5.8: Power spectral plots at 1800 m offset (a) top fracture-layer reflection (b) bottom fractured-layer reflection for the relaxation times (tau0) considered. There is a remarkable drop in the maximum power in the bottom layer reflections. The survey line is perpendicular to the fracture strike direction (90° from the strike).

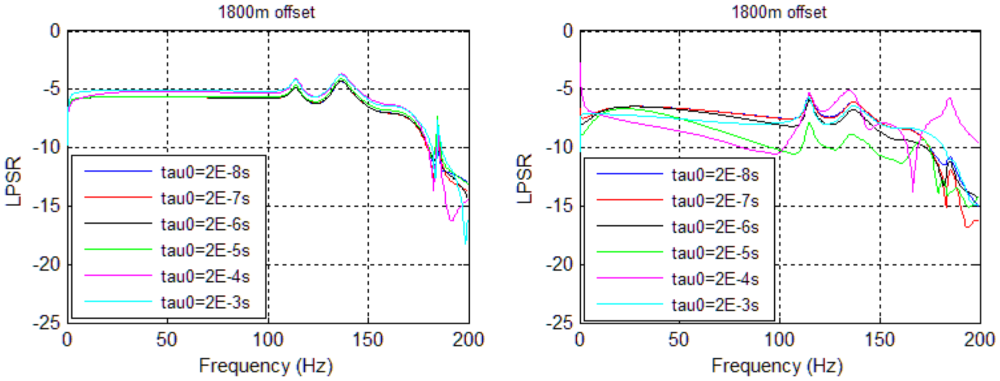

(a) (b)

Figure 5.9: Logarithm of Power Spectral Ratio (LPSR) against frequency plots for the relaxation times considered at an offset of 1800 m (a) Top fractured-layer reflection (b) Bottom-fractured layer reflection. The plots are stable between the frequency bandwidth of 20 - 90 Hz.

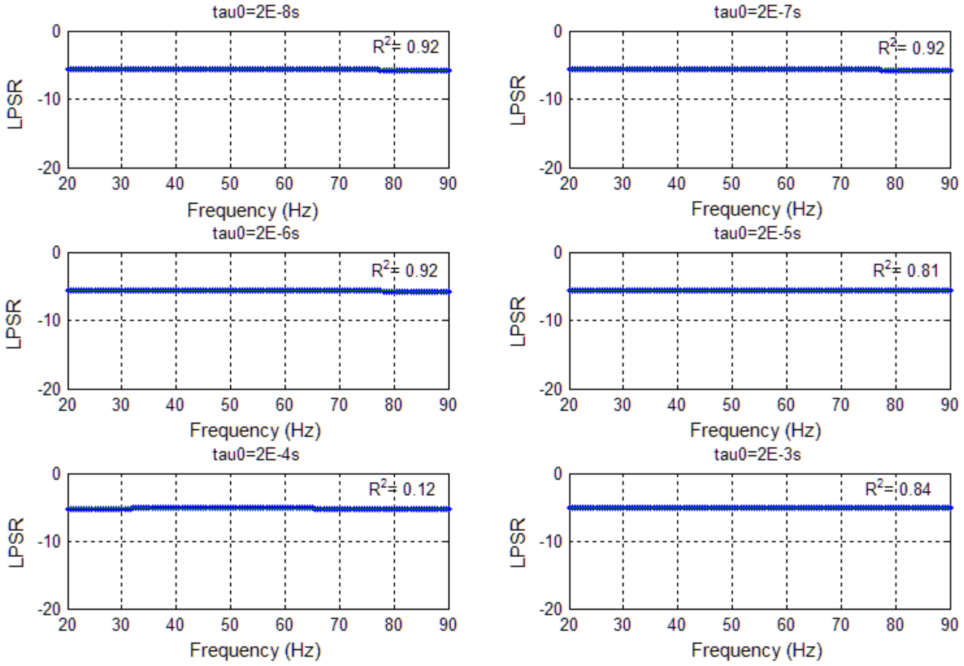

Figure 5.10: LPSR plots against frequency for the relaxation times (tau0) considered at a fixed offset of 1800 m for top fractured-layer reflection. These relaxation times are associated with fluid flow at the grain scale. The blue asterisks indicate the data points while the green line indicates the fitted line.

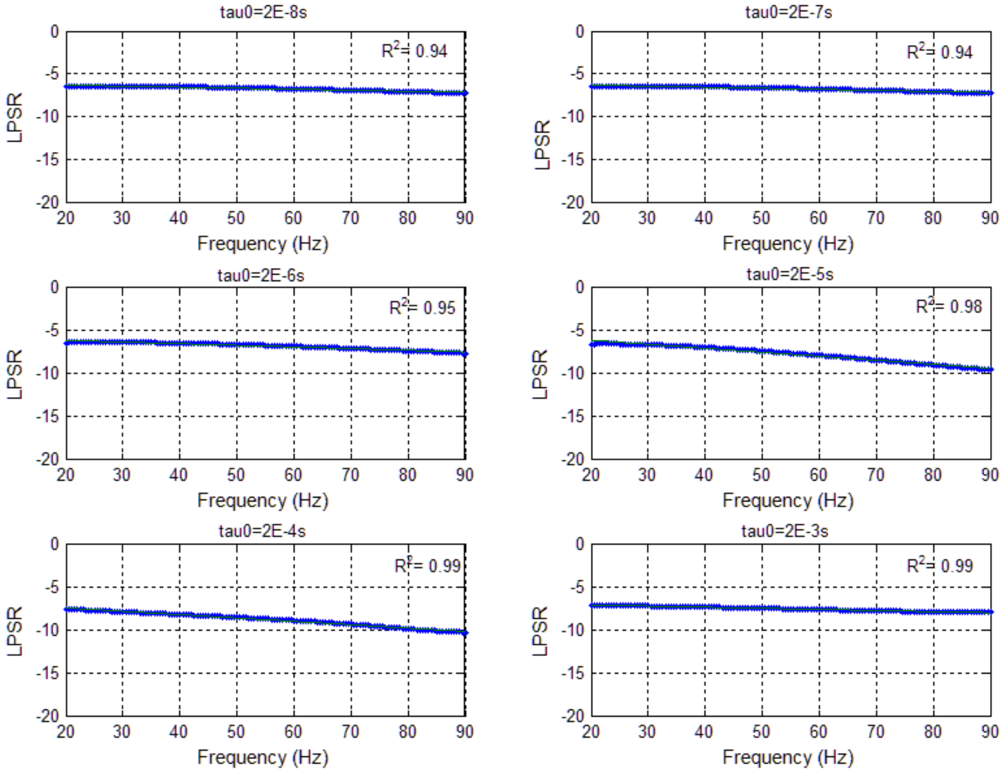

Figure 5.11: LPSR plots against frequency for the relaxation times (tau0) considered at a fixed offset of 1800 m for bottom fractured-layer reflection. These relaxation times are associated with fluid flow at the grain scale. The blue asterisks indicate the data points while the green line indicates the fitted line.

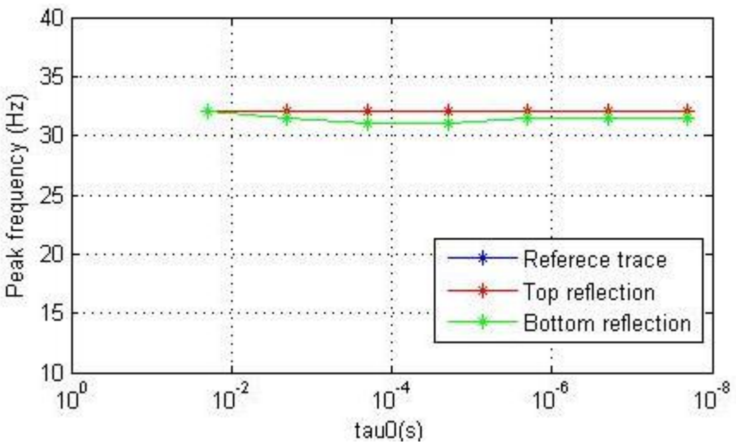

Figure 5.12: Peak frequency variation with relaxation times (tau0). The peak frequency of the reference event coincides with that of the top fractured-layer reflection. These relaxation times are associated with fluid flow at the grain scale. There is an obvious variation in the peak frequencies between tau0 values of 2 x 10^{-3} s and 2 x 10^{-6} s and no significant variation in the peak frequencies outside this range for the bottom fractured-layer reflection.

5.3.4 Results and analysis of results

The results of the analysis show that the induced P-wave attenuation is dependent on the relaxation time and hence fluid mobility (Figure 5.13). Lower attenuation values (1/Q) are obtained at relaxation times ≤ $2x10^{-6}$ s (or relaxation frequency ≥ 500 kHz) and ≥ $2x10^{-3}$ s (relaxation frequency ≤ 500 Hz) respectively. However higher attenuation values are obtained between relaxation times of $2x10^{-6}$ s - $2x10^{-3}$ s with maximum attenuation at a relaxation time of around $2x10^{-5}$s (or relaxation frequency of 50 kHz). These relaxation times and corresponding frequencies are associated with fluid flow at the grain scale. With fracture radius of 10 cm and grain size of 200 μm, the relaxation times at the fracture scale and the corresponding frequencies can be computed using Equation (5.10). Thus, attenuation occurs within a frequency range of 1 - 1000 Hz with a maximum attenuation around a frequency of 100 Hz. Noting that there is a 2π ambiguity in the definition of the frequencies in the modelling codes (personal discussion with Chapman, M., 20/03/2012), the frequencies translate into 0.6 - 160 Hz and f ≈ 20 Hz respectively. High fluid mobility implies lower relaxation times and vice versa. Thus, fluid mobility divides the relaxation time or frequency into three zones; high relaxation time zone, intermediate relaxation zone and low relaxation time zone (Figure 5.12). There is low fluid mobility in the high relaxation time zone which implies that the cracks and fractures are isolated in terms of fluid flow, tending to Hudson's theory (1980). The induced attenuation is low in this zone. The fluid mobility is high in the low relaxation time zone, implying that the cracks and fractures are connected in terms of fluid flow and the induced attenuation is also low in the zone, tending to Gassmann's theory. In between these two zones, attenuation occurs with a maximum magnitude at a relaxation time of $2x10^{-5}$ s (or relaxation frequency of 50 kHz) at the grain scale and a corresponding frequency of around 20 Hz at the fracture scale. Thus, the introduction of fractures causes attenuation at lower frequencies depending on the size of the fractures compared with grain size as predicted by Chapman's model (2003).

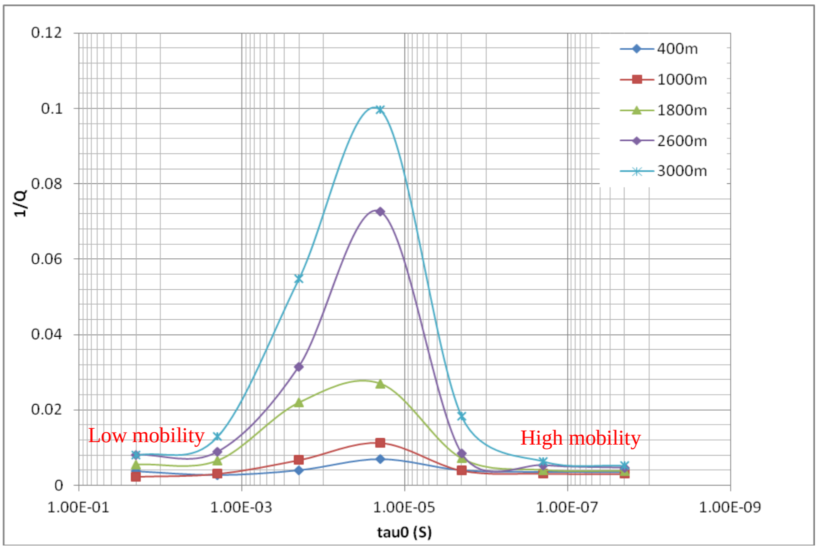

Figure 5.13: 1/Q as a function of relaxation times (tau0) for selected offsets. Low attenuation values are obtained at lower and higher relaxation times where the fluid mobility is high and low respectively. Between these ranges, the attenuation is high with a peak value at a relaxation time of around $2x10^{-5}$ s. These relaxation times are associated with fluid flow at the grain scale.

5.4 Effects of attenuation anisotropy

In this section, I examine the effects of attenuation anisotropy using the same theoretical model as in section 5.3 with the sole aim of comparing the magnitude of the anisotropy with that caused by dry cracks or fractures.

5.4.1 Theoretical model and experimental set up

The theoretical model and the experimental set up is the same as in the case of section 5.3 where I investigated the effect of fluid mobility on P-wave attenuation. The results of the study in section 5.3 indicate that maximum attenuation occurs in the fractured-layer at a relaxation time of 20 µs at the grain scale. This value of relaxation time was used in this section and the synthetic data were computed from the theoretical model at four azimuths; 0°, 45°, 60° and 90° relative to the fracture strike direction which corresponds to 0° azimuth. The acquisition geometry is the same as in section 5.3. Figure 5.14 shows the synthetic gathers computed from the theoretical model for the vertical component of particle displacement. The red and green arrows indicate the top and bottom fractured-layer reflections respectively while the pink ellipse highlights the converted wave.

5.4.2 Q estimation

I made use of the same procedure as in section 5.3 to compute the interval Q values in the fractured-layer for the four azimuthal synthetic gathers. For the reference trace, I used the first trace from the top model reflection at an offset of 0 m. Sample power spectra are shown in Figure 5.15 for selected offsets. There is a significant drop in the power spectrum for the bottom fractured-layer as we go in the direction away from the fracture strike direction towards the fracture normal, indicative of more attenuation. Sample plots of the LPSR against frequency for selected offsets are shown in Figures 5.16 and 5.17 for the top and bottom fractured-layer reflections respectively. As in the case of section 5.3, the plots are linear within a frequency bandwidth of 20 - 90 Hz and hence linear regression was done using this frequency bandwidth. Sample linear regression plots of the LPSR against frequency for the chosen bandwidth are shown in Figure 5.18 and 5.19 for the top and bottom fractured-layer reflections respectively with their corresponding R^2 values. Figure 5.20 shows the variation of the peak frequencies with offsets for the four azimuths considered. There is no noticeable variation in the peak frequencies between the reference trace and the top fractured-layer reflections. However, there is a remarkable increase in the peak frequencies with increasing offset and azimuth away from the fracture strike direction for the bottom fractured-layer reflection, indicative of increasing attenuation with offset and azimuth away from the fracture strike direction.

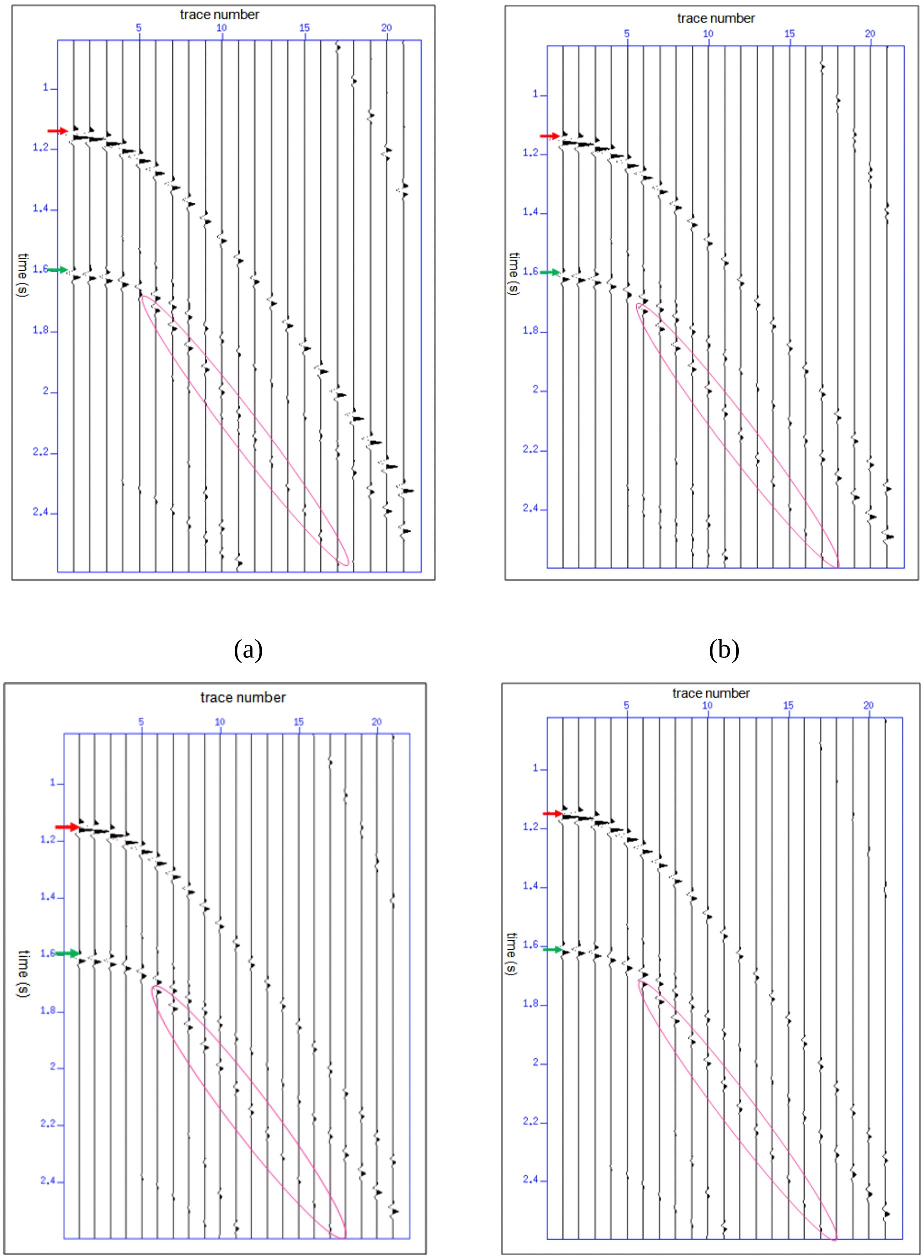

(a) (b)

(c) (d)

Figure 5.14: Sample synthetic gathers for the vertical component of the particle displacement (a) 0° azimuth (b) 45° azimuth (c) 60° azimuth (d) 90° azimuth. The red and green arrows indicate the top and bottom fractured-layer reflections respectively while the pink ellipse highlights the converted wave and the trace spacing is 200 m.

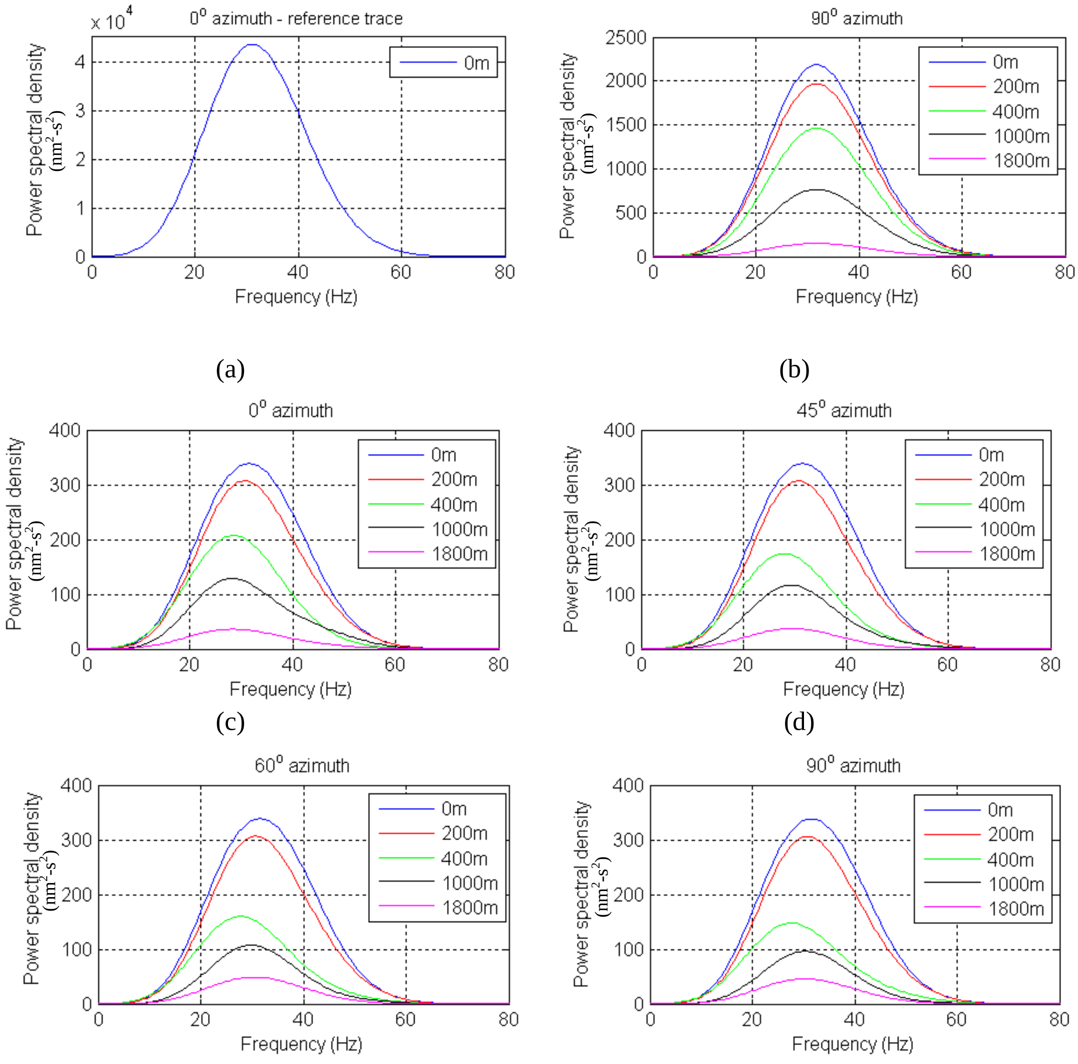

(a) (b)

(c) (d)

(e) (f)

Figure 5.15: Power spectra (a) Reference trace (top model reflection) - 0 m offset and 0° from strike (b) Top fractured-layer reflection - 90° from strike (c) Bottom fractured-layer reflection – parallel to strike (d) Bottom fractured-layer reflection - 45° to strike (e) Bottom fractured-layer reflection - 60° to strike (f) Bottom fractured layer reflection - 90° to strike.

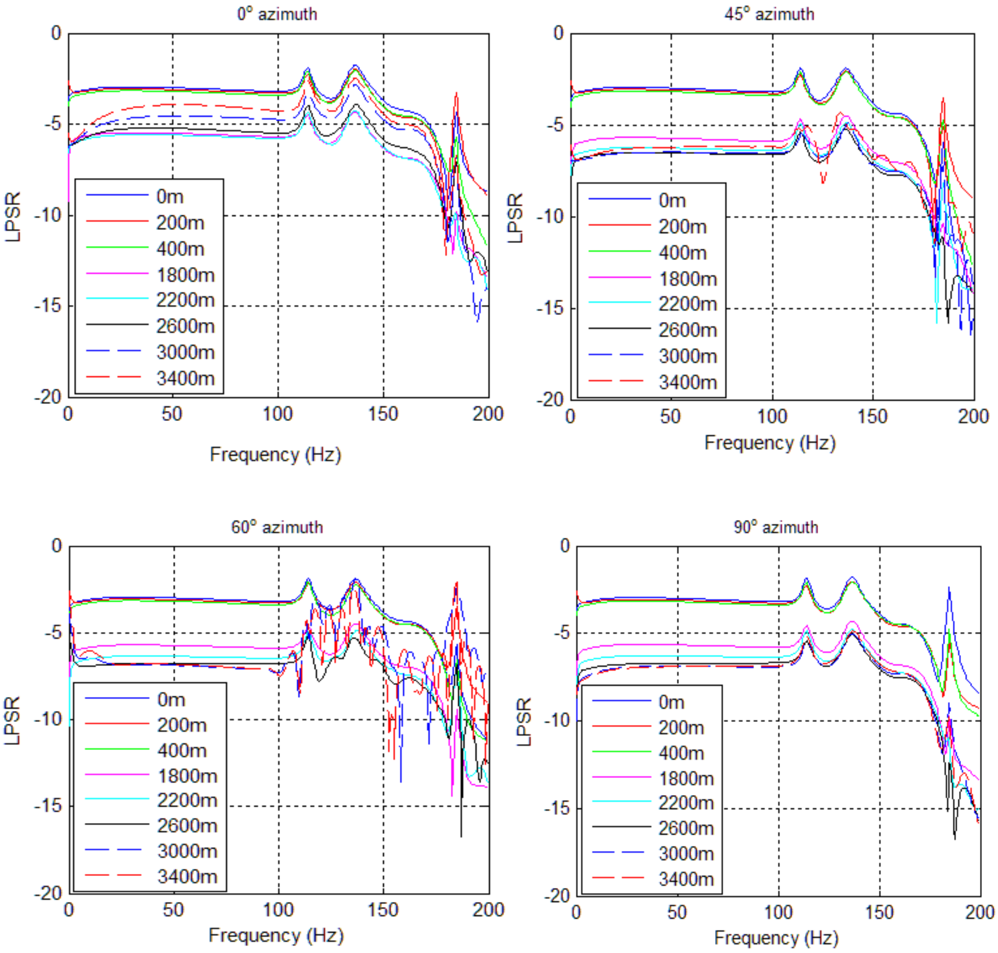

Figure 5.16: Log Power Spectral Ratio (LPSR) against frequency plots for top fractured layer reflection. The inserted legend indicates the various offsets. The plots are approximately linear within the frequency bandwidth of 20 - 90 Hz.

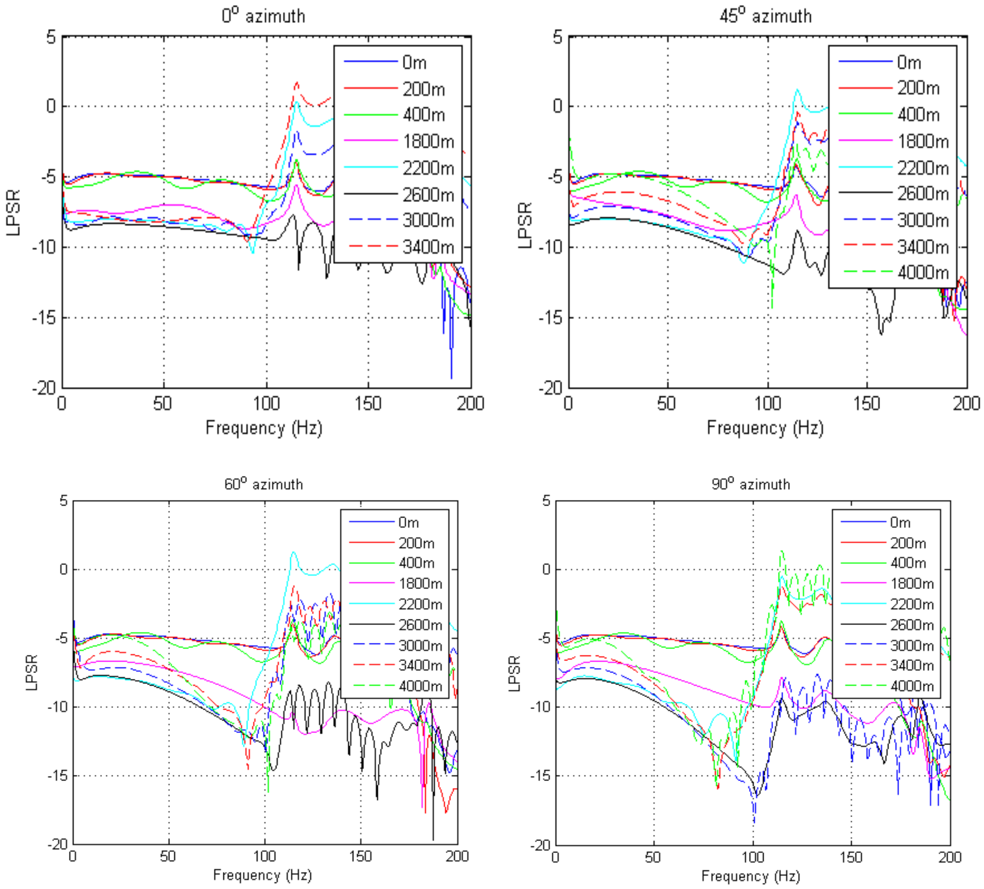

Figure 5.17: Log Power Spectral Ratio (LPSR) against frequency plots for bottom fractured-layer reflection. The inserted legend indicates the various offsets. The plots are approximately linear within the frequency bandwidth of 20 - 90 Hz.

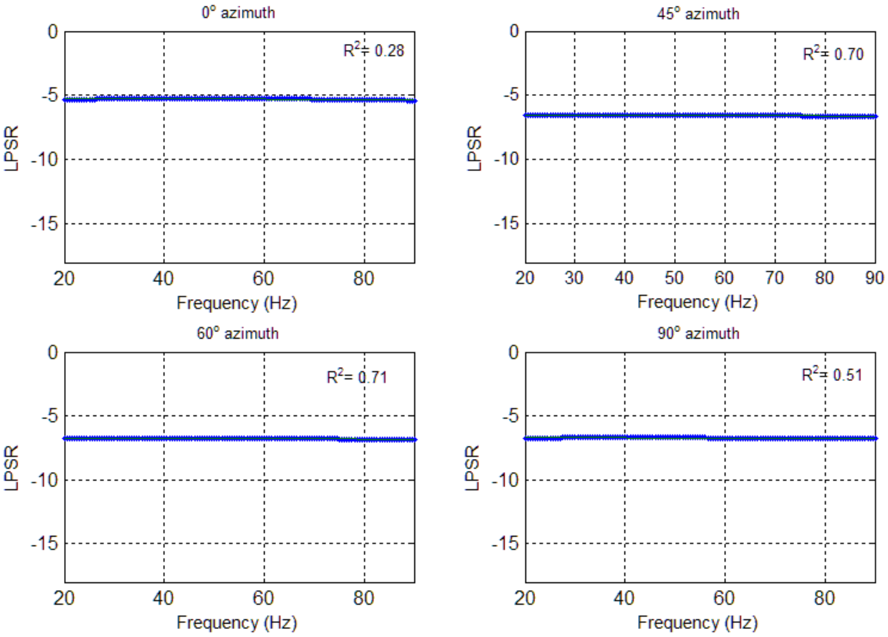

Figure 5.18: LPSR plots against frequency for different azimuths at a fixed offset of 2600 m for top fractured-layer reflection. The blue asterisks indicate the data points while the green line indicates the fitted line.

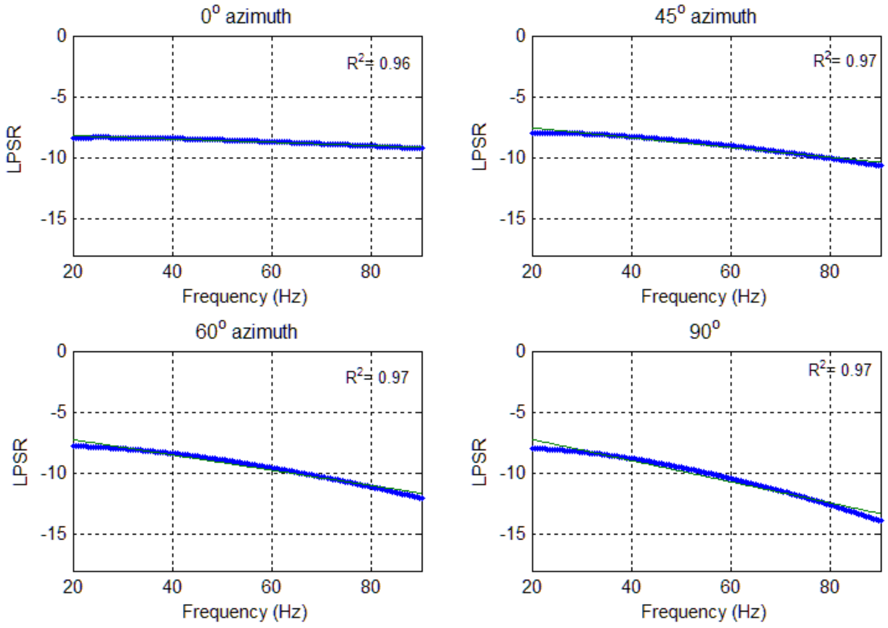

Figure 5.19: LPSR plots against frequency for different azimuths at a fixed offset of 2600 m for bottom fractured layer reflection. The blue asterisks indicate the data points while the green line indicates the fitted line.

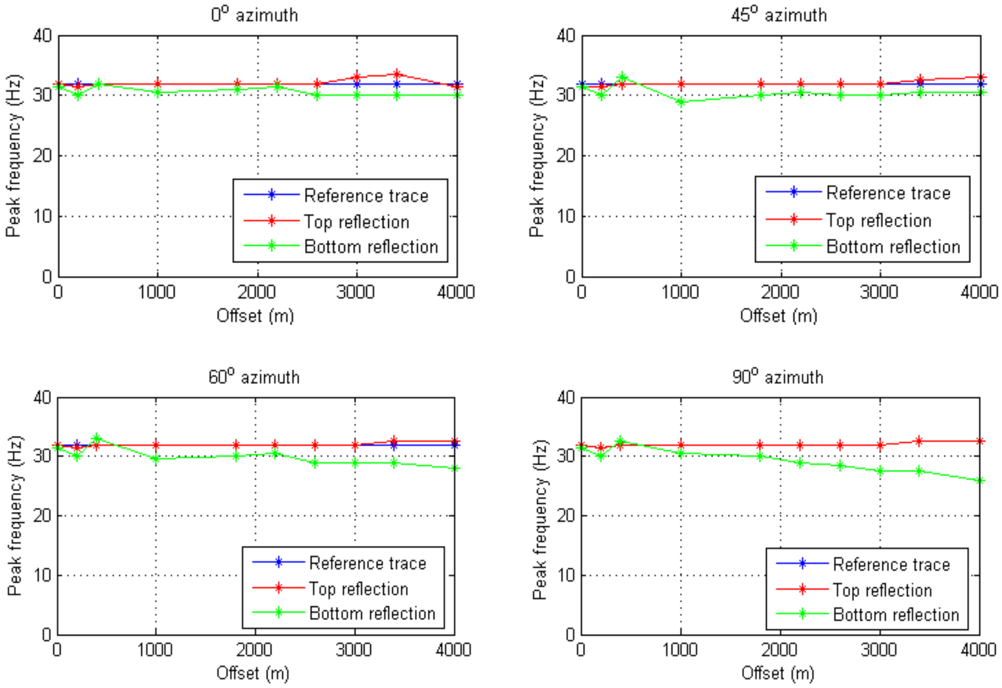

Figure 5.20: Peak frequencies as a function of offset for the four azimuths considered. There is a remarkable increase in the peak frequencies in the direction away from the fracture strike.

5.4.3 Results and analysis of results

The results of the study show that attenuation varies both with incidence angle (offset) and azimuth relative the fracture strike direction. Attenuation increases with incidence angle (offset) and also away from the fracture strike direction with maximum attenuation normal to the fractures (Figure 5.21). Azimuthal variations in the observed attenuation are elliptical to a good approximation (Figure 5.22). However, the results show that a minimum of 400 m offset (8.4° incidence angle) corresponding to an offset depth ratio of 0.4 to the top of the fractured-layer and 0.25 to the bottom of the fractured-layer respectively is required to reveal the azimuthal variations. For any given azimuth angle θ measured from the North direction (y-axis), the distance from the centre of the ellipse to the surface corresponds to the Q value for that azimuth. The major axis of the Q - ellipse corresponds to the fracture strike where attenuation is a minimum, while the minor axis corresponds to the fracture normal where attenuation is a maximum. Such plots, which are analogous to slowness surfaces, are a convenient graphic representation of attenuation anisotropy. These results are consistent with the results of the physical modelling study I did in Chapter 4.

The observed attenuation anisotropy also obeys a cosine fit of the form given in Equation (2.51). Figure 5.23 shows the cosine fits to the results for selected offsets for the four azimuthal angles of survey. The azimuth of maximum attenuation from the fits is 90° which corresponds to the fracture normal (Figure 5.24). The magnitude of the attenuation anisotropy increases with offset (or incidence angle) as predicted by Chapman's model (2003). This was determined by taking half of the difference between the maximum attenuation in the fracture normal direction and the minimum attenuation in the fracture strike direction.

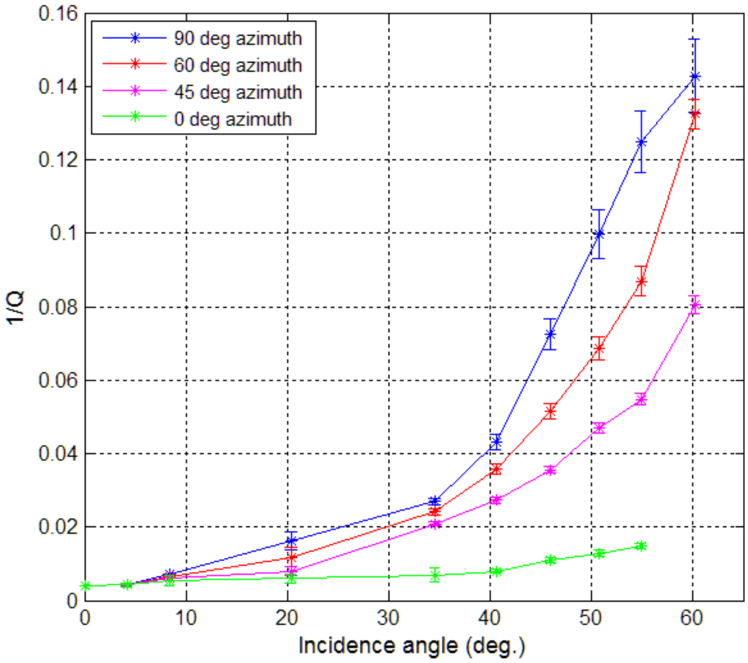

Figure 5.21: Q profiles against incident angles. Attenuation increases with increasing incident angles. There no significant change of attenuation with incidence angle in the fracture strike azimuth.

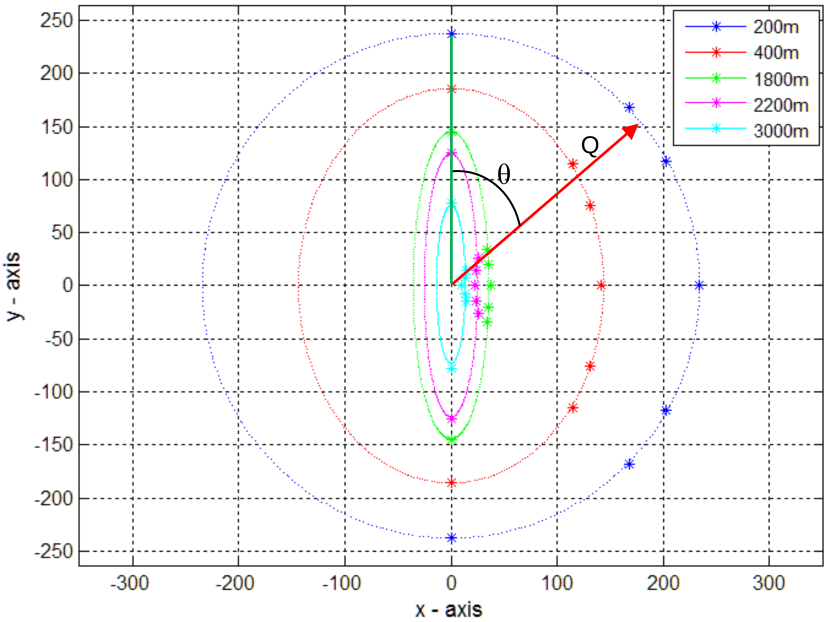

Figure 5.22: Q anisotropy ellipse. The ellipse has a centre at (0, 0) and the distance from the centre of the ellipse to the surface (red arrow) at any given azimuth angle θ measured from the North direction (y-axis), corresponds to the Q value for that azimuth. Azimuthal variations in Q are elliptical and the degree of anisotropy increases with offset (polar angle). However, a minimum of 400 m is required to reveal the anisotropy. The major axis of the ellipse corresponds to fracture strike while the minor axis corresponds to the fracture normal.

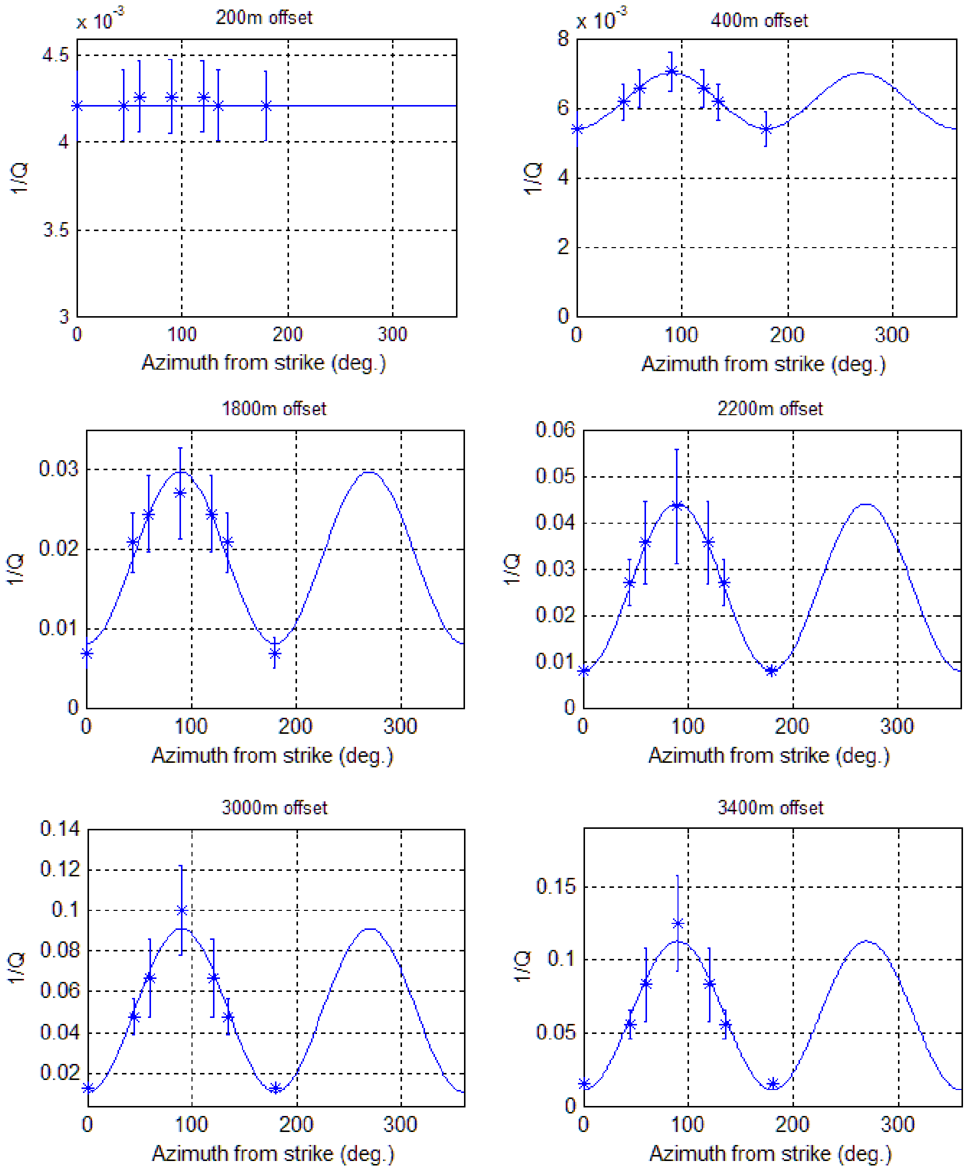

Figure 5.23: Cosine fits of estimated 1/Q values against azimuth for given offsets. The amplitude of the attenuation anisotropy increases with offset. Maximum attenuation occurs 90° from the fracture strike direction.

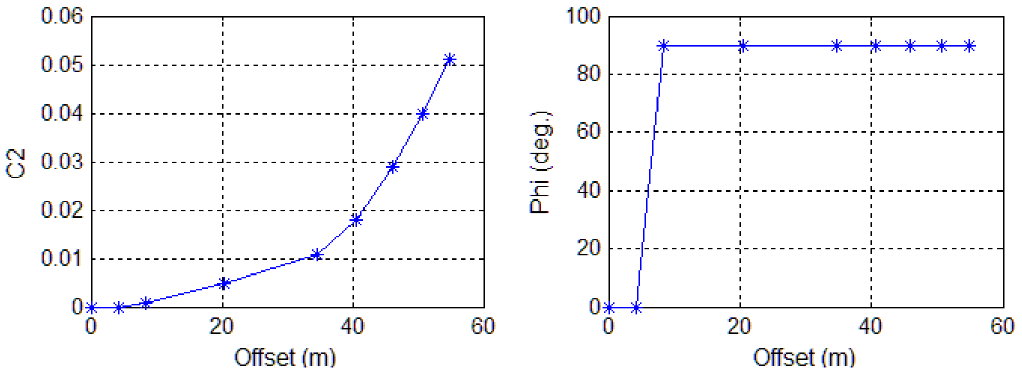

(a) (b)

Figure 5.24: Inverted parameter from cosine fits (a) C2. The degree of anisotropy increases with incidence angle. (b) Angle of minimum Q (maximum attenuation) - 90° from strike direction corresponding to fracture normal.

5.5 Summary and conclusions

In this Chapter, I have carried out a synthetic modelling study of the effects of P-wave attenuation in fractured porous rock. Firstly, I have investigated the effects of fluid mobility on the induced attenuation by considering a range of relaxation times in Chapman's poro-elastic model and then used the value of the relaxation time that gives maximum attenuation in the model to investigate the effects of attenuation anisotropy in the model. The results of the study show that the induced attenuation is sensitive to the relaxation times. Very low attenuation values (1/Q) are obtained at relaxation times $\leq 2x10^{-6}$ s (or relaxation frequency $\geq$ 500 kHz) and $\geq 2x10^{-3}$ s (or relaxation frequency $\leq$ 200 Hz) respectively. In between these two limits, dispersion occurs and higher attenuation magnitudes are obtained with a maximum around a relaxation time of $2.0x10^{-5}$ s (or relaxation frequency of 50 kHz). These relaxation times and corresponding frequencies are associated with the fluid flow at the grain scale. At the fracture scale, these frequencies translate into 0.6 - 160 Hz and with a maximum attenuation around a frequency of 20 Hz. Higher relaxation times imply that more time is required to relax the pressure gradient generated by the propagation of P-waves in the rock and the pore pressure is therefore out of equilibrium resulting in the high frequency regime. Fluid mobility is low in this regime and the model tends to Hudson's (1980) model of non-communicating cracks or fractures. On the other hand, lower relaxation times mean that less time is needed to relax the pressure gradient generated by wave propagation in the rock and the pore pressure equilibrium is enhanced resulting in the low frequency regime. Fluid mobility is high in this regime and Gassmann’s relation is valid.

The induced attenuation increases in magnitude with incidence (polar) angle (offset) and away from the fracture strike direction, which is consistent with the predictions of Chapman’s model (2003) and the results of the walk away VSP studies of Maultzsch *et al.,* (2007). Azimuthal variations in the induced attenuation are elliptical and the fracture orientations are obtained from the axes of the ellipse. The major axis of the Q ellipse corresponds to the fracture strike while the minor axis corresponds to the fracture normal. The observed attenuation anisotropy is also well fitted by a ‘cos2θ’ (where θ is angle from fracture strike direction) function, giving the angle of maximum attenuation normal to the fracture strikes showing a good agreement with the results of the ellipse fitting. However, a minimum offset of 400 m corresponding to an offset-depth ratio of 0.4 and 0.25 respectively to the top and bottom of the fractured-layer is required to reveal the anisotropy. The magnitude of the observed attenuation anisotropy is found to be dependent on the incidence angle (offset); increasing with offset up to a maximum of 5.1 % at 3400 m offset which is higher than an average magnitude of 2.6 % observed in the case of the dry rocks modelled in Chapter 4. Fluid exchange between the pores and fractures during wave propagation leads to increased attenuation in addition to that caused by the scattering effects due to the aligned fractures.

Chapter 6 Effect of fracture thickness on P-wave attenuation: a seismic physical modelling study

In this Chapter, I use the seismic physical modelling approach as in the case of Chapter 4 to investigate the effects of aligned fractures with the same density but different thicknesses or apertures on P-wave attenuation. The same fracture density can result from either a few large cracks or many small ones in the same volume of background material, and an understanding of these effects could be of great importance in fractured hydrocarbon reservoir characterization to differentiate between the effects caused by thin micro-cracks and large open fractures. Here I show that P-wave attenuation is also sensitive to this aspect of fracture morphology.

6.1 Introduction

Hudson's theory (1980 and 1981) is often used to study the propagation of seismic waves in fractured media and provides a link between fracture density and measured azimuthal anisotropy. However, the theory fails to account for the issues of fracture scale lengths. For instance, many small cracks or a few large cracks within the same volume of material can result in the same fracture density. Furthermore, equal number of cracks with the same radius but with varying thicknesses or aperture within the same volume of material can also give rise to the same fracture density. In reservoir rocks, it is possible to have aligned fractures of the same density but at different scales and consequently the investigation of the effects of the fracture scale lengths and thicknesses on seismic wave response may be of great interest in fractured reservoir characterization.

Wei *et al.,* (2007a and 2007b) and Wei *et al.,* (2008) used the seismic physical modelling approach to examine the effects of fracture scale lengths on seismic wave velocity and amplitude for both P- and S-transmitted waves. They simulated a set of aligned fractures by embedding thin round low-velocity chips of the same density and thickness (0.14 mm) but varying diameter (ranging from 2.5 - 6 mm) into an isotropic background material on the basis of Hudson's (1980) assumption of thin penny-shape fractures and used the pulse-transmission method to study the influence of the fracture diameter on the transmitted data (Figure 6.1). The results of their measurements show that both P- and S- wave velocities increase with fracture diameter especially for wave propagation parallel to the fracture strike. They argued that as the diameter increases the number of fractures decreases to keep the density constant, resulting in a decrease in the amount of scattering and an increase in the wave velocity. Their results also reveal that the amount of shear-wave splitting decreases as the fracture diameter increases also as a result of the reduction in the number of fractures as the diameter increases. Wei *et al.,* (2007) further investigated the influence of fracture thickness or aperture by embedding thin round chips of the same diameter (2.1 mm) but varying thicknesses (ranging from 0.1 - 0.35 mm) into an isotropic background material. Their results show significant changes in the P-wave amplitude and waveforms with increasing thicknesses. As the chips' thickness increases, the P-wave is significantly attenuated as illustrated in Figure 6.2 with more attenuation perpendicular to the fractures. However, their study fails to provide quantitative estimates of the observed attenuation from the waveforms. Thus, the motivation in this chapter is to extend the previous studies by Wei *et al.,* (2007) to reflected seismic data by estimating the amount of scattered attenuation caused by fractures of varying thicknesses but of the same density to provide more understanding of these scattering effects on P-wave amplitude.

As in the case of the seismic physical modelling study of Chapter 4, the set up of the physical modelling experiment is inspired by Hudson's (1980) assumption of penny-shaped fractures. A known number of round thin low-velocity chips with fixed diameter but varying thicknesses are embedded into an isotropic base material to simulate a set of aligned vertical fractures and the fracture density is derived based on Hudson's theory (1980 and 1981).

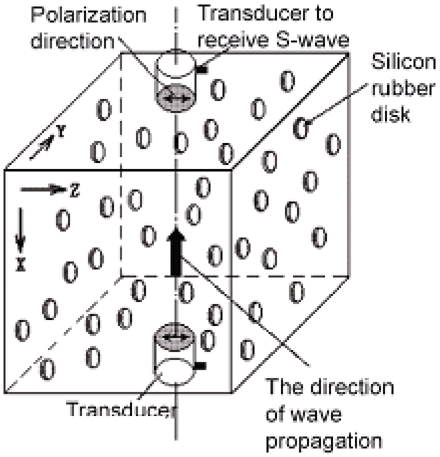

Figure 6.1: Investigation of effects of fracture scale length on seismic response (from Wei *et al.*, 2007b). Thin round chips with the same thickness but varying diameter are embedded into an isotopic material to simulate a set of aligned vertical fractures. The pulse and transmission method is used to measure the seismic response in the model.

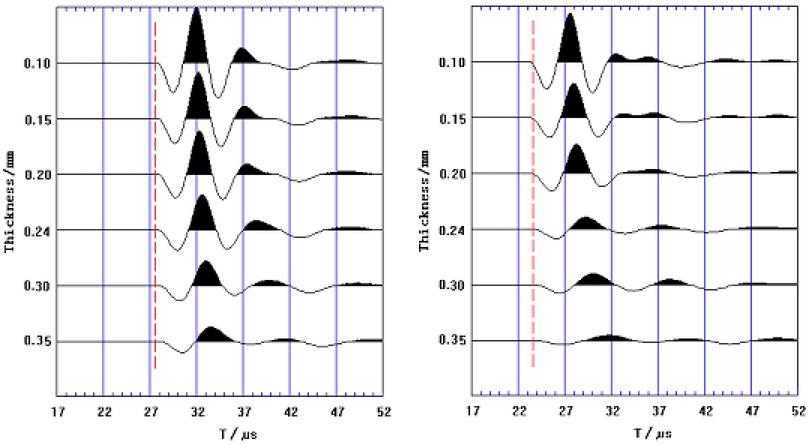

Figure 6.2: Comparison of P-waves recorded for the fractured models with different thicknesses (from Wei *et al.*, 2007b). (a) Parallel to the fracture strike (b) Perpendicular to fracture strike. The wave is attenuated more in the direction perpendicular to the fractures.

6.2 The physical model

As in the case of the physical model used in chapter 4, the physical model and the experimental data used in this chapter were obtained in the China National Petroleum Corporation (CNPC) Geophysical Laboratory in China. In this section, I describe the construction of the physical model and the experimental set-up for data acquisition.

6.2.1 Construction of the physical model

The physical model is constructed from two horizontal layers (Figure 6.3). The first layer is made from a mixture of epoxy resin and silicon rubber and has a thickness of 38 mm, P-wave velocity of 2150 m/s, S-wave velocity of 1100 m/s and density of 1.15 g/cm^3. The second layer is made from epoxy resin with a thickness of 75.5 mm, P-wave velocity of 2573 m/s, S-wave velocity of 1200 m/s and density of 1.18 g/cm^3. The P- and S-wave velocities of the materials in the model were measured by using the pulse and transmission method as in Wei *et al.*, (2007a and 2007b) (personal discussion with X. Y. Li and J. Wei, 30/09/2008) and their values were given to me. The measurement errors in these velocities are unavailable. However, typical accuracy of ultrasonic velocity measurement can be ± 1.0 % (King and Marsden, 2002). To simulate fractures with varying thicknesses, thin penny-shaped chips made from a mixture of epoxy resin and silicon rubber with a fixed diameter of 3 mm and

P - wave velocity of 1300 m/s are randomly embedded in the isotropic background of the second layer to make the layer anisotropic. The chips are arranged to form six fractured blocks with their thicknesses as 0.10, 0.15, 0.20, 0.25, 0.30 and 0.35 mm respectively in each block. Each block is made up of 30 layers of epoxy resin. Once a layer is laid, 360 thin chips are randomly embedded into the layer and another layer is added on the top. The whole process is repeated until a total of 30 layers were achieved. All the six fracture blocks have the same fracture density of 7.95 %. Details of the fracture model parameters are given in Table 6.1. The model is constructed with a scale of 1:10,000 for spatial dimensions and time measurements and is a simplified analogous representation of a fractured reservoir with varying fracture thicknesses or aperture. Although the simulated fractures may not be real fracture analogues in a typical fractured reservoir setting, this study is expected to provide useful information on the effects of voids in the rock on P-wave attenuation and a basis for further theoretical development since there is no theory at the moment to explain this kind of situation.

6.2.2 Experimental set-up and data acquisition

The pulse and transmission method was used to record the seismic reflection data from the physical model in a direction perpendicular to the fracture strike. 2-D reflection data were acquired in a water tank where the base model was submerged (Figure 6.4). The water depth to the top of the model is 100 mm, making the net thickness of the overburden above the anisotropic layer to be 138 mm. The physical modelling system is the same as that used in Chapter 4 (Figure 4.3).

With the velocity in the fractured layer as 2573 m/s (given to me) and a centre frequency of 230 kHz, the dominant wavelength generated is 11.2 mm (wavelength λ = velocity/frequency) compared with the fracture diameter of 3 mm. The source and receiver were located on the water surface. For the first shot gather located 500 mm from the edge of the tank (Figure 6.4), a single shot was fired into a single receiver at a minimum offset of 16 mm, the receiver was then moved a distance of 2 mm away and another shot fired until a total of 120 receiver positions were occupied at a spacing of 2 mm for the single shot position. The shot was then moved a distance of

2mm in the direction of the receiver and the procedure repeated. A total of 220 shots were made at 2 mm intervals. The model acquisition parameters are scaled up by 1:10,000 for spatial dimensions and time measurements while the frequencies are scaled down by 10,000:1. Details of the acquisition geometry are summarized in Table 6.2

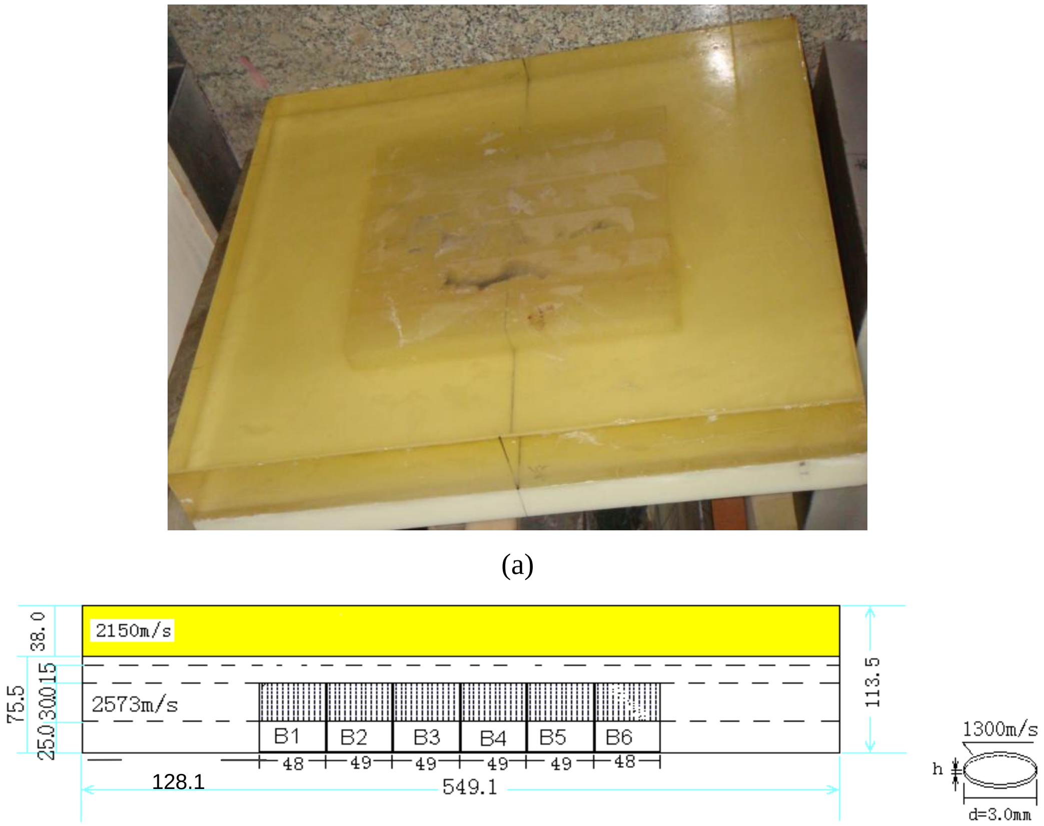

(a)

(b)

Figure 6.3: Physical model made up of two layers (a) Base model (b) Sectional view of base model. The first layer is isotropic with a P-wave velocity of 2150 m/s and density of 1.15 g/cm^3 while the second layer has six fractured blocks (each of same density), B1 to B6 in order of increasing chip thickness. The isotropic background of this layer has a P-wave velocity of 2573 m/s and a density of 1.175 g/cm^3. The numbers shown indicate model dimensions in millimetres and the model is scaled up by 1:10,000 for spatial dimensions and time measurements.

Table 6.1: Model parameters of fracture models. The dimensions are scaled up to 1: 10,000. Dimensions shown are not converted to real scaling.

Model number/block	B1	B2	B3	B4	B5	B6
No. of layers	30	30	30	30	30	30
No. of chips per layer	360	360	360	360	360	360
Total no. of chips in model	10800	10800	10800	10800	10800	10800
Chip thickness (mm)	0.10	0.15	0.20	0.25	0.30	0.35
Layer thickness (mm)	1.59	1.63	1.63	1.61	1.63	1.58
Radius of each chip (mm)	1.5	1.5	1.5	1.5	1.5	1.5
Volume of base material	458640	458640	458640	458640	458640	458640
Fracture density (%)	7.95	7.95	7.95	7.95	7.95	7.95

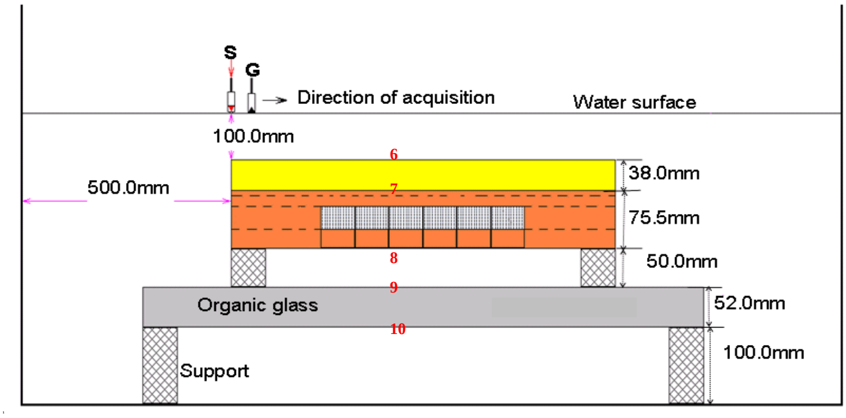

Figure 6.4: Experimental set up. Base model submerged in a water tank. S and G are the shot and receiver positions respectively. The blue numbers indicated specify the reflection interfaces and the model dimensions shown are scaled up 1:10000. 2-D data was acquired normal to the fracture strikes.

Table 6.2: Summary of data acquisition geometry - all the acquisition parameters given are not converted to actual scales. The model dimensions and acquisition parameters are scaled up by 1:10000 while the frequency is scaled down by 10000:1.

Water depth to base model (mm)	100
Number of shot	220
Shot interval (mm)	2
Receiver interval (mm)	2
Number of receivers	120
Minimum offset (mm)	16
Maximum offset (mm)	254
Fold of cover	60
Number of samples	4096
Sample rate (µs)	0.1

6.3 Data description

As in the case of the data used in chapter 4, the physical modelling data have similar features to real field data. The raw data is comprised of 220 shot gathers with 120 traces in each gather. The trace spacing is the equivalent of 20 m for a field-scale experiment, while the minimum and maximum offsets are 160 m and 2540 m respectively, after applying the appropriate acquisition scaling. Figure 6.5 shows a sample shot gather of the data. The red numbers corresponds to the reflection from the interfaces indicated in Figure 6.4. The data quality is very good and all the reflection events of interest are free from noise contaminations. The target events are the reflections from the top of the base model (number 6), top of the fractured-layer (number 7) and bottom of the fractured-layer (number 8). These three reflections are continuous in the gathers. Unlike the data used in chapter 4, the thickness of the second layer is sufficient for the top and bottom reflections from the layer to be well isolated allowing more offset data to be used in the attenuation analysis. The event indicated as a question mark (?) is a multiple of the reflection from top of the base model.

6.4 Data processing

Since the data has high a signal-to-noise ratio, minimal processing was done on the data in order to preserve all the amplitude information needed for attenuation analysis as in the case of the data used in Chapter 4. Consequently, the following processing sequence was applied: geometry configuration, common mid-point (CMP) sorting, trace-muting, velocity analysis and NMO correction. Stacking was also included in the processing sequence for ease of event identification and picking of the travel times to the target layers, even though the Q values were estimated from the pre-stack CMP gathers.

The data were sorted from shot gathers into 558 CMP gathers spaced at 10m apart. From the model parameters and acquisition geometry, the fractured blocks lie approximately between CMP(s) 120 and 412 with CMP(s) 144, 192, 242, 290, 340 and 388 corresponding to the centres of the fractured blocks B1, B2, B3, B4, B5 and B6 respectively. A sample CMP gather is shown in Figure 6.6 where top mute has been applied to remove the direct arrival noise. The reflections from the various interfaces are highlighted by the red numbers.

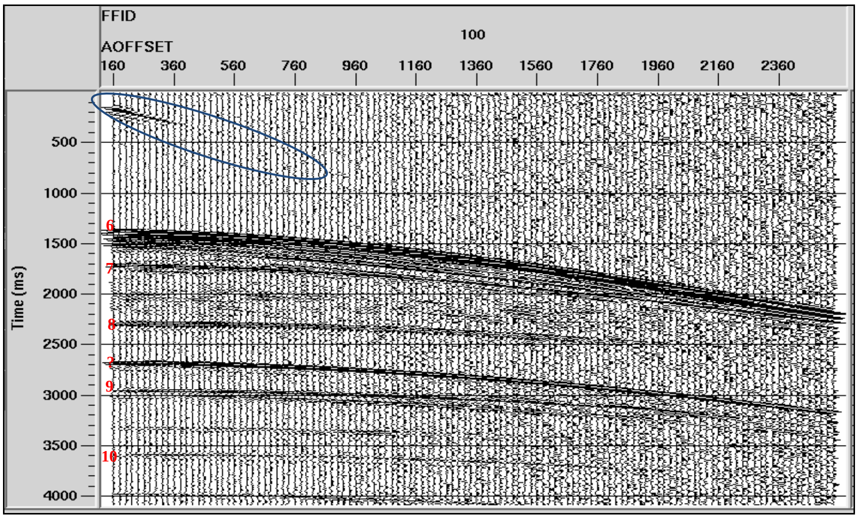

Figure 6.5: Sample shot gather - field file ID number (FFID) 100 comprising 120 traces with trace spacing of 20 m. The red numbers indicate reflections from the interfaces shown in Figure 6.4 while the question mark highlights multiple of top model reflection. Direct arrival noise is highlighted in the blue ellipse.

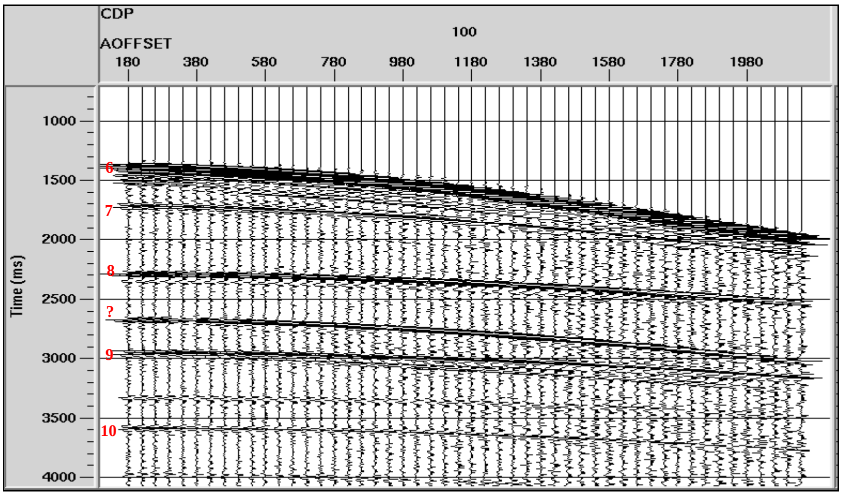

Figure 6.6: Sample CMP gather (CMP 100) with top mute applied to get rid of the direct arrival noise. The red numbers indicate reflections from the interfaces shown in Figure 6.4 while the question mark highlights multiple of top model reflection.

Prior to the interactive velocity analysis, 5 CMP gathers were combined to form super gathers and the velocity pre-computed using minimum and maximum guide values of 1000 m/s and 4000 m/s respectively. The interactive velocity analysis panel is shown in Figure 6.7. The velocity model was used to apply NMO correction to the data. A sample NMO-corrected gather is shown in Figure 6.8 with no stretch mute applied while the stacked section is shown in Figure 6.9. Scattering effects caused by the simulated fractures are observed on the stacked section within the time window bounding the top and bottom fractured-layer reflections (numbers 7 and 8 respectively - Figure 6.9).

The reflection from the top of the base model occurs at a two-way travel time of 1387 ms, while those from the top and bottom of the fractured-layer occur at two-way travel times of 1717 ms and 2286 ms respectively. Table 6.3 shows a comparison of the stacking velocities computed based on the model layer velocities (given to me) and those obtained from interactive velocity analysis picking for CMP 100 (where there are no fractures) in the third layer. The percentage difference between the measured stacking velocities and the computed ones ranges from 0.5 - 6.0 % which is indicative of good quality of data processing.

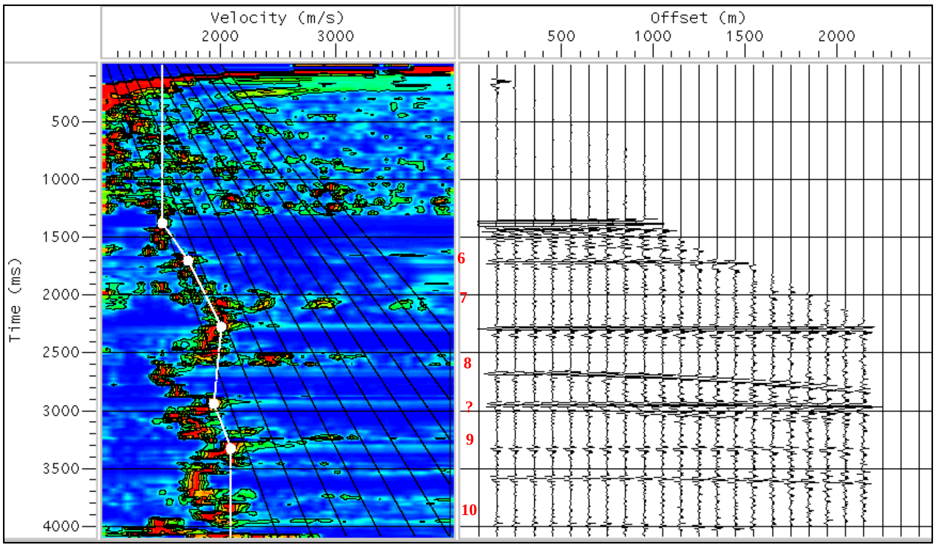

Figure 6.7: Interactive velocity analysis panel showing the amplitudes of the stack as a function of velocity and time (left-hand diagram) and the NMO-corrected traces for the optimal velocity (right-hand diagram). The white line on the left hand diagram indicates the optimal velocity picks and NMO correction has been applied to the data with a stretch mute of 30 %. The red numbers on the right hand diagram indicate specific reflections from the same interfaces numbered on Figure 6.4.

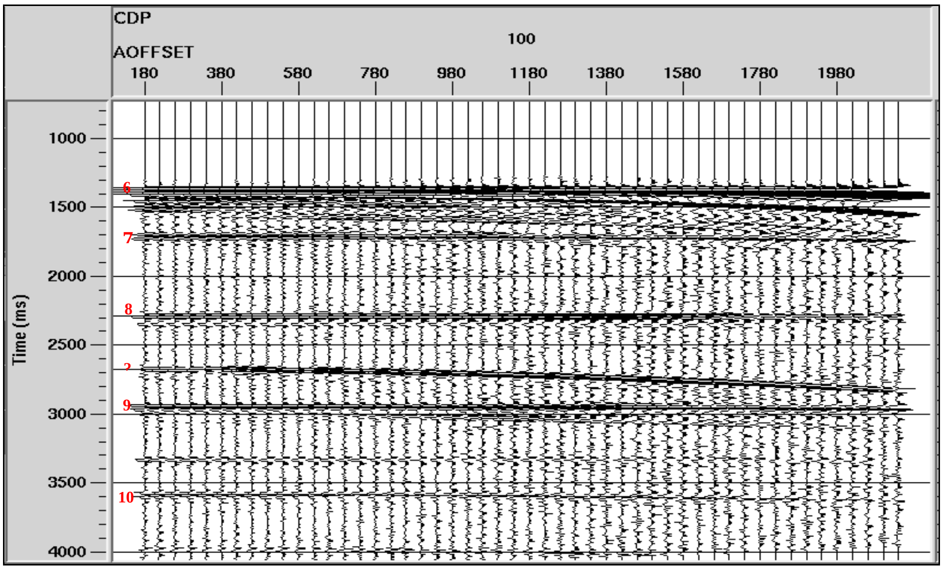

Figure 6.8: Sample NMO-corrected gather. The red numbers indicate reflections from the interfaces shown in Figure 6.4 while the question mark highlights a multiple of top model reflection. NMO stretch effects are obvious at far offsets especially for the top model reflection.

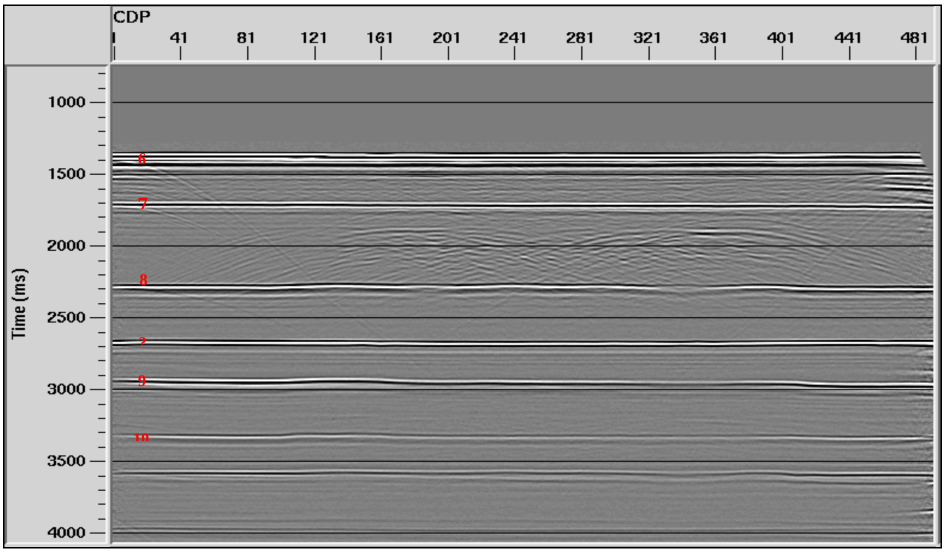

Figure 6.9: Stacked section showing the reflections. The red numbers indicate reflections from the interfaces shown in Figure 6.4 while the question mark highlights multiple of top model reflection. Scattering effects are observed in the fractured layer arising from multiple scattering caused by the fractures.

Table 6.3: Comparison of computed stacking velocities based on actual model velocities and the measured stacking velocities from interactive velocity analysis picking (CMP 100). Overall, the percentage difference between the two velocities ranges from 0.5 - 6.0 %, and increase systematically with model depth as the errors propagate.

Layer number	V_{stack} actual m/s	V_{stack} measured m/s	% difference
1	1500	1493	0.5
2	1657	1712	3.3
3	1936	2003	3.5
4	1846	1935	4.8
5	1970	2088	6.0

6.5 Q estimation

I made use of the same procedures applied to the physical modelling data in Chapter 4 to estimate the quality factor, Q from the pre-processed NMO - corrected CMP gathers. I started the attenuation analysis with an offset range of 160 - 1340 m. This offset range was finally reduced to 160 - 940 m as a result of the linearity of the Log Spectral Power Ratio (LSPR) slopes plot against squared offset within this range. I applied a constant FFT window width of 130 ms to all the target events with the windows tapered using the Hanning Taper as in Chapter 4. Figures 6.10 and 6.11 show sample spectra for CMP gathers 120 and 224. A shift in the peak frequencies to the lower frequency end is observed for the two gathers between the top and bottom fractured-layer reflection. Also, there is a noticeable decrease in the magnitudes of the spectral power which are indicative of attenuation effects due to the scattering of the wave energy in the fractured-layer.

Figure 6.12 shows sample plots of the Log Spectral Power ratios (LSPR) versus frequency for selected offsets for CMP 120. I carried out a sensitivity analysis to assess the effects of the regression bandwidth on the measured interval Q values in the fractured-layer. Table 6.4 shows the sensitivity of the interval Q values to the regression bandwidth for CMP gathers 160 and 260 respectively. All the results show some consistency in the Q estimates except for regression bandwidths of 5 - 30 Hz and 10 - 30 Hz. Stable attenuation estimates can be made by the use a wide frequency bandwidth, but this is limited by the bandwidth present in the data. Hence, I chose a frequency bandwidth of 10 - 40 Hz for linear regressions of the LSPR versus frequency for all the CMP gathers analysed. This frequency bandwidth lies within the signal bandwidth where the spectral plots are stable (Figures 6.10 and 6.11) and is common to all the three reflections analyzed. Sample linear regression plots of the LPSR against frequency for the chosen bandwidth are shown in Figure 6.13 with their corresponding R^2 values. The value of R^2 for a perfect fit is 1. The red dashed lines indicate a 95 % confidence interval on the fitted line. The confidence interval provides a boundary for all possible straight lines through the data points and there is a 95 % chance that the interval encloses the best-fitting regression line while the remaining 5 % implies that the line could lie outside the confidence bounds. Generally 19 out of 20 points are included within these bounds, but there are significant systematic deviations from the random fluctuation assumed in the determination of these error bounds which lead to a lower portion in some parts of the curve.

The absolute value of the gradient is observed to increase with the thickness of the chips which indicates an increase in scattering and hence attenuation. Figure 6.14

shows sample plots of the LSPR slopes versus squared offset for CMP 260. The plot is linear within an offset range of 160 - 940 m. Hence, this offset range was finally selected for the attenuation analysis in all the CMP(s) analyzed.

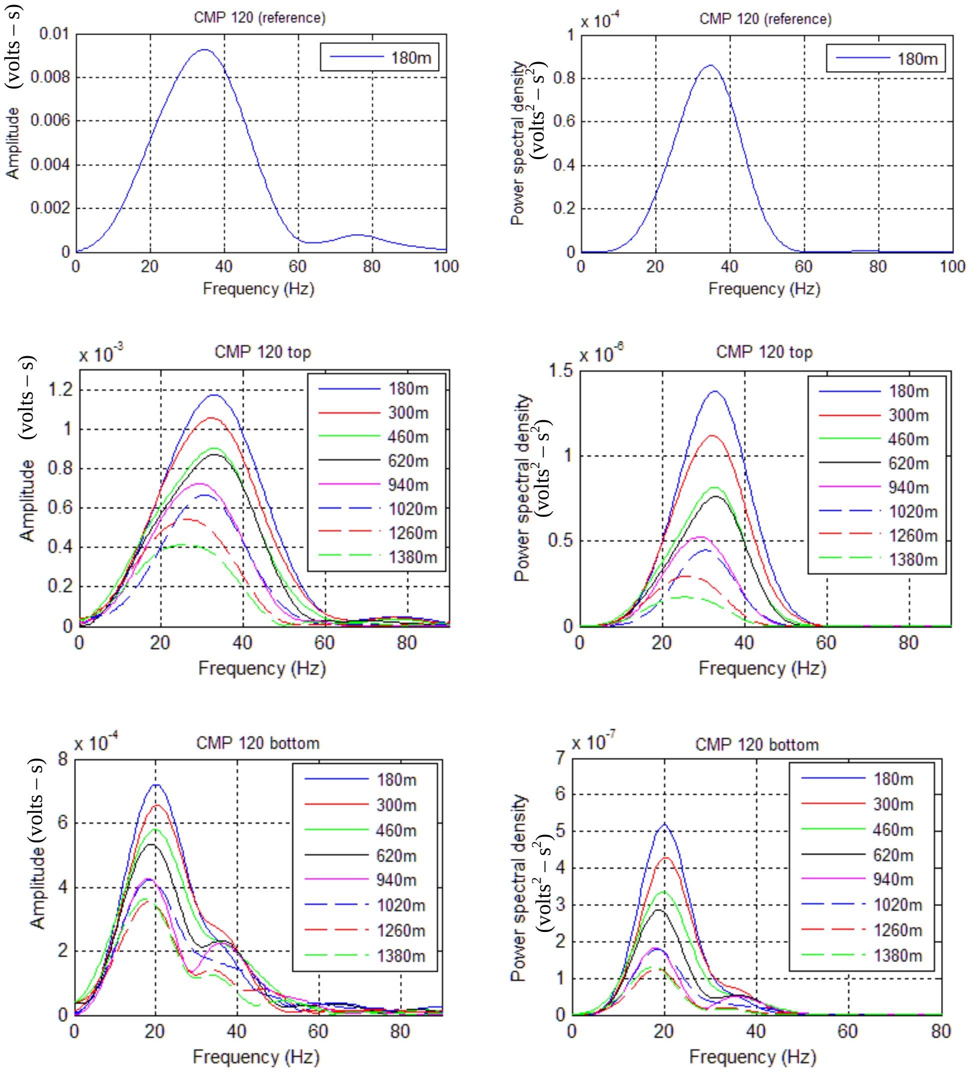

Figure 6.10: Sample spectra for CMP 120. There is a noticeable decrease in peak frequencies between the top and bottom reflections and also in the magnitude of the spectral.

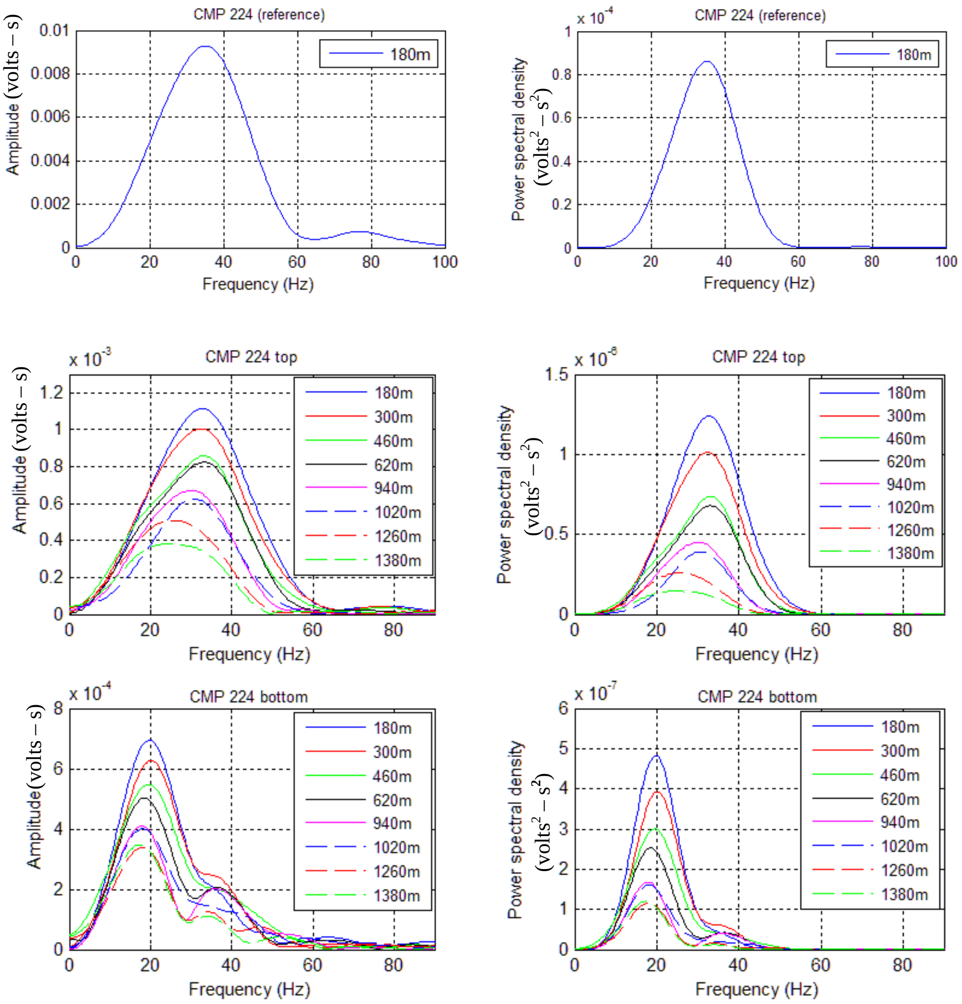

Figure 6.11: Sample spectra for CMP 224. There is a noticeable decrease in peak frequencies between the top and bottom reflections and also in the magnitude of the spectral power.

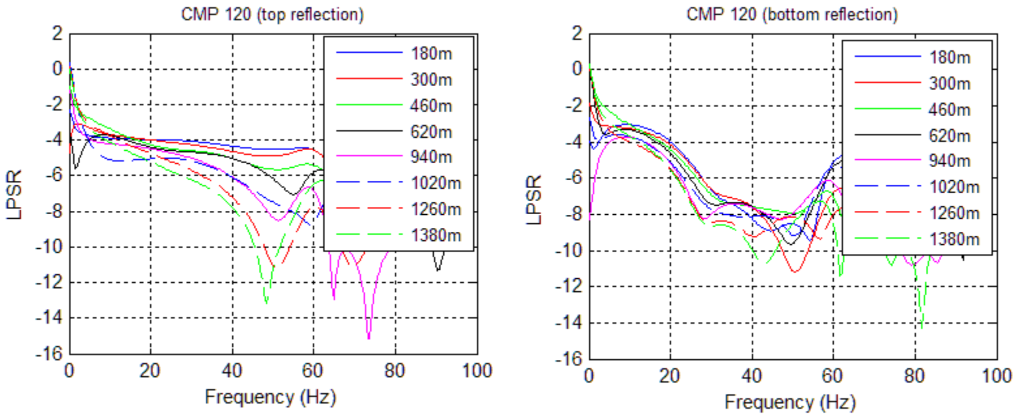

(a) (b)

Figure 6.12: Log Spectral Power Ratio (LSPR) against frequency plots (CMP 120). (a) Top fracture layer reflection. (b) Bottom fractured layer reflection.

Table 6.4: Sensitivity of the interval Q values in the fractured-layer to the regression bandwidth

Frequency bandwidth (Hz)	Interval Q (CMP 160)	Interval Q (CMP 260)
10 - 50	14.5	14.2
5 - 50	16.4	14.6
5 - 40	18.4	11.9
5 - 30	12.1	8.3
10 - 30	7.6	5.9
10 - 40	15.2	10.1

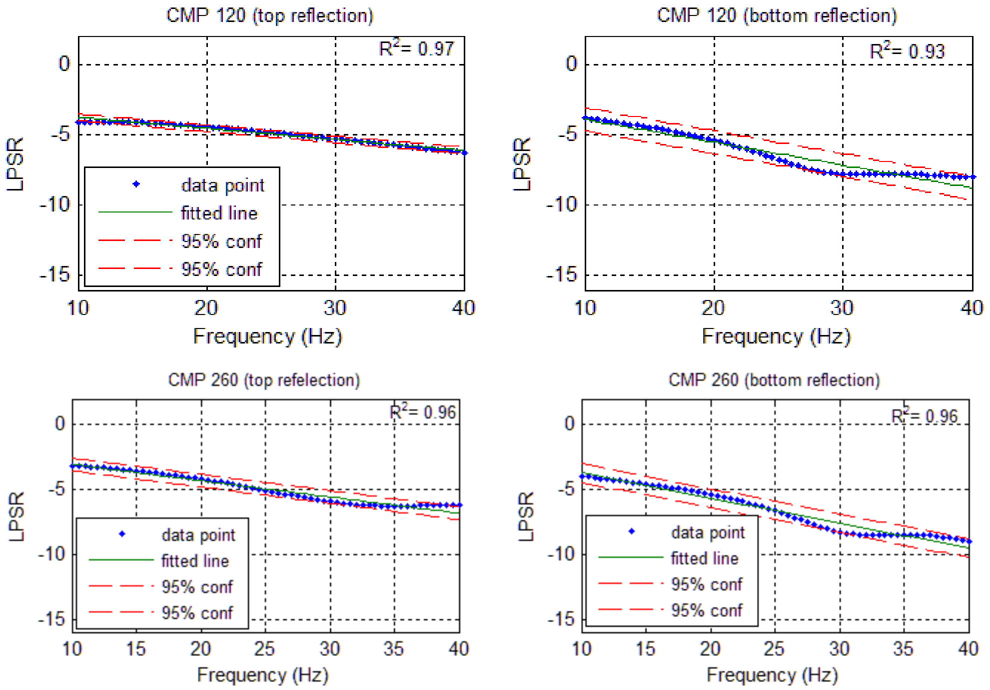

Figure 6.13: Linear regression of Log Spectral Power Ratios (LSPR) against frequency for selected CMP(s) at a fixed offset of 900 m. All the plots show good fits of the LSPR versus frequency within the bandwidths used and the confidence intervals indicated. The magnitude of the slope increases with chip's thickness, and are used as inputs to the second regression.

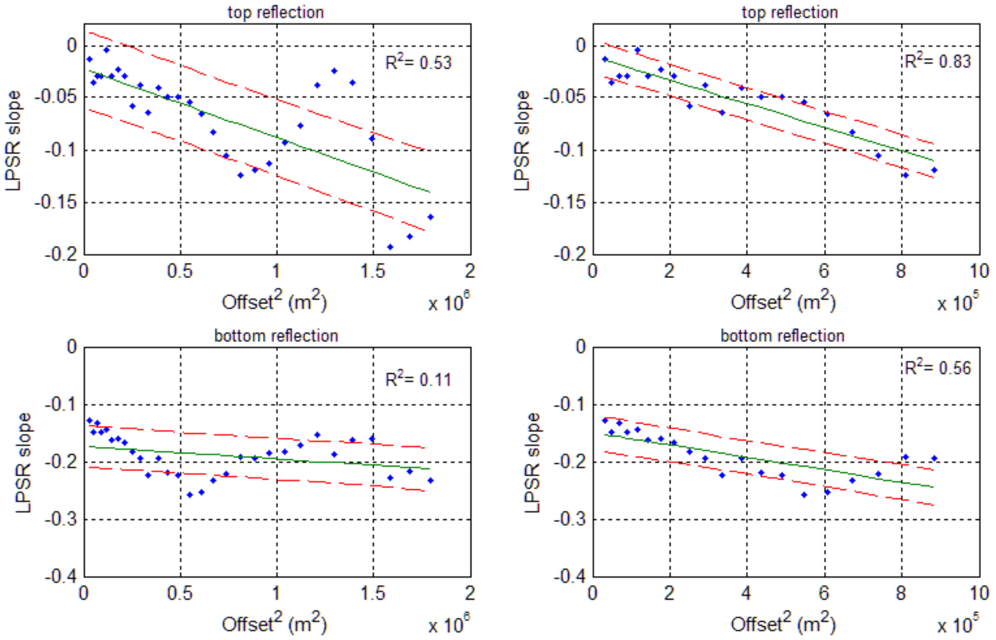

Figure 6.14: Linear regression of power ratio slopes against the square of offset (CMP 260). The LSPR slope intercept is used to compute Q down to the reflector. The plots are approximately linear up to an offset of 940 m. Thus, an offset range of 160 - 940 m was used for the final regression analysis. The asterisks indicate the data point, the green line indicate the fitted line while the red dashed lines indicate 95 % confidence interval on the fitted line

6.6 Results and analysis

The results of the attenuation analysis show that the magnitude of the log spectral ratio slopes varies with the thickness of the chips, indicative of a systematic dependence of the scattering attenuation on the thickness (which is meant to model the effect of aperture in an underground crack). Higher interval Q values are obtained for the CMPs at both ends of the survey line (below CMP 100 and beyond CMP 400) where there are no fractures (Figure 6.15). The Q values decrease systematically in the direction of increasing chips thickness from the left edge of block B1 (CMP 120) to the edge of block B6 (CMP 410), implying more scattering in the direction of increasing chips thickness. This trend is shown in Figure 6.16 for the CMP(s) corresponding to the centres of the fractured blocks respectively.

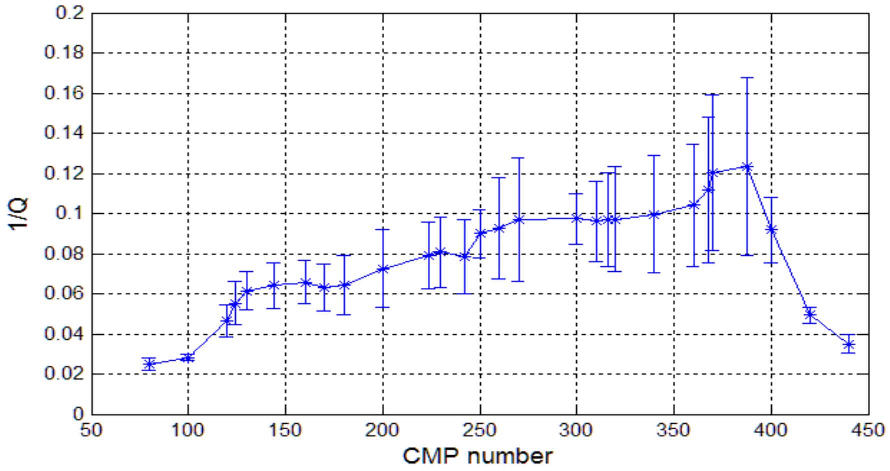

Figure 6.15: 1/Q results for the fracture blocks against CMP numbers: Fractured blocks lie between CMP(s) 120 and 410 respectively. There is a systematic increase in the induced attenuation (inverse Q) in the direction of increasing chips thickness from CMP 120 to CMP 410. However the attenuation is less at the ends of the line where there are no fractures.

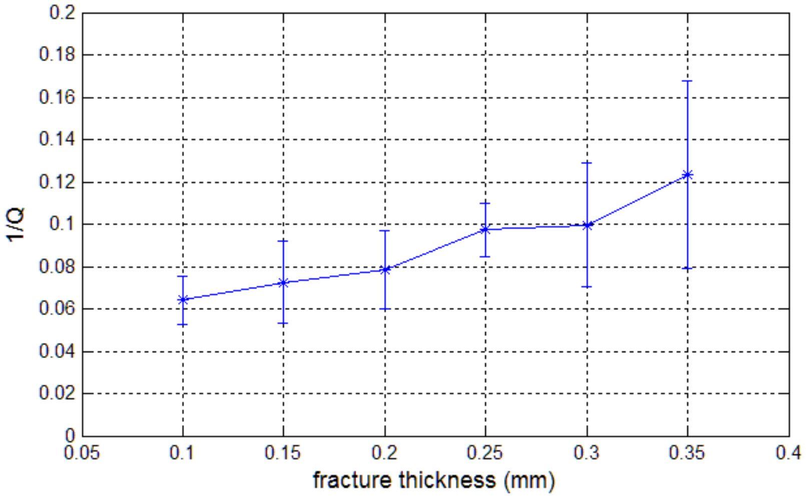

Figure 6.16: I/Q profile against chip's thickness. Q decreases with increasing chip's thickness, implying more attenuation.

6.7 Summary and conclusions

I have examined the effects of fracture thickness or aperture on P-wave reflected scattered energy through seismic physical modelling. A set of aligned fractures is known to greatly influence the propagation of seismic waves by causing scattering of the wave energy resulting in seismic coda trailing the primary reflection. The resultant effect is a gradual loss in the wave energy which can be observed in amplitude changes as the wave propagates through the medium.

In this chapter, I have quantified the scattering effects for a set of fracture models with the same density and radius but varying thicknesses through attenuation estimates. The results of the attenuation analysis reveal that P-wave attenuation has a direct relationship with fracture thickness. Attenuation (inverse Q) increases systematically and linearly with fracture thickness, implying proportionately more scattering of the wave energy as the wave propagates in the direction of increasing thickness. Although the simulated fractures may not be real fracture analogues in a typical fractured reservoir setting, the results provide information which might be useful in examining the effects of voids in the rock on P-wave attenuation and may provide a basis for further theoretical development to distinguish the effects caused by thin micro cracks and large open fractures.

Chapter 7 Finite-difference modelling of attenuation anisotropy in discrete fracture model

In this chapter, I carry out a finite-difference modelling study using the standard staggered-grid 3D finite-difference modelling scheme to examine the effects of scattering attenuation caused by a set of aligned vertical fractures. This complements the work described in Chapter 4, and allows a comparison of physical and numerical techniques for modelling layered anisotropic media. Although the finite-difference method can account for all kinds of waves, this chapter focuses only on the anisotropic scattering effects on the P-wave and how these effects relate to the fracture orientations.

7.1 Introduction

The wave equation can be solved numerically by the use of the finite-element method, the pseudo-spectral method or the finite-difference method. Each of these methods can account for all types of waves and complex sub-surface structures but have their own advantages and disadvantages (Graves, 1996). For example, the finite element method can handle irregular grids and boundaries but its computational process is complicated and time - consuming (Bansal and Sen, 2008; Hua *et al.*, 2009). The finite-difference method has the advantage of being very efficient and having high speed (Igel *et al.*, 1995; Hua *et al.*, 2009) and has been applied successfully to model seismic wave propagation in elastic media. Kelly *et al.*, (1976) generated synthetic seismic data using a finite-difference scheme in 2-D acoustic media. The staggered-grid finite-difference scheme was first introduced by Madariaga (1976) and later by Virieux (1984 and 1986) to simulate seismic wave propagation in 2-D elastic media using a velocity-stress formulation and has since become very popular in modelling seismic wave propagation (e.g. Moczo *et al.*, 2000). Several attempts have been made to extend the existing 2-D finite difference algorithms to 3-D elastic media which have been successful especially because of advances in computer technology (e.g. Igel *et al.*, 1995; Graves, 1996; Moczo *et al.*, 2000; Willis *et al.*, 2006; Bansal and Sen., 2008).

The main aim of this chapter is to compare the seismic results of the physical model described in Chapter 4 with a numerical model based on the finite-difference technique. The physical model results are used as means of validating the results of the numerical model, which can then be applied to other situations with more confidence. In this chapter, I make use of the generic 3-D anisotropic elastic finite-difference code developed by Xu *et al.*, (2010) to model the propagation of seismic waves through layered anisotropic media. Specifically, I used a simplified fractured reservoir model with four horizontal layers based on the physical model of Fig 4.2a. The code makes use of a standard staggered-grid with an explicit 8th-order operator in space and 2nd - order operator in time to solve the first-order wave equations expressed in terms of velocity and stress. The fractures were represented by grid cells containing equivalent anisotropic medium using the equivalent medium theory of Coates and Schoenberg (1995). I extracted 2-D section from the 3-D cube in four azimuths relative to the fracture strike direction and computed the Q values in the anisotropic layer using the QVO-spectral ratio method discussed in section 3.3. I start the chapter by giving a brief description of the implementation of the finite-difference scheme in a model with discrete fracture set.

7.2 Finite-difference modelling of discrete fracture sets

The linear slip model of Schoenberg (1980) can be used to model a single fracture as a non-welded interface across which traction is continuous while displacement is not (Coates and Schoenberg, 1995; Schoenberg and Sayers, 1995). The interface has a negligible thickness compared with the seismic wavelength. With the introduction of the linear slip deformation into an elastic medium, the resulting effective stiffness tensor is expressed as the reciprocal of the sum of the background compliance of the host unfractured medium and the compliance of the fractures (Equations (2.42) and (2.43)). The fracture compliance is made up of two independent elements which are the normal fracture compliance S_N and the tangential fracture compliance S_T respectively. These elements are dependent on the infill of the fractures. I used this approach in this chapter to model anisotropic seismic wave propagation in a four-layered theoretical model. Xu *et al.*, (2010) used the same approach to model the propagation of seismic wave in a medium with aligned vertical fractures to investigate the influence of fracture cell spacing on the resulting wavefield and found that the magnitude of the P-wave anisotropy increased systematically with decreasing fracture cell spacing while the degree of scattering in the wave energy weakens with fracture cell spacing.

7.2.1 Velocity - stress formulation in anisotropic media

The strain-stress relationship for a linear elastic and anisotropic medium can be expressed by the generalized Hooke's law as:

$$\sigma_{ij} = c_{ijkl}\varepsilon_{kl} \tag{7.1}$$

From the equations of Newton's second law, the elastodynamic wave equation which relates stiffness to displacement can be written in the form (in the presence of body forces (f_i) :

$$\rho \frac{\partial^2 \mathrm{u_i}(\mathrm{x},\mathrm{t})}{\partial \mathrm{t}^2} = \frac{\partial \sigma_{\mathrm{ij}}}{\partial \mathrm{x_j}} + f_{\mathrm{i}}\, , \tag{7.2}$$

where ρ is density. Substituting for stress from Equation (7.1) and re-arranging gives the wave equation as:

$$\rho \frac{\partial^2 \mathrm{u}_\mathrm{i}(\mathrm{x},\mathrm{t})}{\partial \mathrm{t}^2} = \frac{\partial}{\partial \mathrm{x}_\mathrm{j}}\left[\mathrm{c}_\mathrm{ijkl}(\mathrm{x})\varepsilon_\mathrm{kl}(\mathrm{x},\mathrm{t})\right] + f_\mathrm{i}\,, \tag{7.3}$$

where u_i is the i^th^ component of the displacement and t is time. Combining Equation 7.3 with the definition of the strain tensor (Equation (2.6)) gives the general wave equation for a 3D inhomogeneous anisotropic media as:

$$\rho \frac{\partial v_i(x,t)}{\partial t} = \frac{\partial}{\partial x_j}\left[c_{ijkl}(x,t)\frac{\partial u_{k(x,t)}}{\partial x_l}\right] + f_i\,, \tag{7.4}$$

where v_i is particle velocity. Also, by differentiating Equation (7.1) with respect to time and noting the expression for the strain tensor in Equation (2.6), we can write:

$$\frac{\partial \sigma_{ij}}{\partial t} = c_{ijkl}\frac{\partial}{\partial x_l} v_{kl} \tag{7.5}$$

Equations (7.4) and (7.5) constitute the first-order linear partial differential velocity-stress equations for a general inhomogeneous anisotropic media. These equations can be solved using finite-difference schemes. Taylor’s expansion is used to perform temporal and spatial derivatives of the quantities in the equations and any order of Taylor series expansion can be performed. However, more accurate results can be obtained with higher-order Taylor series in time and space (Marfurt, 1984) but at the cost of high computational expense (Bansal and Sen, 2008).

7.2.2 Staggered-grid finite-difference implementation

In order to solve Equations (7.4) and (7.5) using finite-difference modelling, all the quantities must first be discretized. A common discritization method is the use of the standard staggered grid (SSG) scheme (Madariaga 1976; Virieux, 1984 and 1986) which has the advantage of having the differential operators centred at the same point in space and time, enabling the calculation of the spatial derivatives at half the grid size (Graves, 1996; Bansal and Sen, 2008).

The different components of the stress tensor and the velocities have to be defined at different locations on the grids. The staggered grid mesh and the locations where the components have to be defined are illustrated in Figure 7.1 with four grids overlapping each other for the 2-D case. The locations where the density and other elements of the stiffness tensor have to be defined are also indicated in the figure. The stiffness tensor and the diagonal elements of the stress tensor are defined at the corner of the cell while the off-diagonal element of the stress tensor is defined at a different location (Figure 7.1). This necessitates the interpolation of some of the elements of the stiffness tensor. In the same manner, the buoyancy b (inverse of density) also has to be interpolated since it is not defined at the same location as the components of the particle velocity. In the 3-D case, the stress, stiffness and velocity components have to be defined at seven different locations (Igel *et al.*, 1995) and as in the 2-D case, some of the elements of the stiffness tensor and the buoyancy also have to be interpolated to the locations where they are required.

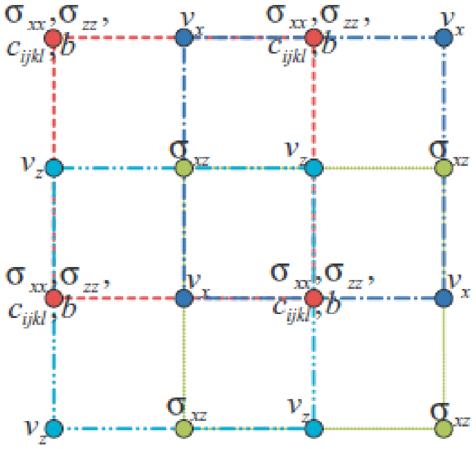

Figure 7.1: Staggered grid scheme discritization in 2-D (from Bansal and Sen, 2008). Four grids are staggered to each other and the locations of the medium parameters are shown on the staggered grid mesh.

7.2.3 Theoretical model and experimental set-up

The theoretical model consists of four isotropic horizontal layers (Figure 7.2). To simulate a fractured reservoir model, a set of aligned vertical fractures was introduced into the third layer using the method of Coates and Schoenberg (1995).

Details of the model parameters are given in Table 7.1. The fractures are represented by grid cells each of size 10 m x 10 m x 10 m and the entire model was divided into 300 x 300 x 300 grids. The thickness of each fracture cell is equivalent to the length of a single grid cell (10 m) and the fracture spacing is regarded as the distance from one vertical fracture cell to the next vertical fracture cell. I made the same assumption as in Vlastos *et al.*, (2003) that the normal and tangential fracture compliances are the same and have a value of $5.6\text{x}10^{-10}$ mPa^{-1} and computed the synthetic data from the model with a fracture cell spacing of 120 m. The values of the fracture compliance assumed may not conform to the compliances of the physical models because it is hard to reproduce natural conditions exactly given the difficulties of making the models in the first place. Lubbe and Worthington (2006) have argued that the values of the fracture compliance used by Vlastos *et al*., (2003) are relatively high and maintained that for numerical modelling to be of practical use, it is essential to obtain the required values of the fracture compliance from field measurements which might be a difficult task. Nevertheless, the tangential and normal compliance ratio of unity assumed in the numerical modelling is indicative of the case of dry fractures (e.g. Liu *et al*., 2000).

A Ricker wavelet with a centre frequency of 20 Hz was used as the source wavelet and the source was located on the surface of the model at (x = 500 m, y = 1500 m and z = 0). The P-wave length in the fractured layer is 131 m, making the ratio of the fracture cell spacing to the seismic wavelength approximately 0.9. The receivers were spread out in the x- and y- directions at a fixed spacing of 10 m in each direction as illustrated in Figure 7.2. Data were recorded with a sampling rate of 1ms and a total time of 3 s. I extracted a 2-D section from the 3-D cube in four azimuthal angles (0°, 26°, 45° and 90°) relative to the fracture strike direction which is the 0^{o} azimuth.

The reflections from the model boundaries are considered as undesirable waves in the final recorded synthetic data and therefore need to be suppressed or removed. To this end, the edges of the model were set to be absorbing boundaries by applying an exponential decaying function of the form given by (Cerjan, *et al.*, 1985) at the limited boundary layers of the model to attenuate the energy at the boundary of the model. The FD modelling code is parallel-programmed with the library OpenMp which allows the use of CPU cores in a single PC to compute one or more shot gathers (Xu, 2011). The computation in this thesis was done on a PC Linux cluster using the Sun Grid Engine (SGE) job dispatch system and it took approximately 8 hours with a single CPU core.

Figure 7.4 shows the synthetic data in the four azimuths. The red arrow indicates direct waves, the blue arrow indicate the reflection from the top of the second layer while the green and yellow arrows indicate reflections from the top and bottom of the fractured-layer respectively. The pink arrow indicates the P-S converted wave from the top of the fractured-layer. Scattering effects caused by the aligned fractures are noticeable in the four gathers below the reflection from the top of the fractured-layer (green arrow). My aim is to analyze the reflected waves from the top and bottom of the fractured-layer (labelled HTI in yellow in Fig 7.2) to quantify these scattering effects through attenuation estimates in the four azimuthal gathers to see how these relate to the fracture orientations. The results of the seismic physical modelling study of Chapter 4 show that the scattered energy exhibits anisotropic behaviour which can be linked with the fracture properties.

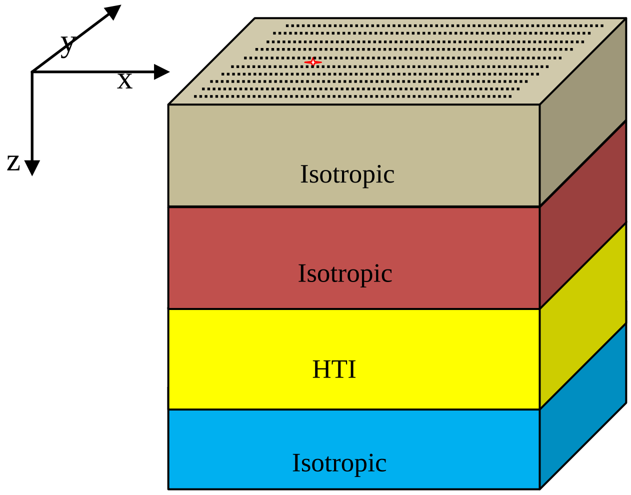

Figure 7.2: Geometry of the theoretical model. The third layer constitutes the anisotropic layer with vertical aligned fractures. The fractures in layer 3 produce a horizontally transverse isotropic medium with a fast wave direction parallel to the z-axis. The source (red star) was located on the surface of the model at (x = 500 m, y = 1500 m and z = 0) while the receivers were spread out in the x- and y-directions at a spacing of 10 m in each direction along the black dotted lines.

Table 7.1: Theoretical model parameters for studying the effects of discrete fractures

Layer	v_p (m/s)	v_s (m/s)	ρ (kg/m^3)	Thickness (m)
1	1500	100	1000	400
2	2314	1100	1150	800
3	2610	1300	1750	800
4	3100	1800	2200	Half-space

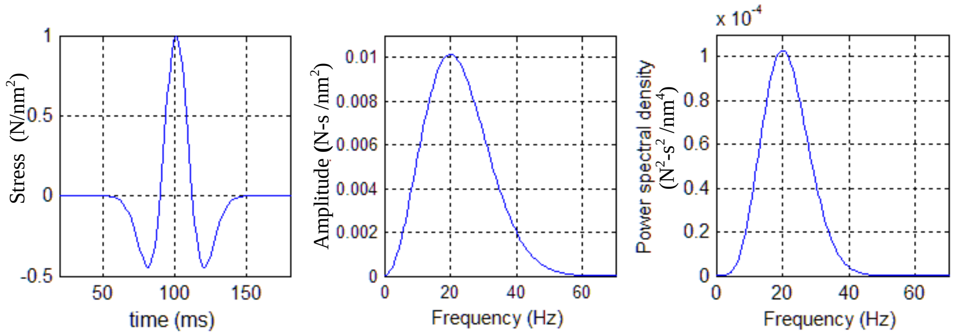

(a). (b). (c).

Figure 7.3: Ricker wavelet used as source wavelet (a) time series (b) amplitude spectrum (c) power spectrum. The centre frequency is 25 Hz.

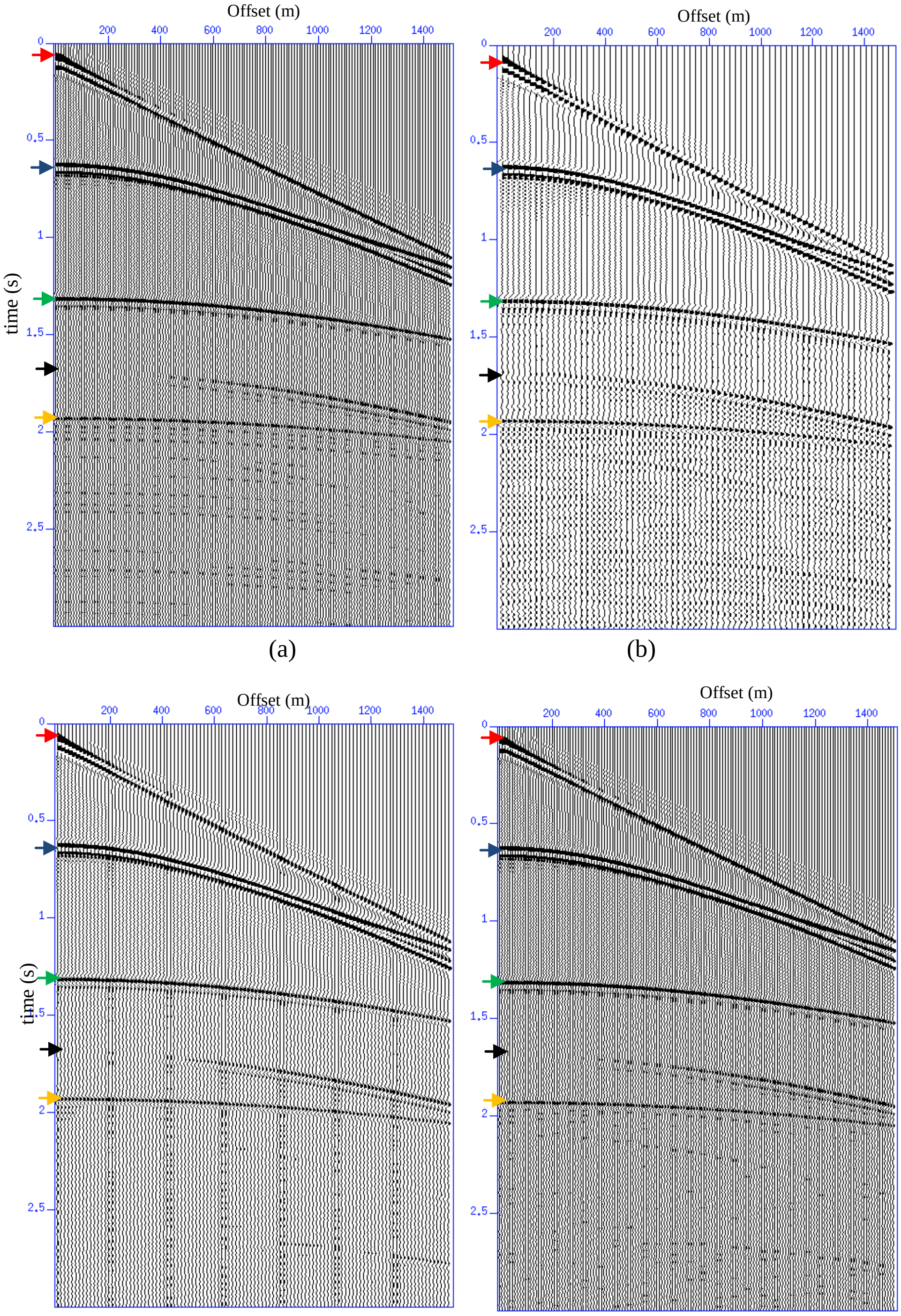

(a) (b)

(c) (d)

Figure 7.4: 2-D gather extracted from the 3-D cube at (a) 0° azimuth (b) 26° azimuth (c) 45° azimuth (d) 90° azimuth. The red arrow indicates direct waves, the blue arrow indicate the reflection from the top of the second layer while the green and yellow arrows indicate reflections from the top and bottom of the fractured-layer respectively. The black arrow indicates P-S converted wave from the top of the fractured-layer.

7.3 Q estimation

I made use of the same procedure as in section 5.2 to compute the interval Q values in the fractured-layer for the four azimuthal synthetic gathers. The first trace from the top model reflection at 0 m offset and 0° azimuth was used as the reference for comparison of the spectral ratios (Figure 7.5). The reference trace pulse shape is proportional to the time derivative of the input Ricker wavelet. Thus, the peak frequency of the reference trace is higher than that of the input Ricker wavelet as predicted by Equation (3.27). The power spectra of the reflection events from the top and bottom of the anisotropic layer and their ratios to that of the reference event were computed according to Equation (4.1). Sample power spectral plots are shown in Figures 7.6 and 7.7 for selected offsets for the top and bottom of the fractured-layer respectively. The simulated fractures cause scattering which results in seismic coda behind the primary reflection. Figure 7.8 shows the effect of the coda on the spectra if included in the analysis window. The coda causes scattering in the peak frequency of the wavelet and changes in the amplitude. I selected the window in such a way that the seismic coda was not included in analysis window. Sample plots of the LPSR against frequency for selected offsets for the top and bottom of the fractured-layer are shown in Figures 7.9 and 7.10 respectively. I used a constant window length of 160 ms and frequency bandwidth of 5 - 30 Hz for linear regression of the spectral ratios. This frequency bandwidth is common to all the reflections analyzed and also lies within the signal bandwidth. Sample linear regression plots of the LPSR against frequency for the chosen bandwidth are shown in Figures 7.11 and 7.12 for the top and bottom fractured-layer reflections respectively with their corresponding R^2 values.

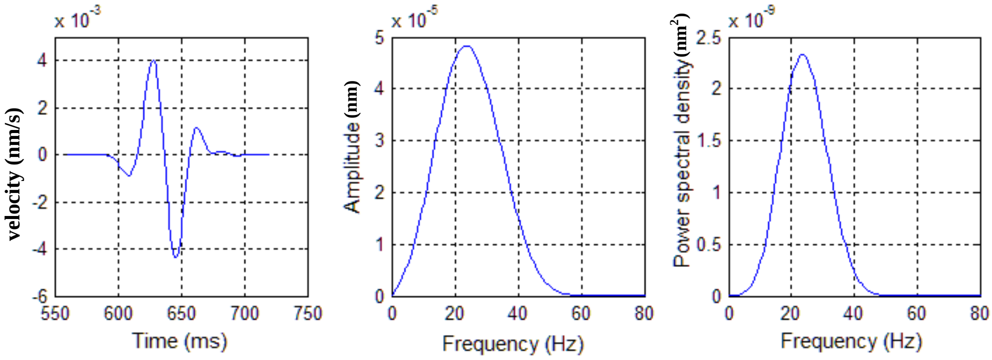

(a) (b)

Figure 7.5: Reference event - first trace reflection from top of model at 0 m (a) time series with window length of 140 ms (b) Power spectrum

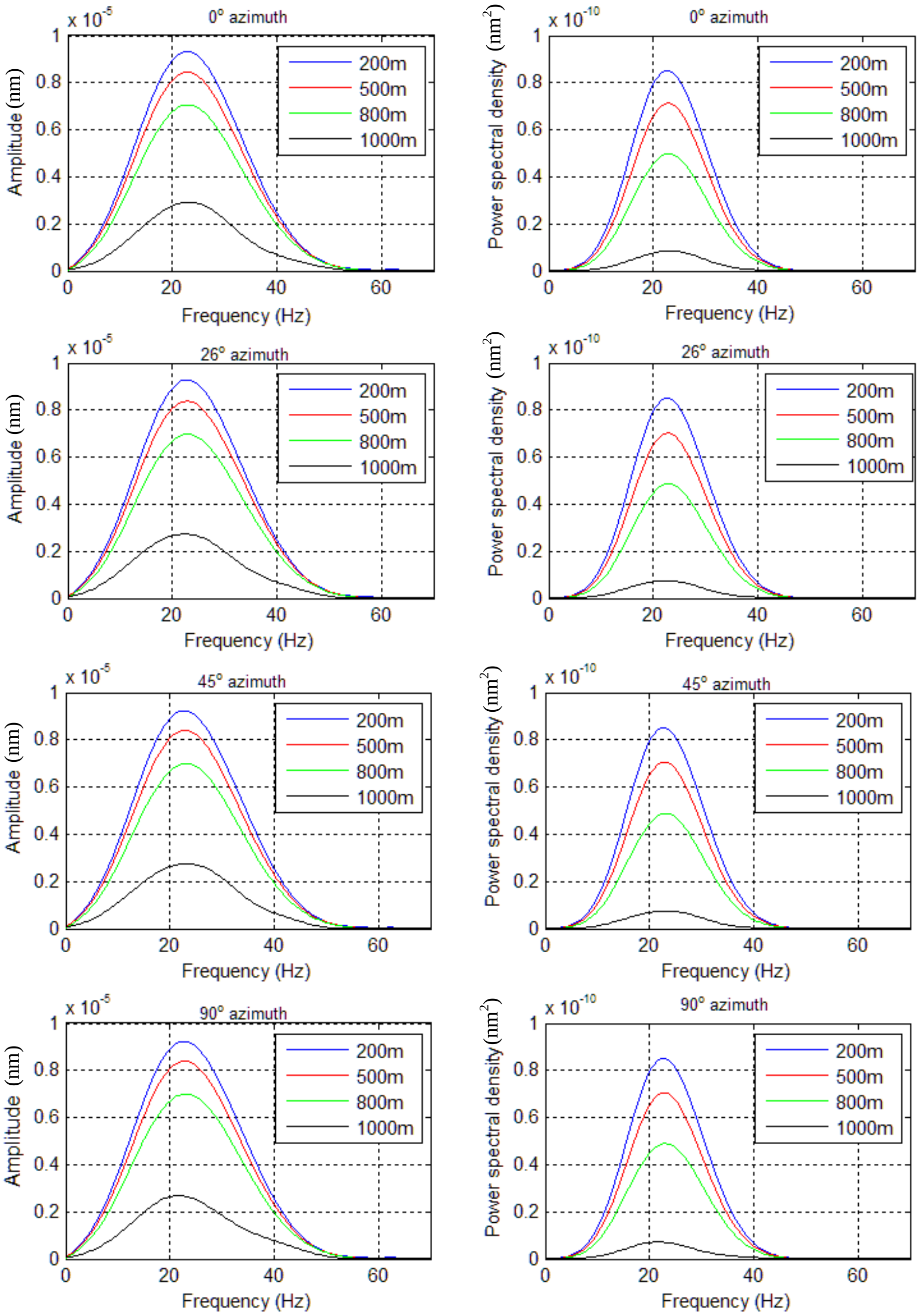

Figure 7.6: Sample spectra for top fractured-layer reflection for selected offsets. The inserted legend indicates the various offsets.

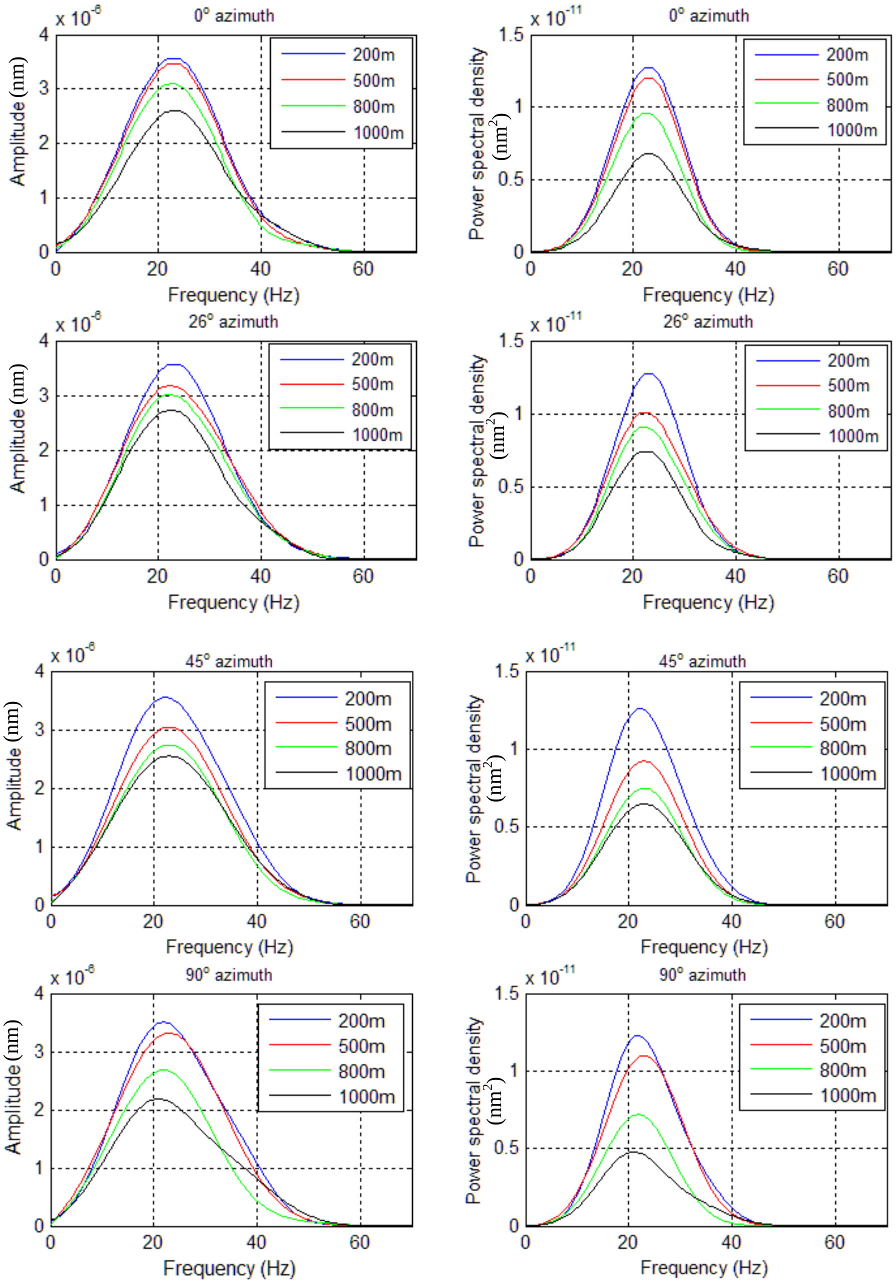

Figure 7.7: Sample spectra for bottom fractured-layer reflected for selected offsets. The inserted legend indicates the various offsets

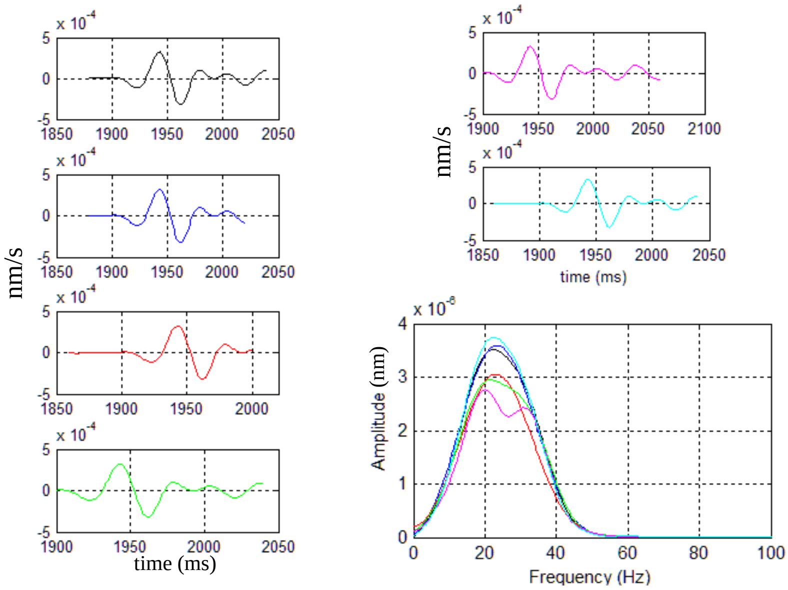

Figure 7.8: Effect of windowing on the peak frequencies and amplitude. The simulated fractures cause scattering which results in seismic coda behind the primary reflection. The coda causes scattering in the peak frequency of the wavelet and changes in the amplitude.

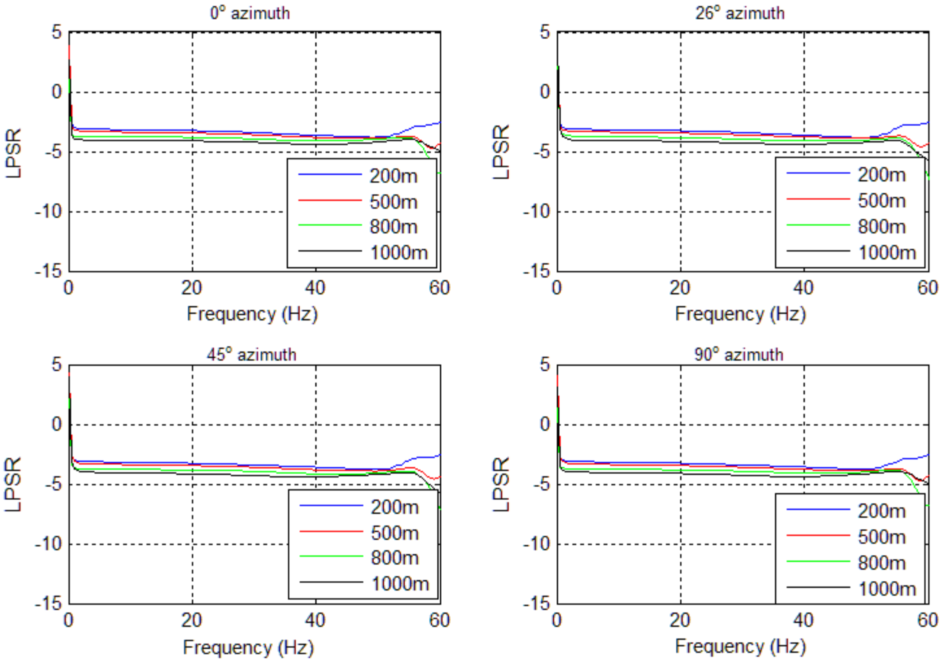

Figure 7.9: Log Power Spectral Ratio (LPSR) against frequency plots for the top fractured-layer reflection. The inserted legend indicates the various offsets.

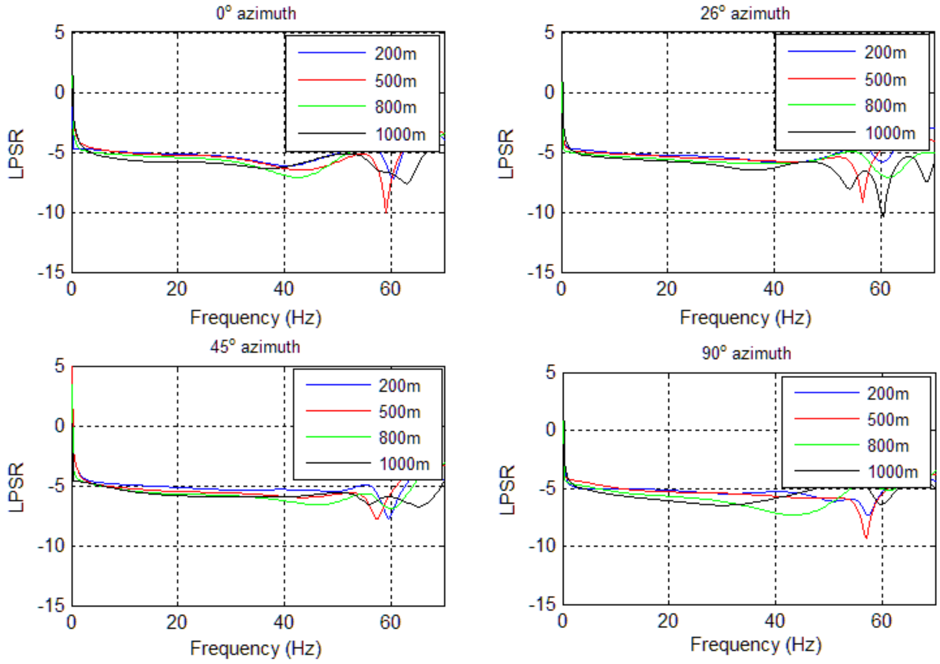

Figure 7.10: Log Power Spectral Ratio (LPSR) against frequency plots for the bottom fractured-layer reflection. The inserted legend indicates the various offsets.

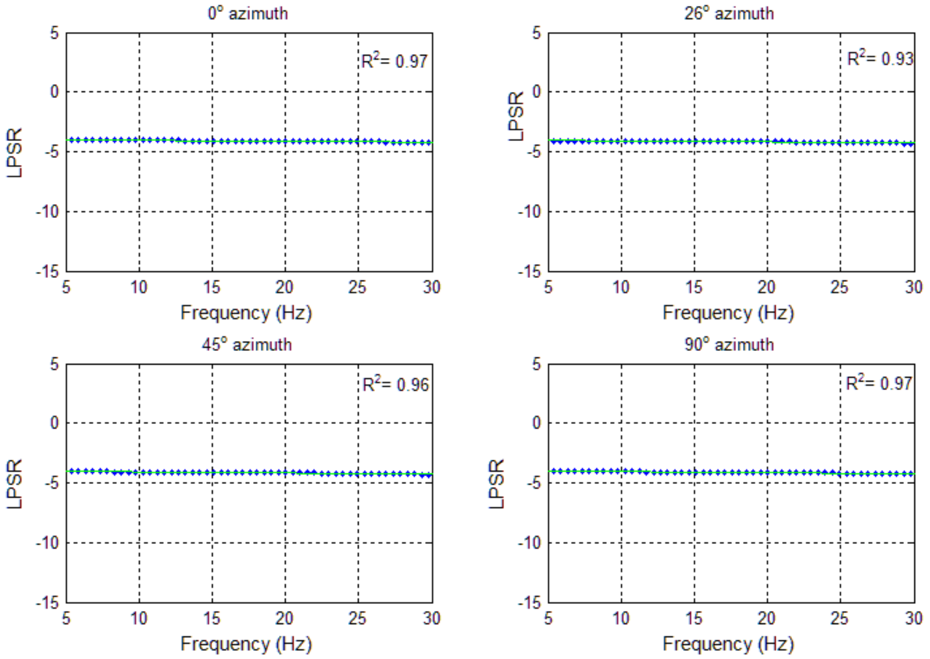

Figure 7.11: Sample LPSR plots against frequency for at a fixed offset of 1000 m for top fractured-layer reflection. The blue asterisks indicate the data points while the green line indicates the fitted line.

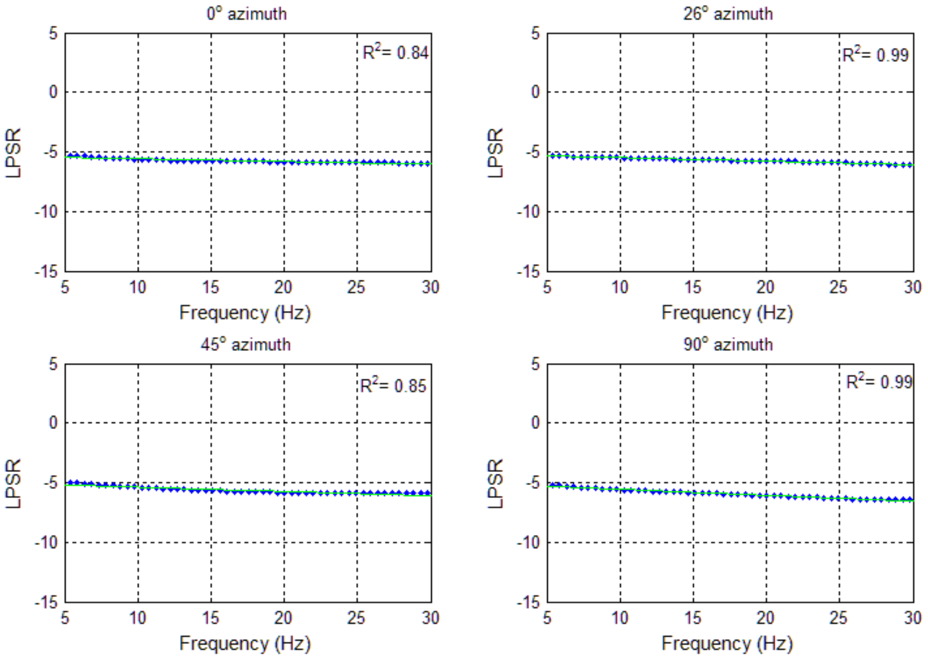

Figure 7.12: Sample LPSR plots against frequency at a fixed offset of 1000 m for bottom fractured-layer reflection. The blue asterisks indicate the data points while the green line indicates the fitted line.

7.4 Results and analysis of results

The induced attenuation measured from the results of section 7.3 is observed to increase both with increasing offset and angle away from the fracture strike direction (Figure 7.13). Maximum attenuation occurs in the direction normal to the fracture strikes. The azimuthal variations in the induced attenuation are elliptical (Figure 7.14). For any given azimuth angle θ measured from the North direction (y-axis), the distance from the centre of the ellipse to the surface corresponds to the Q value for that azimuth. The major axis of the ellipse corresponds to the fracture strike where attenuation is a minimum, while the minor axis corresponds to the fracture normal where attenuation is a maximum. However, a minimum of 200 m offset corresponding to an offset depth ratio of 0.2 to the top of the fractured-layer and 0.1 to the bottom of the fractured-layer respectively is required for the azimuthal variations in the induced attenuation to occur. Such plots, which are analogous to slowness surfaces, are a convenient graphic representation of attenuation anisotropy.

The observed attenuation anisotropy is also well fitted by a ‘cos2θ’ function (Figure 7.15), where θ is azimuthal angle and the result of the fitting shows that attenuation is maximum normal to the fracture strikes which is consistent with the results of the ellipse fitting. The magnitude of the anisotropy also increases with offset (Figure 7.16).

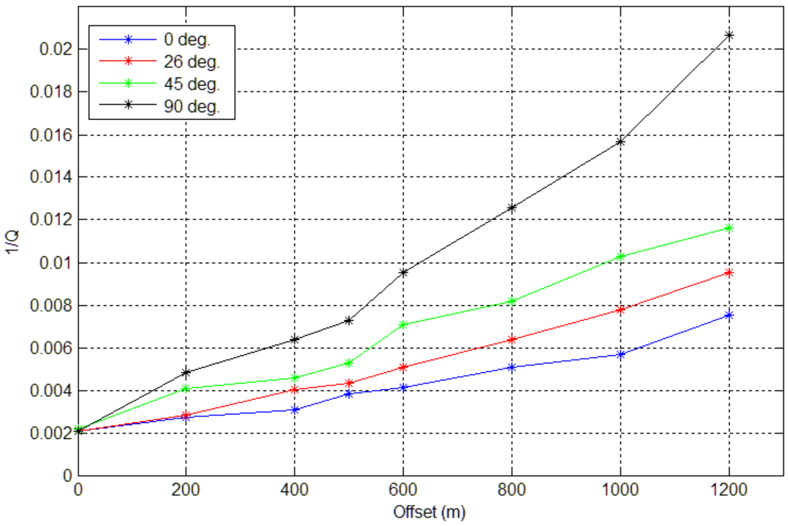

Figure 7.13: Q profiles against offsets. There is a systematic increase in attenuation with increasing offsets. No significant change of attenuation with offsets occurs in the fracture strike azimuth.

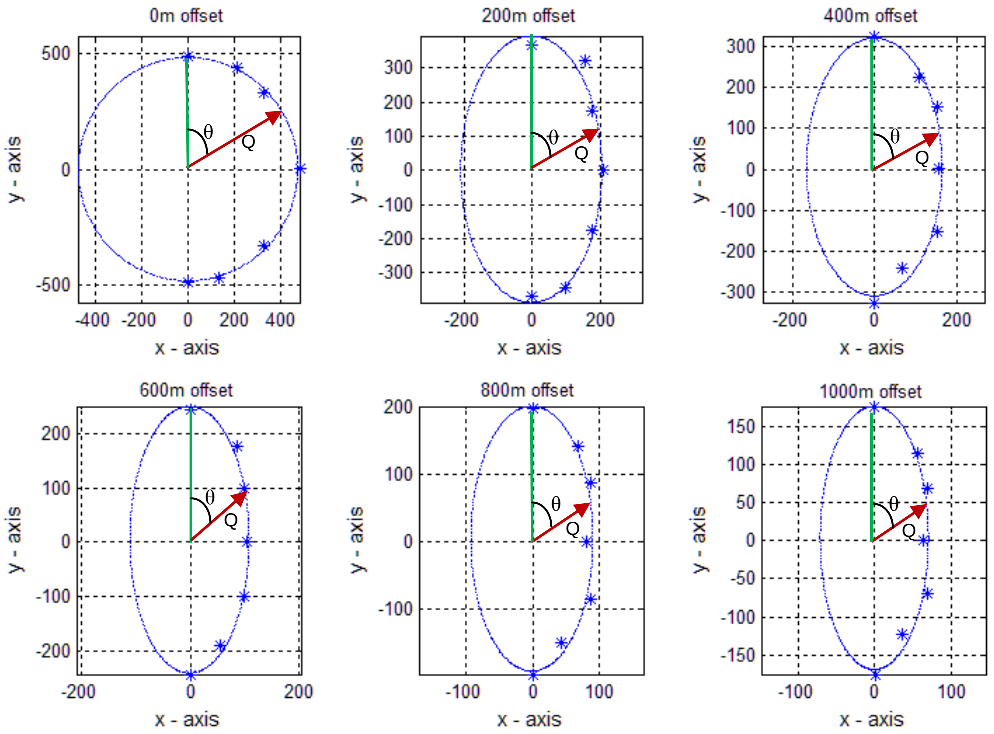

Figure 7.14: Q anisotropy ellipse. The ellipse has a centre at (0, 0) and the distance from the centre of the ellipse to the surface (red arrow) at any given azimuth angle θ measured from the North direction (y-axis), corresponds to the Q value for that azimuth. Azimuthal variations in Q values are elliptical and the magnitude of the anisotropy increases with offset. The major axis of the ellipse corresponds to fracture strike while the minor axis corresponds to the fracture normal. No variations occur at 0m offset.

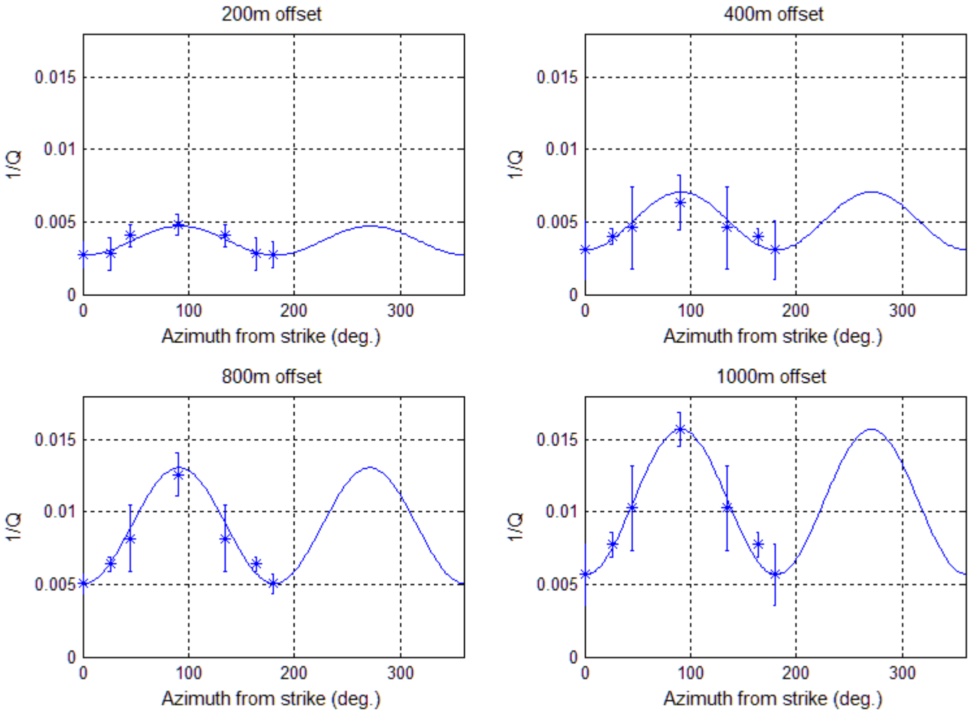

Figure 7.15: Cosine fit of estimated 1/Q values against azimuth for selected offsets. The amplitude of the attenuation anisotropy increases with offsets. Maximum attenuation occurs 90° from the fracture strike direction.

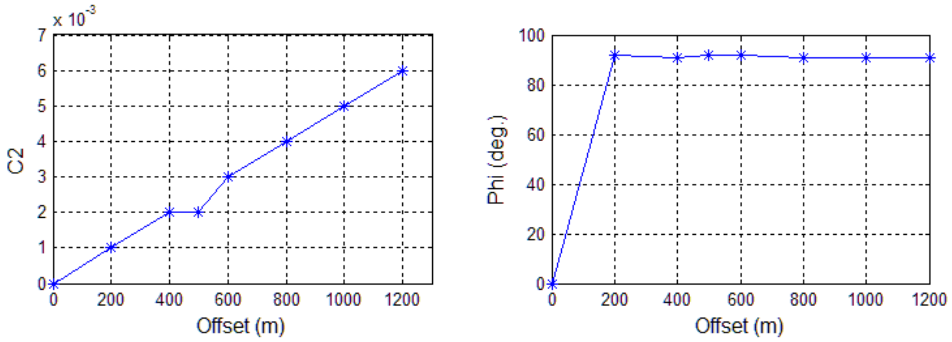

(a) (b)

Figure 7.16: Inverted parameters from cosine fits of 1/Q results (a) C2. The degree of anisotropy increases with offsets (b) Angle of minimum Q (maximum attenuation) - 90° from strike direction corresponding to fracture normal and a minimum of 200 m offset is required for the azimuthal anisotropy to occur.

Compared with the physical modelling results of chapter 4, the results of the finite difference modelling study also demonstrate that a population of aligned fractures with scale length on the order of the seismic wavelength causes scattering which results in attenuation. The comparison of the results of the two approaches is illustrated in Figures 7.17 and 7.18. There are some differences in the results for the two cases. Firstly, the average magnitude of the attenuation anisotropy in the numerical model is 0.02 % (Figure 7.17 right) which is much smaller than the 2.6 % in the case of the physical model (Figure 7.17 left). This may indicate that the tractions and the fracture compliances assumed in the numerical model are lower than those used in the physical one, likely due to the way the physical model is manufactured and the differences in materials used. Secondly, the errors in Q estimates in the physical model are slightly bigger than those from the numerical model, though this would be expected with real data. In both cases, the scattering attenuation is anisotropic, with a characteristic elliptical variation with azimuth. The amount of scattering is more in the fracture normal direction than in the fracture strike direction. Also, the fracture orientations are inferred from the axes of the Q ellipse in both cases (Figure 7.14). On the whole, the good agreement of the two results within error limits provides a significant validation for the numerical model.

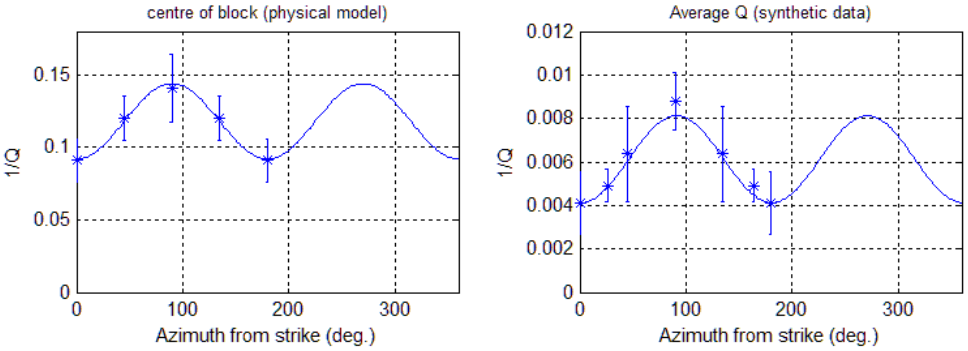

Figure 7.17: Comparison of the cosine fitting results of the physical and finite difference results. Maximum attenuation occurs 90° from the fracture strike direction in both cases. The magnitude of anisotropy is greater in the physical modelling case than in the finite difference modelling case.

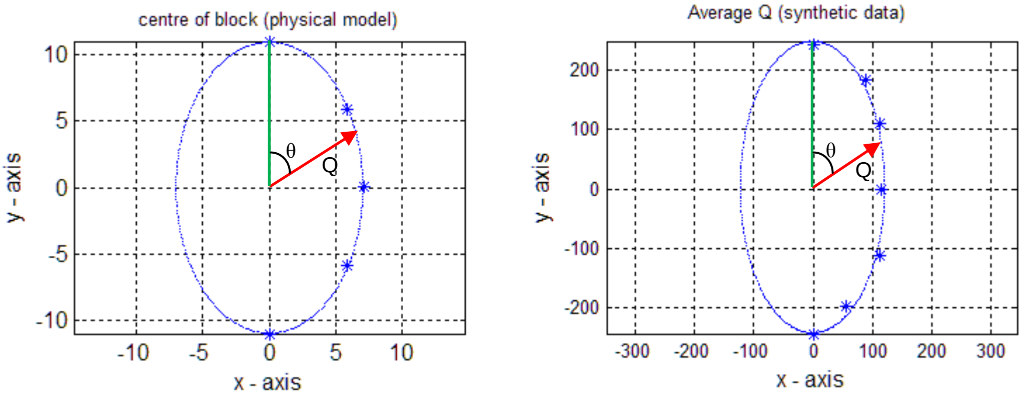

(a) (b)

Figure 7.18: Comparison of the ellipse fitting results of the physical and finite difference results. (a) Q anisotropy result for the physical model in chapter 4. (b) Q anisotropy (averaged) result from finite difference modelling. The ellipse has a centre at (0, 0) and the distance from the centre of the ellipse to the surface (red arrow) at any given azimuth angle θ measured from the North direction (y-axis), corresponds to the Q value for that azimuth. The major axis of the ellipse corresponds to fracture strike while the minor axis corresponds to the fracture normal in both cases.

7.5 Summary and conclusions

In this chapter I have carried out a numerical modelling study of anisotropic wave propagation in fractured media using a 3-D finite-difference technique. The fracture model is simulated by using the linear slip deformation model of Schoenberg (1980). A set of aligned fractures results in scattering of the seismic wavefield which exhibits anisotropic behaviour.

I have quantified the scattered energy through attenuation estimates using the QVO-spectral ratio method in four azimuthal angles relative to the fracture strike direction. The induced attenuation caused by the scattering from the fractures (averaged over the frequency range used) is observed to increase both with increasing offset and azimuth away from the fracture strike direction. The observed anisotropy in the P-wave attenuation is elliptical and the fracture orientations are obtained quite accurately from the axes of the ellipse. The major axis of the Q ellipse corresponds to the fracture strike while the minor axis corresponds to the fracture normal. The observed attenuation anisotropy is also well fitted by a $\cos 2\theta$ function, giving the angle of maximum attenuation normal to the fracture strikes showing a good agreement with the results of the ellipse fitting. A minimum offset of 200 m corresponding to an offset-depth ratio of 0.2 and 0.1 respectively to the top and bottom of the fractured-layer is however required to reveal the anisotropy. The magnitude of the observed attenuation anisotropy is found to be dependent on offset; increasing with offset up to a maximum of 0.6 % at 1200 m offset.

These results are consistent with those of the physical modelling study of Chapter 4 in the sense that fractures cause scattering, resulting in attenuation. The attenuation exhibits a characteristic elliptical variation with azimuth away from the fracture strike direction, allowing the fracture orientations to be obtained from the axes of the ellipse. Also, the azimuthal variations in the attenuation are well fitted with a $\cos 2\theta$ function. However, there are some differences in the two cases. Firstly, the errors in Q estimates in the physical model are slightly bigger, though this would be expected with real data. More significant is the observation that the absolute magnitude of the attenuation anisotropy in the numerical model is smaller than the data from the actual physical model imply. This may indicate the tractions and the fracture compliances assumed in the numerical model are lower than those used in the physical one, likely due to the way the physical model is manufactured and the differences in materials used. The good agreement within error provides a significant validation for the numerical model, but would not have been possible unless the physical model had not also been constructed as a good quality reproduction of its design as a reasonable representation of an aligned fracture set in a layered medium. Overall, the results confirm the practical utility of using attenuation anisotropy as a useful diagnostic tool for delineation of fractures from seismic data, in a way that complements the use of other seismic attributes, at least for the relatively simple geometries of subsurface structure investigated here.

Chapter 8 Synthetic modelling study of the effects of CO_2 on seismic attenuation

The presence of CO_2 in the reservoir can result in changes in seismic properties such as travel time, velocity, amplitude and attenuation. Therefore such changes can provide useful information for the characterization the reservoir. In this chapter, I extend the work I did in Chapter 5 to examine the effects of two types of pore fluid (brine and CO_2 in the supercritical state) saturation on P-wave attenuation, at different levels of saturation, with particular focus on the effects of CO_2. Firstly, I examine the effects of mobility and then saturation on the induced attenuation, to compare the results with those for dry rocks. I finally take a look at a real field data example from the Sleipner gas field in the North Sea to see if the results of the synthetic studies can provide a guide for the interpretation of the field case.

8.1 Introduction

CO_2 is a natural constituent of hydrocarbon reservoirs with saturations varying from 2 - 80 % (Roberts, 2009). It is also often deliberately injected into hydrocarbon reservoirs to enhance production rates and sweep efficiencies, and in future will be deliberately stored in subsurface reservoirs and saline aquifers as a means of mitigating climate change from the burning of fossil fuels. At surface temperatures and pressures, CO_2 exists in the gaseous phase but exhibits supercritical behaviour above the critical point (temperature Tc = 31.1 ^{o}C and pressure Pc = 7.38 MPa) (David *et al.*, 2008). White (1975) has demonstrated that the presence of a gas in the rock can have a substantial influence on the seismic wave velocity and attenuation, depending on the degree of saturation, permeability, frequency and porosity. The presence of CO_2 in the reservoir either in the gaseous or supercritical state can cause significant changes in the seismic properties such as travel time, velocity, amplitude and attenuation and thus, an understanding of its influence could be of great importance in the study of hydrocarbon reservoir properties. For instance, Davis *et al.,* (2003) reported that CO_2 can cause a change of 4 - 6 % in P-wave velocity and 5 - 10 % in S-wave velocity. Time-lapse studies for monitoring CO_2 sequestration have also shown that the presence of CO_2 can cause significant changes in both the P- and S- wave velocities (e.g. Arts *et al.,* 2004; Chadwick *et al.*, 2005, Amir and Landro, 2009). The attenuation of seismic wave energy in rocks apart from being dependent on the physical state of the rocks also depends on the saturation conditions of the rocks (e.g. Kuster and Toksoz, 1974). For instance, P-wave attenuation has been shown to be more in partially saturated rocks than in fully saturated rocks (e.g. White, 1975; Toksoz *et al.*, 1979; Johnson *et al.*, 1979; Winkler and Nur, 1982; Klimentos, 1995).

In this chapter, I examine the effects of CO_2 held in the pore space on seismic attenuation, through synthetic modelling. To provide a realistic scenario for the modelling study, I use the published properties of CO_2 measured in the Sleipner gas field in the North Sea (Chadwick *et al.*, 2005). David *et al.,* (2008) observed significant changes in the calculated bulk seismic velocity and density in CO_2-saturated porous reservoir rocks under field conditions, where the CO_2 may exist either as a supercritical fluid or as a supercritical gas (Figure 8.1). In both cases, the bulk density decreases systematically and linearly with increasing percentage of CO_2 saturation, though more markedly for the supercritical gas case. The P-wave velocity shows a clear non-linear relationship with saturation. For the supercritical fluid case, there is a remarkable decrease in the P-wave velocity between zero and 30 % CO_2

saturation and thereafter very little or no change in the velocity. For the supercritical gas case however, the decrease in the P-wave velocity is even more non-linear, being prominent only up to 10 % CO_2 saturation. By contrast the S-wave velocity is insensitive to the percentage saturation.

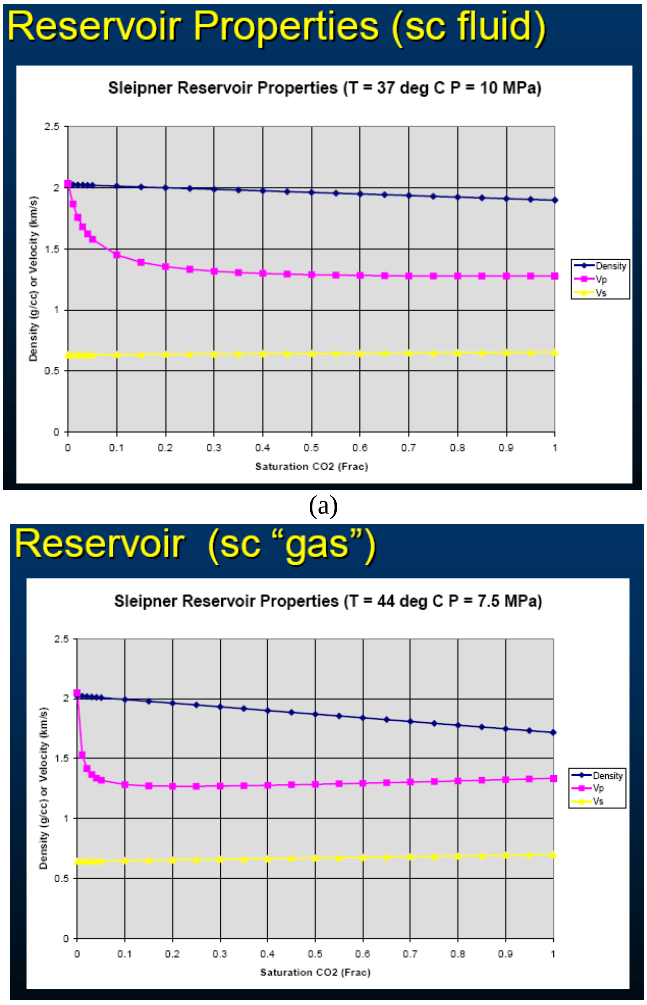
Reservoir Properties (sc fluid)

Sleipner Reservoir Properties (T = 37 deg C P = 10 MPa)

(a)

Reservoir (sc "gas")

Sleipner Reservoir Properties (T = 44 deg C P = 7.5 MPa)

(b)

Figure 8.1: Effects of CO_2 saturation on the P- (magenta curve) and S-wave (yellow line) velocities and density (blue line) of rocks at the Sleipner field (a) CO_2 as a supercritical fluid (b) CO_2 as a supercritical gas (from David *et al.*, 2008). In both cases, there is a remarkable change in the P-wave velocity at lower percentages of CO_2 saturation whereas the S-wave velocity is not sensitive to CO_2 saturation. There is more change in the bulk density for the gas case than the fluid case especially at higher percentages of saturation.

My main aim in this chapter is to investigate the changes cause by the presence of the CO_2 at varying percentages of saturation on P-wave attenuation and compare the attenuation signature with that of dry rocks. The theoretical model used consists of four horizontal isotropic layers. To simplify the treatment and provide a reference model, I first consider a pure isotropic model with no fluid saturation and no cracks, analogous to the dry rock case with no cracks. I then consider a case in which the third layer in the model is saturated with CO_2 at concentrations varying from 0 to 100 % and for crack densities of 0.01, 0.02 and 0.03 respectively. I finally examine a real field data example from the Sleipner gas field in the North Sea to see how the results agree with the synthetic modelling results.

8.2 Effect of mobility

The exchange of fluid between the pores in the rock as a result of the pressure gradients generated by the propagation of seismic wave causes attenuation. Changes in the times required to relax the pressure gradient could result in changes in the fluid mobility and hence the induced attenuation. An inverse relationship exists between fluid mobility and relaxation times. In this section, my aim is to investigate the effects of fluid mobility on the induced P-wave attenuation by considering a range of values of relaxation times from $5x10^{-1}$ to $5x10^{-6}$ s using Chapman's (2003) poro-elastic model given two different types of fluid saturation. I assumed the fluid mobility in this case to be the effective mobility of the two fluids.

A uniform saturation of the pores and cracks with two types of fluids (for example brine and CO_2) will result in a change of the effective fluid bulk modulus, viscosity and density (Chapman and Liu 2006 and David *et al.*, 2008). The resulting attenuation is sensitive to the changes in the effective fluid bulk modulus as well as the fluid viscosity (Chapman and Liu, 2006; Maultzsch *et al.*, 2007).

For partial saturation conditions with homogeneous mixing of brine and CO_2, the effective fluid bulk modulus K_{eff} could be computed using Wood's formula as (Mavko *et al.*, 2009, pp. 282):

$$\frac{1}{K_{eff}} = \frac{S_w}{K_w} + \frac{1-S_w}{K_c}, \tag{8.1}$$

where K_w is the bulk modulus of brine, K_c is the bulk modulus of CO_2 and S_w is the percentage of brine saturation.

8.2.1 Theoretical model and experimental set-up

The theoretical model is made up of four horizontal isotropic layers. To investigate the effects of CO_2, a porous fluid-saturated material is introduced into the third layer and squirt flow between the pores in the matrix is taken into consideration. The material is saturated with brine and CO_2 (in the supercritical state) at different degrees of concentrations. The elastic properties of the porous material are computed using the poroelastic model of Chapman (2003) reviewed in section 5.2. I considered the case of 10 % CO_2 saturation to examine mobility effects and computed the effective fluid bulk modulus using Equation (8.1). To model the effect of fluid saturation in a porous but un-fractured medium, I set the fracture density to zero so that the model returns to the earlier model of Chapman *et al.*, (2002). The brine and CO_2 properties are based on the data from the Sleipner field in the North Sea (Chadwick *et al.*, 2005). The field is a site for large scale CO_2 injection project specifically designed as a greenhouse gas mitigation measure (Chadwick *et al.*, 2005). CO_2 has been injected since 1996 into the Utsira Sand reservoir in the field. The Utsira Sand which is saline aquifer has a thickness of 200 - 300 m and CO_2 exists in the reservoir in the supercritical phase (Chadwick *et al.*, 2005). Details of the model parameters used are given in Table 8.1.

Synthetic data were computed from the theoretical model using the 'ANISEIS' software (Taylor, 2001) which makes use of the reflectivity method, for the case in which the third layer is 90 % saturated with brine and 10 % CO_2 for crack densities of 0.01, 0.02 and 0.03 respectively. A Ricker wavelet (which has the dimension of volume) with a centre frequency of 25 Hz and a start time of 100 ms was used as the source wavelet (Figure 8.2). The source is an explosive source and was placed on the surface of the model. The software modifies the explosive source placed on top of the model such that outward waves are suppressed and only contributions from waves directed into the model are generated (Taylor, 2001). Twenty-one receivers were also placed on the surface of the model, at a regular spacing of 100 m, and a source - receiver spacing of 100 m was maintained. Data were recorded with a sampling interval of 1 ms and a total time of 3 s. Sample synthetic gathers are shown in Figure 8.3 for the vertical component of particle displacement with the reflections from the top and bottom of the fluid-saturated layer highlighted by the red and green arrows respectively.

Table 8.1: Theoretical model parameters for studying the effects of CO_2

Layer parameters

Layer	**v_p (m/s)**	**v_s (m/s)**	**ρ (kg/m^3)**	**Thickness (m)**
1	1800	750	1100	400
2	2270	850	2100	600
3	2850	1350	2450	300
4	3800	1800	2600	Half-space

Saturated layer parameters (layer 3)

fracture density	0
CO_2 bulk modulus	0.008 Gpa
Brine bulk modulus	2.305 Gpa
porosity	0.37
frequency	50 Hz

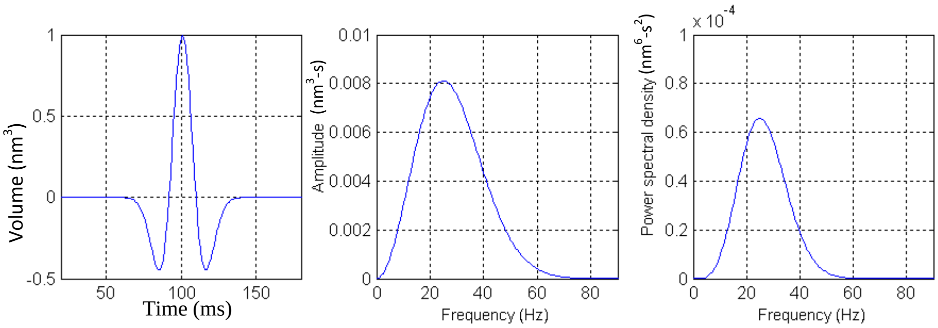

(a). (b). (c).

Figure 8.2: Ricker wavelet used as source wavelet (a) time series (b) amplitude spectrum (c) power spectrum. The centre frequency is 25 Hz. The wavelet has dimension of volume.

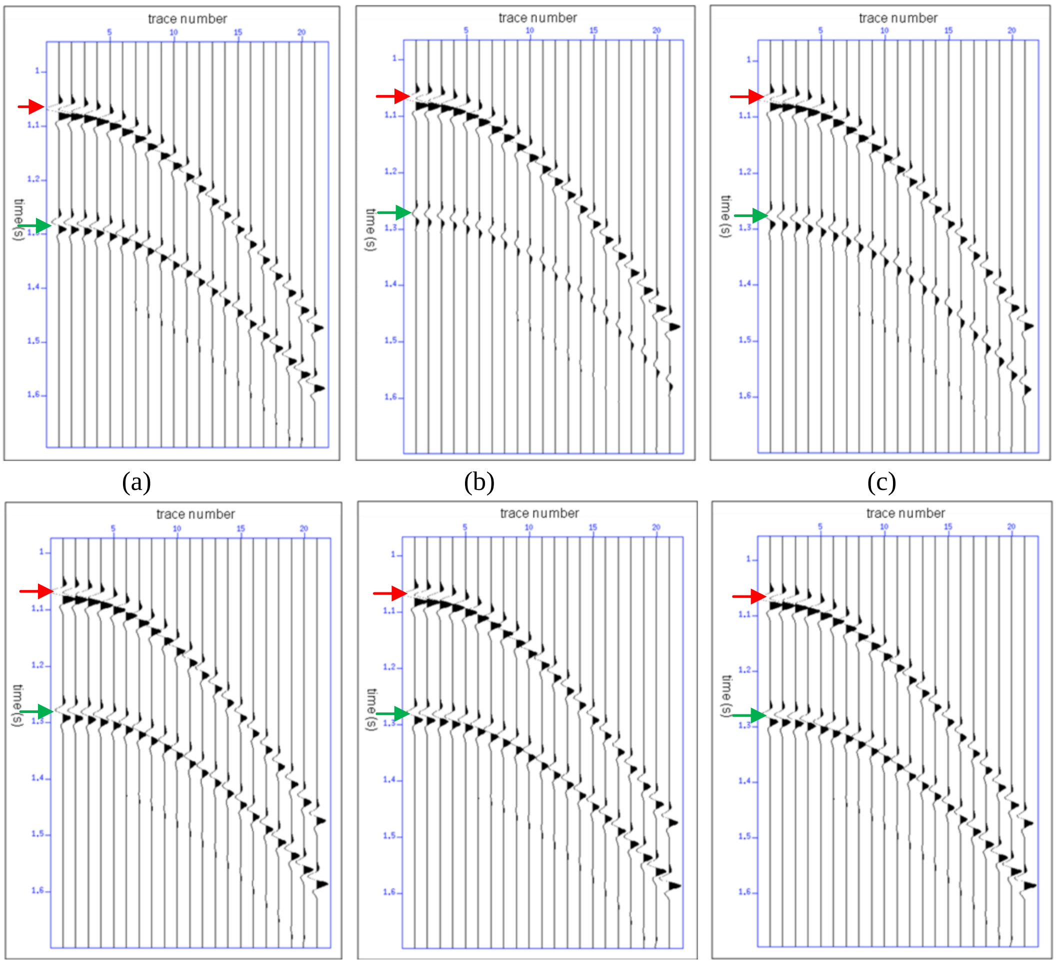

(a) (b) (c)

(d) (e) (f)

Figure 8.3: Sample synthetic gathers for a crack density of 0.01 and CO_2 saturation of 10 %: (a) relaxation time = 5e-1 s (b) relaxation time = 5e-2 s (c) relaxation time = 5e-3 s (d) relaxation time = 5e-4 s (e) relaxation time = 5e-5 s (f) relaxation time = 5e-6 s. The red arrow indicates reflection from the top of the fluid-saturated layer while the green arrow indicates reflection from the bottom of the layer.

8.2.2 Q estimation

I used the QVO-spectral ratio method discussed in Chapter 3 to estimate the seismic quality factor Q from the synthetic data. In each gather, the first trace from the top model reflection at 0 m offset was used as the reference trace for comparison of the spectral ratios (Figure 8.4). The far field pulse shape (reference trace in this case) is proportional to the time derivative of the input Ricker wavelet (as shown in Appendix A). Thus, the peak frequency of the reference trace is higher than that of the input Ricker wavelet as predicted by Equation (3.27). For each trace in the gather and for the top and bottom fluid-saturated layer reflection, I formed the spectral ratios according to Equation (4.1) and performed a simple least-squares regression of the logarithm of the power spectral ratios (LPSR) against frequency. Figure 8.5 shows sample plots of the power spectra at the various values of relaxation times considered at a fixed offset of 900 m. I used a constant FFT time window of 180ms to compute the power spectra, and a frequency bandwidth of 20 - 90 Hz where the spectral ratio plots were approximately linear (Figure 8.6) for the linear regression. Sample linear regression plots of the LPSR against frequency for the chosen bandwidths are shown in Figures 8.7 and 8.8 for the top and bottom fluid-saturated layer reflections respectively with their corresponding R^2 values. The Q values down to the top and bottom of the fluid-saturated layer were computed from the slopes p using Equation (3.12) and the errors in the slopes were used to compute the associated errors in the computed Q values. With the pair of Q values computed down to the top and bottom of the layer, 1 used the layer-stripping method of Dasgupta and Clark (1998) to compute the interval Q value in the layer using Equation 3.8 and the associated errors using Equation (3.9) respectively.

The entire procedure was repeated for all the traces in the gather following the hyperbolic travel path and the average interval Q in the fluid saturated-layer was computed from the mean of all the estimated interval Q values in the layer. Figure 8.9 illustrates the variation of the peak frequencies with the relaxation times. There is no variation in the peak frequencies for the reference event and the top fluid-saturated layer reflection (black and red lines). However for the bottom saturated layer reflection, slight variations are noticeable in the peak frequencies, indicative of varying degrees of attenuation at these relaxation times.

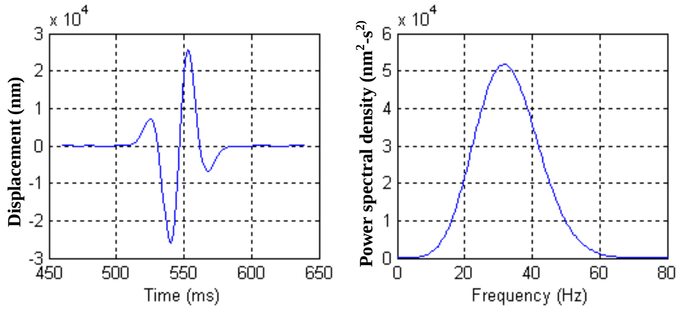

(a) (b)

Figure 8.4: Reference trace - top model reflection at 0 m offset (a) Time series with a window length of 180 ms (b) Power spectrum. The wavelet is proportional to the time derivative of the source wavelet.

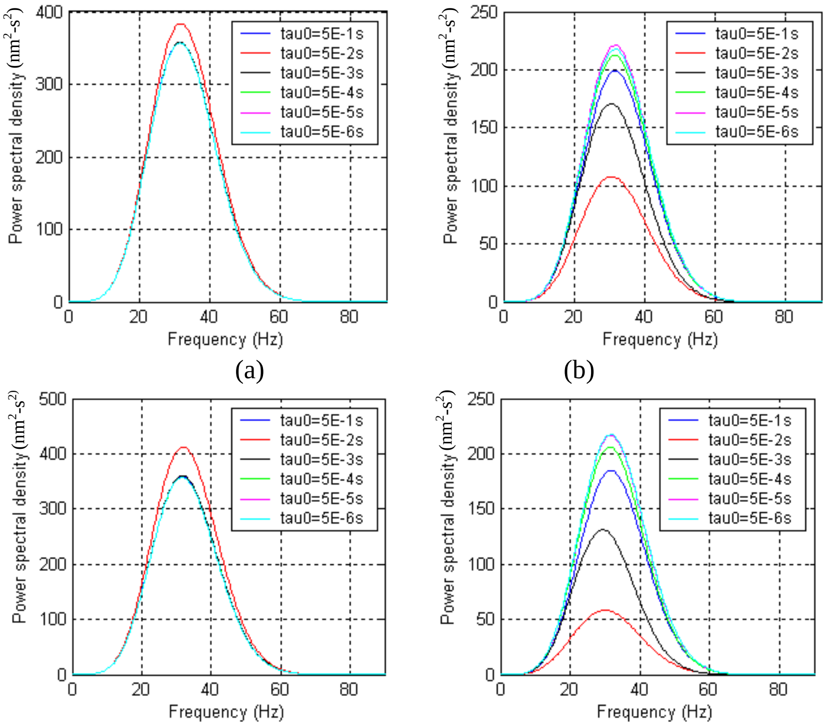

(a) (b)

(c) (d)

Figure 8.5: Power spectra at a fixed offset of 900 m and CO_2 saturation of 10 % in the fluid-saturated layer (a) top reflection: 0.01 crack density (b) bottom reflection: 0.01 crack density (c) top reflection: 0.02 crack density (d) bottom reflection: 0.03 crack density.

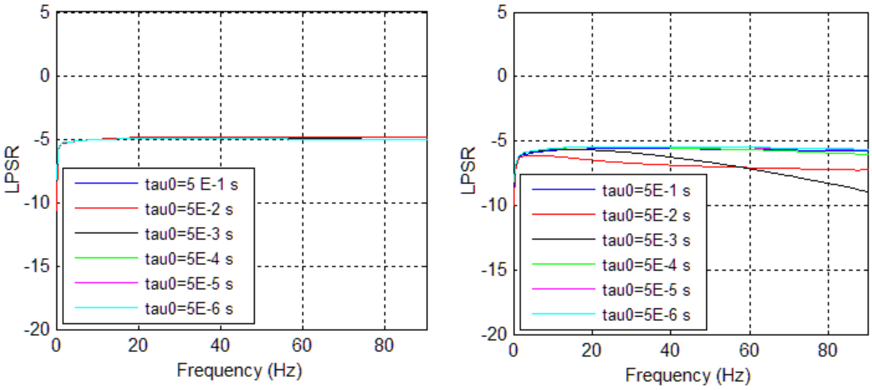

(a) (b)

Figure 8.6: Log Power Spectral Ratio (LPSR) against frequency plots for the different relaxation times considered at a fixed offset of 900 m, crack density of 0.02 and CO_2 saturation of 10 % (a) Top layer reflection (b) bottom layer reflection. The plots are all stable between the frequency bandwidth of 20 - 90 Hz.

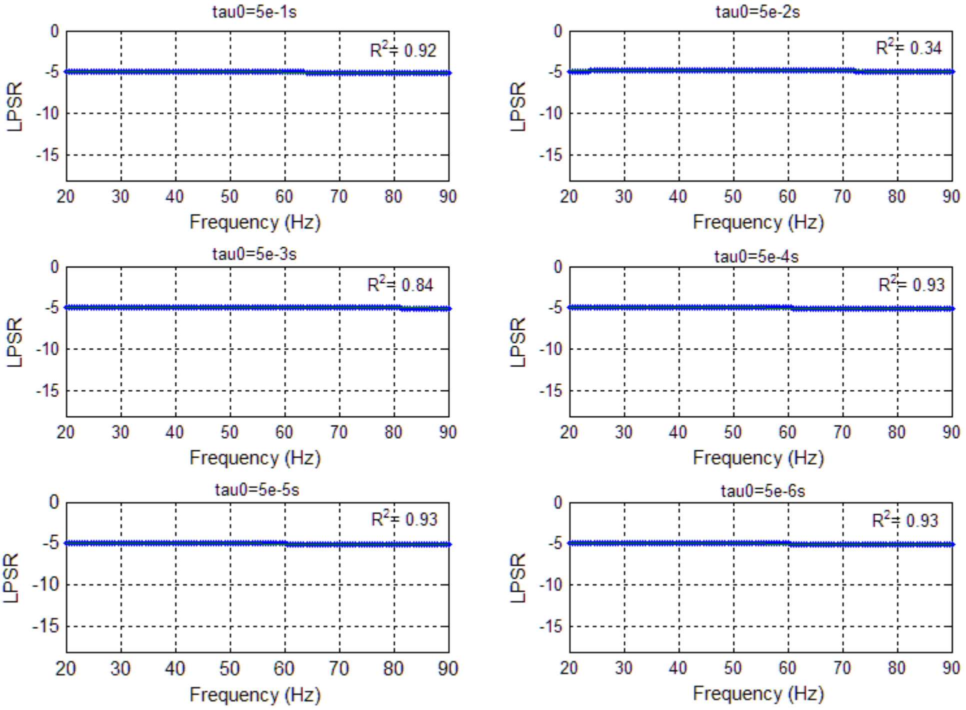

Figure 8.7: LPSR plots against frequency for different values of relaxation times (tau0) at a fixed offset of 900 m for top fluid-saturated layer reflection. The blue asterisks indicate the data points while the green line indicates the fitted line.

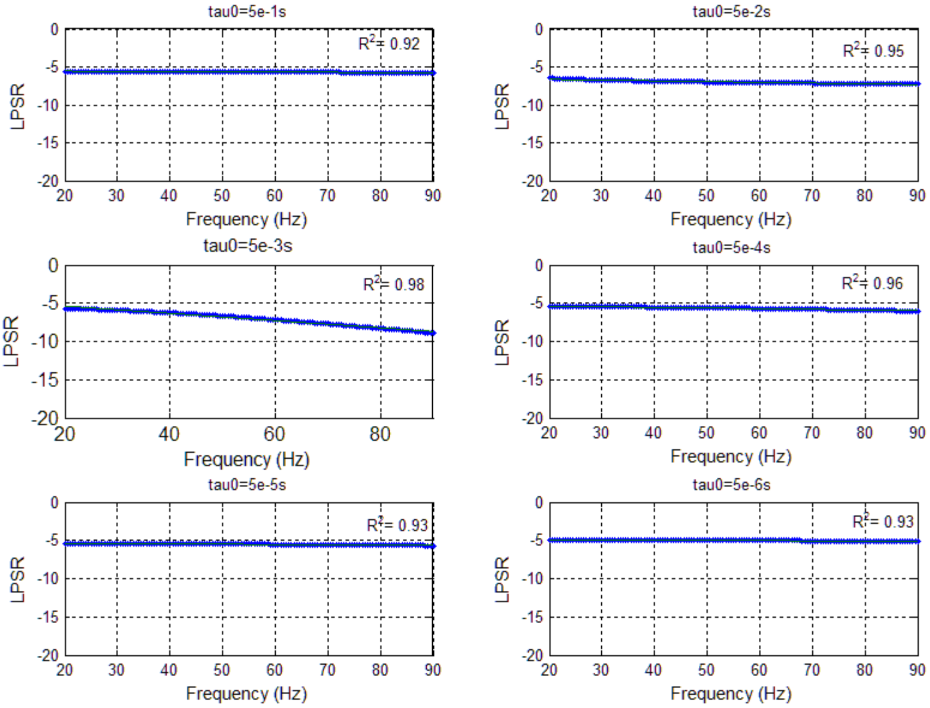

Figure 8.8: LPSR plots against frequency for different values of relaxation times (tau0) at a fixed offset of 900 m for bottom CO_2 saturated layer reflection. The blue asterisks indicate the data points while the green line indicates the fitted line.

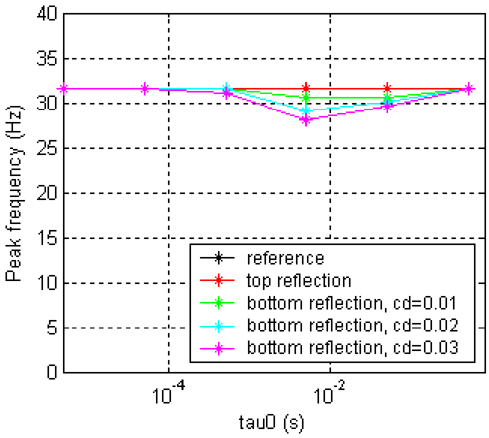

Figure 8.9: Peak frequencies as a function of relaxation times. The peak frequency of the reference event coincides with that of the top fractured-layer reflection. There are obvious variations in the peak frequencies between relaxation time values of 5 x 10^{-1} s and 5 x 10^{-4} s with a minimum at relaxation time = 5 x 10^{-3} s.

8.2.3 Results and analysis

The results of the analysis show that the relaxation time controls the frequency bandwidth over which attenuation occurs as in the case of the study in chapter 5. The induced P-wave attenuation is dependent on the relaxation time and hence fluid mobility (Figure 8.10). Very low attenuation values (1/Q) are obtained at relaxation times ≤ $5\text{x}10^{-4}$ s (or relaxation frequency ≥ 2 kHz) and ≥ $5\text{x}10^{-2}$ s (or relaxation frequency ≤ 20 Hz) respectively. However higher values of attenuation are obtained between relaxation times of $5\text{x}10^{-4}$ - $5\text{x}10^{-2}$ s (or frequency of 20 - 2000 Hz) with maximum attenuation around a relaxation time of $5\text{x}10^{-3}$ s (or relaxation frequency of 200 Hz). Noting that there is a 2π ambiguity in the definition of the frequencies in the modelling codes (Personal discussion with Chapman, M., 20/03/2012), these frequencies translate into 3 - 320 Hz and $f \approx 30$ Hz respectively. High fluid mobility implies lower relaxation times and vice versa. Thus, fluid mobility divides the relaxation time (or relaxation frequency) into three zones; high relaxation time zone, intermediate relaxation zone and low relaxation time zone (Figure 8.10). There is low fluid mobility in the high relaxation time zone which implies that the cracks are isolated in terms of fluid flow, tending to Hudson’s theory (1980). The fluid mobility is high in the low relaxation time zone, implying that the cracks are connected in terms of fluid flow tending to Gassmann’s theory. Very little or no attenuation occurs in these limiting cases. In between these two limiting cases, high attenuation occurs with a maximum magnitude around a relaxation time of $5\text{x}10^{-3}$ s. The magnitude of the attenuation is observed to increase with increasing crack density.

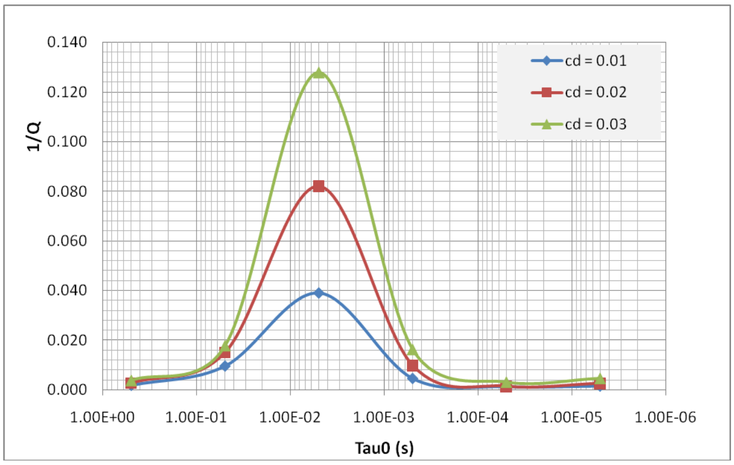

Figure 8.10: 1/Q as a function of relaxation times (tau0) for CO_2 saturation of 10 %. Very little or no attenuation occurs at lower and higher relaxation times where the fluid mobility is high and low respectively. Between these limits, the attenuation is high with a maximum value at a relaxation time of $5x10^{-3}$ s.

8.3 Sensitivity to CO_2 saturation

In this section, I examine the sensitivity of P-wave attenuation to CO_2 saturation. I start by considering a pure isotropic model case with no cracks and no fluid saturation and then the case in which the third layer is saturated with brine and CO_2 (in the supercritical state) at different percentage concentrations and computed the resultant effective bulk modulus of the two fluid saturations using Equation (8.1). At lower brine saturation, the effective fluid bulk modulus is dominated by the bulk modulus of CO_2. The reverse is the case at higher brine saturation. The induced attenuation might be sensitive to these changes in the effective fluid bulk modulus which is the major subject in this section.

8.3.1 Theoretical model and experimental set up

The theoretical model and the experimental set up is the same as in the case of section 8.2 where I investigated the effects of fluid mobility on P-wave attenuation. The results of the study in section 8.2 indicate that maximum attenuation occurs in the fluid-saturated layer at a relaxation time of 5000 μs. I made use of this value of relaxation time in this section to compute the synthetic data from the theoretical model with the porous material in the third layer saturated with brine and CO_2 at different degrees of concentrations ranging from 0 to 100 %. A 0 % CO_2 saturation implies that the material is fully saturated with brine while 100 % CO_2 saturation means that the material is fully saturated with CO_2. The acquisition geometry is the same as in section 8.2. Figure 8.11 shows sample synthetic gathers computed from the theoretical model. The red and green arrows indicate the top and bottom fluid-saturated layer reflections respectively.

8.3.2 Q estimation

I made use of the same procedure as in section 8.2 to compute the interval Q values in the fluid-saturated layer for the various degrees of concentrations considered. Sample power spectra are shown in Figure 8.12 for selected percentages of CO_2 saturation and crack densities of 0.2 and 0.3 respectively at a fixed offset of 900 m. There is a significant drop in the power spectral density for the bottom layer reflection with decreasing percentage of CO_2 saturation from 100 % to a minimum at 10 % saturation. However, the power density is a maximum at 0 % CO_2 saturation when the material is 100 % saturated with brine. These observations are indicative of the sensitivity of the wave attenuation to the varying degrees of CO_2 saturation. Figure 8.13 shows sample plots of the LPSR against frequency for selected offsets. As in the case of section 8.2, the plots are linear within a frequency bandwidth of 20 - 90 Hz and hence linear regression was done using this frequency bandwidth. Sample linear regression plots of the LPSR against frequency for the chosen bandwidth are shown in Figure 8.14 with their corresponding R^2 values. Figure 8.15 shows the variation of the peak frequencies with offsets for the different percentages of CO_2 saturation considered. There is no noticeable variation in the peak frequencies between the reference trace and the top fluid saturated layer reflection as expected. However, there are remarkable variations in the peak frequencies with the percentage of CO_2 saturation for the bottom fluid-saturated layer reflection especially between 0 - 40 % saturation. The peak frequency is minimum at 10 % and maximum at 0 % CO_2 saturations respectively. This behaviour is indicative of the sensitivity of the induced P-wave attenuation to percentages of CO_2 saturation.

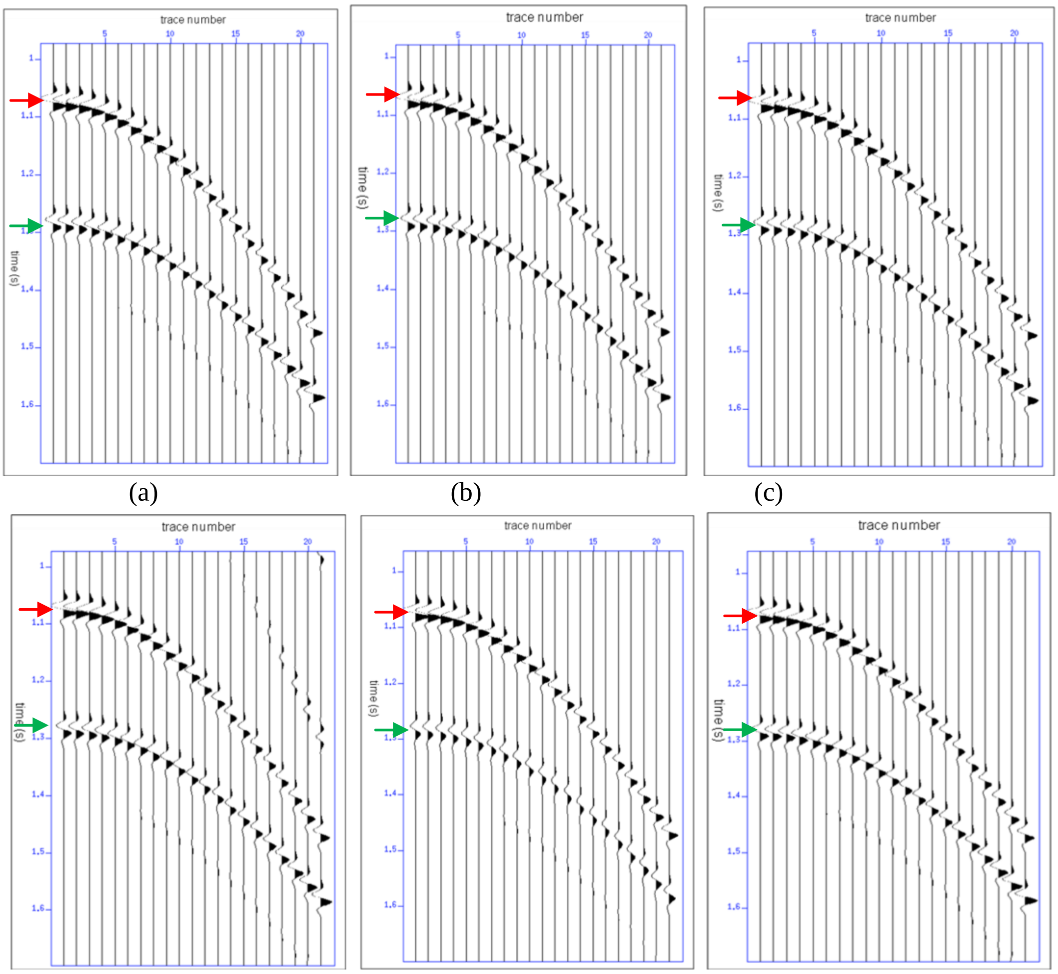

(a) (b) (c)

(d) (e) (f)

Figure 8.11: Sample synthetics for the vertical component of particle displacement (a) crack density 0.01, CO_2 saturation 0 % (b) crack density 0.01, CO_2 saturation 10 % (c) crack density 0.01, CO_2 saturation 30 % (d) crack density 0.01, CO_2 saturation 100 % (e) crack density 0.03, CO_2 saturation 10 % (f) Pure isotropic case with no cracks and no fluid saturation.

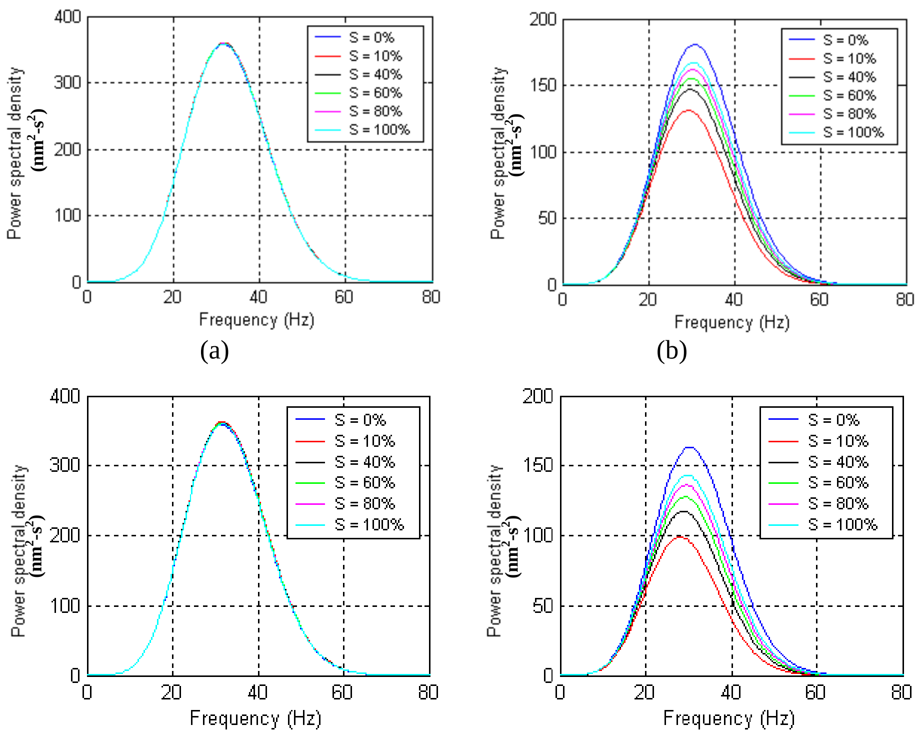

(a) (b)

(c) (d)

Figure 8.12: Power spectra at 900 m offset for the fluid-saturated layer reflections (a) top layer: 0.02 crack density (b) bottom layer: 0.02 crack density (c) top layer: 0.03 crack density (d) bottom layer: 0.03 crack density.

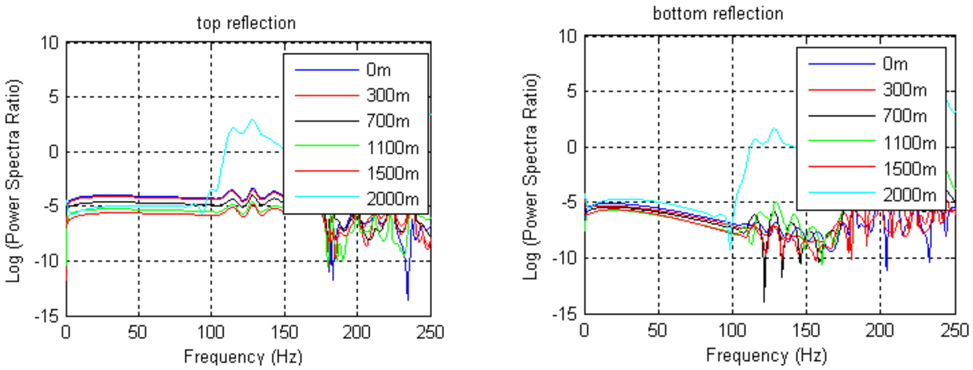

Figure 8.13: Sample Log Power Spectra Ratio (LPSR) versus frequency plot for crack density 0.01 and 10 % CO_2 saturation. The inserted legend indicates the selected offsets. The plots are linear within the frequency bandwidth of 20 - 90 Hz.

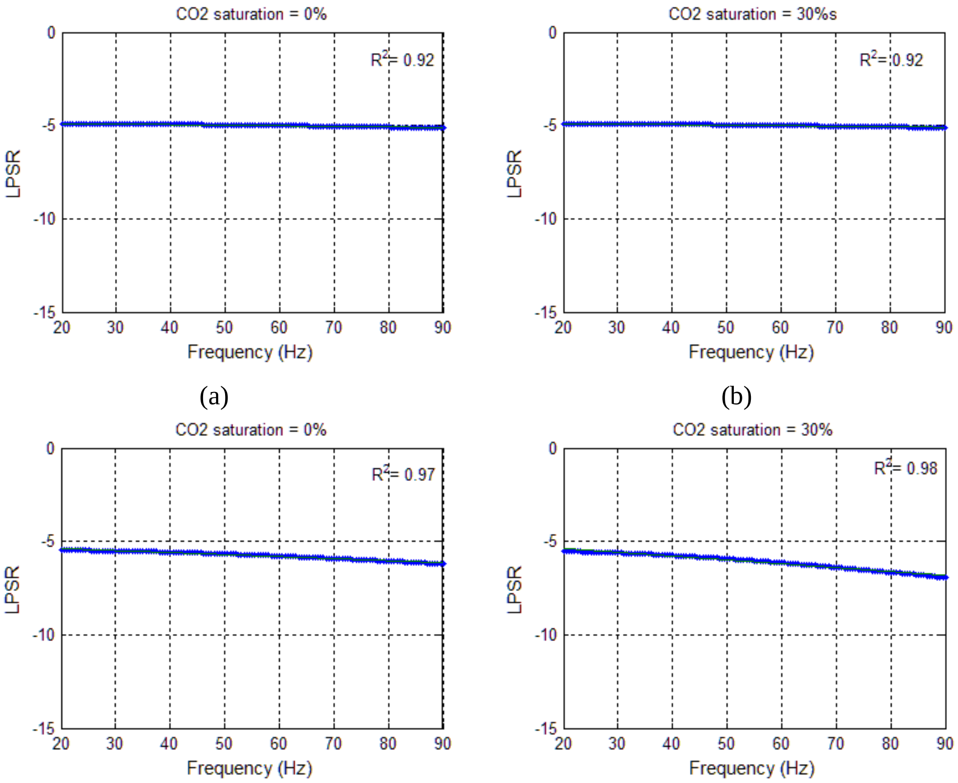

(a) (b)

(c) (d)

Figure 8.14: LSPR plots against frequency for CO_2 saturations of 0 and 30 % at a fixed offset of 900 m (a) top layer reflection - 0 % CO_2 (b) top layer reflection - 30 % CO_2 (c) bottom layer reflection - 0 % CO_2 (d) bottom layer reflection - 30 % CO_2. The blue asterisks indicate the data points while the green line indicates the fitted.

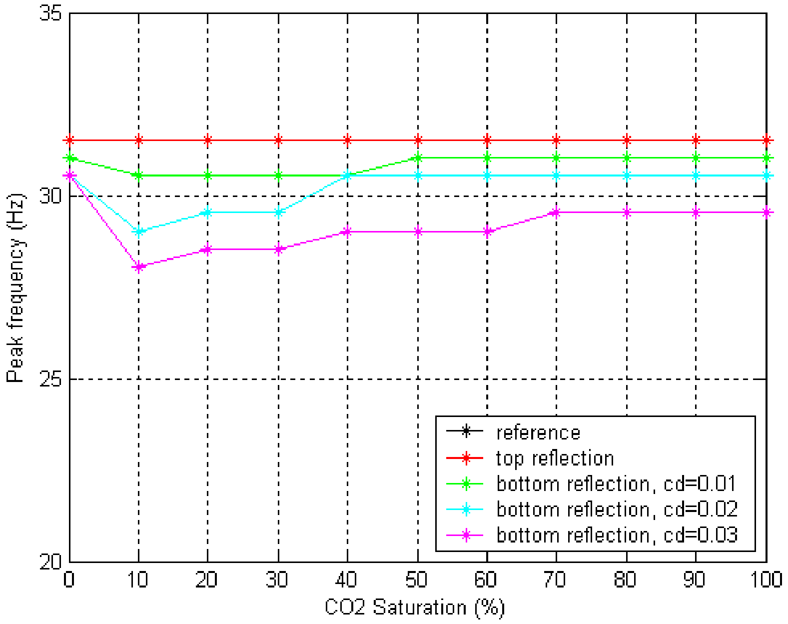

Figure 8.15: Peak frequency - CO_2 saturation plot at a fixed offset of 900 m. There are remarkable variations in the peak frequencies with varying percentages of CO_2 saturations and a minimum peak frequency occurs at 10 % saturation for the bottom layer reflection. The reference peak frequency coincides with the top reflection peak frequency.

8.3.3 Results and analysis

The results of the analysis show that higher Q values are obtained in the fluid-saturated layer at 0 % CO_2 saturation and lower values at 100 % CO_2 saturation for the three crack densities considered (Figure 8.16). The Q values are observed to decrease gradually with decreasing percentages of CO_2 saturation from 100 % to 10 % for a given crack density, implying more attenuation with decreasing percentages of saturation. The Q values are also observed to decrease systematically both with increasing crack density and offset. This implies that the induced P-wave attenuation increases with crack density and offset. There is a remarkable change in the induced attenuation for CO_2 saturations of 10 - 30 % (Figure 8.17). Beyond this percentage range of saturation, the induced attenuation decreases gradually with increasing percentage of CO_2 saturation. Maximum attenuation (up to 0.15) occurs at 10 % CO_2 saturation. For the pure isotropic case with no cracks and fluid saturation, there is no noticeable attenuation (pink circle in Figure 8.17). Over all, the results show that the presence of CO_2 in the third layer causes more attenuation.

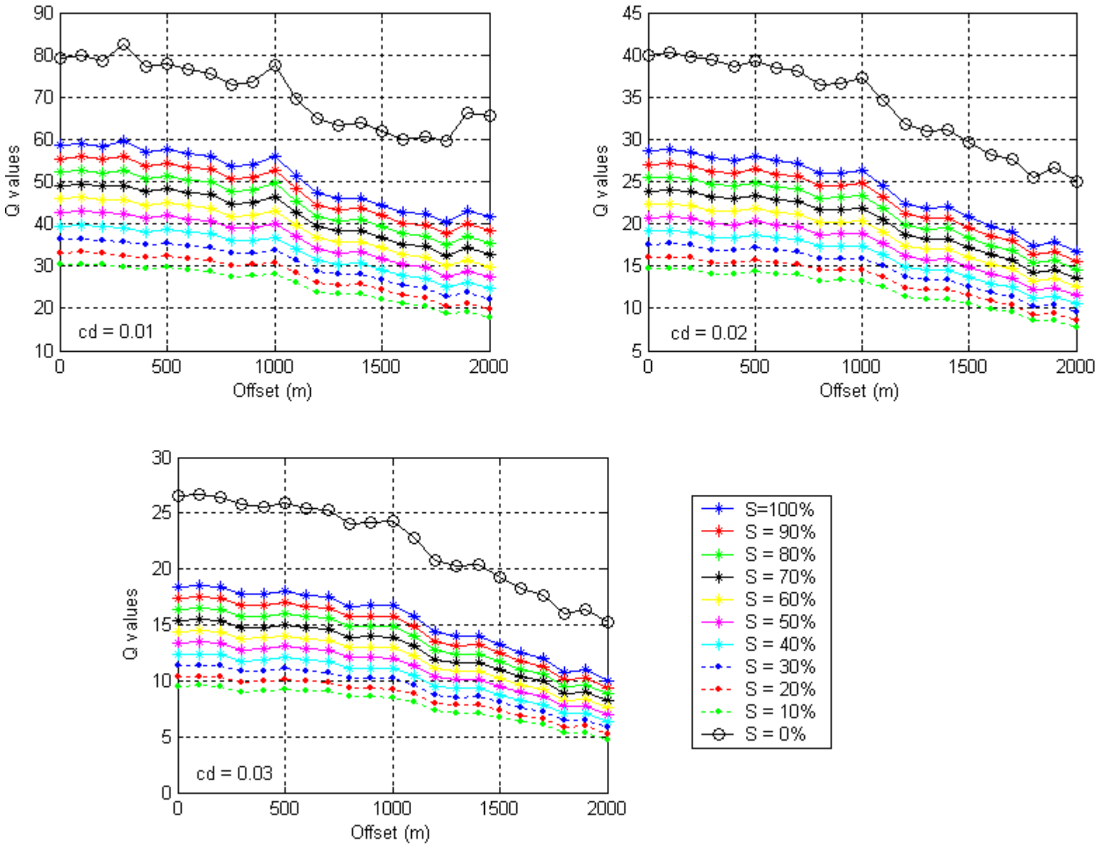

Figure 8.16: Q profile against CO_2 saturation for different degree of saturations. Q decreases systematically with saturation and is minimum at 10 % saturation

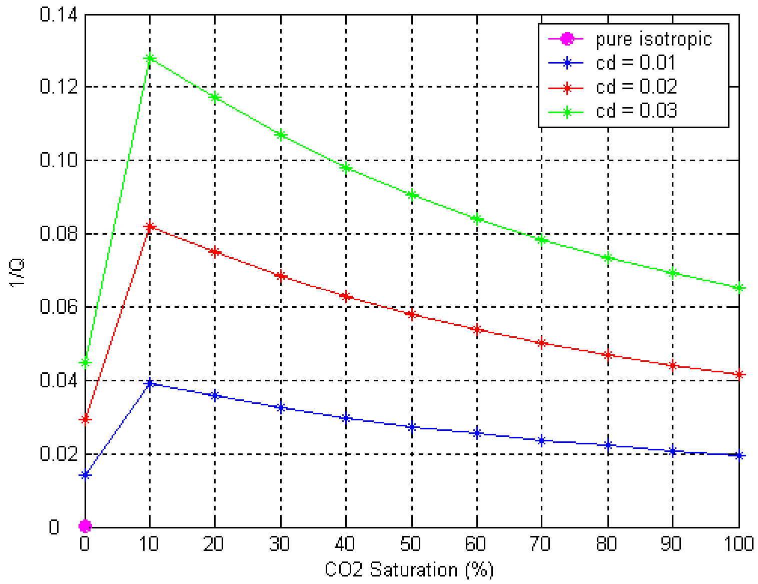

Figure 8.17: 1/Q profile against CO_2 saturation for different crack densities. No attenuation occurs in the pure isotropic case with no cracks and no fluid saturation. The induced attenuation is a maximum at 10 % CO_2 saturation.

8.4 Real data example

In this section, I apply the same technique as in section 8.2 to estimate the seismic quality factor, Q from a 3-D seismic data set from the Sleipner gas field in the North Sea with the aim of investigating the influence of the presence of CO_2 on the induced attenuation. The field is a site for large scale CO_2 injection project specifically designed as a greenhouse gas mitigation measure (Chadwick *et al.*, 2005). Millions of tonnes of CO_2 have been injected since 1996 into the Utsira Sand, which constitutes a major saline aquifer in the field (Chadwick *et al.*, 2005; Bickle *et al.*, 2007; Arts, *et al.*, 2008) with over 11 million tonnes by 2010 (Chadwick *et al.*, 2010). The Sleipner gas field lies towards the southern limit of the Utsira Sand (Figure 8.18). The Utsira sand reservoir is 800 - 900 m deep and 200 - 300 m thick (Chadwick *et al.*, 2005). The sand is clean and largely un-cemented with porosities ranging from 0.30 - 0.42 (Zweigel *et al.*, 2004). Silty mudstone of thickness varying from 50 - 100 m forms the immediate reservoir cap rock in the Sleipner area (Chadwick *et al.*, 2005).

CO_2 produced in the Sleipner gas field has been injected into the Utsira Sand reservoir since 1996 at some depth of 1012 m below sea level and 200 m below the reservoir top (Chadwick *et al.*, 2005 and 2006; *Arts et al.*, 2008). At this depth, CO_2 forms a compressible but buoyant supercritical fluid of low viscosity and high mobility (Chadwick *et al.*, 2005). Various geophysical methods have been used to monitor the injected CO_2 plume (Chadwick *et al.*, 2006; Bickle *et al.*, 2007; Arts *et al.*, 2008) to verify that the CO_2 is being confined safely within the primary storage reservoir. 3-D seismic data were acquired in 1994 prior to the CO_2 injection and then after the injection in 1999, 2001, 2002, 2004, and 2006 respectively and the interpreted seismic sections are shown in Figure 8.19. The CO_2 plume is imaged on the seismic sections as a prominent feature, comprising a number of bright sub-horizontal reflections, growing with time (Arts *et al.*, 2008). Beneath the plume is a strong velocity push down arising from the decrease in the seismic velocity through the CO_2 saturated rock than the unsaturated part of the rock.

I made use of the 3-D data acquired in 2006 to investigate the effect of the injected CO_2 on P-wave attenuation. Figure 8.20 shows an inline seismic section extracted from the 3-D data. The green and red lines indicate the top and base of the Utsira Sand respectively. The CO_2 plume is highlighted by the red ellipse.

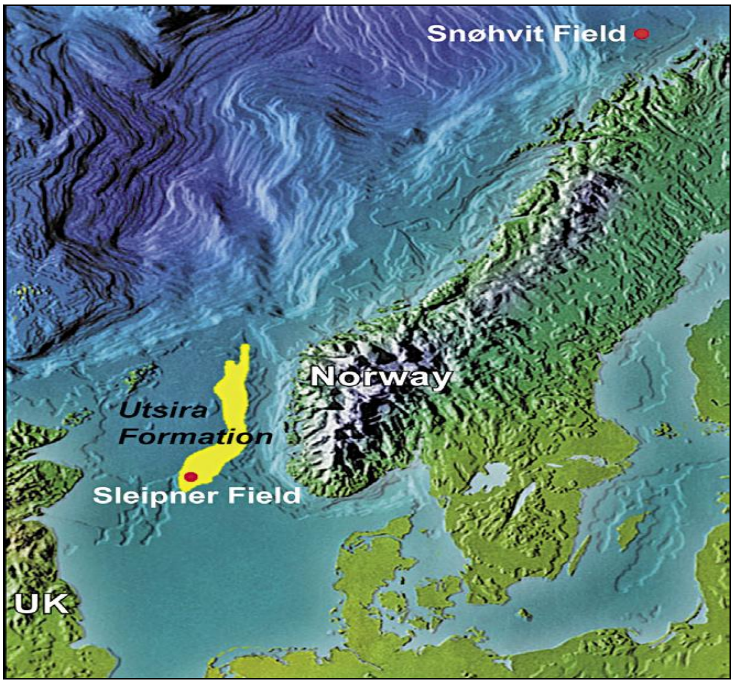

Figure 8.18: Map of the Sleipner gas field in the North Sea (after Arts *et al.*, 2008). The Sleipner gas field lies towards the southern limit of the Utsira Sand.

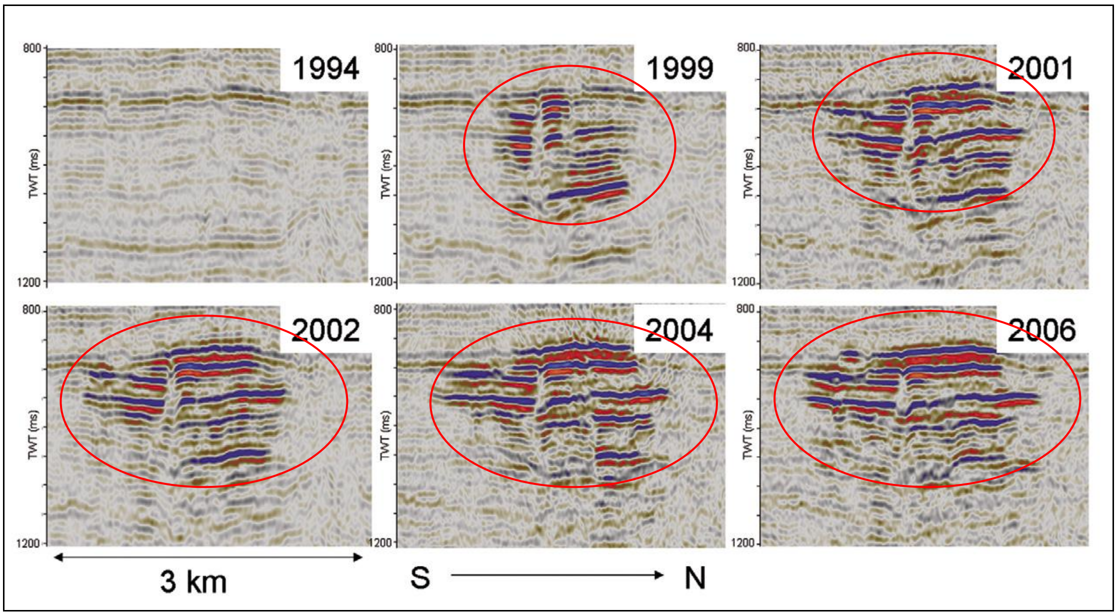

Figure 8.19: Development of the CO_2 plume over the years imaged with seismic data (after Arts *et al.*, 2008). The red circle highlights the CO_2 plume which is observed to grow with time across the seismic sections. No CO_2 injection occurs for the 1994 data.

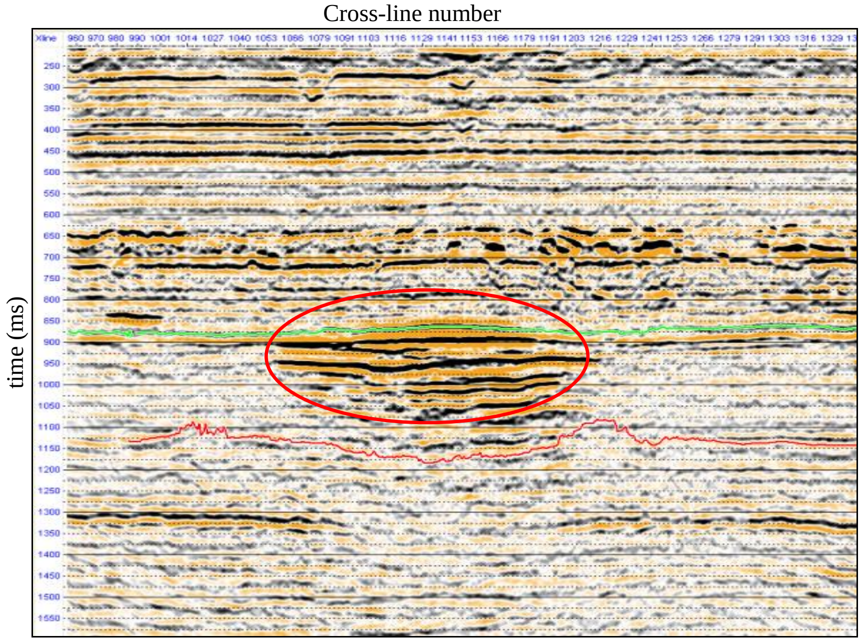

Figure 8.20: Inline seismic section showing the CO_2 plume (Chen *et al.*, 2010) for the 2006 data. The green line indicates the top of the Utsira Sand while the red line indicates the base of the Sand. The CO_2 plume is highlighted by the red ellipse and lies between CDP(s) 350 and 750.

8.4.1 Q estimation

I made use of the same procedure as in section 8.2 to estimate the Q values in the fluid saturated-layer for the pre-stack CMP gathers. A sample CMP gather is shown in Figure 8.21. The events I analysed are the top saturated-layer reflection indicated by the green arrow which corresponds to the top of the Utsira Sand and the reflection beneath the CO_2 plume indicated by the red arrow. The base Utsira Sand reflection (indicated as red line in Figure 8.20) is not prominent on the pre-stack gathers and thus very difficult to pick. This necessitated the choice of the next prominent event beneath the CO_2 plume for analysis.

For the reference trace, I used a strong shallow reflection event at 38 m offset at a two-way travel time of 90 ms (first trace, blue arrow, Figure 8.21) and a constant window length of 50 ms. Figure 8.22 shows the time series of the reference trace and the corresponding spectra. Listed below are the steps I took in this analysis:

1. Careful isolation and windowing of the event with a constant window length of 50 ms (Figure 8.22a)

2. multiplying the windowed event by the Hanning taper (Figure 8.22b and c)
3. Computing the Fourier transform of the windowed event using FFT
3. Computing the amplitude spectrum from the absolute value of the FFT (Figure 8.22d)
4. Taking the square of the amplitude to get the spectral power (Figure 8.22e)

The recorded signal has some direct current (DC) component which is not sinusoidal unlike the alternating current (AC) component. Consequently, the amplitude spectrum (Figure 8.22d) does not start at the origin. This shift is noticeable in the plot (amplitude axis) although it is negligibly small. When the power spectral estimates are made from the square of the amplitudes, these negligible small numbers (amplitudes) are squared up giving still very small numbers which now make the plot to look very smooth and “Gaussian” (Figure 8.22e). In some situations, the DC component may not be very small. In such cases, it is possible to subtract off the average value of the windowed trace, removing the DC component. Of course this procedure is not theoretically justified and may corrupt the amplitudes at non-zero frequencies.

I made use of a constant time window of 90 ms to window the target reflections from the top and bottom of the fluid-saturated later for FFT. The choice of the window length was in such a way as to isolate the target events as much as possible. Figure 8.23 shows sample plots of the power spectra for the top and bottom layer reflections respectively. The spectra are very noisy owing to interference effects of noise and internal multiples that may be included in the analysis window. Figure 8.24 shows sample plots of the LPSR against frequency for selected offsets. The effects of internal multiples are again very pronounced in the plots, resulting in oscillations of the spectral ratios associated with constructive and destructive interference in the scattered energy. However, the plots show a rough linear trend within a frequency bandwidth of 20 - 80 Hz which is approximately within the signal bandwidth. Consequently, I made use of this frequency bandwidth for linear regression. This bandwidth is common to all the events analysed. For each CMP gather, I computed the Q value in the fluid-saturated layer on a trace-by-trace basis and repeated the entire procedure for all the traces in the gather following the hyperbolic travel path. I then computed the average interval Q value in the fluid- saturated layer by taking the mean of all the estimated interval Q values in the layer at each offset.

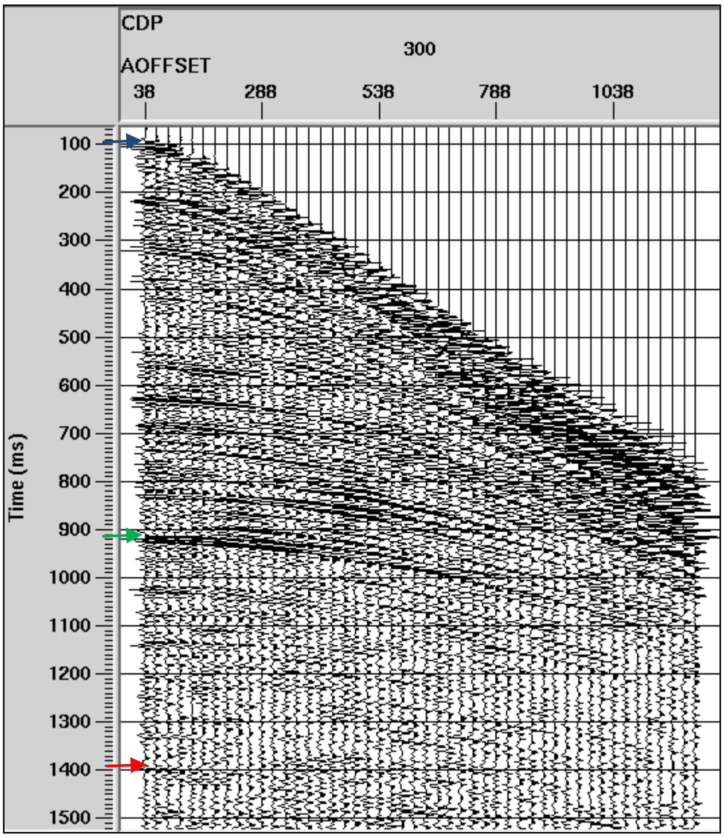

Figure 8.21: **S**ample gather used for attenuation analysis (CDP 300). The blue arrow is the reference trace, the green arrow indicates the top Utsira Sand reflection and the red arrow indicates reflection beneath the CO2 plume.

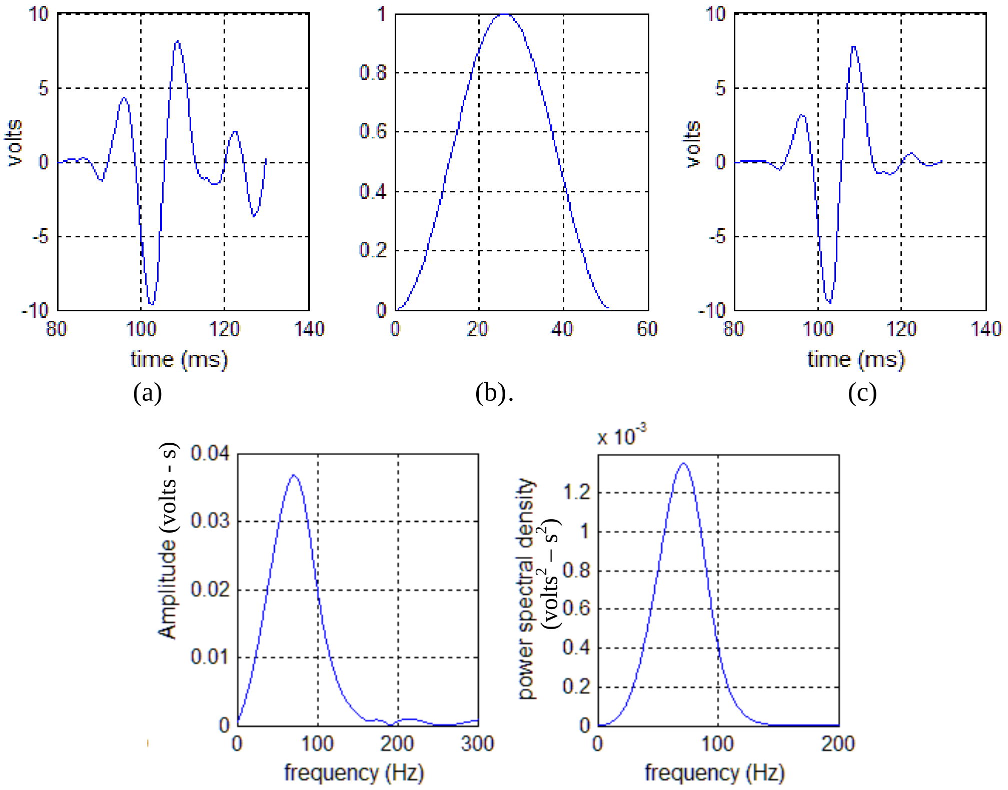

(a) (b). (c)

(d) (e)

Figure 8.22: Reference trace (blue arrow on Fig 8.21) - a strong shallow reflection at 38 m offset and two-way travel time of 90 ms (CMP 300) (a) Time series without application of Hanning window (b) Hanning window (c) Time series with application of Hanning window (d) amplitude spectrum (e) power spectrum

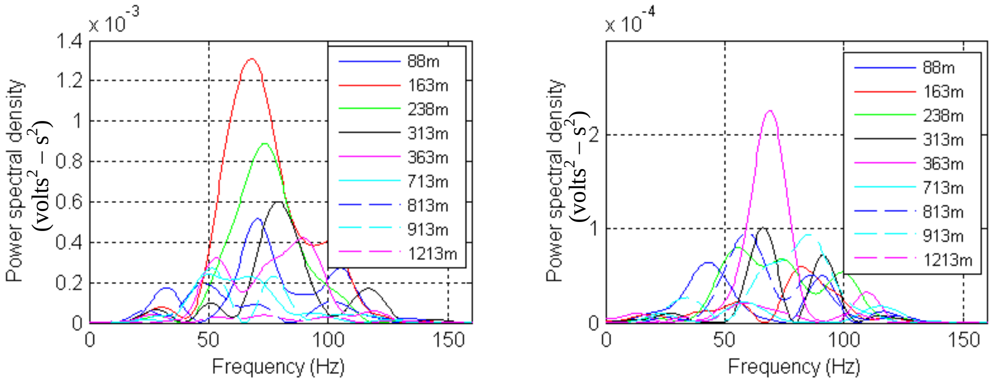

(a) (b)

Figure 8.23: Sample power spectra for the fluid-saturated layer (CMP 460) (a) top reflection (green arrow on Fig 8.21) (b) bottom reflection (red arrow on Fig 8.21). The scattering effects observed in the spectra are attributed to internal multiples entering into the analysis window. The inserted legend indicates the offsets.

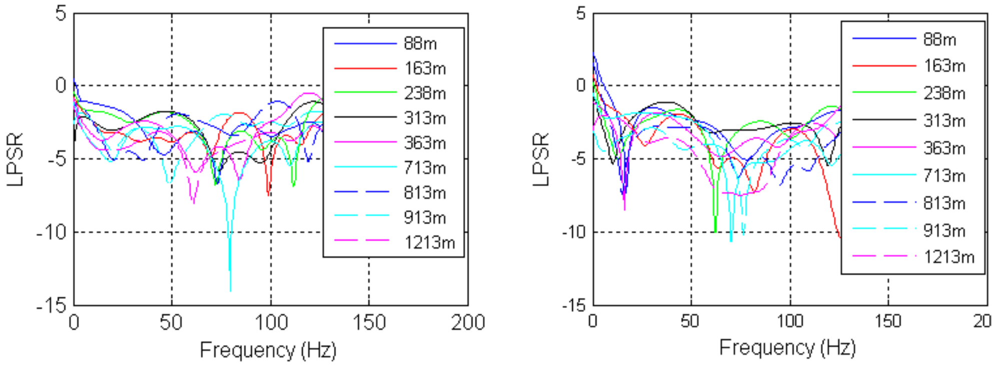

Figure 8.24: Sample Log Power Spectral Ratio (LPSR) against frequency plots for fluid-saturated layer (CDP 200) (a) top reflection (b) bottom layer. The effects of multiples in the analysis window result in the instability of the spectra. The inserted legend indicates the various offsets. A frequency bandwidth of 20 - 80 Hz was selected for regression.

8.4.2 Preliminary results and comments

The preliminary results of the inferred Q estimation from the spectral ratios of Figure 8.24 are displayed in Figure 8.25 for a selected number of CDP gathers analyzed against the offsets. The Q profiles are highly noisy and unstable with a considerable number of negative Q values which can be attributed to scattering of energy to higher frequencies seen in some of the spectra of Figure 8.24 and other noise interference, and not to anelastic absorption or energy dissipation. This can be ameliorated to some extent by stacking and taking an average: the computed average of the estimated Q values for all the CDP(s) analysed produces a much smaller error bar and physically plausible positive values for the inferred Q, even within this error (Figure 8.26). The CO_2 plume lies between CDP(s) 350 and 750 (Chen *et al*., 2010) where the average Q values show systematic decrease and is a minimum at CDP 480 which corresponds to the centre of the plume. Higher average Q values are obtained outside this range of CDP(s) at either ends of the centre of the plume. It is possible that the absolute Q values in the fluid-saturated layer may have been overestimated owing to the difficulty in picking the exact base Utsira Sand reflection which necessitated the choice of the next prominent event beneath the CO_2 plume for analysis instead. Although the observed Q variations might be indicative of the fact that the injected CO_2 causes more attenuation, further work is still needed to improve the stability of the results and in particular to separate out the effects of internal multiple-scattering attenuation. In specific terms, the spectral estimates could be made by using other forms of transforms like the S-transform and the continuous wavelet transform. In addition, more pre-processing work could be done to suppress the internal multiples in the data in order to improve the S/N ratio prior to attenuation analysis. The modified version of the QVO method by Reine *et al.*, (2009) could also be tried on the data to gain more confidence in the interpretation of the observed Q anomaly in the fluid-saturated layer.

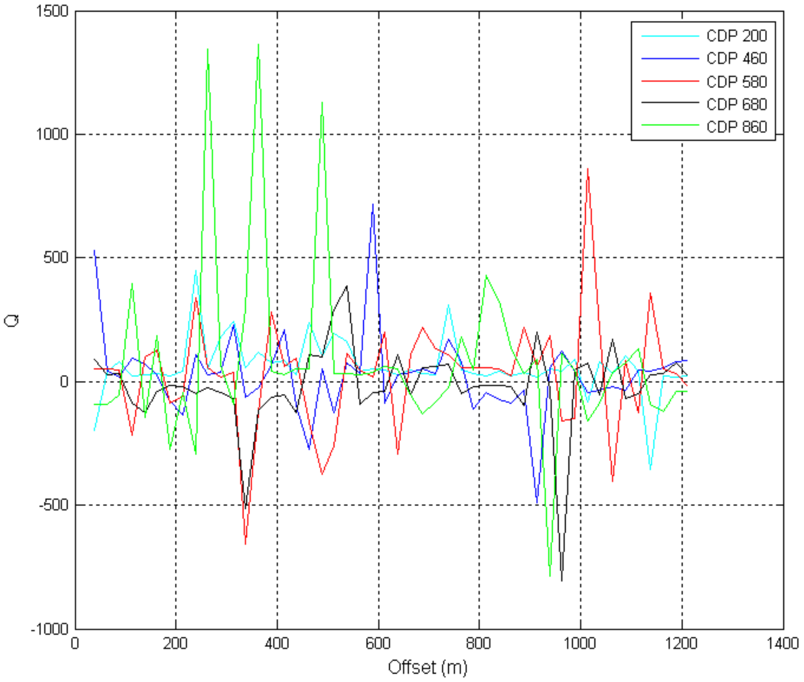

Figure 8.25: Q profile against offset for selected CDP(s) for the fluid-saturated layer. There is a huge amount of scatter in the profile due to the problem of proper isolation of the target events from the many internal multiples in the data.

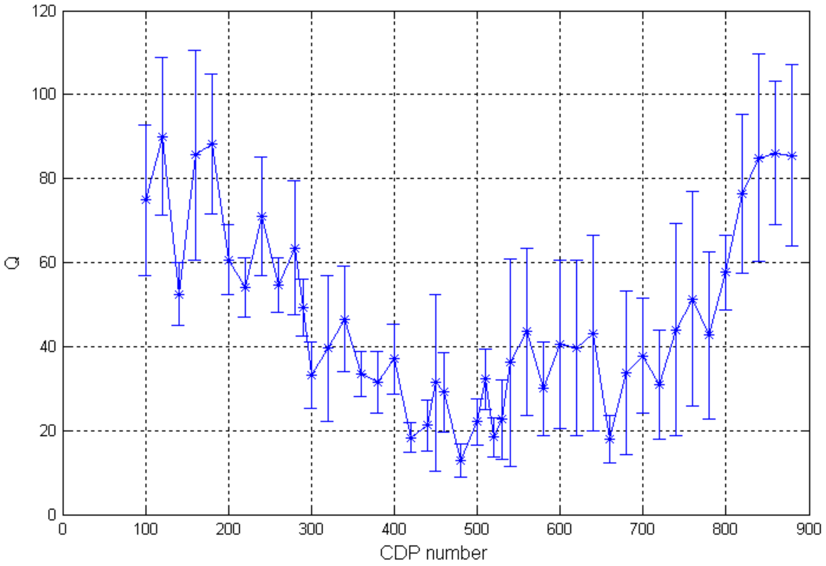

Figure 8.26: Average Q values against CDP number for the fluid-saturated layer. The CO_2 plume lies between CDP 350 and 750 where the average Q values show systematic decrease and is a minimum at CDP 480 which corresponds to the centre of the plume.

8.5 Summary and conclusion

In this chapter, I have investigated the effects of two types of fluid saturation on P-wave attenuation with particular attention to the effects of CO_2. Firstly, I have investigated the influence of mobility on the induced attenuation given a CO_2 saturation of 10 % by considering a range of relaxation times using the poro-elastic model of Chapman (2003). The results of the analysis show that the induced attenuation is sensitive to the relaxation times. For relaxation times $\leq 5.0\text{x}10^{-4}$ s and $\geq 5.0\text{x}10^{-2}$ s, little or no attenuation is observed in the synthetic data. At lower relaxation times, the fluid has little time to flow to neutralize the pressure gradient caused by the propagation of the seismic waves whereas at higher relaxation times, the fluid has sufficient time to flow for pressure equilibration. The fluid mobility is high at lower relaxation times and low at higher relaxation times respectively. In terms of fluid flow, the cracks are isolated at the lower limit but communicating at the higher limit respectively. In between these limits, high attenuation occurs with a maximum attenuation at a relaxation time of 5000 μs for the model properties considered.

I have also examined the sensitivity of the induced attenuation to the degree of CO_2 saturation. The results show that the induced attenuation is higher for 100 % CO_2 saturation than 0 % saturation, implying that the CO_2 causes more attenuation. The attenuation increases with decreasing percentage of CO_2 saturation from 100 % to a maximum at 10 % saturation. The attenuation at higher percentages of saturation especially at 100 % CO_2 is higher than that at 0 % saturation when the material is fully saturated with brine possibly because the properties of CO_2 in the supercritical phase where it behaves as a liquid were used in the modelling. Significant changes occur in the induced attenuation between 10 - 30 % saturation and thereafter very gradual changes occur. No attenuation occurs in the pure isotropic case where the material is neither saturated with fluid nor contains any cracks. The results show that the P-wave attenuation is more sensitive to CO_2 saturation than velocity most especially at higher concentrations when compared to the velocity calculations of David *et al.,* (2008). The induced attenuation increases with crack density as well as offset which are all consistent with the predications of Chapman (2003).

Finally I have also extended the modelling studies in this chapter to a real field data case from the Sleipner gas field where over 11 million tonnes of CO_2 have been injected into the Utsira Sand aquifer since 1996 (Chadwick *et al.*, 2010). The results seem to agree with that of the synthetic studies in the sense that the presence of CO_2 causes more attenuation (lower inferred Q values averaged over all of the traces). However, there exists a lot of scatter in the Q profile results due to (a) the difficulty in picking the exact reflection below the CO_2 plume layer, and (b) the internal multiple interference effects which constitutes a major factor hindering the interpretation of the observed anomaly in the average Q values for the fluid-saturated layer. Theoretically and from the results of the synthetic modelling studies, the presence of CO_2 in the layer should cause increased attenuation. Even though, this effect is observed in the real data, care has to be taken in linking the observed effect to the presence of CO_2 in the layer at this stage. Improvements in the stability of the results can possibly be achieved by trying other techniques like the modified version of the QVO method by Reine *et al.,* (2009) and carrying out some pre-processing work to suppress the internal multiples in the data before attenuation analysis to gain more confidence in the interpretation of the observed Q anomaly in the fluid-saturated layer.

Chapter 9 Conclusions and suggestions for future studies

9.1 Conclusions

In this thesis, I have studied the effects of attenuation anisotropy in fractured porous media, using complementary seismic physical and numerical modelling approaches. The seismic physical modelling approach involves the building of a real, appropriately-scaled model in the laboratory to simulate a fractured reservoir and the recording of its seismic reflection response using the pulse and transmission method. The numerical modelling approach involves solving the seismic wave equation using numerical methods such as the reflectivity method or the finite difference method. In both approaches, the fracture properties in the simulated models are known *a priori*, and I seek to find a link between the attenuation attribute of the seismic response and the known properties from the models. The results provide a clear physical basis for using P-wave attenuation anisotropy to characterize fractured reservoirs with similar properties to the models studied here.

P-wave scattering attenuation anisotropy

Fractures with scale length on the order of the seismic wavelength cause scattering of seismic wave energy which results in seismic coda. The scattered energy is greater in the direction normal to the fractures than in the fracture strike direction. This azimuthal anisotropy in the scattered energy is useful in the determination of the orientations of the fractures. I used the complementary seismic physical (scale-model laboratory experiments) and numerical (finite-difference) modelling approaches to study these scattering anisotropic behaviour and quantified the amount of scattering through estimates of the attenuation factor (the inverse of the seismic quality factor Q) to get more insight into the current use of the scattering energy for delineating fractures from seismic data.

In both approaches, the induced attenuation increases away from the fracture strike direction towards the fracture normal and is maximum normal to the fractures. The observed azimuthal variations in the P-wave attenuation are elliptical, allowing the fracture orientations to be obtained from the axes of the ellipse. The major axis of the Q ellipse corresponds to the fracture strike where minimum attenuation occurs while the minor axis corresponds to the fracture normal where maximum attenuation occurs. The observed attenuation anisotropy is also well fitted by a '$\cos 2\theta$' function (θ is the survey azimuth angle) and maximum attenuation occurs normal to the fracture strike. The results of the ellipse fitting and the cosine fitting are both consistent with the known fracture orientations in the simulated fractured reservoir models and also with the azimuthal anisotropy observed in the stacking velocities in the fractured layer.

Compared with the results of the seismic physical modelling, the magnitude of the scattering attenuation in the finite-difference approach is dependent on the polar angle or source receiver offset, increasing with offset and azimuth away from the fracture strike direction. More significantly, the absolute magnitude of the attenuation anisotropy in the numerical model is smaller when compared with that of the seismic physical modelling results. This may indicate the tractions and the fracture compliances assumed in the numerical model are lower than those used in the physical one, likely due to the way the physical model is manufactured. Furthermore, the uncertainty in the Q estimates is higher in the case of the physical modelling data as would be expected in the real field data case.

Overall, the results of the two approaches demonstrate that azimuthal variations of scattering attenuation are elliptical and that the fracture orientations can be obtained from the axes of the ellipse. These results confirm the practical utility of using attenuation anisotropy as a useful diagnostic tool for delineation of fractures from seismic data, in a way that complements the use of other seismic attributes, at least for the relatively simple geometries of subsurface structure investigated here.

Effects of fluid saturation on P-wave attenuation anisotropy

Empirically, the magnitude of P-wave attenuation anisotropy is greater in fluid-saturated rocks than in dry rocks. The pressure gradient generated by a seismic wave propagating in a fractured fluid-saturated porous rock causes exchange of fluid between the fractures and the surrounding pore space, resulting in attenuation. I studied the effects of fluid saturation on P-wave attenuation using the poro-elastic model of Chapman (2003) to gain more understanding of the fluid effects. Firstly, I investigated the effects of fluid mobility on the induced attenuation by considering a range of relaxation times in Chapman’s (2003) poro-elastic model. The relaxation time strongly controls the frequency range over which attenuation occurs. Little or no attenuation occurs at low (≤ 500 Hz) or high (≥ 500 kHz) frequencies or their equivalent relaxation times. In between these two limits, attenuation occurs with a maximum magnitude around a relaxation time of $2.0\text{x}10^{-5}$ s (or frequency of 50 kHz). These relaxation times and the associated frequencies are associated with the fluid flow at the grain scale. The introduction of fractures causes attenuation at lower frequencies depending on the size of the fractures compared with the grain size as predicted by Chapman’s model (2003). Thus at the fracture scale, these frequencies translate into 0.6 - 160 Hz with a maximum attenuation around a frequency of 20 Hz.

The induced attenuation increases in magnitude with incidence (polar) angle (offset) and away from the fracture strike direction, which is consistent with the predictions of Chapman’s model (2003) and the results of the walk away VSP studies of

Maultzsch *et al.*, (2007). Azimuthal variations in the induced attenuation are elliptical and are also well fitted by a ‘cos2θ’ function, allowing the fracture orientations to be obtained from the axes of the ellipse. The major axis of the Q ellipse also corresponds to the fracture strike direction where less attenuation occurs while the minor axis corresponds to the fracture normal direction where maximum attenuation occurs. A minimum offset of 400 m (or incidence angle of 8.4°) corresponding to an offset-depth ratio of 0.4 and 0.25 to the top and bottom of the fractured-layer respectively is, however, needed to reveal the azimuthal variations in the induced attenuation. The magnitude of the attenuation anisotropy increases with offset and is higher than the case of the dry fractured rocks.

Effect of fracture thickness or aperture

Hudson’s (1980, 1981) equivalent theory provides a means of obtaining crack density information from measurement of anisotropy. However, the same crack density can result from many small cracks, from a few large cracks or from an equal number of cracks with the same radius but varying thicknesses (or aperture) in the same volume of background material. This ambiguity highlights the inability of the theory to distinguish between the underlying causes of anisotropy. I studied the effects of fracture thickness or aperture on P-wave scattering attenuation through seismic physical modelling. The induced attenuation increases with fracture thickness or aperture, implying more scattering of the seismic wave energy as the wave propagates in the direction of increasing thickness or aperture. Although the simulated fractures may not be real fractured analogues, this result indicates the potential of using P-wave attenuation to get information which might be useful in examining the effects of voids in carbonate rocks and also provide a basis for further theoretical development to distinguish the effects caused by thin micro cracks and large open fractures.

Effects of CO_2 saturation

Seismic attenuation depends not only on the physical state of the rocks, but also on the nature of the fluid saturation in the pores of the rock. I studied the effects of two types of fluid saturation (brine and CO_2 in the supercritical state) on P-wave attenuation, with particular attention to the effects of CO_2 using the CO_2 properties at the Sleipner gas field in the North Sea. Firstly, I investigated the influence of fluid mobility on the induced attenuation given a CO_2 saturation of 10 % by considering a range of relaxation times using the poro-elastic model of Chapman (2003). The fluid mobility is assumed to be the effective mobility of the two fluids and viscosity effects are not taken into account. Again the relaxation time strongly controls the frequency band over which attenuation occurs. Little or no attenuation occurs at low ($\leq 5.0 \mathrm{x} 10^{-6}$ s) or high $\geq 5 \mathrm{x} 10^{-2}$ s) relaxation times. In between these limits, high attenuation occurs with a maximum attenuation around a relaxation time of 5000 μs. This is slightly higher than the case of a single fluid saturation in the pores of the rock possibly because it is weakly dependent on the effective fluid bulk modulus.

I also studied the sensitivity of the induced attenuation to the degree of CO_2 saturation. The induced attenuation is influenced by the effective fluid bulk modulus which is dependent on the percentages of saturation of CO_2. The attenuation is very sensitive to the percentage of CO_2 saturation and is higher for 100 % CO_2 saturation than for 0 % saturation, implying that the CO_2 causes more attenuation than brine. Another factor that affects the magnitude of the induced attenuation is the crack density. The attenuation increases with increasing crack density as well as with offset which are all consistent with the predictions of Chapman (2003). No attenuation occurs in the pure isotropic case where the material is neither saturated with fluid nor contains any cracks. The attenuation increases with decreasing percentage of CO_2 saturation from 100 % to a maximum at 10 % saturation. The attenuation at higher percentages of saturation especially at 100 % CO_2 is higher than that at 0 % saturation when the material is fully saturated with brine possibly because the properties of CO_2 in the supercritical phase where it behaves as a liquid were used in the modelling. Significant changes occur in the induced attenuation between 10 - 30 % saturation and thereafter only very gradual changes occur. The results show that the P-wave attenuation is even more sensitive to CO_2 saturation than velocity, most especially at higher concentrations when compared to the velocity calculations of David *et al.*, (2008).

Finally, I extended the synthetic modelling studies to a real field data scenario from the Sleipner gas field where over 11 million tonnes of CO_2 have been injected into the Utsira Sand aquifer since 1996. Although the results from the field data example seem to agree with that of the synthetic studies in the sense that the presence of CO_2 causes more attenuation, care has to be taken in linking this effect to the presence of CO_2. This is due the scatter in the Q profile results probably caused by the internal multiple interference effects for the fluid-saturated layer. This demonstrates that the accuracy of Q estimate from seismic data is highly dependent on the data quality. In analysing physical or numerical models, the synthetic data quality is high and the Q estimates are not affected by interference effects such as multiple reflections. Improvements in the stability of the results for the field data example can possibly be achieved by trying other techniques of Q estimation, especially the modified version of the QVO method by Reine *et al.,* (2009) to gain more confidence in the interpretation of the observed Q anomaly in the fluid-saturated layer.

On the whole, the results of this thesis demonstrate that a set of aligned vertical fractures (HTI media) causes attenuation of P-waves. The induced attenuation exhibits characteristic variations with azimuths which are elliptical. The major axis of the Q ellipse corresponds to the fracture strike direction where minimum attenuation occurs while the minor axis corresponds to the fracture normal direction where maximum attenuation occurs. Azimuthal variations in the attenuation are also well fitted with a $\cos 2\theta$ function where θ is the survey azimuth and maximum attenuation occurs in the direction normal to the fracture strikes. These findings could help to resolve the 90° ambiguity in the fracture orientation obtained from AVOA analysis observed by Hall and Kendall (2000 and 2003). Thus, given a full-azimuthal seismic data, the fracture orientations can be inferred from measurement of attenuation anisotropy to supplement the use of amplitudes, travel time, velocity and AVO gradient attributes

The results of the thesis also demonstrate that P-wave attenuation anisotropy is sensitive to fluid saturation in the pores of the rocks. The induced attenuation anisotropy has a higher magnitude in fluid saturated fractured rocks than in dry fractured rocks. The introduction of CO_2 for example, into brine causes significant changes in the fluid bulk modulus resulting in more attenuation.

9.2 Suggestions for future studies

The results from this thesis demonstrate that P-wave attenuation anisotropy is a potential tool for characterization of the hydrocarbon reservoirs. However, there are still a few issues which need to be addressed to have a fuller understanding of the use of this attribute in geophysical exploration. Considering the work done in this thesis, I will suggest the following future studies in this subject area:

- Physical modelling to study the effects of fracture radius on seismic attenuation. A fractured model with the same density and aperture or thickness but with varying diameter could be built to study the effects of fracture radius though this might be quite a difficult task.
- Effect of noise in the models. This study has demonstrated that the presence of noise in the data could influence the Q estimates. Multiples entering into the analysis window might results in erroneous Q estimates which cannot be interpreted geologically. Thus, introducing noise into the physical model data might depict a more realistic field data and allow other techniques of Q estimation to be tested
- Geologic structures such as faults and anticline could be introduced into the physical models to investigate their effects on seismic attenuation.
- The synthetic study demonstrates that the presence of CO_2 in the pores of the rocks causes more seismic attenuation but fractures were not considered in the theoretical model used in the study. Further work is needed to quantify the additional effect of fractures on the results.
- Real data example: the difficulty in isolating the target reflection events and the influence of internal multiples constitute the major factors hindering the interpretation of the observed anomaly in the average Q values for the fluid-saturated layer. Improvements in the stability of the results could possibly be achieved by trying other spectral estimation techniques such as the use of the S-transform and the continuous wavelet transform. More pre-processing work could be done to suppress the noise and internal multiples in the data in order

to improve the S/N ratio prior to attenuation analysis. The modified version of the QVO method by Reine *et al.*, (2009) could also be tried on the data to gain more confidence in the interpretation of the observed Q anomaly in the fluid-saturated layer.

References

Aki, K. and Richards, P. G., 2002. Quantitative Seismology - 2nd Edition. University Science Books.

Amir, G and Landro, M., 2009. Estimation of thickness and velocity changes of injected carbon dioxide layers from pre-stack time-lapse seismic data. *Geophysics*, **74**(2), 017- 028.

Arts, R., Chadwick, A., Eiken, O., Thibeau, S. and Nooner, S., 2008. Ten years' experience of monitoring CO2 injection in the Utsira Sand at Sleipner, offshore Norway. *First Break*, **26**, 65 - 72.

Arts, R., Eiken, O., Chadwick, A., Zweigel, P., van der Meer, L. and Zinszner, B., 2004. Monitoring of CO2 injected at Sleipner using time-lapse seismic data. *Energy,* **29**, 1383 - 1392.

Bakulin, A., Grechka, V. and Tsvankin, I., 2000. Estimation of fracture parameters from reflection seismic data-Part 1: HTI model due to a single fracture set. *Geophysics*, **65**(6), 1788 - 1801.

Bansal, R. and Sen, M.K., 2008. Finite-difference modelling of S-wave splitting in anisotropic media. *Geophysical Prospecting*, **56**, 293 - 312.

Barnes, A. E., 1992. Another look at NMO stretch. *Geophysics*, **57**, 749 - 751.

Batzle, M. L., Han, D. H. and Hofmann, R., 2006. Fluid mobility and frequency-dependent seismic velocity - Direct measurements. *Geophysics,* 71(1), N1 - N9.

Batzle, M., Hofmann, R. and Prasad, M, 2005. Seismic Attenuation: Observations and Mechanisms. *75th Annual International Meeting, Expanded Abstract, SEG,* 1565 - 1568.

Berryman, J . G., 1979. Long-wave elastic anisotropy in transversely isotropic media. *Geophysics*, **44**(5), 896 - 917.

Berryman, J.G., 1980. Long-wavelength propagation in composite elastic media. *Journal of the Acoustical Society of America*, **68**, 1809 - 1831.

Bickle, M., Chadwick, A., Huppert, H. E., Hallworth, M. and Lyle, S., 2007. Modelling carbon dioxide accumulation at Sleipner: Implications for underground carbon storage. *Earth and Planetary Science Letters,* **255**, 164 - 176.

Biot, M.A., 1956. Theory of propagation of elastic waves in a fluid-saturated porous solid. **I**. low frequency range and **II**. higher frequency range. *Journal of the Acoustical Society of America*, **28**, 168- 191.

Block, L., Cheng, C. H., Fehler, M. and Phillips, W. S., 1994. Seismic imaging using micro-earthquakes induced by hydraulic fracturing. *Geophysics,* **59**, 102 -112.

Booth, D. C., 1982. The anisotropic reflectivity technique. PhD thesis, University of Edinburgh.

Booth, D. C. and Crampin, S., 1983. The anisotropic reflectivity technique: Theory. *Geophysical Journal of the Royal Astronomical Society*, **72**, 755 - 766.

Brown, R. J. S., and Korringa, J., 1975. On the dependence of the elastic properties of porous rock on the compressibility of the pore fluid. *Geophysics*, **40**, 608 - 616.

Burns, D. R., Willis M. E., and Toksöz, M. N., 2007. Fracture properties from seismic scattering. *The Leading Edge*, 1186 - 1196.

Bush, I. and Crampin, S., 1991. Paris Basin VSPs: Case history establishing combinations of fine-layer (or lithologic) anisotropy and crack anisotropy from modelling shear wavefields near point singularities. *Geophysical Journal International,* **107**, 433 - 447.

Carter, A. J., 2003. Seismic wave attenuation from surface seismic reflection surveys - An exploration tool. PhD thesis, University of Leeds.

Castoro, A., White, R. E. and Thomas, R. D., 2001. Thin-bed AVO: Compensating for the effects of NMO on reflectivity sequences. *Geophysics*, **66**, 1714-1720.

Cerjan, C., Kosloff, D., Kosloff, R. and Resef, M., 1985. A non-reflecting boundary condition for discrete acoustic and elastic wave equations. *Geophysics*, **50**, 705-708.

Chadwick, R. A., Arts, S. and Eiken, O., 2005. 4D seismic quantification of a growing CO_2 plume at Sleipner, North Sea. In: Dore, A.G. and Vining, B. (Eds.). Petroleum Geology: *North-West Europe and Global Perspectives- Proceedings of the 6th Petroleum Geology Conference*, 1385 - 1399.

Chadwick, A., Arts, R., Eiken, O., Williamson, P. and Williams, G., 2006. Geophysical monitoring of the CO_2 plume at Sleipner, North Sea: An outline review. *Advances in the Geological Storage of Carbon Dioxide*, 303 - 314.

Chadwick, R. A., Williams, G., Delepine, N., Clochard, V., Labat, K., Sturton, S., Buddensiek, M.-L., Dillen, M., Nickel, M., Lima, A. L., Arts, R., Neele, F. and Rossi, G., 2010. Quantitative analysis of time-lapse seismic monitoring data at the Sleipner CO_2 storage operation: *The Leading Edge*, **29**, 170 - 177.

Chakraborty, A. and Okaya, D., 1995. Frequency-time decomposition of seismic data using wavelet-based methods. *Geophysics*, **60**, 1906 - 1916.

Chapman, C. H., 2004. Fundamentals of Seismic Wave Propagation. Cambridge University Press.

Chapman, M., 2001. Modelling the wide-band laboratory response of rock samples to fluid and pressure changes. PhD thesis, University of Edinburgh.

Chapman, M., 2003. Frequency-dependent anisotropy due to meso-scale fractures in the presence of equant porosity. *Geophysical Prospecting*, **51**, 369-379.

Chapman, M. and Liu, E., 2006. Seismic attenuation in rocks saturated with multi-phase fluids. *76th Annual International Meeting, SEG, Extracted Abstracts*, 1988-1992.

Chapman, M., Zatsepin, S. V. and Crampin, S., 2002. Derivation of a microstructural poroelastic model. *Geophysical Journal International*, **151**, 427 - 451.

Chapman, M., Maultzsch, S., Liu, E. and Li, X. Y., 2003. The effect of fluid saturation in an anisotropic multi-scale equant porosity model. *Journal of Applied Geophysics*, **54**, 191 - 202.

Cheadle, S. P., Brown, R. J. and Lawton, D. C., 1991. Orthorhombic anisotropy: A physical seismic modelling study. *Geophysics*, **56**, 1603 - 1613.

Chen, S. Q., Chadwick, A. and Li, X. Y., 2010. CO_2 induced dispersion and attenuation effects: a case study. *EAP Annual Report*, **73**, C4-1 - C4-11.

Chichinina,T., Sabinin, V. and Ronquillo-Jarillo, G. 2006. QVOA analysis: P-wave attenuation anisotropy for fracture characterization. *Geophysics*, **71**(3), C37 - C48.

Chung, H. and Lawton, D. C., 1995. Frequency characteristics of seismic reflections from thin beds. *Canadian Journal of Exploration Geophysics*, 31, 32-37.

Clark, R. A., Benson, P. M., Carter, A. J. and Guerrero Moreno, C. A., 2009. Anisotropic P-wave attenuation measured from a multi-azimuth surface seismic reflection survey. *Geophysical Prospecting*, **57**, 835 - 845.

Clark, R. A., Carter, A. J., Nevill, P. C. and Benson, P. M., 2001. Attenuation measurement from surface seismic data - Azimuthal variation and time lapse case studies: *63rd Conference and Technical Exhibition, Expanded Abstracts*, EAGE, L-28.

Coates, R. T. and Schoenberg, M., 1995. Finite-difference modelling of faults and fractures. *Geophysics*, **60** (5), 1514 - 1526.

Contreras, P., Grechka, V. and Tsvankin, I., 1999. Moveout inversion of P-wave data for horizontal transverse isotropy. *Geophysics*, **64** (4), 1219 - 1229.

Crampin, S., 1981. A review of wave motion in anisotropic and cracked elastic-media. *Wave Motion*, **3**, 343 - 391.

Crampin, S., 1989. Suggestions for a consistent terminology for seismic anisotropy. *Geophysical Prospecting*, **37**, 753 - 770.

Dasgupta, R. and Clark, R., 1998. Estimation of Q from surface seismic reflection data. *Geophysics*, **63**(6): 2120 - 2128.

Dasios, A., Astin, T. R. and McCann, C., 2001. Compressional-wave Q estimation from full-waveform sonic data. *Geophysical Prospecting*, **49**, 353 - 373.

David, L., Don, A., Wright, R., Dave, M. and Cole, S., 2008. Seismic monitoring of CO2 geo-sequestration: realistic capabilities and limitations. *78th Annual International Meeting, Extracted Abstracts*, *SEG*, 2841 - 2845.

Davis, T. L., Terrell, M. J., Benson, R. D., Cardona, R., Kendall R. and Winarsky, R., 2003. Multicomponent seismic characterization and monitoring of CO2 flood at Weyburn Field, Saskatchewan. *The Leading Edge*, **22**, 696 - 697.

Dunkin, J. W. and Levin, E. K., 1973. Effects of normal moveout on a seismic pulse. *Geophysics*, **38**, 635 - 642.

Dvorkin, J. and Mavko, G., 2006. Modelling attenuation in reservoir and non-reservoir rock. *The Leading Edge*, **25**(2):194 - 197.

Dvorkin, J., Mavko, G. and Nur, A., 1995. Squirt flow in fully saturated rocks. *Geophysics*, **60**, 97 - 107.

Eshelby, J. D., 1957. The determination of the elastic field of an ellipsoidal inclusion, and related problem. *Proceedings of the Loyal Society of London*, **A241**, 376 - 396.

Fuchs, K. and Muller, G., 1971. Computation of synthetic seismograms with the reflectivity method and comparison with observations. *Geophysical Journal of the Royal Astronomical Society*, **23**, 417 - 433.

Futterman, W. I., 1962. Dispersive body waves. *Journal of Geophysical Research,* **85**, 5279 - 5211.

Gardner, G. H. F., Wyllie, M. R. J. and Droschak, D. M., 1964. Effects of pressure and fluid saturation on the attenuation of elastic waves in sands. *Journal of Petroleum Technology,* **16**, 189 - 198.

Gassmann, F., 1951. Uber die Elastizitat poroser Medien. *Vierteljahresschr. der Naturforsch. Ges*. Zurich, 96, 1 - 21.

Graves R.W., 1996. Simulating seismic wave propagation in 3D elastic media using staggered-grid finite difference. *Bulletin of the Seismological Society of America,* **86** (4), 1091-1106.

Gray, D. and Head, K., 2000. Fracture detection in Manderson Field: A 3-D AVAZ case history. *The Leading Edge*, **19**(11), 1214 - 1221.

Grechka, V., Contreras, P. and Tsvankin I., 2000. Inversion of normal moveout for monoclinic media. *Geophysical Prospecting,* **48***,* 577 - 602.

Grechka, V. and Tsvankin, I., 1998. 3-D description of normal moveout in anisotropic inhomogeneous media: *Geophysics*, **63**, 1079 - 1092.

Guerrero Moreno C. A., 2006. Fractured induced seismic wavespeed and attenuation anisotropy in hydrocarbon exploration. PhD thesis, School of Earth Sciences, University of Leeds.

Hackert, C. L. and Parra, J. O., 2004. Improving Q estimates from seismic reflection data using well-log-based localized spectral correction. *Geophysics,* **69**(6), 1521 - 1529.

Hall, M., 2006. Resolution and uncertainty in spectral decomposition. *First Break*, **24**, 43 - 47.

Hall, S. A. and Kendall, J. M., 2000. Constraining the interpretation of AVOA for fracture characterization, in Anisotropy: Fractures, converted waves, and case studies. *SEG*, 107 - 144.

Hall, S. A. and Kendall, J. M., 2003. Fracture characterization at Valhall: Application of P-wave amplitude variation with offset and azimuth AVOA analysis to a 3D ocean-bottom data set. *Geophysics,* **68**, 1150 - 1160.

Hall, S. A., Kendall, J. M., Barkved, O. I. and Mueller, M. C., 2000. Fracture characterization using P-wave AVOA in 3D OBS data. *SEG, Expanded Abstracts*, 1409 - 1412.

Hall, S. A., Kendall, J. M. and Barkved, O. I., 2002. Fractured reservoir characterization using P-wave AVOA analysis of 3D OBC data. *The Leading Edge*, 776 - 781.

Han, D. and Batzle, M. L., 2004. Gassmann's equation and fluid-saturation effects on seismic velocities. *Geophysics*, **69**(2), 398 - 405.

Hauge P. S., 1981. Measurements of attenuation from vertical seismic profiles. *Geophysics*, **46**, 1548 - 1558.

Helle, H. B., Pham, N. H. and Carcione, J. M., 2003. Velocity and attenuation in partially saturated rocks: poroelastic numerical experiments. *Geophysical Prospecting*, **51**, 551 - 566.

House, N., Fuller, B. and Shemeta, J., 2004. Integration of surface seismic, 3D VSP, and microseismic hydraulic fracture mapping to improve gas production in a tight complex reservoir. *74th Annual International Meeting, Expanded Abstracts, SEG,* 414 - 416.

Hua, L. G., Fan, L. X and Gen, Z. M., 2009. The application of staggered-grid Fourier pseudo-spectral differentiation operator in wavefield modelling. *Chinese Journal of Geophysics,* **52**(1), 214 - 221.

Hudson J. A., 1980. Overall properties of a cracked solid. *Mathematical Proceedings of the Cambridge Philosophical Society*, **88**, 371 - 384.

Hudson, J. A., 1981. Wave speeds and attenuation of elastic waves in material containing cracks. *Geophysical Journal of the Royal Astronomical Society*, **64**, 133 - 150.

Hudson, J. A., Liu, E. and Crampin, S., 1996. The mechanical properties of materials with interconnected cracks and pores. *Geophysical Journal International*, **124**, 105 - 112.

Hustedt, B. G. and Clark, R. A., 1999. Source/receiver array directivity effects on marine seismic attenuation measurements. *Geophysical Prospecting*, **47**, 1105 - 1119.

Igel, H., Mora, P. and Riollet B., 1995. Anisotropic wave propagation through finite-difference grids. *Geophysics*, **60**(4), 1203 - 1216.

Isaac, J. H and Lawton, D. C., 1999. Image mispositioning due to dipping TI Media: A physical seismic modelling study. *Geophysics,* **64**, 1230 - 1238.

Jeng, Y., Tsai, J-Y. and Chen, S-H., 1999. An improved method of determining near-surface Q. *Geophysics*, **64**(5), 1608 - 1617.

Jenner, E., 2002. Azimuthal AVO: Methodology and data examples. *The Leading Edge*, **21**, 782 - 786.

Johnson, D. H., 1981. Attenuation: A state of the art summary. Seismic Wave Attenuation, SEG Geophysical Reprint Series, 123 - 135.

Johnson, D., Toksoz, M. and Timur, A., 1979. Attenuation of seismic waves in dry and saturated rocks: II. Mechanisms. *Geophysics*, **44**(4): 691 - 711.

Johnson, D. H. and Toksöz, M. N., 1980. Ultrasonic P and S wave attenuation in dry and saturated rocks under pressure. *Journal of Geophysical Research*, **85**, 925 - 936.

Jones, D. J., 1986. Pore fluids and frequency-dependent wave propagation in rocks. *Geophysics*, **51**, 1939 - 1953.

Jones, S. M., Astin, T . R., McCann, C. and Sothcott J., 1997. The effect of the degree of saturation on ultrasonic velocity and attenuation in sandstones, *67th Annual International Meeting, Expanded Abstracts, SEG*, P1023.

Kelly, K.R., Ward, R.W., Treitel, S., Alford, R.M., 1976. Synthetic seismograms: a finite- difference approach. *Geophysics*, **41**(1), 2 - 27.

King, M. S. and Marsden, J. R., 2002. Velocity dispersion between ultrasonic and seismic frequencies in brine-saturated reservoir sandstones. *Geophysics*, **67**(1), 254 - 258.

Klimentos, T., 1995. Attenuation of P- and S-waves as a method of distinguishing gas and condensate from oil and water. *Geophysics*, **60**, 447 - 458.

Klimentos, T. and McCann , C., 1990. Relationship among compressional wave attenuation, porosity, clay content, and permeability in sandstones. *Geophysics,* **55**(8), 998 - 1014.

Kuster, G. T. and Toksoz, M. N., 1974. Velocity and attenuation of seismic waves in two-phased media: part II. Experimental results. *Geophysics*, **39**(5), 607 - 618.

Landro, A. M. and Amundsen, L., 2010. Marine seismic sources Part II. *GEOExPro,* **7**(2). Available at: http://www.geoexpro.com/article/Marine_Seismic_Sources_Part_II/ebec6542.aspx

Lange, J. N. and Almoghrabi, H. A., 1988. Lithology discrimination for thin layers using wavelet signal parameters. *Geophysics*, **53**(12), 1512-1519.

Leonard, T. and Hsu, J. S. J., 1999. Bayesian Methods: an analysis for statistician and interdisciplinary researchers. Cambridge University Press.

Li, X. Y., 1997. Fracture reservoir delineating using multi-component seismic data. *Geophysical Prospecting*, **54**, 39 - 64.

Li, X. Y., 1999. Fracture detection using azimuthal variation of P-wave moveout from orthogonal seismic survey lines. *Geophysics*, **64**, 1193 - 1201.

Li, X. Y., Liu, Y. J., Liu, F., Shen, Li, Q. and Qu, S., 2003. Fracture delineation using land 3D seismic data from Yellow River delta, China. *The Leading Edge*, **22**, 680 - 684.

Liu, E., Hudson, J. A. and Pointer, T., 2000. Equivalent medium representation of fractured rock. *Journal of Geophysical Research*, **105**, 2981 - 3000.

Liu, E., Queen, J. H., Li, X. Y., Chapman, M., Maultzsch, S., Lynn, H. B. and Chesnokov, E. M., 2003. Observation and analysis of frequency - dependent anisotropy from a multi-component VSP at Bluebell- Altamont Field, Utah. *Journal of Applied Geophysics*, **54**, 319 - 333.

Liu, H-P., 1988. Effect of source spectrum on seismic attenuation measurements using the pulse-broadening method. *Geophysics*, **53**(12), 1520 - 1526.

Liu, Y. J., 2003. Analysis of P-wave Seismic Reflection Data for Azimuthal Anisotropy. PhD thesis, University of Edinburgh.

Lubbe, R. and Worthington, M. H., 2006. A field investigation of fracture compliance. *Geophysical Prospecting*, **54**, 319 - 332.

Lucet, N. and Zinszner, B., 1992. Effects of heterogeneities and anisotropy on sonic and ultrasonic attenuation in rocks. *Geophysics*, **57**, 1018 - 1026.

Luo, M., Arihara, N., Wang, S., Di, B. and Wei, J., 2006. Abnormal transmission attenuation and its impact on seismic-fracture prediction - A physical modelling study. *Geophysics*, **71**, D15 - D22.

Luo, M. and Evans, B. J., 2004. An amplitude-based multi-azimuth approach to mapping fractures using p-wave 3D seismic data. *Geophysics*, **69**(3), 690 - 698.

Lynn H. B., 2004. The winds of change. Anisotropic rocks – their preferred direction of fluid flow and their associated seismic signatures – Part 1. *The Leading Edge* **23**, 1156 - 1162.

Lynn, H. and Beckham, W., 1998. P-wave azimuthal variations in attenuation, amplitude and velocity in 3-D field data: Implications for mapping horizontal permeability anisotropy. *68th Annual International Meeting, Expanded Abstracts, SEG*, 193 - 196.

MacBeth, C., 1999. Azimuthal variation in P-wave signatures due to fluid flow. *Geophysics*, **64**(4), 1181 - 1192.

Madariaga, R., 1976. Dynamics of an expanding circular fault. *Bulletin of the Seismological Society of America*, **66**, 639 - 666.

Mallick, S., Craft, K. L., Meister, L. J. and Chambers, R. E., 1998. Determination of the principal directions of azimuthal anisotropy from P-wave seismic data. *Geophysics*, **63**, 692 - 706.

Marfurt K. J., 1984. Accuracy of finite-difference and finite-element modelling of the scalar and elastic wave equations. *Geophysics*, **49**, 533 - 549.

Matheney, M. P and Nowack, R. B., 1995. Seismic attenuation values obtained from instantaneous-frequency matching and spectral ratios. *Geophysical Journal International*, **123**, l -15.

Matsushima, J., Suzuki, M., Kato, Y., Nibe, T. and Rokugawa, S., 2008. Laboratory experiments on compressional ultrasonic wave attenuation in partially frozen brines. *Geophysics*, **73**(2), N9 - N18.

Maultzsch, S., 2005. Analysis of frequency-dependent anisotropy in VSP data. PhD thesis, University of Edinburgh.

Maultzsch, S., Chapman, M. Liu, E. and Li, X. Y., 2003. Modelling frequency-dependent seismic anisotropy in fluid-saturated rock with aligned fractures:

Implication of fracture size estimation from anisotropic measurements *Geophysical Prospecting*, **51**, 381 - 392.

Maultzsch, S., Chapman, M., Liu, E. and Li, X. Y., 2007. Modelling and analysis of attenuation anisotropy in multi-azimuth VSP data from Clair field. *Geophysical Prospecting,* **55**, 627 - 642.

Mavko, G. and Jizba, D., 1991. Estimating grain-scale fluid effects on velocity dispersion in rocks. *Geophysics*, **56**, 1940 - 1949.

Mavko, G. M., and Nur, A., 1979. Wave attenuation in partially saturated rocks, *Geophysics*, **44**, 61 - 178.

Mavko, G., Mukerji, T. and Dvorkin, J., 2009. *The Rock Physics Handbook - 2nd edition*. Cambridge University Press.

Minsley, B., Willis, M. E., Krasovec, M., Burns, D. and Toksöz, M. N., 2004. Investigation of a fractured reservoir using P-wave AVOA analysis: A case study of the Emilio Field with support from synthetic examples. *74th Annual International Meeting, Expanded Abstracts, SEG, 248* - 251.

Moczo, P., Kristek, J. and Halada, L., 2000. 3D fourth-order staggered-grid finite-difference schemes: stability and grid dispersion. *Bulletin of the Seismological Society of America*, **90**(3), 587 - 603.

Mukerji, T. and Mavko, G., 1994. Pore fluid effects on seismic velocity in anisotropic rocks. *Geophysics,* **59**, 233 - 244.

Muller, T. M., Gurevich, B. and Lebedev, M., 2010. Seismic wave attenuation and dispersion resulting from wave-induced flow in porous rocks - A review. *Geophysics*, **75**(5), 75A147 - 75A164.

Murphy, W. F., 1985. Sonic and ultrasonic velocities: Theory versus experiment. *Geophysical Research Letters*, **12**, 85 - 88.

Nishizawa, O., 1982. Seismic velocity anisotropy in a medium containing oriented cracks-transversely isotropic case. *Journal Physics of the Earth*, **30**, 331 - 347.

Odebeatu, E., Zhang, J., Chapman, M., Liu, E. and Li, X. Y., 2006. Application of spectral decomposition to detection of dispersion anomalies associated with gas saturation. *The Leading Edge*, **25**, 206 - 210.

O'Connell, R. J. and Budiansky, B., 1974. Seismic velocities in dry and saturated cracked solids. *Journal of Geophysical Research*, **79**, 5412 - 5426.

O'Connell, R. J. and Budiansky, B., 1977. Viscoelastic properties of fluid saturated cracked solids, *Journal of Geophysical Research*, **82**, 5719 - 5735.

O'Doherty, R. F. and Anstey, N. A., 1971. Reflections on amplitudes. *Geophysical Prospecting*, **19**, 430 - 458.

Press, W. H., Teukolsky, S. A., Vetterling, W. T. and Flannery, B. P., 2007. Numerical Recipes: *The art of scientific computing* - 3rd Edition. Cambridge University Press.

Pujol J. and Smithson S., 1991. Seismic wave attenuation in volcanic rocks from VSP experiments. *Geophysics*, **56**, 1441 - 1455.

Pyrak-Nolte, L. J., Myer, L. R. and Cook, N. G. W., 1990. Transmission of seismic waves across single natural fractures. *Journal of Geophysical Research*, **95**, 8617 - 8638.

Qian, Z., Chapman, M., Li, X. Y., Dai, H. C., Liu, E., Zhang, Y. and Wang, Y., 2007. Use of multi-component seismic data for oil-water discrimination in fractured reservoirs. *The Leading Edge*, **26**, 1176 - 1184.

Quan, Y. and Harris, J. M., 1997. Seismic attenuation tomography using the frequency shift method. *Geophysics*, **62**(3), 895 - 905.

Raikes, S. A. and White R. E., 1984. Measurements of earth attenuation from downhole and surface seismic recordings. *Geophysical Prospecting*, **32**, 892 - 919.

Rathore, J. S., Fjaer, E., Holt, R. M. and Renlie, L., 1995. P- and S-wave anisotropy of a synthetic sandstone with controlled crack geometry. *Geophysical Prospecting*, **43**, 711 - 728.

Reine, C., van der Baan, M. and Clark, R., 2009. The robustness of seismic attenuation measurements using fixed-and variable-window time-frequency transforms. *Geophysics*, **74**(2), WA123 - WA135.

Ricker, N., 1940. The form and nature of seismic waves and the structure of seismograms. *Geophysics*, **5**, 348-366.

Ricker, N., 1945. The computation of output disturbances from amplifiers for true wavelet inputs. *Geophysics*, **10**, 207-220.

Rioul, O. and Vetterli, M., 1991. Wavelets and signal processing: *IEEE Signal Processing Magazine*, 14 - 38.

Roberts, J., 2009. Developing the Rock Physics Model - Improved Carbon Dioxide Mixing Rules for Carbon Capture and Storage. *71st Conference and Technical Exhibition, EAGE, Expanded Abstracts*.

Robertson, J. D. and Nogami, H. H., 1984. Complex seismic trace analysis of thin beds. *Geophysics*, **49**, 34 - 352.

Rongrong, L., Rickett, J. and Stefani, J., 2006. Angle-dependent attenuation estimates from a walk-away VSP. *76th Annual International Meeting, SEG, Expanded Abstracts*, 2136 - 2140.

Ruger, A., 1997. P-wave reflection coefficients for transversely isotropic models with vertical and horizontal axis of symmetry. *Geophysics*, **62**, 713-722.

Ruger A., 1998. Variation of P-wave reflectivity with offset and azimuth in anisotropic media. *Geophysics*, **63**, 935 - 947.

Sams, M. and Goldberg D., 1990. The validity of Q estimates from borehole data using spectral ratios. *Geophysics*, **55**, 97 - 101.

Sayers, C. M., 2002. Fluid-dependent shear-wave splitting in fractured media. *Geophysical Prospecting,* **50**, 393 - 401.

Sayers, C. M. and Ebrom, D. A., 1997. Seismic travel time analysis for azimuthally anisotropic media: Theory and Experiment. *Geophysics,* **62**, 1570 - 1582.

Schoenberg, M., 1980. Elastic wave behaviour across linear-slip interfaces. *Journal of the Acoustical Society of America,* **68**, 516 - 1521.

Schoenberg, M. and Douma, J., 1988. Elastic-wave propagation in media with parallel fractures and aligned cracks. *Geophysical Prospecting,* **36**, 571 - 590.

Schoenberg, M. and Protazio, J., 1992. 'Zoeppritz' rationalized and generalized to anisotropy. *Journal of Seismic Exploration*, **1**, 125 - 144.

Schoenberg, M. and Sayers C., 1995. Seismic anisotropy of fractured rock. *Geophysics,* **60**, 204 - 211.

Schultz, C. A. and Toksöz, M. N., 1995. Reflections from a randomly grooved interface: ultrasonic modelling and finite-difference calculation. *Geophysical Prospecting*, **43**, 581 - 594.

Sena, A. G., 1991. Seismic traveltime equations for azimuthally anisotropic and isotropic media: Estimation of interval elastic properties. *Geophysics,* **56**, 2090 - 2101.

Shaw, F., Worthington, M. H., White, R. S., Anderson. M. S. and Petersen, U. K., 2008. Seismic attenuation in Faroe Islands basalts. *Geophysical Prospecting,* **56**, 5 - 20.

Shearer, P. M., 1999. Introduction to seismology. Cambridge University Press.

Shen, F., Sierra, J., Burns, D. R. and Toksöz, M. N., 2002. Azimuthal offset-dependent attributes applied to fracture detection in a carbonate reservoir. *Geophysics*, **67**, 355 - 364.

Sheriff, R., 1975. Factors affecting seismic amplitudes. *Geophysical Prospecting*, **23**, 125 - 138.

Sheriff, R. E. and Geldart, L. P., 1995. Exploration Seismology - 2nd Edition. Cambridge University Press.

Sothcott, J., McCann, C. and O'Hara, S., 2000. The influence of two pore fluids on the acoustic properties of reservoir sandstones at sonic and ultrasonic frequencies. *70th Annual International Meeting, SEG, Expanded Abstracts,* 1883 - 1886.

Spencer, T. W., Sonnadt, J. R. and Butlers, T. M., 1982. Seismic Q-Stratigraphy or dissipation. *Geophysics*, **47**(1), 16-24.

Stockwell, R. G., Mansinha, L. and Lowe, R. P., 1996. Localization of the complex spectrum: The S transform: *IEEE Transactions on Signal Processing*, **44**, 998 - 1001.

Taylor, D., 2001. ANISEIS v5.2 Manual. Applied Geophysical Software Inc., Houston.

Thomsen, L., 1986. Weak elastic anisotropy. *Geophysics*, **51**(10), 1954 - 1966.

Thomsen, L., 1995. Elastic anisotropy due to aligned cracks in porous rock. *Geophysical Prospecting*, **43**, 805 - 830.

Tod, S. R., 2001. The effects on seismic waves of interconnected nearly aligned cracks. *Geophysical Journal International*, **146**, 249 - 263.

Toksõz, M. N. Johnston, D. H. and Timur, A., 1979. Attenuation of seismic waves in dry and saturated rocks: I. Laboratory measurements: *Geophysics*, **44**, 681 - 690.

Tonn, R., 1991. The determination of the seismic quality Q from VSP data: A comparison of different computational methods. *Geophysical Prospecting*, **39**, 1- 27.

Tsvankin, I., 2001. Seismic signatures and analysis of reflection data in anisotropic media: Handbook of Geophysical Exploration, vol. 29. Pergamon: Amsterdam.

Virieux J., 1984. SH-wave propagation in heterogeneous media: Velocity-stress finite-difference method. *Geophysics*, **49**, 1933 - 1957.

Virieux J., 1986. P-SV wave propagation in heterogeneous media: Velocity-stress finite-difference method. *Geophysics*, **51**, 889 - 901.

Vlastos, S., Liu, E., Main, I. G. and Narteau, C., 2003. Numerical simulation of wave propagation in 2-D fractured media: scattering attenuation at different stages of growth of fracture population. *Geophysical Journal International*, **171**, 865 - 880.

Walsh, J. B., 1966. Seismic wave attenuation in rock due to friction. *Journal of Geophysical Research,* **71**, 2591 - 2599.

Wang, S., Li, X. Y., Qian, Z., Di, B. and Wei, J., 2007. Physical modelling studies of 3-D P-wave seismic for fracture detection. *Geophysical Journal International*, **168**, 745 - 756.

Wang, Z., 2001. Fundamentals of seismic rock physics. *Geophysics*, **66**(2), 398 - 412.

Wei, J. X., 2004. A physical model study of different fracture densities. *Journal of Geophysics and Engineering*, **1**(1), 70 - 76.

Wei, J., Di, B. and Li, X Y., 2007a. Effects of fracture scale length and aperture on seismic waves: An experimental study. *77th Annual International Meeting, Expanded Abstracts, SEG*, 168 - 173.

Wei, J. X., Di, B. R. and Li., X. Y., 2007b. Effects of fracture scale length and aperture on seismic wave propagation: An experimental study. *Journal of Seismic Exploration*, **16**, 265 - 280.

Wei, J., Di, B. and Wang, Q., 2008. Experimental study on the effect of fracture scale on seismic wave characteristics. *Petroleum Science*, **5**, 119 - 125.

White, J. E., 1975. Computed seismic speeds and attenuation in rocks with partial gas saturation. *Geophysics*, **40**(2), 224 - 232.

White, R. E., 1992. The accuracy of estimating Q from seismic data. *Geophysics*, **57**(11) 1508 - 1511.

Wild, P. and Crampin, S., 1991. The range of effects of azimuthal isotropy and EDA anisotropy in sedimentary basins. *Geophysical Journal International*, **107**, 513 - 529.

Williamson, J. H., 1968. Least-squares fitting of a straight line. *Canadian Journal of Physics*, **46**, 1845 - 1847.

Willis, M. E., Burns, D. R., Rao, R., Minsley, B., Toksöz, M. N. and Vetri, L., 2006. Spatial orientation and distribution of reservoir fractures from scattered seismic energy. *Geophysics*, **71**(5), 043 - 051.

Willis, M. E., Pearce, F., Burns, D. R., Byun, J. and Minsley, B., 2004a. Reservoir fracture orientation and density from reflected and scattered seismic energy. *66th Annual International Meeting, EAGE, Extended Abstract.*

Willis, M. E., Rao, R., Burns, D., Byun, J. and Vetri, L. 2004b. Spatial orientation and distribution of reservoir fractures from scattered seismic energy: *72nd Annual International Meeting, Expanded Abstracts, SEG,* 1535 - 1538.

Winkler, K.W., 1986. Estimates of velocity dispersion between seismic and ultrasonic frequencies. *Geophysics*, **51**, 183 - 189.

Winkler, K. W., 1985. Dispersion analysis of velocity and attenuation in Berea sandstone. *Journal of Geophysical Research*, **90**, 3793 - 6800.

Winkler, K. W. and Nur, A., 1982. Seismic attenuation: effects of pore fluids and frictional sliding. *Geophysics*, **47**, 1 - 15.

Winterstein, D. F., 1990. Velocity anisotropy terminology for geophysicists. *Geophysics,* **55** (8) 1070 - 1088.

Xu, Y., 2011. Analysis of P-wave seismic response for fracture detection: modeling and case studies. PhD thesis, University of Edinburgh.

Xu, Y., Chapman, M., Li, X. Y. and Main. I. G., 2010. Fracture spacing effects on seismic anisotropy and scattering: A 3D numerical simulation study on discrete fracture models. *72nd EAGE Conference and Exhibition, Expanded Abstract.*

Yardley, G. S. and Crampin, S., 1991. Extensive - Dilatancy Anisotropy: Relative information in VSPs and reflection surveys. *Geophysical Prospecting*, **39**, 337 - 355.

Zhang, C. and Ulrych, T., 2002. Estimation of quality factors from CMP records. *Geophysics*, **67**(5), 1542 - 1547.

Ziolkowski, A., 1993. Determination of the signature of a dynamite source using source scaling, part 1: Theory. *Geophysics,* **58**(8), 1174 - 1182.

Zweigel, P., Arts, P., Lothe, A. E. and Lindeberg, E. B. G., 2004. Reservoir geology of the Utsira Formation at the first industrial-scale underground CO_2 storage site (Sleipner area, North Sea). In: Baines, S. and Worden, R. H. (eds.) Geological Storage for CO_2 Emissions Reduction. Geological Society, London, Special Publication, **233**, 165 - 180.

Appendix A: Anisotropic reflectivity method as implemented in ‘Aniseis’

Mark Chapman

1. Introduction

This note outlines the theory behind the implementation of the reflectivity method for anisotropic layered models in the commercial software package “ANISEIS”. While the theory for wave propagation in anisotropic materials has long been well established (Crampin, 1981), the particular approximations in “ANISEIS” appear to date from the work of Booth (1982), on which the description below is primarily based.

We emphasise two key points. Firstly, we identify the user defined “wavelet” with the volume injection function of Ziolkowski (1993). Secondly, we show that “ANISEIS” uses a “far-field” approximation - no attempt is made to model the near source term, and the solution is likely to break down completely in the vicinity of the source. This is consistent with numerical tests which have suggested that the solution is unreliable within a wavelength of the source. After a stationary phase approximation, the “pulse-shape” in the far field is shown to be proportional to the time derivative of the volume injection function.

We begin with the analytical solution for an explosive source in a homogeneous medium, and show how this can be manipulated into a sum of plane waves in the far-field. The basic plane wave ansatz of the “ANISEIS” method is then introduced, and we show how this is matched to the analytical solution in the source layer. This allows plane waves to be propagated individually through the model with standard procedures.

2. Analytical solution for an explosive source in an infinite homogeneous medium

The analytical solution to the problem of an explosive source in an infinite medium is spherically symmetric and given as (Ziolkowski, 1993):

$$\phi(R,t) = \frac{1}{R} f(t - \frac{R}{c}) ; \qquad \text{(A1)}$$

where ϕ is the displacement potential, f is the volume injection function, R is the distance from the source and c is the wavespeed. Taking the temporal Fourier transform of this equation, we obtain:

$$\phi(\mathrm{R},\omega) = \frac{\mathrm{F}(\omega)}{\mathrm{R}} \exp(\mathrm{i}\omega\frac{\mathrm{R}}{\mathrm{c}}) \qquad \text{(A2)}$$

The Sommerfeld integral states (Aki and Richards, 2002, p. 194):

$$\frac{1}{R}\exp(i\omega\frac{R}{c}) = \int_0^\infty \frac{k}{\gamma} J_0(kr)\exp(-\gamma z)dk ; \qquad \text{(A3)}$$

where:

$$\gamma = \sqrt{\frac{\omega^2}{c^2} - k^2} ; \qquad \text{(A4)}$$

$$r = \sqrt{x^2 + y^2} ; \qquad \text{(A5)}$$

so that (A1) can be written as:

$$\phi(R,\omega) = F(\omega)\int_0^\infty \frac{k}{\gamma} J_0(kr)\exp(-\gamma z)dk \qquad \text{(A6)}$$

The displacements may be evaluated from the spatial derivatives of (A6):

$$u_z(\omega) = \frac{\partial \phi}{\partial z} = -F(\omega)\int_0^\infty kJ_0(kr)\exp(-\gamma z)dk\,; \tag{A7}$$

$$u_r(\omega) = \frac{\partial \phi}{\partial r} = -F(\omega)\int_0^\infty \frac{k^2}{\gamma} J_1(kr)\exp(-\gamma z)dk\,; \tag{A8}$$

We now introduce the notation:

$$k_1 = \frac{\omega}{c}\,; \tag{A9}$$

$$v_1 = i\gamma\,; \tag{A10}$$

Allowing us to define the polarization vector as $(\sin\theta, \cos\theta)$ where:

$$\cos\theta = \frac{v_1}{k_1}\,; \tag{A11}$$

$$\sin\theta = \frac{k}{k_1} \tag{A12}$$

In these variables we have:

$$u_z(\omega) = -F(\omega)\int_0^\infty \frac{kk_1}{v_1}\cos\theta J_0(kr)\exp(-\gamma z)dk\,; \tag{A13}$$

$$\mathrm{u_r}(\omega) = -\mathrm{iF}(\omega)\int_0^\infty \frac{\mathrm{kk_1}}{\mathrm{v_1}}\sin\theta \mathrm{J_1(kr)}\exp(-\gamma \mathrm{z})\mathrm{dk} \tag{A14}$$

We now consider the far-field behaviour of these expressions in the limit $kr >> 0$ in which (see Abramovich and Stegun, 1970, p. 364):

$$J_0(kr) \approx \frac{1}{\sqrt{2\pi kr}}\exp(-i[kr - \frac{\pi}{4}])\,; \tag{A15}$$

$$J_1(kr) \approx iJ_0(kr) \tag{A16}$$

With these approximations, we have:

$$u_z(\omega) = -F(\omega)\exp(\frac{i\pi}{4})\int_0^{\infty}\frac{k_1}{v_1}\sqrt{\frac{k}{2\pi r}}\cos\theta\exp(-ikr-\gamma z)dk\,; \tag{A17}$$

$$u_r(\omega) = F(\omega)\exp(\frac{i\pi}{4})\int_0^{\infty}\frac{k_1}{v_1}\sqrt{\frac{k}{2\pi r}}\sin\theta\exp(-ikr-\gamma z)dk \tag{A18}$$

3. Modelling the source in “ANISEIS”

The general form for a plane wave propagating in an anisotropic medium is given by Booth (1982) as:

$$u_j = a_j \exp[i\omega(t - s_k x_k)]; \tag{A19}$$

where the a_j are the polarizations and the s_k are the slownesses. The concept of “ANISEIS” is to develop the solution in each layer entirely in terms of plane wave solutions to the wave equation in each layer. Specifically, the solution for the wavefield at a point (x, y, z) is assumed to be of the form:

$$\mathrm{u_i}(\omega) = F(\omega(\sum_{p=1}^{6}\int_{-\infty}^{\infty}\int_{-\infty}^{\infty} Sh^m(p)a_i^m(p)expi(k_x x + k_y y - \omega q_3\{z - d_m\})dk_x dk_\mathrm{y} \tag{A20}$$

In which we have 6 wave types (P, SV, SH up- and down-going), S is a source term, $h^m(p)$ is the “excitation factor” of the p’th wave type in the m’th layer and d_m is the depth of the m’th layer.

This representation is attractive in the anisotropic case since the theory for handling plane waves in anisotropic media is well established. For a given combination of (ω, k_x, k_y) the Christoffel equation reduces to a bi-cubic on the six admissible vertical wave numbers k_z, and the polarizations a_i can be obtained from an eigenvector problem. Reflection and transmission coefficients at a planar interface can also be calculated, allowing us to define the anisotropic propagator matrices - a procedure which appears to date from Crampin (1970).

To model the source, we require reconciling equation (A20) with the analytical solutions developed earlier. Critically, it is not possible to identify equation (A20) with the full solutions (A7) and (A8) which contain the "near source" term. It is however possible to match (A20) to the "far-field" expressions (A17) and (A18), and this forms the basis of the "ANISEIS" approximation.

For the case of the outgoing wavefield from the source in the first, isotropic, layer, there is only one wave type (p=1) and equation (A20) reduces to:

$$u_i = G(\omega)\int_{-\infty}^{\infty}\int_{-\infty}^{\infty} Sha_i \exp(ik_x x + ik_y y - \gamma z)dk_x dk_y \tag{A21}$$

We now move to polar coordinates in the (x, y) plane, so that

$$x = r\cos\phi_0 ; \tag{A22}$$

$$y = r\sin\phi_0 ; \tag{A23}$$

$$k_x = k\cos\phi ; \tag{A24}$$

$$k_y = k\sin\phi ; \tag{A25}$$

Noting that $dk_x dk_y = kdkd\phi$, equation (A21) can be written as:

$$u_z = -G(\omega)\int_0^{\infty}\int_0^{2\pi} kSh\cos\theta\exp(ikr\cos[\phi-\phi_0]-\gamma z)d\phi dk ; \tag{A26}$$

$$u_r = G(\omega)\int_0^{\infty}\int_0^{2\pi} kSh\sin\theta\exp(ikr\cos[\phi-\phi_0]-\gamma z)d\phi dk ; \tag{A27}$$

The symmetry of the problem, and the fact that from Aki and Richards (2002, p. 194):

$$J_0(x) = \frac{1}{2\pi}\int_0^{2\pi} \exp(ix\cos\phi)d\phi\,; \tag{A28}$$

allow us to write:

$$u_z = -2\pi G(\omega)\int_0^{\infty} kSh\cos\theta J_0(kr)\exp(-\gamma z)dk\,; \tag{A29}$$

$$u_r = 2\pi G(\omega)\int_0^{\infty} kSh\sin\theta J_0(kr)\exp(-\gamma z)dk\,; \tag{A30}$$

Using the far-field approximation (A15) once again, we obtain for $kr >> 0$:

$$u_z = -\sqrt{2\pi}G(\omega)\exp(\frac{i\pi}{4})\int_0^{\infty} Sh\sqrt{\frac{k}{r}}\cos\theta\exp(-ikr-\gamma z)dk\,; \tag{A31}$$

$$u_r = \sqrt{2\pi}G(\omega)\exp(\frac{i\pi}{4})\int_0^{\infty} Sh\sqrt{\frac{k}{r}}\sin\theta\exp(-ikr-\gamma z)dk\,; \tag{A32}$$

To match these expressions to those in (A17) and (A18), we identify $G(\omega)$ with the Fourier transform of the volume injection function and write:

$$S = \frac{k_1}{v_1}\,. \tag{A33}$$

The term h acts as a normalisation constant which accounts for the strength of the source.

These solutions may also be considered in the time domain. The inverse Fourier transform for the vertical component can be written as:

$$u_z(r,z,t) = \frac{1}{\sqrt{8\pi^2}}\exp(\frac{i\pi}{4})\int_{-\infty}^{\infty} d\omega i\omega G(\omega)\int_0^{\infty}\frac{1}{c\gamma}\sqrt{\frac{k}{r}}\cos\theta\exp(-ikr-\gamma z+i\omega t)dk \tag{A34}$$

The integral over dk may be evaluated by the method of stationary phase. For fixed large r, z the condition for stationarity is:

$$r + \frac{d\gamma}{dk} z = 0 ; \tag{A35}$$

from which we deduce the stationary wave number k_0 as:

$$k_0 = \frac{|r\omega|}{c\sqrt{z^2 + r^2}} ; \tag{A36}$$

and correspondingly we introduce:

$$\gamma_0 = \sqrt{\frac{\omega^2}{c^2 - k_0^2}} . \tag{A37}$$

We then have the approximation:

$$\int_0^\infty \frac{1}{c\gamma} \sqrt{\frac{k}{2\pi r}} \cos\theta \exp(-ikr + \gamma z) dk = \frac{1}{2c\gamma_0} \sqrt{\frac{k_0}{2rz\gamma_0''}} \cos\theta \exp(-ik_0 r + \gamma_0 z - \frac{i\pi}{4}) , \tag{A38}$$

Examining the dependencies on ω, we find that:

$$\gamma_0 \propto \omega ; \tag{A39}$$

$$k_0 \propto \omega ; \tag{A40}$$

$$\gamma_0'' \propto \frac{1}{\omega} ; \tag{A41}$$

so that the expression:

$$\frac{1}{2c\gamma_0}\sqrt{\frac{k_0}{2rz\gamma_0''}}\cos\theta\,; \qquad \text{(A42)}$$

is independent of ω. We can therefore write (A34) in the form:

$$u_z(r,z,t) = \int_{-\infty}^{\infty} i\omega G(\omega) I(r,z)\exp(-i\omega\{s_r r + s_z z - t\})d\omega \qquad \text{(A43)}$$

where $\exp(-i\omega\{s_r r + s_z z - t\})$ is a solution to the wave equation in the first layer. From equation (A43) it can be seen that the pulse shape in the far-field will be proportional to the time derivative of the user-defined volume injection function.

4. References

Abramowitz, M. and Stegun, I.A., 1970. Handbook of Mathematical Functions. 9th edition, Dover Publications Inc.

Aki, K. and Richards, P.G., 2002. Quantitative Seismology- 2nd edition, University Science Books.

Booth, D. C., 1982. The Anisotropic Reflectivity Technique. PhD Thesis, University of Edinburgh.

Crampin, S., 1970. The dispersion of surface waves in multilayered anisotropic structures. *Geophysical Journal of the Royal Astronomical Society.*, **21**, 387-402.

Crampin, S., 1981. A review of wave motion in anisotropic and cracked elastic media. *Wave Motion*, **3**, 343-391.

Ziolkowski, A. M., 1993. Determination of the signature of a dynamite source using source scaling, Part I: Theory. *Geophysics*, **58**(8), 1174-1182.

Appendix B: Publications

Ekanem, A. M.*, Li, X. Y., Chapman, M. and Main, I. G., 2011. Synthetic modelling study of the effect of P-wave anisotropy in fractured media. *73rd EAGE Conference and Exhibition, Barcelona,* Extended abstract.

Ekanem, A. M.*, Wei, J., Li, X. Y., Chapman, M. and Main, I. G., 2010. Physical modelling studies of the effect of fracture thickness on P-wave attenuation. *72nd EAGE Conference and Exhibition,* Extended abstract.

Ekanem, A. M.*, Wei, J., Li, X. Y., Chapman, M. and Main, I. G., 2009. P-wave Attenuation Anisotropy in Fractured Media: Results from Laboratory ‘Scale model. *71st EAGE Conference and Exhibition,* Extended abstract.

Ekanem, A. M.*, Wei, J., Wang, S. Di, B., Li, X. Y., and Chapman, M., 2009. Fracture detection from 2-D seismic data: A seismic physical modelling study. *79th Annual International Meeting, SEG,* Expanded abstract

Ekanem, A. M., Wei, J., Wang, S. Di, B. and Li, X. Y.,* 2009. P-wave Attenuation Anisotropy in Fractured Media: A seismic physical modelling study. *CPS/SEG International Geophysical Conference and Exposition, Beijing, China,* Expanded abstract